

Transport phenomena and capacitance of open quantum semiconductor nanostructures

Von der Fakultät für Mathematik, Naturwissenschaften und Informatik
der Brandenburgischen Technischen Universität Cottbus

zur Erlangung des akademischen Grades

Doktor der Naturwissenschaften
(Dr. rer. nat.)

genehmigte Dissertation

vorgelegt von

Diplom-Physiker
Paul Nicolae Racec

geboren am 15.04.1972 in Campulung Moldovenesc, Rumänien

Gutachter: Prof. Dr. rer. nat. habil. Ernst Sigmund

Prof. Dr. rer. nat. habil. Wolfgang Hansen

Research Professor Dr. Alexandru Aldea

Tag der mündliche Prüfung: 16.07.2002

Abstract

We consider semiconductor devices that are composed of two parts, first a mesoscopic quantum structure constituting the active region, and, second, a classical environment with larger typical length scales. While in general the classical environment should be represented by a drift-diffusion model we consider here only simple contacts which we take as ideal metals with infinite conductivity. The transport through the quantum structure is described like in the Landauer-Büttiker formalism through electronic scattering wave-functions which define the electron density in the quantum system. Further sources of the self-consistent Coulomb field are layers of classical charges in the contacts at each of the interfaces to the quantum system. We present further a capacitance model that takes into account the openness of the quantum structure and the existence of finite contacts embedding the system. The analysed structures are considered at very low temperatures. As particular structures we study simple tunnelling barriers and a field induced two-dimensional electron gas in a special GaAs/Al_xGa_{1-x}As heterostructure.

For the single-barrier tunnelling structures, the capacitance presents oscillations with applied bias, with maxima every time a (Fabry-Perot like) resonance crosses the chemical potential in the source reservoir. Furthermore, at the same voltages, the conductance exhibits shoulders.

For the field induced two dimensional electron gas, based on our self-consistent calculations, we are able to perform a detailed analysis of the interaction between the quantum system and the contact reservoir. We find that the quasi-bound state that exists in the nearly closed system develops at the transition to the open system into a separate type of resonance with distinct characteristics. Excellent quantitative agreement shows that this transition is seen in the measured step in the C-V characteristic on MIS-type semiconductor heterostructure.

The R -matrix method can be used to reduce computing times for the calculation of transmission probabilities in mesoscopic semiconductor systems. We generalise results for strictly one-dimensional transport to systems which show confinement in more dimensions like a point contact. The formalism is applied to a tunnelling barrier with a Kronig-Penney-type potential modulation in the lateral direction. In the limit of very high barriers we find resonances which are created by the mismatch of the wave functions inside and outside the barrier. It is shown that this type of resonance has a qualitatively different behaviour than resonant tunnelling peaks.

Contents

1	Introduction	3
2	Formalism and models	7
2.1	The R-matrix formalism for 1D scattering problems	9
2.1.1	General form of scattering states for 1D problems	9
2.1.2	S-matrix formulation of 1D scattering problems	13
2.1.3	R-matrix formulation of 1D scattering problems	14
2.1.4	Relation between R- and S-matrix	17
2.1.5	R-matrix representation of the scattering states	19
2.2	Electronic charge density	20
2.3	Poisson equation	22
2.3.1	Assumptions	23
2.3.2	Green's function for Poisson equation	24
2.4	Mean-field approximation	26
2.4.1	Hartree approximation	27
2.4.2	Self-consistent procedure	29
2.5	Current through mesoscopic structures	33
2.5.1	Coherent tunneling	33
2.6	Capacitance of mesoscopic structures	39
2.6.1	Charge balance	39
2.6.2	Plate charges Σ_1 and Σ_2	40
2.7	Characteristics of GaAs/Al _x Ga _{1-x} As/GaAs structures	43
3	Capacitance of a field-induced 2DEG	45
3.1	The structure	45
3.2	Flat band configuration	48
3.2.1	N_A doping effect	52
3.3	Applied bias	55
3.3.1	Wigner Eisenbud functions	56
3.3.2	Wave functions and quasi bound states	57
3.4	Comparison to the MOS	61
3.5	Capacitance	63

3.5.1	Impenetrable barrier	68
3.6	Intermediate resonance	69
3.6.1	Analytical calculations: Fano resonances	72
3.7	Models for high voltages: quasi bound states	76
3.7.1	Charge distribution	77
3.7.2	The potential energy	80
3.8	Exchange correlations effects	82
3.9	Summary	87
4	Capacitance of a single-tunneling barrier	89
4.1	The structure	89
4.2	Potential and electronic density distributions	91
4.2.1	Without applied bias	92
4.2.2	With applied bias	93
4.3	Tunneling current	97
4.3.1	Connection between current and quasi-bound states	99
4.3.2	Conductance	101
4.4	Capacitance	102
4.5	Summary	104
5	Laterally modulated tunneling barrier	107
5.1	Formalism for two-dimensional systems	108
5.1.1	Transmission probabilities with the R -matrix	108
5.1.2	Scattering states as Bloch functions	110
5.1.3	S -matrix theory	112
5.1.4	Construction of the R -matrix	114
5.2	Conductance	116
5.3	Single-level approximation	117
5.4	Laterally modulated barrier	118
5.4.1	Transport through a single structure	124
5.5	Summary	126
6	Conclusions	129
A	Hartree-Fock equations	131
B	List of symbols	139
	Bibliography	141

Chapter 1

Introduction

In the ohmic regime the conductance G of a rectangular three-dimensional conductor is directly proportional to its cross-sectional surface S and inversely proportional to its length L

$$G = \sigma S/L, \quad (1.1)$$

where the conductivity σ , an intensive quantity, is the same anywhere in the material and it is a material characteristic. The conductance G is calculated then taking into account the dimensions of the semiconductor piece [1].

With the permanent requirement in microelectronics for a constant scaling down in size of integrated circuits appears the normal question: How small can one make the dimensions before this ohmic behavior breaks down? In this way appears a new category of systems: the *mesoscopic* systems are the systems that are much larger than microscopic objects like atoms, but not large enough to be 'ohmic' [2]. At low temperatures, the conductance of mesoscopic samples can not be found by combining the conductivity of its smaller parts, which means that the scaling theory does not work anymore.

There are three characteristic length scales [3]: i) the *Fermi* wavelength, $\lambda_F = 2\pi/k_F$, which is related to the Fermi energy of the electrons $\epsilon_F = \hbar^2 k_F^2 / (2m^*)$ ($\lambda_F \approx 10\text{nm}$ in semiconductors, $\lambda_F \approx 1\text{nm}$ in metals); ii) the *mean free path*, l , which is the distance that an electron travels before its initial momentum is destroyed ($l \approx \mu\text{m}$ in high-quality semiconductors); and iii) the *phase-relaxation* length (also called dephasing length or coherence length) L_ϕ , which is the distance that an electron travels before its initial phase is destroyed ($L_\phi \approx \mu\text{m}$) and is much larger than the mean free path. These length scales vary widely from one material to another and are strongly affected by temperature, magnetic fields, etc. A conductor usually shows ohmic behavior if its dimensions are much larger than any of these characteristic length scales.

In the last decades, at the beginning of 1980s, it has become possible through the modern growing techniques [4] MBE (molecular beam epitaxy) and MOCVD (metal-organic chemical vapor deposition), to grow structures and devices for which the characteristic dimensions are actually smaller than the appropriate mean free paths

of interest. This provides samples with very intriguing properties: in GaAs/Al_xGa_{1-x}As semiconductor heterostructures it is possible at low temperatures to reach high concentrations of transport carriers, $N_s = 10^{11}\text{cm}^{-2}$, with very high mobilities of $10^6\text{cm}^2/\text{Vs}$ [5, 6] which allows for construction of very fast devices [7, 8, 9]. But in such devices, the *classical* Boltzmann equation it is not anymore suitable for describing transport properties. To describe transport properties through structures with dimensions that vary on the order of the de Broglie wavelength of carriers, the non-locality of the particle invalidates the simplifying approximation of instantaneous (in both space and time) phase-randomizing collisions, which allows for decoupling of higher-order particle distributions functions in the Boltzmann equations [2], Chap. 2.7. For structures with characteristic length L smaller than the mean free path l , i.e. $L \ll l$, one may assume that the particles move through the active region without scattering. This is termed *ballistic transport* [2]. If the total length of the system is smaller than the coherence length, i.e. $L \ll L_\phi$, then the phase coherence can be maintained over the transport distance so that the electron can be described by a wave function extended over the whole system.

In conclusion, the *mesoscopic* devices or *nanostructures* are the high quality semiconductor devices for which the characteristic length of the active region can be comparable to or smaller than the Fermi wavelength λ_F . The charge carriers can be described fully in quantum mechanical formalism and very interesting quantum effects can be exploited [10].

Over the last two decades transport has been investigated in a multitude of different mesoscopic semiconductor systems [3, 11]. Many phenomena such as the universal conductance fluctuations [12], the Aharonov-Bohm oscillations [13], the quantum Hall effect [14] and its quenching in small systems [15], the quantized conductance in ballistic point contacts [16], Coulomb blockade oscillations [17], and chaotic dynamics in quantum dots [18] have been discussed in the well known theory pioneered by Landauer and Büttiker [19, 20, 21, 22, 23] and Tsu and Esaki [24]. This approach describes transport through transmission probabilities of electronic scattering wave functions. Therefore, the understanding and the practical evaluation of transmission- and reflection coefficients play a crucial role in many problems of quantum transport.

Especially when the system involves more than one essential dimension the practical calculation of the transmission coefficients proves difficult. We distinguish between two different types of approaches to solve this problem. In the first type the transmission is calculated directly by numerically solving the Schrödinger equation for each energy with scattering boundary conditions. Examples for this type are the recursive Green's function technique [25, 26] and a similar recursive procedure to obtain the wave functions directly [27]. This approach has the disadvantage that it provides no analytical insight. The second type approaches make use of the general S-matrix theory [28] to reformulate the problem. In this way, it is possible to find analytical properties as well as to gain numerical advantages. The reference to the general S-matrix theory is particularly valuable in the discussion of isolated or in-

interacting transport resonances which can be represented by poles of the S-matrix in the complex energy plane. Examples for the second type approaches are the spectral projection method as developed in Refs. [29], the effective Hamiltonian description [30] and the R-matrix approach which is used in this thesis.

The R-matrix method is a two-step procedure (see Sect. 2.1): At first, the R-matrix is constructed in a time-consuming step solving the Schrödinger equation with particular boundary conditions. We call the resulting eigenfunctions Wigner-Eisenbud functions and the eigenenergies Wigner-Eisenbud energies. Then, the S-matrix and thus the scattering states which contain information about transmission between incident and evanescent states are constructed in a relatively fast second step. This two-step procedure is one of the numerical advantages of the R-matrix method. The analytical advantage of the R-matrix theory is that it provides a natural description for resonant transport and transport in multipole devices.

The R-matrix method has originally been developed in the context of scattering cross sections in nuclear- and atomic physics [31]. More recently the R-matrix method has been applied to calculate the transmission of electromagnetic modes in microcavities [32]. The application of the R-matrix technique to mesoscopic semiconductor systems was demonstrated in an initiating paper by Smrčka [33] for one-dimensional structures. In a strongly simplified version, namely in the single level approximation, the R-matrix has also been used in multidimensional systems to analyze the statistics of isolated tunneling peaks in a Coulomb blockade system [18, 34, 35].

In many cases a comparison with experimental structures requires the consideration of Coulomb interaction. Therefore we integrated the Coulomb interaction in the R-matrix scheme on a Hartree level (Sect. 2.4). All the models are performed at very low temperatures, i.e. $T \leq 4.2K$.

The structure of this thesis is as following:

In Chap. 2 we present our model used to treat the transport problems through mesoscopic structures. The R-matrix method for one-dimensional tunneling systems is reviewed in Sec. 2.1. After that, we present the calculation of the electronic density distribution in quantum mechanical formalism and the self-consistent scheme for open systems in mean-field approximation. We present the two principal concepts of characterizing transport in mesoscopic structures: the tunneling current and the capacitance. The tunneling current is calculated in Landauer-Büttiker formalism. For the capacitance we present a new model which takes into account the openness of the system and the existence of finite contacts embedding the system. The capacitance model is based on the ancestry of the carriers and not on their spatial distribution.

We analyze in Chap. 3 the capacitance of a field induced two dimensional electron gas (2DEG) sandwiched between a back contact and a blocking barrier. The peculiarities of the structure are that the quantum system is in contact only with one reservoir and the blocking barrier suppresses the charge transfer from one side to the other side of the structure. Based on our models, we perform a detailed anal-

ysis of the interaction of a quantum system, in our case the field-induced 2DEG, with the contacts through particle exchange. Our capacitance model provides a very accurate description of the capacitance measurements performed on the MIS-type semiconductor heterostructures.

In Chap. 4, we analyze a single-tunneling barrier, which is in contact with two reservoirs and also a tunneling current flows. There is no spacer between the highly-doped layers and the tunneling barrier. The same self-consistent scheme for open systems is used. It is shown that the capacitance exhibits oscillations with applied bias, with maxima at the same voltages where the conductance presents shoulders. Furthermore, these voltages correspond to the configurations where Fabry-Perot resonances cross the chemical potential on the source reservoir.

In Chap. 5 we extend the R-matrix formalism to two-dimensional systems. The analyzed structure is a tunneling barrier with a periodical lateral modulation. We consider no applied bias between source and drain contacts and we do not take into account the Coulomb interaction. For strong modulation we find a transition from the known quantized conductivity in e^2/h of a single point contact for small average barrier height, to a series of resonant peaks of height e^2/h for high barriers. At weak modulation we demonstrate that the miniband structure of the lateral dispersion can be resolved in dc transport in the forward direction in the limit of large average barrier height.

In the last chapter are presented the conclusions of this thesis.

Chapter 2

Formalism and models

The subject of this thesis are quantum semiconductor nanostructures. The quantum confinement for the nanostructures we consider is achieved through the growth of heterogeneous layers having different bandgaps which can lead to a quantization perpendicular to the substrate surface.

The general geometry is sketched in the Fig. 2.1.

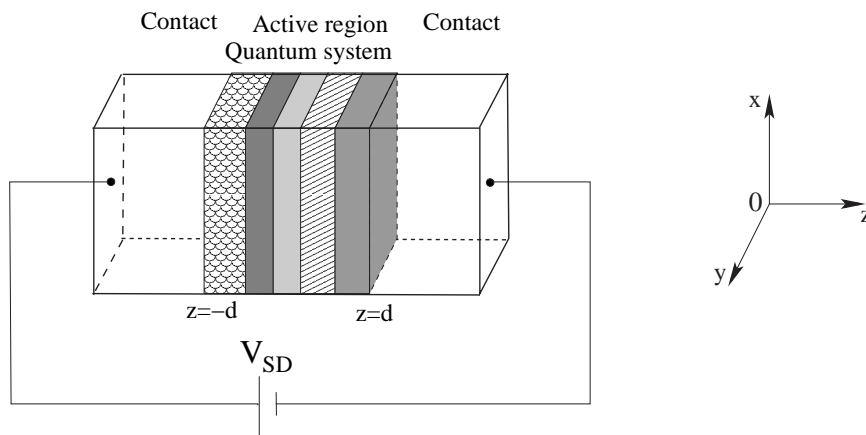


Figure 2.1: General geometry of the samples.

We will restrict our discussion of transport in nanostructures only to the conduction band states. The direction of transport is parallel to the growth direction. The electronic states will be described within the envelope function approximation [36]. The applicability of the envelope function approximation in mesoscopic systems has been discussed in a review by Burt [37]. The main achievement of this approximation is that the wave function in mesoscopic structures can be written as

$$\Phi(\mathbf{r}) = \sum_j \phi_j(\mathbf{r}) u_{j0}(\mathbf{r}), \quad (2.1)$$

where j is the band index and $u_{j0}(\mathbf{r})$ is the periodic part of Bloch functions at $k = 0$, which contains the information about the material. $\phi_j(\mathbf{r})$, the so called *envelope function*, contains information about the geometrical structure of the sample. The envelope function equation in the *effective mass approximation* is a Schrödinger type equation

$$\left(-\frac{\hbar^2}{2} \frac{\partial}{\partial z} \frac{1}{m^*(z)} \frac{\partial}{\partial z} - \frac{\hbar^2}{2m_{\perp}^*} \nabla_{\perp}^2 + V(z) \right) \phi(x, y, z) = E\phi(x, y, z), \quad (2.2)$$

where $m^*(z)$ and m_{\perp}^* are the effective mass parallel and perpendicular to the direction of transport, respectively. ∇_{\perp} is calculated with respect to the direction perpendicular to the direction of transport. $V(z)$ is the effective potential in the direction of growth and is mainly given by the conduction-band offsets of the heterostructure. It can also include contributions from the ionized dopants, free carriers, and the applied potential itself, in a self-consistent calculation.

Since for the heterojunction system without lateral gates the potential variation is only in the direction of growth (in our case z -direction), the solution is separable as

$$\phi_{n,k_x,k_y} = \frac{1}{\sqrt{L_x L_y}} \psi_n(z) \exp(ik_x x) \exp(ik_y y), \quad (2.3)$$

corresponding to free electron motion in the plane (x, y) parallel to the interfaces, with L_x, L_y being the lateral lengths of the system. The one-dimensional eigenfunctions $\psi_n(z)$ satisfy the equation

$$-\frac{\hbar^2}{2} \frac{d}{dz} \frac{1}{m^*(z)} \frac{d}{dz} \psi_n(z) + V(z) \psi_n(z) = \epsilon_n \psi_n(z), \quad (2.4)$$

where n labels the eigenstates in the growth direction.

Assuming, for simplicity, parabolic bands, the total energy relative to the band minima is thus

$$E_{n,k_x,k_y} = \frac{\hbar^2(k_x^2 + k_y^2)}{2m_{\perp}^*} + \epsilon_n. \quad (2.5)$$

In Fig. 2.1, V_{SD} denotes the total external bias applied between contacts, while V_{sd} will be used further for the bias drop only on the quantum structure. Depending on how the quantum structure is contacted there can be a difference between these two quantities.

We will assume further, for simplicity, the same effective mass over the whole structure. This assumption is correct as long as the analyzed effects are not strongly influenced by the effective mass variation. One can also choose the same mass over the whole structure, when the transport time is short and the electron does not feel the differences in the lattice structure.

2.1 The R-matrix formalism for 1D scattering problems

We will solve the scattering problem (2.4) in the R-matrix formalism. This method is described in Ref. [93] based on the Lippmann-Schwinger equation for the case with no applied bias between the contacts in the transport direction. In this section we will describe this formalism for one-dimensional tunneling systems with a finite potential difference V_{sd} between both sides of the barrier. The scattering potential $V(z)$, Fig. 2.2, is given generally by $V = V_L$ in the left (source-) contact, $z < -d$, and $V = V_R$ for the right (drain-) contact, $z > d$. Within the scattering area, $-d < z < d$, the potential is allowed to vary arbitrarily.

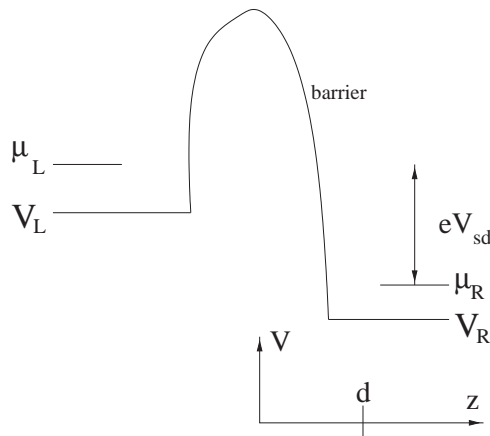


Figure 2.2: One-dimensional scattering potential. The chemical potentials of the contacts μ_L and μ_R are separated by the applied bias energy eV_{sd} .

2.1.1 General form of scattering states for 1D problems

An effectively 1D scattering process can be described by the time-independent Schrödinger equation

$$\left[-\frac{\hbar^2}{2m^*} \frac{d^2}{dz^2} + V(z) - \epsilon \right] \psi(z, \epsilon) = 0, \quad (2.6)$$

where $V(z)$ is the scattering potential. Here ϵ is the kinetic energy in the direction of transport, given by Eq. (2.5). We split the potential $V(z) = V_0(z) + \Delta V(z)$ in an unperturbed potential V_0 and a potential perturbation $\Delta V(z)$. We choose

$$V_0(z) = V_L \Theta(-z) + V_R \Theta(z), \quad (2.7)$$

so that $\Delta V(z) = V(z) - V_0(z)$ vanishes for $|z| > d$. Equation (2.6) can be rewritten as

$$\left[\frac{\hbar^2}{2m^*} \frac{d^2}{dz^2} - V_0(z) + \epsilon \right] \psi(z, \epsilon) = \Delta V(z) \psi(z, \epsilon). \quad (2.8)$$

We now interpret this equation as an inhomogeneous differential equation, where the left hand side is the Schrödinger equation of the unperturbed particle, and the potential on the right hand side is treated as an inhomogeneous term. The inhomogeneous Schrödinger equation can be solved using the unperturbed Green function $\mathcal{G}_0(z, z'; \epsilon)$ which is the solution of the equation

$$\left[\frac{\hbar^2}{2m^*} \frac{d^2}{dz^2} - V_0(z) + \epsilon \right] \mathcal{G}_0(z, z'; \epsilon) = \delta(z - z'). \quad (2.9)$$

Using the matching conditions, the Green's function $\mathcal{G}_0(z, z'; \epsilon)$ can be found analytically [38], and reads for $z' < 0$

$$\begin{aligned} \mathcal{G}_0(z, z'; \epsilon) &= \frac{m^*}{\hbar^2} \frac{1}{ik_L} \left[e^{-ik_L(z-z')} + \frac{k_L - k_R}{k_L + k_R} e^{-ik_L(z+z')} \right], & z < z' \\ &= \frac{m^*}{\hbar^2} \frac{1}{ik_L} \left[\frac{k_L - k_R}{k_L + k_R} e^{-ik_L(z+z')} + e^{ik_L(z-z')} \right], & z' < z < 0 \\ &= \frac{m^*}{\hbar^2} \frac{2}{ik_L + ik_R} e^{-ik_L z' + ik_R z}, & z > 0 \end{aligned} \quad (2.10)$$

whereas for $z' > 0$,

$$\begin{aligned} \mathcal{G}_0(z, z'; \epsilon) &= \frac{m^*}{\hbar^2} \frac{2}{ik_L + ik_R} e^{-ik_L z + ik_R z'}, & z < 0 \\ &= \frac{m^*}{\hbar^2} \frac{1}{ik_R} \left[\frac{k_R - k_L}{k_L + k_R} e^{-ik_R(z+z')} + e^{ik_R(z-z')} \right], & 0 < z < z' \\ &= \frac{m^*}{\hbar^2} \frac{1}{ik_R} \left[e^{ik_R(z-z')} + \frac{k_R - k_L}{k_L + k_R} e^{ik_R(z+z')} \right], & z > z'. \end{aligned} \quad (2.11)$$

The Schrödinger equation of the unperturbed particle

$$\left[-\frac{\hbar^2}{2m^*} \frac{d^2}{dz^2} + V_0(z) - \epsilon \right] \psi_0^{L/R}(z, \epsilon) = 0 \quad (2.12)$$

has as solutions the scattering wave functions for a single-step potential, $\psi_0^{L/R}(z, \epsilon)$. Application of standard matching techniques yields [39] Chap. 5.4, for $\epsilon \geq V_L \geq V_R$

$$\psi_0^L(z, \epsilon) = \begin{cases} \exp(ik_L z) + \frac{k_L - k_R}{k_L + k_R} \exp(-ik_L z), & z < 0 \\ \frac{2k_L}{k_L + k_R} \exp(ik_R z), & z > 0 \end{cases} \quad (2.13)$$

$$\psi_0^R(z, \epsilon) = \begin{cases} \frac{2k_R}{k_L + k_R} \exp(-ik_L z), & z < 0 \\ \exp(-ik_R z) - \frac{k_L - k_R}{k_L + k_R} \exp(ik_R z), & z > 0 \end{cases} \quad (2.14)$$

There are two orthogonal eigenstates for each energy, ψ_0^L and ψ_0^R , which have the physical meaning that a particle of energy ϵ can be moving to the right (ψ_0^L) or to the left (ψ_0^R) with the momentum

$$k_{L/R} = \sqrt{\frac{2m^*}{\hbar^2}(\epsilon - V_{L/R})}. \quad (2.15)$$

By means of $\mathcal{G}_0(z, z'; \epsilon)$ the Schrödinger equation (2.8) can be transformed to an equivalent integral equation

$$\psi(z, \epsilon) = \psi_0(z, \epsilon) + \int_{-d}^{+d} dz' \mathcal{G}_0(z, z'; \epsilon) \Delta V(z') \psi(z', \epsilon), \quad (2.16)$$

where $\psi_0(z, \epsilon)$ is the solution of the unperturbed Schrödinger equation (2.12). We have thus obtained the *Lippmann-Schwinger* equation. It is not really a solution of the Schrödinger equation, as the unknown wave function $\psi(z, \epsilon)$ still enters the right hand side of the equation but it provides the required asymptotic form of the scattering states. Substituting Eqs. (2.10) and (2.11) in Eq. (2.16) we find for $z \leq -d$

$$\psi^L(z, \epsilon) = a^L(\epsilon) \exp(ik_L z) + b^L(\epsilon) \exp(-ik_L z), \quad (2.17)$$

with $a^L(\epsilon) = 1$ and

$$\begin{aligned} b^L(\epsilon) &= \frac{k_L - k_R}{k_L + k_R} + \frac{m^*}{\hbar^2} \frac{1}{ik_L} \int_{-d}^0 dz' \left[e^{ik_L z'} + \frac{k_L - k_R}{k_L + k_R} e^{-ik_L z'} \right] \Delta V(z') \psi^L(z', \epsilon) \\ &+ \frac{m^*}{\hbar^2} \frac{2}{ik_L + ik_R} \int_0^d dz' e^{ik_R z'} \Delta V(z') \psi^L(z', \epsilon). \end{aligned} \quad (2.18)$$

For $z \geq d$ we obtain

$$\psi^L(z, \epsilon) = c^L(\epsilon) \exp(ik_R z) + d^L(\epsilon) \exp(-ik_R z), \quad (2.19)$$

with

$$d^L(\epsilon) = 0$$

and

$$\begin{aligned} c^L(\epsilon) &= \frac{2k_L}{k_L + k_R} + \frac{m^*}{\hbar^2} \frac{1}{ik_L} \int_0^d dz' \left[e^{-ik_R z'} - \frac{k_L - k_R}{k_L + k_R} e^{ik_R z'} \right] \Delta V(z') \psi^L(z', \epsilon) \\ &+ \frac{m^*}{\hbar^2} \frac{2}{ik_L + ik_R} \int_0^d dz' e^{-ik_L z'} \Delta V(z') \psi^L(z', \epsilon). \end{aligned} \quad (2.20)$$

Corresponding results are obtained for ψ^R : for $z \geq d$

$$\psi^R(z, \epsilon) = c^R(\epsilon) \exp(ik_R z) + d^R(\epsilon) \exp(-ik_R z), \quad (2.21)$$

with $d^R(\epsilon) = 1$ and

$$\begin{aligned} c^R(\epsilon) &= \frac{k_R - k_L}{k_L + k_R} + \frac{m^*}{\hbar^2} \frac{1}{ik_R} \int_0^d dz' \left[e^{-ik_R z'} - \frac{k_L - k_R}{k_L + k_R} e^{ik_R z'} \right] \Delta V(z') \psi^R(z', \epsilon) \\ &+ \frac{m^*}{\hbar^2} \frac{2}{ik_L + ik_R} \int_{-d}^0 dz' e^{-ik_L z'} \Delta V(z') \psi^R(z', \epsilon) \end{aligned} \quad (2.22)$$

and for $z \leq -d$

$$\psi^R(z, \epsilon) = a^R(\epsilon) \exp(ik_L z) + b^R(\epsilon) \exp(-ik_L z) \quad (2.23)$$

with $a^R(\epsilon) = 0$ and

$$\begin{aligned} b^R(\epsilon) &= \frac{2k_R}{k_L + k_R} + \frac{m^*}{\hbar^2} \frac{1}{ik_L} \int_{-d}^0 dz' \left[e^{ik_L z'} + \frac{k_L - k_R}{k_L + k_R} e^{-ik_L z'} \right] \Delta V(z') \psi^R(z', \epsilon) \\ &+ \frac{m^*}{\hbar^2} \frac{2}{ik_L + ik_R} \int_0^d dz' e^{ik_R z'} \Delta V(z') \psi^R(z', \epsilon). \end{aligned} \quad (2.24)$$

ψ^L is interpreted as *scattering state coming from the left* reservoir with an incident- and a reflected wave described in Eq. (2.17) and a transmitted wave described in Eq. (2.19) and ψ^R has the interpretation of *scattering state coming from the right* reservoir with an incident- and a reflected wave described in Eq. (2.21) and a transmitted wave described in Eq. (2.23).

We then define

$$t^L(\epsilon) = c^L(\epsilon) \quad (2.25)$$

and

$$t^R(\epsilon) = b^R(\epsilon) \quad (2.26)$$

as transmission amplitudes from left to right and right to left, respectively. The reflection amplitudes are defined analogously:

$$r^L(\epsilon) = b^L(\epsilon) \quad (2.27)$$

and

$$r^R(\epsilon) = c^R(\epsilon). \quad (2.28)$$

These coefficients are functions of the particle energy in direction of transport, ϵ .

The probability flux density, or "current", is defined as [39], Sec. 5.3.,

$$j_z = \frac{\hbar}{2m^*i} \left(\psi^* \frac{d}{dz} \psi - \psi \frac{d}{dz} \psi^* \right). \quad (2.29)$$

Using the asymptotic form of the left incident scattering state, Eq. (2.17), we can calculate the incident probability current density

$$j_{inc}^L(\epsilon) = \frac{\hbar k_L}{m^*} |a^L(\epsilon)|^2 = \frac{\hbar k_L}{m^*} \quad (2.30)$$

and the reflected probability current density

$$j_{refl}^L(\epsilon) = \frac{\hbar k_L}{m^*} |b^L(\epsilon)|^2. \quad (2.31)$$

Thus, we can define the *reflection coefficient* (or *reflection probability*) as ratio of reflected current to incident current

$$R^L(\epsilon) = \frac{j_{refl}^L(\epsilon)}{j_{inc}^L(\epsilon)} = |b^L(\epsilon)|^2 = |r^L|^2. \quad (2.32)$$

The transmitted probability current density is calculated using Eq. (2.19),

$$j_{trans}^L(\epsilon) = \frac{\hbar k_R}{m^*} |c^L(\epsilon)|^2 \quad (2.33)$$

so that the *transmission coefficient* (or *transmission probability*) is the ratio of transmitted current to incident current

$$T^L(\epsilon) = \frac{j_{trans}^L(\epsilon)}{j_{inc}^L(\epsilon)} = \frac{k_R}{k_L} |c^L(\epsilon)|^2 = \frac{k_R}{k_L} |t^L(\epsilon)|^2. \quad (2.34)$$

Analogously, we can define the transmission and reflection coefficients for the scattering states coming from the right, $T^R(\epsilon) = (k_L/k_R)|t^R(\epsilon)|^2$ and $R^R = |r^R(\epsilon)|^2$, respectively. Based on the probability current density conservation, we have for any energy $\epsilon \geq V_L \geq V_R$

$$T^L(\epsilon) + R^L(\epsilon) = 1, \quad T^R(\epsilon) + R^R(\epsilon) = 1. \quad (2.35)$$

Due to time-reversal symmetry, that reflects the microscopic reversibility of quantum mechanics itself, we have the following symmetry properties

$$T^L(\epsilon) = T^R(\epsilon), \quad R^L(\epsilon) = R^R(\epsilon), \quad (2.36)$$

showing that the transmission and reflection probabilities are independent of the direction of the incident wave upon the barrier.

2.1.2 S-matrix formulation of 1D scattering problems

To establish the S-matrix we introduce a decomposition

$$\psi = \psi^{in} + \psi^{out}, \quad (2.37)$$

of a general state $\psi = \alpha\psi^L + \beta\psi^R$ with α and β complex numbers, into an incoming part ψ^{in} and an outgoing part ψ^{out} . This is equivalent to setting other two linear solutions of the Eq. (2.6) ψ^{in} and ψ^{out} instead of ψ^L and ψ^R . Using the solutions of the unperturbed system, (2.13) and (2.14), we set for $z \leq -d$:

$$\psi^{in}(z, \epsilon) = \alpha \exp(ik_L z) \quad (2.38)$$

and for $z \geq d$

$$\psi^{in}(z, \epsilon) = \beta \exp(-ik_R z). \quad (2.39)$$

The corresponding outgoing parts

$$\psi^{out}(z, \epsilon) = \psi(z, \epsilon) - \psi^{in}(z, \epsilon) \quad (2.40)$$

are then

$$\psi^{out}(z, \epsilon) = [\alpha r^L(\epsilon) + \beta t^R(\epsilon)] \exp(-ik_L z) \quad (2.41)$$

for $z \leq -d$ and

$$\psi^{out}(z, \epsilon) = [\alpha t^L(\epsilon) + \beta r^R(\epsilon)] \exp(ik_R z) \quad (2.42)$$

for $z \geq d$.

The S-matrix is defined as

$$\psi^{out}(z, \epsilon) = S(z, -\mathcal{L})\psi^{in}(-\mathcal{L}, \epsilon) + S(z, \mathcal{L})\psi^{in}(\mathcal{L}, \epsilon), \quad (2.43)$$

mapping the ingoing wavefunction at two points $\pm\mathcal{L}$ with arbitrary $\mathcal{L} \geq d$ to the outgoing wavefunction outside of $[-\mathcal{L}, \mathcal{L}]$. To establish a relation between the S-matrix and the transmission- and reflection coefficients we define the 2×2 - matrix

$$\hat{S} = \begin{bmatrix} S(-\mathcal{L}, -\mathcal{L}) & S(-\mathcal{L}, +\mathcal{L}) \\ S(+\mathcal{L}, -\mathcal{L}) & S(+\mathcal{L}, +\mathcal{L}) \end{bmatrix}. \quad (2.44)$$

Inserting the forms for $\psi^{in/out}$ into Eq. (2.43) we obtain

$$\begin{bmatrix} r^L & t^R \\ t^L & r^R \end{bmatrix} = \begin{bmatrix} e^{-i2k_L \mathcal{L}} S(-\mathcal{L}, -\mathcal{L}) & e^{-i(k_L+k_R)\mathcal{L}} S(-\mathcal{L}, +\mathcal{L}) \\ e^{-i(k_L+k_R)\mathcal{L}} S(+\mathcal{L}, -\mathcal{L}) & e^{-i2k_R \mathcal{L}} S(+\mathcal{L}, +\mathcal{L}) \end{bmatrix}. \quad (2.45)$$

In this way the transmission and reflection coefficients can be constructed from the S-matrix at two points $\pm\mathcal{L}$. In our formulation, Eq. (2.43), the S-matrix connects the wave function and not only the coefficients of a linear combination of (plane) waves. But writing the S-matrix elements for a fixed \mathcal{L} , Eq. (2.44), we have the same expression as in Weisbuch and Vinter [40], Chap. 2, Eq. (33d). The reflection and transmission coefficients are related to the S-matrix by a similar relation as for the case of no applied bias [93] which is obtained if we substitute k_L and k_R by k_z .

2.1.3 R-matrix formulation of 1D scattering problems

Next we want to give a practical method for calculating the scattering states and in turn to calculate the S-matrix, based on the general idea that one can express a wave function in terms of a *suitable* orthonormal and complete system of functions.

Such a system of functions is provided by the Wigner-Eisenbud functions $\chi_l(z)$, used first in nuclear physics [41], which are the solutions of the Schrödinger-type equation

$$\left[-\frac{\hbar^2}{2m^*} \frac{d^2}{dz^2} + V(z) \right] \chi_l(z) = \epsilon_l \chi_l(z), \quad (2.46)$$

with the Neumann boundary conditions

$$\left. \frac{d\chi_n}{dz} \right|_{-\mathcal{L}} = \left. \frac{d\chi_n}{dz} \right|_{\mathcal{L}} = 0. \quad (2.47)$$

The Wigner-Eisenbud energies ϵ_l and functions $\chi_l(z)$ are real [41]. These functions are defined only on the interval $[-\mathcal{L}, \mathcal{L}]$. They are an orthonormal and complete system of functions. Let us demonstrate the orthonormality of this system. We can write Eq. (2.46) also for l' index

$$\left[-\frac{\hbar^2}{2m^*} \frac{d^2}{dz^2} + V(z) \right] \chi_{l'}(z) = \epsilon_{l'} \chi_{l'}(z). \quad (2.48)$$

We multiply (2.46) with $\chi_{l'}(z)$ and (2.48) with $\chi_l(z)$ and after that we subtract them and integrate the result over the interval $[-\mathcal{L}, \mathcal{L}]$:

$$-\frac{\hbar^2}{2m^*} \int_{-\mathcal{L}}^{\mathcal{L}} dz \left[\chi_l(z) \frac{d^2}{dz^2} \chi_{l'}(z) - \chi_{l'}(z) \frac{d^2}{dz^2} \chi_l(z) \right] = (\epsilon_l - \epsilon_{l'}) \int_{-\mathcal{L}}^{\mathcal{L}} dz \chi_l(z) \chi_{l'}(z) \quad (2.49)$$

Integrating the left side by parts and using the boundary conditions (2.47) we have for $l \neq l'$

$$(\epsilon_l - \epsilon_{l'}) \int_{-\mathcal{L}}^{\mathcal{L}} dz \chi_l(z) \chi_{l'}(z) = 0$$

and that means:

$$\int_{-\mathcal{L}}^{\mathcal{L}} \chi_l(z) \chi_{l'}(z) dz = 0 \quad \text{for } l \neq l' \quad (2.50)$$

The normalization condition for this system of functions is written as

$$\frac{1}{2\mathcal{L}} \int_{-\mathcal{L}}^{\mathcal{L}} \chi_l(z) \chi_l(z) dz = 1 \quad (2.51)$$

By analogy to the Sturm-Liouville systems, it is assumed the completeness of this system of functions for the interval $[-\mathcal{L}, \mathcal{L}]$,

$$\sum_{l=1}^{\infty} \chi_l(z) \chi_l(z') = \delta(z - z') \quad (2.52)$$

We would like to expand the scattering states in the basis of the Wigner-Eisenbud functions. We multiply (2.6) by $\chi_l(z)$, conjugate complex (2.46) and multiply it by $\psi(z, \epsilon)$, subtract both equations and integrate the result over the interval $[-\mathcal{L}, \mathcal{L}]$. At the end we obtain:

$$-\frac{\hbar^2}{2m^*} \int_{-\mathcal{L}}^{\mathcal{L}} dz \left[\chi_l(z) \frac{d^2}{dz^2} \psi(z, \epsilon) - \psi(z, \epsilon) \frac{d^2}{dz^2} \chi_l(z) \right] = (\epsilon - \epsilon_l) \int_{-\mathcal{L}}^{\mathcal{L}} dz \psi(z, \epsilon) \chi_l(z)$$

The left side can be integrated by parts and using the Wigner-Eisenbud boundary conditions (2.47) it is obtained that

$$\frac{\hbar^2}{2m^*} \left[\chi_l(-\mathcal{L}) \frac{d\psi}{dz}(-\mathcal{L}, \epsilon) - \chi_l(\mathcal{L}) \frac{d\psi}{dz}(\mathcal{L}, \epsilon) \right] = (\epsilon - \epsilon_l) \int_{-\mathcal{L}}^{\mathcal{L}} \psi(z, \epsilon) \chi_l(z) dz. \quad (2.53)$$

At this point we introduce the normal derivative of the wavefunction (which contains the sign):

$$\psi_S(\pm\mathcal{L}, \epsilon) = \pm \frac{1}{m^*} \frac{d\psi}{dz}(\pm\mathcal{L}, \epsilon) \quad (2.54)$$

and obtain:

$$-\frac{\hbar^2}{2} \frac{\chi_l(-\mathcal{L})\psi_S(-\mathcal{L}, \epsilon) + \chi_l(\mathcal{L})\psi_S(\mathcal{L}, \epsilon)}{\epsilon - \epsilon_l} = \int_{-\mathcal{L}}^{\mathcal{L}} \psi(z, \epsilon) \chi_l(z) dz \quad (2.55)$$

Since $\{\chi_l(z)\}$ is an orthonormal basis, then we can expand the wave function $\psi(z, \epsilon)$ in terms of the $\chi_l(z)$ but only for $z \in [-\mathcal{L}, \mathcal{L}]$:

$$\psi(z, \epsilon) = \sum_{l=1}^{\infty} a_l(\epsilon) \chi_l(z), \quad (2.56)$$

where

$$a_l(\epsilon) = \frac{1}{2\mathcal{L}} \int_{-\mathcal{L}}^{\mathcal{L}} \psi(z, \epsilon) \chi_l(z) dz \quad (2.57)$$

The above expansion is true in the sense of "mean convergence" as defined in functional analysis. That means

$$|\psi(z, \epsilon) - \sum_{l=1}^{\infty} a_l(\epsilon) \chi_l(z)|^2 \rightarrow 0 \quad (2.58)$$

but this is not true locally, as for a particular point z_0 one has

$$\psi(z_0, \epsilon) \neq \sum_{l=1}^{\infty} a_l(\epsilon) \chi_l(z_0) \quad (2.59)$$

so that we can **not** write $\frac{d}{dz}\psi(\pm\mathcal{L}, \epsilon) = \sum_{l=1}^{\infty} a_l(\epsilon) \frac{d}{dz}\chi_l(\pm\mathcal{L}) = 0$

Defining Green's function for the Wigner-Eisenbud problem as

$$G(z, z'; \epsilon) = \frac{1}{2\mathcal{L}} \sum_{l=1}^{\infty} \frac{\chi_l(z) \chi_l(z')}{\epsilon - \epsilon_l} \quad (2.60)$$

and inserting (2.55) and (2.57) into (2.56) we can write the wavefunctions

$$\psi(z, \epsilon) = -\frac{\hbar^2}{2} [G(z, \mathcal{L}; \epsilon)\psi_S(\mathcal{L}, \epsilon) + G(z, -\mathcal{L}; \epsilon)\psi_S(-\mathcal{L}, \epsilon)] \quad (2.61)$$

We *define* the R -matrix elements by:

$$R(z, z'; \epsilon) = -\frac{\hbar^2}{2}G(z, z'; \epsilon) = -\frac{\hbar^2}{4\mathcal{L}} \sum_{l=1}^{\infty} \frac{\chi_l(z)\chi_l(z')}{\epsilon - \epsilon_l} \quad (2.62)$$

and obtain the general expression of the wavefunction in terms of its normal derivatives

$$\psi(z, \epsilon) = R(z, -\mathcal{L}; \epsilon)\psi_S(-\mathcal{L}, \epsilon) + R(z, \mathcal{L}; \epsilon)\psi_S(\mathcal{L}, \epsilon) \quad z \in [-\mathcal{L}, \mathcal{L}]. \quad (2.63)$$

Thus, the R -matrix elements relate the total wavefunction to its normal derivatives at $\pm\mathcal{L}$. As it is shown in Eq. (2.62), the R -matrix elements can be constructed using the Wigner Eisenbud functions. For the one-dimensional case, we find

$$R(\pm\mathcal{L}, \pm\mathcal{L}) = \frac{\hbar^2}{4\mathcal{L}} \sum_{n=1}^{\infty} \frac{\chi_n(\pm\mathcal{L})\chi_n(\pm\mathcal{L})}{\epsilon_n - \epsilon}, \quad (2.64)$$

where ϵ_n are the eigenenergies associated with the Wigner-Eisenbud problem.

If we want to calculate the normal derivative of the wave function at the points $\pm\mathcal{L}$, because of the mean convergence series in (2.64) we have to use the expressions which are outside of the scattering region (i.e. (2.17) and (2.19) for ψ_L , and (2.21) and (2.23) for ψ_R). The wave function and its first derivative are anyway continuous.

2.1.4 Relation between R- and S-matrix

We will construct further the relation between the R -matrix and S -matrix, where we define \hat{R} analogous to \hat{S} ,

$$\hat{R} = \begin{bmatrix} R(-\mathcal{L}, -\mathcal{L}) & R(-\mathcal{L}, +\mathcal{L}) \\ R(+\mathcal{L}, -\mathcal{L}) & R(+\mathcal{L}, +\mathcal{L}) \end{bmatrix}. \quad (2.65)$$

Using the relations (2.38) and (2.41), we can write for $z \leq -d$:

$$\frac{d\psi^{in}}{dz} = ik_L\psi^{in}, \quad (2.66)$$

$$\frac{d\psi^{out}}{dz} = -ik_L\psi^{out}, \quad (2.67)$$

and using (2.39) and (2.42) for $z \geq d$:

$$\frac{d\psi^{in}}{dz} = -ik_R\psi^{in}, \quad (2.68)$$

$$\frac{d\psi^{out}}{dz} = ik_R\psi^{out}. \quad (2.69)$$

The wave functions are decomposed into an incoming- and an outgoing part,

$$\begin{pmatrix} \psi(-\mathcal{L}) \\ \psi(+\mathcal{L}) \end{pmatrix} = \begin{pmatrix} \psi^{in}(-\mathcal{L}) \\ \psi^{in}(+\mathcal{L}) \end{pmatrix} + \begin{pmatrix} \psi^{out}(-\mathcal{L}) \\ \psi^{out}(+\mathcal{L}) \end{pmatrix} \quad (2.70)$$

and we can write

$$\begin{pmatrix} \psi_S(-\mathcal{L}) \\ \psi_S(+\mathcal{L}) \end{pmatrix} = \frac{i}{m^*} \hat{K} \begin{pmatrix} \psi^{out}(-\mathcal{L}) \\ \psi^{out}(+\mathcal{L}) \end{pmatrix} - \frac{i}{m^*} \hat{K} \begin{pmatrix} \psi^{in}(-\mathcal{L}) \\ \psi^{in}(+\mathcal{L}) \end{pmatrix} \quad (2.71)$$

where \hat{K} is a 2×2 -matrix with the elements

$$\hat{K} = \begin{bmatrix} k_L & 0 \\ 0 & k_R \end{bmatrix}. \quad (2.72)$$

If we note

$$\begin{aligned} \hat{\Psi} &= \begin{pmatrix} \psi(-\mathcal{L}) \\ \psi(+\mathcal{L}) \end{pmatrix}, & \hat{\Psi}_S &= \begin{pmatrix} \psi_S(-\mathcal{L}) \\ \psi_S(+\mathcal{L}) \end{pmatrix}, \\ \hat{\Psi}^{out} &= \begin{pmatrix} \psi^{out}(-\mathcal{L}) \\ \psi^{out}(+\mathcal{L}) \end{pmatrix}, & \hat{\Psi}^{in} &= \begin{pmatrix} \psi^{in}(-\mathcal{L}) \\ \psi^{in}(+\mathcal{L}) \end{pmatrix}, \end{aligned} \quad (2.73)$$

then we can work in a matrix form

$$\begin{aligned} \hat{\Psi} &= \hat{R} \hat{\Psi}_S, \\ \hat{\Psi}_S &= \frac{i}{m^*} \hat{K} \hat{\Psi}^{out} - \frac{i}{m^*} \hat{K} \hat{\Psi}^{in}, \\ \hat{\Psi} &= \hat{\Psi}^{out} + \hat{\Psi}^{in}, \end{aligned} \quad (2.74)$$

which implies

$$\frac{i}{m^*} \hat{R} (\hat{K} \hat{\Psi}^{out} - \hat{K} \hat{\Psi}^{in}) = \hat{\Psi}^{out} + \hat{\Psi}^{in}. \quad (2.75)$$

So, we have

$$\begin{aligned} \left(\frac{i}{m^*} \hat{R} \hat{K} - 1\right) \hat{\Psi}^{out} &= \left(\frac{i}{m^*} \hat{R} \hat{K} + 1\right) \hat{\Psi}^{in}, \\ \hat{\Psi}^{out} &= \hat{S} \hat{\Psi}^{in}, \end{aligned} \quad (2.76)$$

or

$$\left(\frac{i}{m^*} \hat{R} \hat{K} - 1\right) \hat{S} = \left(\frac{i}{m^*} \hat{R} \hat{K} + 1\right). \quad (2.77)$$

Finally, for each ϵ the relation between the R - and the S -matrix [33] is

$$\hat{S}(\epsilon) = -(1 - \frac{i}{m^*} \hat{R}(\epsilon) \hat{K})^{-1} (1 + \frac{i}{m^*} \hat{R}(\epsilon) \hat{K}). \quad (2.78)$$

This relation is similar with the relation for the case without applied bias [93], only that the \hat{K} matrix has another form. The information stored by the S-matrix or by the R-matrix is the same, one has to choose the suitable procedure to extract it.

2.1.5 R-matrix representation of the scattering states

The distance between \mathcal{L} and d has no relevant importance for the scattering problem. Considering the boundary points for the Wigner-Eisenbud problem equal to the boundaries of the scattering region, i.e. $\mathcal{L} = d$, the Wigner-Eisenbud energies become the eigenenergies of the closed counterpart of our scattering system [42].

So, we have the scattering states in the R-matrix formalism

$$\psi_n^L(z) = \frac{1}{\sqrt{L_z}} \begin{cases} e^{ik_n z} + r^L e^{-ik_n z}, & -L_z/2 \leq z \leq -d \\ R(z, -d)\psi_S^L(-d) + R(z, d)\psi_S^L(d), & -d \leq z \leq d \\ t^L e^{ik_n z}, & d \leq z \leq L_z/2 \end{cases} \quad (2.79)$$

for the wave function coming from the left reservoir, and

$$\psi_n^R(z) = \frac{1}{\sqrt{L_z}} \begin{cases} t^R e^{-ik_n z}, & -L_z/2 \leq z \leq -d \\ R(z, -d)\psi_S^R(-d) + R(z, d)\psi_S^R(d), & -d \leq z \leq d \\ e^{-ik_n z} + r^R e^{ik_n z}, & d \leq z \leq L_z/2 \end{cases} \quad (2.80)$$

for the wave function coming from the right reservoir. L_z is the total length of the structure in the z -direction, which is much larger than the size of the scattering region ($L_z \gg d$). The energy spectrum corresponding to the electron motion in the direction of transport is quasicontinuous

$$\epsilon = \frac{\hbar^2 k_z^2}{2m^*} = \epsilon_n \quad (2.81)$$

with $k_z = \frac{2\pi}{L_z}n = k_n$, $n \in \mathbf{N}$. The total energy of the particle is

$$E_{n,k_x,k_y} = \frac{\hbar^2}{2m}(k_x^2 + k_y^2) + \epsilon_n, \quad (2.82)$$

where k_x and k_y are the wave vectors associated with the electron free motion in the direction parallel to the interfaces.

The practical procedure for finding the wave functions is:

- solve the Wigner-Eisenbud problem Eq. (2.46), for the scattering potential with the Neumann type boundary conditions (2.47). This is done numerically by standard techniques for solving eigenvalue problems with discrete spectrum. The Wigner-Eisenbud functions are defined on the interval $[-\mathcal{L}, \mathcal{L}]$ and they constitute an orthonormal and complete system of functions Eqs. (2.50), (2.51) and (2.52).
- for each energy ϵ construct the R-matrix elements Eq. (2.64) using the Wigner-Eisenbud energies and functions;

- for each energy ϵ construct the S-matrix elements using the simple matrixial relation (2.78) between R- and S-matrix, where the Λ matrix has the general form (2.72);
- find for any energy ϵ the transmission and reflection coefficients, Eq. (2.45);

The decisive advantage of using R-matrix is that it can be calculated from a given set of Wigner-Eisenbud functions *for all energies*. Otherwise the transmission coefficients should be calculated solving a Schrödinger equation (2.6) with scattering boundary conditions for a continuum of energies. This is usually done in the transfer matrix formalism [43, 44, 45, 92], in which one makes a piecewise constant approximation for the scattering potential. For every energy one has to find the wave vectors in each region with constant potential, after that to compute the transfer matrix elements and to multiply the 2×2 matrixes. This can be a time consuming computation problem which we want to avoid.

The R-matrix formalism gives a more accurate description for a general shape of the scattering potential $V(z)$ and with the help of the Wigner-Eisenbud functions and energies one can obtain the analytical description of the scattering problem in terms of the poles of the S-matrix [46]. Furthermore one can calculate the shape and the width of the tunneling peaks.

- calculate the normal derivative of the wave functions at the boundary points $\pm d$, using the expressions of the wave functions outside the scattering interval;
- use Eq. (2.62) for the R-matrix elements for any $z \in [-d, d]$;
- use Eqs. (2.79) and (2.80) for the wave functions.

2.2 Electronic charge density

In this section we would like to present the application of the R-matrix formalism to the calculation of the electronic charge density distribution in a semiconductor heterostructure. As it was shown in the previous section, the scattering potential $V(z)$ varies only in the direction of transport, and it is constant outside the interval $z \in [-d, d]$. Consequently, the wavefunctions are separable and are given by Eq. (2.3). z dependent part of the wave functions, the so called scattering functions, are solutions of the 1D Schrödinger equation (2.6) and are given in the R-matrix formalism by Eqs. (2.79) and (2.80).

To calculate the electronic charge density in the Landauer-Büttiker formalism, the electrons can be thought of as two Fermi-gases. First, the electrons coming from the source contact: They occupy the single-particle scattering states ϕ_{n,k_x,k_y}^L according to the Fermi-Dirac distribution function $f_{FD}(E_{n,k_x,k_y} - \mu_L)$, where μ_L is the chemical potential of the source contact. Second, the electrons coming from

the drain contact with single-particle states ϕ_{n,k_x,k_y}^R and with the chemical potential μ_R of the drain contact. Summing up for all single-particle states the occupation factor times the localization probability we obtain the electronic density distribution (which multiplied by $-e$ will give the electronic charge distribution)

$$\rho(z) = 2 \sum_{n,k_x,k_y} f_{FD}(E_{n,k_x,k_y} - \mu_L) |\phi_{n,k_x,k_y}^L|^2 + 2 \sum_{n,k_x,k_y} f_{FD}(E_{n,k_x,k_y} - \mu_R) |\phi_{n,k_x,k_y}^R|^2, \quad (2.83)$$

where 2 comes from the spin degeneracy. The electrons are free in the lateral directions and thus the electronic density distribution is

$$\rho(z) = 2 \sum_{n,k_x,k_y} \frac{|\psi_n^L(z)|^2}{L_x L_y} f_{FD}(E_{n,k_x,k_y} - \mu_L) + 2 \sum_{n,k_x,k_y} \frac{|\psi_n^R(z)|^2}{L_x L_y} f_{FD}(E_{n,k_x,k_y} - \mu_R). \quad (2.84)$$

The Fermi-Dirac function

$$f_{FD}(E - \mu) = \frac{1}{e^{\frac{E-\mu}{k_B T}} + 1}, \quad (2.85)$$

gives the equilibrium distribution function in the reservoirs.

In the low temperatures limit, $\mu \rightarrow E_F$ and the values $E_F^{L/R} - V_{L/R}$ are fixed by the doping value in reservoirs through the Sommerfeld model for free electron gas, with spin, considering all the donors ionized [47]

$$N_D = k_F^3 / 3\pi^2. \quad (2.86)$$

As Zimmermann suggested in Ref. [48] for donor concentrations larger than $5 \times 10^{16} \text{cm}^{-3}$ an impurity band forms within the conduction band so that even at low temperature all donors are ionized.

For equal doping we have $E_F^L - V_L = E_F^R - V_R$ and the general relation $E_F^R = E_F^L - eV_{sd}$ for applied bias V_{sd} becomes, of course, $V_R = V_L - eV_{sd}$.

For large L_x, L_y we can transform the summation (2.84) into an integration, and for low temperature, where all the states until E_F are occupied, one can write

$$\begin{aligned} \rho(z) &= 2 \frac{L_x L_y}{2\pi} \sum_n \int_0^{k_F^{(n)}} dk k \frac{|\psi_n^L(z)|^2}{L_x L_y} + 2 \frac{L_x L_y}{2\pi} \sum_n \int_0^{k_F^{(n)}} dk k \frac{|\psi_n^R(z)|^2}{L_x L_y} \\ &= 2 \frac{1}{2\pi} \sum_n \int_0^{k_F^{(n)}} dk k |\psi_n^L(z)|^2 + 2 \frac{1}{2\pi} \sum_n \int_0^{k_F^{(n)}} dk k |\psi_n^R(z)|^2 \end{aligned} \quad (2.87)$$

with $k_F^{(n)} = \sqrt{k_F^2 - k_n^2}$, where the corresponding k_F should be considered for every integral. Furthermore, because $\psi_n^{L/R}(z)$ does not depend on k_x and k_y , we can perform the integration over $k = \sqrt{k_x^2 + k_y^2}$, with an upper limit for $T = 0K$ of

$k_F^{L/R} = \sqrt{\frac{2m^*}{\hbar^2}(E_F^{L/R} - V_{L/R})}$. Hence, for large L_z we obtain in the zero-temperature limit

$$\rho(z) = 2 \frac{L_z}{(2\pi)^2} \left[\int_0^{k_F^L} dk_z \frac{(k_F^L)^2 - k_z^2}{2} |\psi^L(k_z, z)|^2 + \int_0^{k_F^R} dk_z \frac{(k_F^R)^2 - k_z^2}{2} |\psi^R(k_z, z)|^2 \right]. \quad (2.88)$$

The choice of normalization factor $1/\sqrt{L_z}$ in Eqs. (2.79) and (2.80), leads to a density of charge far away from the scattering area independent of the sample length. If L_z is infinite then the normalization constant in front of Eq. (2.79) and (2.80) should be $1/\sqrt{2\pi}$ instead of $1/\sqrt{L_z}$.

Eq. (2.88) can be also written for equal doping reservoirs as

$$\rho(z) = 2 \frac{1}{2\pi} \frac{L_z}{2\pi} \int_{-k_F}^{k_F} |\psi(k_z, z)|^2 \frac{k_F^2 - k_z^2}{2} dk_z \quad (2.89)$$

where the positive wave vectors k_z correspond to the scattering wave functions coming from the left, and those for negative values correspond to the scattering wave functions coming from the right.

To particularize Eq. (2.88) for the case of free electrons (with spin), one has to consider that $L_z |\psi(k_z, z)|^2 = 1$ and thus it is obtained the Sommerfeld expression for electron concentration in metals.

We would like to point out that the Eq. (2.88) takes into account the continuous energy spectrum of the incident electrons, which is a key feature of our method.

Numerical procedures

One important goal in an accurate calculation of the charge distribution (2.88) is the correct integration procedure. We have used the extended trapezoidal rule, as numerical integration method. We also made use of a basic idea for numerical implementation of this method: one can double the number of intervals without losing the benefit of previous work. [49]. The integral is calculated with an user defined accuracy, which was established at 10^{-5} or a maximum number of steps, set at 10000.

Using the analytical description of the poles of the S-matrix [46], we can take into account the quasi-bound states performing the numerical integration over the associated peak. This will be analyzed in detail for the capacitance of field induced 2DEG, Chap. 3. An accurate calculation of the electronic density distribution is of major importance for a self-consistent convergent scheme.

2.3 Poisson equation

In this section we will formulate and solve Poisson equation for effectively one dimensional systems, with respect to the transport properties. For the beginning a number of simplifications are discussed. Most of them are similar to the Poisson equation for Si/SiO₂ system, conditions discussed in detail by Nicollian and Brews in Ref. [50].

Poisson equation is

$$\frac{d^2\varphi(z)}{dz^2} = -\frac{q(z)}{\epsilon_0\epsilon_r} \quad (2.90)$$

where $q(z)$ is the charge density (C/cm^3), $\varphi(z)$ is the electrostatic potential, and ϵ_r is the dielectric permittivity in units of the dielectric permittivity of vacuum, ϵ_0 . The total charge density is

$$q(z) = e \left[p(z) - \rho(z) - N_A^-(z) + N_D^+(z) \right], \quad (2.91)$$

where

- $p(z)$ is the hole concentration [cm^{-3}]
- $\rho(z)$ is the electron concentration [cm^{-3}]
- $N_A^-(z)$ is the ionized acceptor concentration [cm^{-3}]
- $N_D^+(z)$ is the ionized donor concentration [cm^{-3}]

2.3.1 Assumptions

We solve the Poisson equation with certain simplifying conditions. These conditions are:

1. Poisson equation will be solved in one dimension in the direction perpendicular to the heterostructure interfaces, which is also the direction of transport. It is reasonable to treat only one dimension because the field under the gate is uniform and perpendicular to the interface surface. The fringing field at the gate edge is negligible, affecting an area that extends for only a(n) (oxide) barrier thickness from the gate periphery. In practice, the gate diameter is orders of magnitude larger than this area. Therefore, edge effects would become important if the extent of the gate were compared with the barrier thickness.
2. We assume that the impurity concentration in the GaAs is uniform (N_D in the doping region and N_A outside). We know that this assumption does not apply always (for example the thermal treatments causes redistribution of the impurity concentration at the surface). However, the case of a uniform impurity distribution is a good introduction.
3. The holes concentration will be neglected in comparison to the electrons concentration, because we consider highly n-doped reservoirs.
4. The electrons concentration will be calculated from the Schrödinger equation (see Sec. 2.2) and not from thermal equilibrium distribution.

5. Poisson equation will be solved using an approximate charge density. The charge of the dopant ions is accounted for approximately by smearing out the ion charge into a uniform background density. This smearing ignores the discrete nature of these ions as well as statistical variations in their spatial distributions. The charge of electrons and holes is treated in a self consistent field approximation. That is, each electron or hole is treated as though it moved in an *averaged* field. This average field is computed as the field due to the *average* mobile charge density plus the field due to the smeared out the dopant ion charge. Thus each electron or hole can be treated as an *independent* particle in an (approximate) average field. In this approach the average carrier distribution is a function only of the average potential, if one ignores all dependences on more detailed properties of the real potential. Conversely, the average field also is assumed to depend only on the *average* carrier and dopant ion densities, ignoring dependence on more detailed properties of the charge densities. For very large electron or hole concentrations and also at low temperatures, the treatment of electrons and holes as independent particles may fail.

6. Surface quantization is not neglected. Surface quantization occurs as follows: Suppose that a high electric field ($> 10^6$ V/cm) is applied to the structure, attracting a high concentration of free carriers to the blocking barrier surface. Because these carriers cannot flow through the barrier, they are trapped in a narrow potential well at the surface of the barrier. Because the potential well is very narrow, carrier motion is restricted in a direction perpendicular to the interfacial plane. In this direction only standing wave patterns are possible, thus resulting in electric subbands. The energy separation between energy levels in these subbands become important for low temperatures and high fields. Although free carriers are quantized for motion perpendicular to the plane of the interface, they are free to move and are not quantized in directions parallel to the interfacial plane. Fang and Howard [51] were the first to demonstrate surface quantization experimentally.

2.3.2 Green's function for Poisson equation

In this section we would like to present the solution of Poisson equation using Green's function for the problem of a volume charge distribution around N objects (metals) K_j which are at the constant potential U_j , $j = \overline{1, N}$.

Therefore we have to solve the equation

$$\Delta\varphi(\mathbf{r}) = -\frac{1}{\epsilon_0\epsilon_r}q(\mathbf{r}) \quad (2.92)$$

where $q(\mathbf{r})$ is the density of volume charge ($[C/m^{-3}]$) distributed in the system and includes the sign of the charge too, with the following boundary conditions

- $\lim_{|\mathbf{r}| \rightarrow \infty} \varphi(\mathbf{r}) = 0$
- $\varphi(\mathbf{r}) = U_j, \quad \mathbf{r} \in F(K_j), \quad j = 1, \dots, N.$

The solution of the problem is written using Green's function (see Chap. 3 in Ref. [52])

$$\varphi(\mathbf{r}) = \int_V G(\mathbf{r}, \mathbf{r}') q(\mathbf{r}') d\mathbf{r}' - \epsilon_0 \epsilon_r \sum_{j=1}^N U_j \int_{F(K_j)} \nabla_{\mathbf{r}'} G(\mathbf{r}, \mathbf{r}') d\vec{f}' \quad (2.93)$$

where

- $\Delta G(\mathbf{r}, \mathbf{r}') = -\frac{\delta(\mathbf{r}-\mathbf{r}')}{\epsilon_0 \epsilon_r}, \quad \mathbf{r}, \mathbf{r}' \in V$
- $G(\mathbf{r}, \mathbf{r}') = 0, \quad \mathbf{r} \in F(V), \mathbf{r}' \in V$
- $\lim_{|\mathbf{r}| \rightarrow \infty} G(\mathbf{r}, \mathbf{r}') = 0, \quad \mathbf{r}' \in V.$

1D problem

We can apply the above theory to the one dimensional problem. Charge distribution is $q(z)$ (in $[C/m^{-3}]$), $l_1 \leq z \leq l_2$ and for $z \leq l_1$ and $l_2 \leq z$ we have metallic contacts (the potential is constant). So, the boundary conditions become:

$$\varphi(l_1) = U_1, \quad \varphi(l_2) = U_2 \quad (2.94)$$

The geometry of the problem is sketched in the Fig. 2.3.

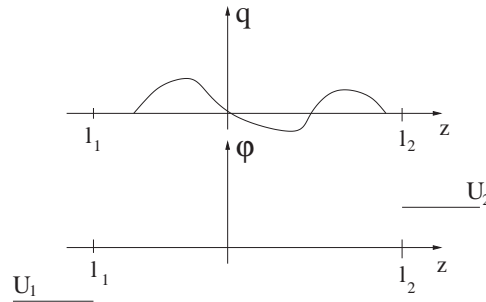


Figure 2.3: The geometry for the 1D charge distribution with two metallic contacts.

The free space 1D Green's function for Poisson equation is

$$G_0(z, z') = -\frac{1}{2\epsilon_0 \epsilon_r} |z - z'| \quad (2.95)$$

to which we can add a homogeneous solution

$$\tilde{G}(z, z') = Azz' + Bz + Cz' + D$$

which makes the resulting Green's function, $G = G_0 + \tilde{G}$, obey the boundary conditions (item b) above).

$$G(z = l_1, z') = G(z = l_2, z') = 0, \quad z' \in (l_1, l_2). \quad (2.96)$$

If one inserts the expressions for $G_0(z, z')$ and $\tilde{G}(z, z')$ into relations (2.96) and equals the coefficients of z, z' and the free term from both relations with zero, one obtains a system which provides the coefficients

$$B = \frac{1}{2\epsilon_0\epsilon_r} \frac{l_2 + l_1}{l_2 - l_1}, \quad D = -\frac{1}{\epsilon_0\epsilon_r} \frac{l_2 \cdot l_1}{l_2 - l_1}, \quad A = -\frac{1}{\epsilon_0\epsilon_r} \frac{1}{l_2 - l_1}, \quad C = B.$$

Green's function becomes

$$G(z, z') = -\frac{1}{\epsilon_0\epsilon_r} \left[\frac{1}{2}|z - z'| + \frac{1}{l_2 - l_1} z \cdot z' - \frac{1}{2} \frac{l_2 + l_1}{l_2 - l_1} (z + z') + \frac{l_2 \cdot l_1}{l_2 - l_1} \right], \quad (2.97)$$

for $l_1 \leq z \leq l_2$, $l_1 \leq z' \leq l_2$. Inserting this expression in Eq. (2.93) one obtains the electrostatic potential

$$\begin{aligned} \varphi(z) &= -\frac{1}{\epsilon_0\epsilon_r} \int_{l_1}^{l_2} \left(\frac{1}{2}|z - z'| + \frac{1}{l_2 - l_1} z \cdot z' - \frac{1}{2} \frac{l_2 + l_1}{l_2 - l_1} (z + z') + \frac{l_2 \cdot l_1}{l_2 - l_1} \right) q(z') dz' \\ &\quad + U_1 + (U_2 - U_1) \frac{z - l_1}{l_2 - l_1}, \quad \text{for } l_1 \leq z \leq l_2, \end{aligned} \quad (2.98)$$

and the associated potential energy, experienced by an electron,

$$\begin{aligned} V_c(z) &= -e\varphi(z) \\ &= \frac{e}{\epsilon_0\epsilon_r} \int_{l_1}^{l_2} \left(\frac{1}{2}|z - z'| + \frac{1}{l_2 - l_1} z \cdot z' - \frac{1}{2} \frac{l_2 + l_1}{l_2 - l_1} (z + z') + \frac{l_2 \cdot l_1}{l_2 - l_1} \right) q(z') dz' \\ &\quad + V_1 + (V_2 - V_1) \frac{z - l_1}{l_2 - l_1}, \quad \text{for } l_1 \leq z \leq l_2, \end{aligned} \quad (2.99)$$

where $V_1 = -eU_1$ and $V_2 = -eU_2$ are the boundary values at the left- and right contact, respectively; e being the elementary charge, $e = 1.60219 \times 10^{-19} \text{C}$.

$V_c(z)$ given by Eq. (2.99) is the solution of the 1D Poisson equation for the charge distribution $q(z)$, inside the interval $[l_1, l_2]$. Outside this interval the potential is constant according to the boundary conditions, $V_c(z \leq l_1) = V_1$ and $V_c(z \geq l_2) = V_2$. $V_c(z)$ contains also information about the induced sheet charges σ_1 and σ_2 , on the surface of the metallic contacts.

2.4 Mean-field approximation

If one wants to account for the effects of the (accumulated) charges in the system on the transport charges and, in turn, on the transport properties, then one has to

include in the scattering potential the interaction between the charges in the system (which can be free charges, as electrons, or fix charges, as ionized impurities). This requires a brief digression on the quantum mechanics of systems with many electrons and a review of the effects of the Coulomb repulsion between electrons.

In general, the wave function Ψ of a system of N particles must be written as

$$\Psi = \Psi(\mathbf{r}_1, \mathbf{r}_2, \dots, \mathbf{r}_N). \quad (2.100)$$

It is a function of the position coordinates, \mathbf{r}_j , for each particle j and cannot be separated generally into individual wave functions.

The many-particle wave function obeys a complex Schrödinger equation. The Hamiltonian of the electron system,

$$H = \sum_j \left[\underbrace{-\frac{\hbar^2}{2m^*} \Delta_j + V_{ext}(\mathbf{r}_j)}_{h(\mathbf{r}_j)} \right] + \frac{1}{2} \sum_{\substack{j,k=1 \\ j \neq k}} \frac{e^2}{4\pi\epsilon_0\epsilon_r |\mathbf{r}_j - \mathbf{r}_k|}, \quad (2.101)$$

has a kinetic energy term for each particle and two potential energy terms. Each electron experiences the same external potential V_{ext} , which would arise from the band-offsets of the heterostructure materials V_h , from the interaction with fix ionized donors $V_{N_D^+}$ and acceptors $V_{N_A^-}$, and from the applied electric fields V_{el} ,

$$V_{ext}(\mathbf{r}) = V_h(\mathbf{r}) + V_{N_D^+}(\mathbf{r}) + V_{N_A^-}(\mathbf{r}) + V_{el}(\mathbf{r}). \quad (2.102)$$

The second potential energy term in (2.101) corresponds to a Coulomb repulsion between each pair of electrons.

This problem it is usually solved in the *mean-field approximation*, expressing the many-particle wave function in terms of one-particle states and using the variational method to determine them.

2.4.1 Hartree approximation

Hartree approximation consists in the assumption that a many-particle wave function can be expressed as a simple product of one-particle states:

$$\Psi(\mathbf{r}_1, \mathbf{r}_2, \dots, \mathbf{r}_N) = \Phi_1(\mathbf{r}_1)\Phi_2(\mathbf{r}_2)\dots\Phi_N(\mathbf{r}_N) \quad (2.103)$$

without taking into account Pauli principle for electrons. $\Phi_i(\mathbf{r}_i)$ is the one-particle state of the electron i , which will be determined. A better approximation for the many-particle wave function (2.100) would be a Slater-determinant which would count for Pauli principle.

Using the variational method for the energy functional calculated with the Slater-form of the many-particle wave functions, as it is shown in Appendix A one obtains

the *Hartree-Fock* equations (A.31). If one neglects the exchange term (Fock term), then we obtain the *Hartree equations*:

$$h(\mathbf{r})\Phi_{\alpha_i}(\mathbf{r}) + \sum_{\tau=1}^N \int d^3r' \frac{e^2 |\Phi_{\alpha_\tau}(\mathbf{r}')|^2}{4\pi\epsilon_0\epsilon_r |\mathbf{r} - \mathbf{r}'|} \Phi_{\alpha_i}(\mathbf{r}) = E_i \Phi_{\alpha_i}(\mathbf{r}), \quad i = 1, \dots, N. \quad (2.104)$$

We have denoted here E_i instead of ϵ_i , because E_i will have the meaning of an eigenenergy of the 3D eigenvalue problem, while ϵ_i will be an eigenenergy of the 1D eigenvalue problem.

The same equations are obtained using the approximation (2.103) of the many-particle wave function and the variational method presented in Appendix A. The Hartree equations give the best approximation to the full N-electron wave function that can be represented as a simple product of one-electron states (but this is incompatible with the Pauli principle) [47], p.332.

The equations (2.104) have a direct physical interpretation: The quantity

$$\tilde{\rho}(\mathbf{r}') = -e \sum_{\tau=1}^N |\Phi_{\alpha_\tau}(\mathbf{r}')|^2 \quad (2.105)$$

has the meaning of the charge density produced by the occupied one-particle states $|\alpha_\tau\rangle$ and produces at \mathbf{r} an electrostatic potential

$$\varphi(\mathbf{r}) = \int d^3r' \frac{\tilde{\rho}(\mathbf{r}')}{4\pi\epsilon_0\epsilon_r |\mathbf{r} - \mathbf{r}'|}. \quad (2.106)$$

Note that $\tilde{\rho} = -e\rho$ contains the electron charge, while ρ does not. An electron situated at position \mathbf{r} experiences the potential energy $V_H(\mathbf{r}) = -e\varphi(\mathbf{r})$, called *Hartree potential* and Eq. (2.104) becomes

$$[h(\mathbf{r}) + V_H(\mathbf{r})] \Phi_{\alpha_i}(\mathbf{r}_i) = E_i \Phi_{\alpha_i}(\mathbf{r}_i). \quad (2.107)$$

Under this form, one can see directly the meaning of mean-field approximation: the electron moves in the electrostatic potential produced by all other electrons.

For our system, which has an effectively one-dimensional scattering potential so that the wave function can be separated as in (2.3), the charge density depends only on z -coordinate (see Eq. (2.88)). In this case, the integral over d^3r can be performed for transverse directions

$$\int d^3r' \frac{\tilde{\rho}(z')}{4\pi\epsilon_0\epsilon_r |\mathbf{r} - \mathbf{r}'|} = - \int dz' \frac{\tilde{\rho}(z')}{2\epsilon_0\epsilon_r} |z - z'| \quad (2.108)$$

which gives in fact the electrostatic potential of charges $\tilde{\rho}(z')$ in free one-dimensional space according to the free-space Green's function (2.95).

Eq. (2.104) is reduced to the one-dimensional Schrödinger-type equation

$$h(z)\psi_{\alpha_i}(z) + \int dz' \frac{e^2 \rho(z') |z - z'|}{2\epsilon_0\epsilon_r} \psi_{\alpha_i}(z) = \epsilon_i \psi_{\alpha_i}(z), \quad i = 1, \dots, N, \quad (2.109)$$

with $h(z) = -\frac{\hbar^2}{2m^*} \frac{d^2}{dz^2} + V_{ext}(z)$. The electronic density distribution $\rho(z)$ is calculated fully quantum mechanically, as described in Sec. 2.2, Eq. (2.88).

The total electrostatic potential and the potential produced by the applied electric fields can be calculated as an effective Coulomb potential $V_c(z) = V_{N_A^-}(z) + V_{N_D^+}(z) + V_H(z) + V_{el}(z)$ through the Poisson equation, as presented in the Sec. 2.3.

So, the scattering potential in the Schrödinger equation is a superposition of the band-offsets of the heterostructure materials and the effective Coulomb potential,

$$V(z) = V_h(z) + V_c(z). \quad (2.110)$$

The supplementary potential V_c makes the Schrödinger equation a nonlinear eigenvalue problem, because the potential depends on the wave functions. This problem is solved iteratively, by *self-consistent* calculations. Numerical methods are needed for an accurate solution.

In our mesoscopic system we are interested in a steady state. The system has to obey two equations in the same time:

- the Schrödinger equation, that describes the quantum features of the system;
- the Poisson equation, that gives the electrostatic potential in the system and involves an averaging procedure.

The above mentioned equations act complementary: having the potential, the Schrödinger equation establishes how many charges are in the system, while having the charge distribution the Poisson equation establishes how the electrostatic potential produced by these charges looks like. These two equations, acting as two "forces", can be brought in equilibrium only by self-consistent calculations.

The self-consistent calculations were involved in many systems: in the Si/SiO₂ systems, for calculating the properties of the silicon space-charge layer [51, 53], in GaAs-Ga_{1-x}Al_xAs heterojunctions [54], for counting the non-vanishing penetration of the wave functions in the barrier zone, or for counting the influence of the magnetic fields parallel to the interfaces [55], in modulation-doped Al_xGa_{1-x}As-GaAs-Al_xGa_{1-x}As heterostructure [5] for explaining the formation of the 2DEG in this kind of structures, and for a fully theoretical modeling of modulation-doped double quantum wells [56]. The self-consistent calculations are also necessary for understanding modern quantum structures as single quantum well transistors (SQWT) [57] or quantum dots [58].

2.4.2 Self-consistent procedure

Contrary to the general self-consistent scheme, known as "self-consistent field approximation" [53] (Fig. 2.4a), in which an initial guess for the potential has to be made, we propose another scheme, for which an initial form for $\rho(r)$ is guessed. which we call "self-consistent charge approximation" (Fig. 2.4b). We need this procedure, because for our interest, the differences between two successive iterations in

charge should be user defined, which does not happen *a priori* in the self-consistent field approximation.

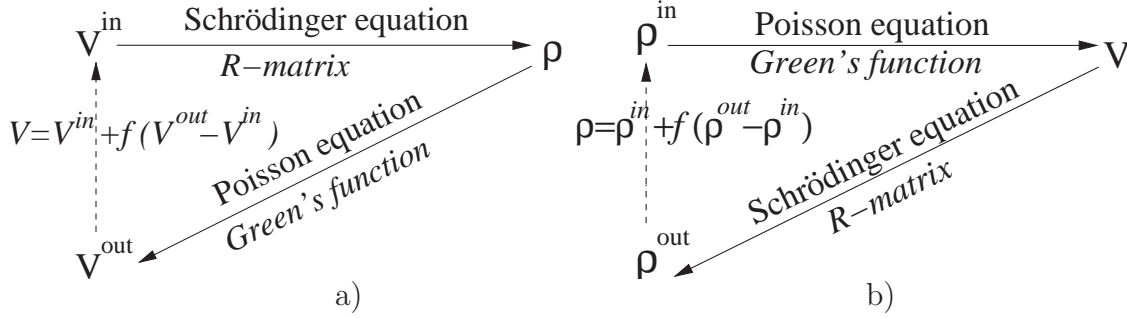


Figure 2.4: The self-consistent iterations scheme for a) self-consistent field approximation and b) self-consistent charge approximation. The Schrödinger equation, solved within the R-matrix formalism, gives for a specified potential and boundary conditions the wave functions and further one can calculate the charge distribution. The Poisson equation gives the electrostatic potential of a specified (total) charge distribution and it is solved by the suitable Green's function.

To start the procedure, one needs to suppose an initial negative charge distribution, and we take such one which fulfill the neutrality in the system.

The *mixing factor* f , which mixes the "in" and "out" quantities from one iteration to give the quantity "in" for the next iteration

$$\rho_{i+1}^{\text{in}} = \rho_i^{\text{in}} + f(\rho_i^{\text{out}} - \rho_i^{\text{in}}) \quad (2.111)$$

should be chosen particularly for every structure and for every guessed initial charge. The experience will help a lot for a good choice. This factor can differ from one iteration to another and this may allow for self controlled convergence procedure. If the iterations go away from the fix point (convergence point), then this factor should be decreased. If the iterations follow the right way to the convergence, then one can accelerate the procedure by increasing this factor. A practical method is to keep a small factor for the first self-consistent procedures (e.g. first bias) and when one becomes familiar with the convergence, one can fix this factor f in specified iterations domain. A concrete discussion about the effect of this factor will be presented in the Sec. 3.2.

The self-consistent iterations are performed until further iterations do not materially alter the result (potential or charge distribution), called fix point or convergent point. The convergent point is achieved when the *convergence parameter*

$$e_i = \frac{\sqrt{\sum_j (\rho^{\text{in}}(z_j) - \rho^{\text{out}}(z_j))^2}}{\min\left(\sqrt{\sum_j (\rho^{\text{in}}(z_j))^2}, \sqrt{\sum_j (\rho^{\text{out}}(z_j))^2}\right)} \quad (2.112)$$

is smaller than the user defined convergence limit ϵ . It is more convenient to work with absolute differences because at relative differences appear small numbers which can lead to some unphysical results. At the same time it is more convenient to work with the differences for the same iteration ('in' and 'out') like with the differences for the successive iterations ('in' for iteration i and 'in' for iteration $i+1$) because in the latter one appears the mix factor f .

Steps in self-consistent procedure

The procedure for calculating the self-consistent potential distribution and charge density follows the steps:

1. consider an initial charge distribution $\rho_{in}(x)$;
2. calculate the Coulomb potential from the Poisson equation with the help of the Green's function;
3. $V(z) = V_h(z) + V_c(z)$, where $V_h(z)$ is the potential coming from the heterostructure band offsets, and $V_c(z)$ is the Coulomb interaction potential calculated self-consistently;
4. calculate the free charge density with the help of the Schrödinger equation $\rho^{out}(z)$;
5. consider a mixture $\rho_{in}(z) + f \cdot (\rho_{out}(z) - \rho_{in}(z))$ for the next charge distribution;
6. verify if the convergence point is achieved; if not then go back to the point 2.

To solve self-consistently the Poisson equation and the Schrödinger equation is equivalent with finding the *stationary* solution of the transport problem.

First guess for the electronic charge

The initial electronic density distribution ρ_0 is chosen as depicted in Fig. 2.5: ρ_0 differs linearly from the ionized donor $N_D^+(z)$ and acceptor $N_A^-(z)$ distribution only around the abrupt variations of the doping profiles. The linear variation is taken of the order of the screening length $\lambda_F = 2\pi/k_F$, where k_F is the Fermi wave number in the reservoir. The impurities are considered completely ionized

$$N_A^-(z) \approx N_A(z) = \begin{cases} 0, & z < z_1, \\ N_A, & z_1 < z < z_2, \\ 0, & z > z_2 \end{cases} \quad (2.113)$$

$$N_D^+(z) \approx N_D(z) = \begin{cases} N_D, & z < z_1, \\ 0, & z_1 < z < z_2, \\ N_D, & z > z_2 \end{cases} \quad (2.114)$$

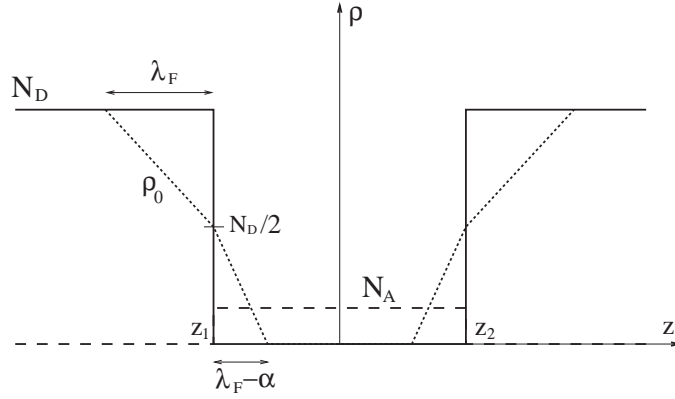


Figure 2.5: Distribution of the donors $N_D(z)$ (solid line), acceptors N_A (long dashed line) and initial electronic density distribution $\rho_0(z)$ (dotted line).

From the neutrality condition for the system of electrons and ionized impurities we determine the parameter α (see Fig. 2.5):

$$2 \frac{\frac{N_D}{2} \lambda_F}{2} - 2 \frac{\frac{N_A}{2} (\lambda_F - \alpha)}{2} - N_A (z_2 - z_1) = 0. \quad (2.115)$$

Biased structure

For a biased structure, we have to specify the boundary conditions for the Poisson equation. The external applied bias V_{sd} imposes in fact the boundary values for the scattering potential:

$$eV_{sd} = E_F^L - E_F^R = V_L - V_R \quad (2.116)$$

where the last identity holds for the same doping in the reservoirs. This condition becomes now

$$eV_{sd} = V_h(-d) - V_h(d) + V_c(-d) - V_c(d) \quad (2.117)$$

which in fact imposes the boundary condition for the Poisson equation $V_c(-d)$ and $V_c(d)$ (i.e. V_1 and V_2 in Sec. 2.3.2)

For a closed system, if there is a potential difference between left and right, then a charge transfer occurs until the inner electric field compensates for the external electric field. So the system constructs such a dipole momentum against the external electric field.

For an open system, the charge flows from one side to another, but in front of the barrier the charge is accumulating and behind of the barrier there is a depletion region. The dipole momentum is now in the same direction as the external electric field.

The self consistent procedure for a new applied bias starts from the previous bias self-consistent solution.

2.5 Current through mesoscopic structures

In Sec. 2.1 we showed how to calculate for one-dimensional potentials the transmission and reflection coefficients. Following Ferry [2], Chap.3.3., we want to present here the calculation of the current flow through a three-dimensional device using the transmission coefficient.

2.5.1 Coherent tunneling

When we looked at the tunneling process in the previous sections, we considered a single one-dimensional traveling wave that propagates through the barrier region and out the other side. As such, we viewed tunneling as an elastic process involving no loss of energy of the particle. In a real structure, the ideal problem consists of a plane wave incident on a barrier potential that is semiinfinite in extent in the two transverse directions and varies only in the third direction. For almost all practical planar barrier devices, this variation in potential is in the growth direction due to the bandgap discontinuities of the heterojunction interfaces, the space charge due to doping and the applied bias. The plane wave has some components of its wavevector (and hence momentum) in the transverse directions parallel to the barrier. Along with our assumption that tunneling is an energy conserving process, we will further assume that the transverse momentum is conserved, that it remains the same before and after the tunneling. This latter assumption is violated in real structures if random inhomogeneities exist in the lateral direction, such as interface roughness and ionized impurities. The main effect is to broaden the effective transmission resonance, reducing the peak-to-valley ration (PVR) of I-V curve in measured structures compared to the ideal model.

To connect the quantum mechanical fluxes to charge current, we need to introduce the statistical mechanical distribution function to tell us the occupancy of current-carrying states incident and transmitted on the barriers. Exactly what distribution function to use is perhaps one of the central issues of describing nonstationary transport in a phase-coherent system such as the nanostructures discussed in this thesis. The model we will use, called also Landauer-Büttiker formalism [19, 24, 21], assumes that we have contacts or reservoirs on the left and right side of a barrier structure that are essentially in equilibrium and are described by the single-particle distribution function such as the Fermi-Dirac distribution characterized by a chemical potential.

The problem is shown in Fig. 2.6 for a generic tunneling barrier. The applied bias separates the chemical potentials on the left and right by an amount eV_{sd} . The Hamiltonian on either side of the barrier is assumed separable into perpendicular (z -direction) and transverse components. If we choose the zero-reference of the potential energy in the system to be the conduction band minimum on the left,

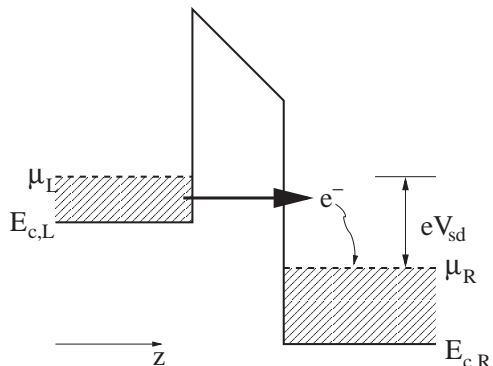


Figure 2.6: Band diagram for a tunnel barrier under bias, illustrating charge flow.

$E_{c,L} = 0$, the energy of a particle before and after tunneling may be written as

$$E = \epsilon + E_t = \frac{\hbar^2 k_{z,L}^2}{2m^*} + \frac{\hbar^2 k_{t,L}^2}{2m^*} \quad (2.118)$$

on the left side, and

$$E = \frac{\hbar^2 k_{z,R}^2}{2m^*} + \frac{\hbar^2 k_{t,R}^2}{2m^*} + E_{c,R} \quad (2.119)$$

on the right side, where $E_{c,R}$ is the conduction band minimum on the right side and k_z and \mathbf{k}_t are the perpendicular and transverse components of the wavevector relative to the barrier. A single, parabolic, isotropic conduction band minimum has been assumed for simplicity. Since the transverse momentum is assumed to be conserved during the tunneling process, then $k_{t,L} = k_{t,R}$, and the transverse energy $E_{t,L} = E_{t,R}$ is the same on both sides for the tunneling electron. Therefore, the z -component of the energy is

$$\epsilon = \frac{\hbar^2 k_{z,L}^2}{2m^*} = \frac{\hbar^2 k_{z,R}^2}{2m^*} + E_{c,R} \quad (2.120)$$

on the left and right sides of the barrier.

As a further approximation, in order to introduce irreversibility into the formalism, we assume that the contacts are perfectly absorbing. This means that when a particle injected from one side reaches the contact region of the other side, its phase coherence and excess energy are lost through inelastic collisions with the Fermi sea of electrons in the contact. Thus we assume that an electron injected from one contact at a certain energy E has a certain probability of being transmitted through the barrier determined by $T(E)$, exits the barrier with the same energy and transverse momentum, and finally is absorbed in the opposite contact, where it loses the energy and memory of its previous state. Current flow in this picture is essentially the net difference between the number of particles per unit time transmitted to the

right and collected versus those transmitted to the left. This view of tunneling is referred to as *coherent* since the particles maintain their phase coherence across the whole structure before losing energy in contacts.

To proceed with this picture, consider the current density perpendicular to the barrier in the z -direction for a given energy E with corresponding z -component ϵ . The incident current density on the barrier from the left due to particles in an infinitesimal volume of momentum space $d\mathbf{k}_L$ around \mathbf{k}_L may be written as

$$j_i = -eD(\mathbf{k}_L)f_L(\mathbf{k}_L)v_z(\mathbf{k}_L)d\mathbf{k}_L, \quad D(\mathbf{k}) = \frac{2}{(2\pi)^3}, \quad (2.121)$$

where f_L is the distribution function on the left side of the barrier, $D(\mathbf{k})$ is the density of states in \mathbf{k} -space (taking in account the spin degeneracy), and the velocity perpendicular to the barrier from the left is

$$v_z(\mathbf{k}_L) = \frac{1}{\hbar} \frac{\partial E(\mathbf{k}_L)}{\partial k_{z,L}} = \frac{\hbar k_{z,L}}{m^*} \quad (2.122)$$

using the parabolic relation (2.120). Here we neglect the possibility that the energy states on the left and right side of the barriers may be quantized due to, for example, band bending, and we, therefore, treat the states as three-dimensional. The transmitted current density from the left to right is simply Eq. (2.121) weighted by the transmission coefficient

$$j_L = \frac{-2e\hbar}{(2\pi)^3 m^*} T(k_{z,L}) f_L(\mathbf{k}_t, k_{z,L}) k_{z,L} dk_{z,L} d\mathbf{k}_t, \quad (2.123)$$

where $T(k_z)$ is the transmission coefficient (see Eq. (2.34)) which for the ideal case is only a function of the perpendicular momentum and energy. Similarly, the transmitted current from right to left may be written for the same energy E and ϵ

$$j_R = \frac{-2e\hbar}{(2\pi)^3 m^*} T(k_{z,R}) f_R(\mathbf{k}_t, k_{z,R}) k_{z,R} dk_{z,R} d\mathbf{k}_t. \quad (2.124)$$

At a given perpendicular energy ϵ , the transmission coefficient is symmetric (see Eq. (2.36)) so that $T(k_{z,L}) = T(k_{z,R}) = T(\epsilon)$, where $k_{z,L}$ and $k_{z,R}$ are connected through the relation (2.120). Further, $k_{z,L} dk_{z,L} = k_{z,R} dk_{z,R} = m^* d\epsilon / \hbar^2$ if we differentiate both sides of (2.120). Therefore, the net current density in the direction of the voltage drop is the difference between the left and right currents densities integrated over all \mathbf{k} , or

$$J_T = \frac{2e}{(2\pi)^3 \hbar} \int_0^\infty d\epsilon \int_0^\infty dk_t k_t \int_0^{2\pi} d\theta T(\epsilon) [f_L(\epsilon, k_t) - f_R(\epsilon, k_t)], \quad (2.125)$$

where the integration over ϵ is from zero to infinity because tunneling from right to left below $\epsilon = 0$ is forbidden.

At this point, no further reduction to Eq. (2.125) can be made unless we make assumptions concerning the nature of the distribution functions on the left and right sides. The lowest-order approximation is to assume that these distributions are given by the equilibrium Fermi-Dirac functions determined by the bulk chemical potentials on the respective sides of the barrier,

$$f_{L/R}(\epsilon, E_t) = \frac{1}{1 + \exp\left(\frac{\epsilon + E_t - \mu_{L/R}}{k_B T}\right)}, \quad (2.126)$$

where T is the lattice temperature and $\mu_{L/R}$ is the chemical potential on the left and right side, respectively. The difference between the two is just the applied bias, $\mu_L = \mu_R + eV_{sd}$. Since the chemical potential is isotropic, the angular integration gives 2π . Likewise, the integration over perpendicular wavevector may be converted to an integral over energy. Assuming parabolic bands, Eq. (2.125) becomes

$$J_T = \frac{4\pi em^*}{(2\pi)^3 \hbar^3} \int_0^\infty d\epsilon T(\epsilon) \int_0^\infty dE_t [f_L(\epsilon, E_t) - f_R(\epsilon, E_t)]. \quad (2.127)$$

For the Fermi function (2.126), the integration over energy is easily evaluated: using the substitution $y = (E_t + \epsilon - \mu)/(k_B T)$ one obtains

$$\int_0^\infty dE_t \frac{1}{1 + \exp\left(\frac{\epsilon + E_t - \mu}{k_B T}\right)} = k_B T \ln \left(1 + \exp\left(\frac{\mu - \epsilon}{k_B T}\right)\right) \quad (2.128)$$

so that Eq. (2.127) becomes

$$J_T(V_{sd}) = \frac{em^* k_B T}{2\pi^2 \hbar^3} \int_0^\infty d\epsilon T(\epsilon) \ln \frac{1 + e^{(\mu_L - \epsilon)/k_B T}}{1 + e^{(\mu_L - eV_{sd} - \epsilon)/k_B T}}, \quad (2.129)$$

sometimes referred to as *Tsu-Esaki formula*, where the particular form was popularized in connection to resonant tunneling diodes[24].

We would like to emphasize at this point the beauty of this formula: all the features of the scattering region are behind of the tunneling probability coefficient. The idea to connect the macroscopic features of the system with the tunneling probability, a quantum mechanical quantity, was first pointed out by Landauer [19], who connected the electrical resistivity to the tunneling and reflection probability. The Eq. (2.129) is a two terminal formula, which was extended by Büttiker to obtain a multiterminal tunneling formula [21] and so emerges the Landauer-Büttiker formalism. This has been very successful in describing electronic transport in mesoscopic systems. This formalism can be obtained as a limit from other transport theories: Datta [59] has shown the evolution from the Keldysh to the Landauer-Büttiker formalism.

The logarithmic term in Eq.(2.129)

$$\xi(\epsilon) = \ln \frac{1 + e^{(\mu_L - \epsilon)/k_B T}}{1 + e^{(\mu_L - eV_{sd} - \epsilon)/k_B T}}. \quad (2.130)$$

is sometimes called the *supply function*, since it more or less determine the relative weight of available carriers at a given perpendicular energy.

If one uses the limit

$$\lim_{T \rightarrow 0} k_B T \ln \left(1 + e^{\frac{\mu_L - \epsilon}{k_B T}} \right) = \mu_L - \epsilon \quad (2.131)$$

calculated with the substitution $y = 1/k_B T$, then Eq. (2.129) becomes for very low temperatures simply

$$J_T(V_{sd}) = \frac{em^*}{2\pi^2\hbar^3} \left[\int_0^{\mu_L} d\epsilon T(\epsilon)(\mu_L - \epsilon) - \int_0^{\mu_L - eV_{sd}} d\epsilon T(\epsilon)(\mu_L - eV_{sd} - \epsilon) \right], \quad (2.132)$$

which has a direct physical representation: all the electrons from the left reservoir, with energies between $[0, \mu_L]$ contribute positively to the current, while the electrons from right reservoir, between $[0, \mu_R] = [0, \mu_L - eV_{sd}]$ contribute negatively to the current. For both reservoirs the contribution has the same form: the transmission probability multiplied with the energy interval between the corresponding chemical potential and the considered energy. In Eq. (2.132), as expected, does not appear the dependence on the temperature anymore.

The same result can be obtained if one note that the derivative of the supply function with respect to the energy, $d\xi(\epsilon)/d\epsilon$ is a difference of two Fermi-Dirac distribution functions

$$\xi'(\epsilon) = \frac{d\xi(\epsilon)}{d\epsilon} = -\frac{1}{k_B T} [f_L(\epsilon, E_t) - f_L(\epsilon + eV_{sd}, E_t)] \quad (2.133)$$

which is practically a constant for $\epsilon \in [\mu_L - eV_{sd}, \mu_L]$ and in turn $\xi(\epsilon)$ is practically a linear decreasing function on the same interval of energy.

If we now consider current through a resonant structure such as a resonant tunneling diode (RTD), the current density is dominated by the resonant portion of the transmission coefficient. For example, if the transmission coefficient is assumed to be very sharp around $\epsilon = \epsilon_n$ using the Lorentzian form [2] Chap.3.2,

$$T(\epsilon) = T_{res} \frac{\Gamma_n^2/4}{\Gamma_n^2/4 + (\epsilon - \epsilon_n)^2} \quad (2.134)$$

where Γ_n is the energetic width of the peak n , we can approximate it as a delta function so that at low temperature, Eq. (2.132) may be integrated to give

$$J_T = \frac{em^* T_{res} \Gamma_n}{4\pi\hbar^3} (\mu_L - \epsilon_n) \quad 0 < \epsilon_n < \mu_L, \quad (2.135)$$

where the asymptotic approximation for the delta function has been employed:

$$\delta(\epsilon - \epsilon_n) = \frac{1}{\pi} \lim_{\Gamma_n \rightarrow 0} \frac{\Gamma_n/2}{\Gamma_n^2/4 + (\epsilon - \epsilon_n)^2}. \quad (2.136)$$

The voltage dependence enters essentially through ϵ_n , the resonant energy. We should mention here that T_{res} and Γ_n are also functions on applied bias V_{sd} . For a symmetric double barrier, with a linear voltage drop equally divided between the two barriers (usually the case for non self-consistent calculations), the well is lowered in potential energy by an amount $eV_{sd}/2$ with respect to the emitter (the left side), and is higher in energy than the collector by the same amount. ϵ_n may therefore be replaced in (2.135) by $\epsilon_n^0 - eV_{sd}/2$, where ϵ_n^0 is the quasi-bound state energy relative to the well bottom. This gives a sudden turn-on of current when $\epsilon_n = \mu_L$, i.e. $eV_{sd} = 2(\epsilon_n^0 - \mu_L)$, and cuts off when $eV_{sd} = 2\epsilon_n^0$ giving rise to negative differential resistance (NDR). The peak occurs when $\epsilon_n = 0$, giving a peak current density

$$J_P = \frac{em^*T_{res}\Gamma_n\mu_L}{4\pi\hbar^3}. \quad (2.137)$$

So that, a very simplified model for a J-V curve for a RTD provides at low temperatures a form represented in the Fig. 2.7.

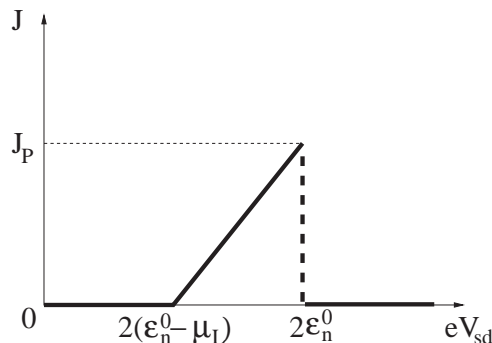


Figure 2.7: A very simplified model for a J-V curve for a RTD at low temperatures.

As can be seen, the peak current depends physically on the chemical potential in the emitter, and hence the doping there, as well as on the product of the peak transmission probability and resonance width. Since both the resonance width and the resonant transmission amplitude increase as the barrier thickness decreases, thin barriers are essential for high peak current densities.

In order to calculate the current-voltage characteristics using Eq. (2.129), the transmission coefficient versus energy is tabulated for each bias point (since the barrier shape continuously changes as a function of bias), and the integration is performed numerically for the current.

The optimal conditions for the resonant tunneling through semiconductor quantum structures have been studied [44, 43, 45, 92].

The formula (2.129) will be used in Chap. 4, to calculate the current flow for a single barrier system, exhibiting Fabry-Perot resonances.

2.6 Capacitance of mesoscopic structures

Capacitance spectroscopy has proven to be a powerful tool to study quantum semiconductor structures because it gives information about the charge density and its location in the studied system. Examples for structures examined so far are heterojunctions [60], simple tunneling barriers as well as multiple barrier structures [61, 62, 63, 64], superlattices [65, 66], two-dimensional electron systems [67, 68, 69, 70, 71, 72], quantum wires [73], and quantum dots [74, 75]. The investigation of these systems require the presence of contacts made from a metallization or from a heavily doped semiconductor material. These contacts are either source- and drain contacts to apply an external potential or sometimes contacts used to define the quantum structure itself (see e.g. the use of top gates in Refs. [73, 74, 75]). Because image charges in the contacts have a major contribution to the charge balance in small systems the explicit structure of the contacts is important for capacitance measurements. A second important common feature is the existence of tunneling currents which cannot be avoided in small structures. Theoretically, this means that the quantum system is an open system exchanging particles with the environment, particularly with the source- and the drain contact.

In this section we propose a *new* capacitance model for a quantum structure that takes into account both of these fundamental aspects, the openness and the existence of finite contacts embedding the system.

2.6.1 Charge balance

For a closed system there is no modification of the amount of charge inside the system at variations of the applied bias. In contrast, for open system there is particle exchange between the system and the contacts which play the role of the reservoirs.

For defining the differential capacitance, we need first to define the charges which belong to the "plates" of the capacitor. For this it is necessary to make a charge balance in the system:

- fix charges from the ionized impurities N_D^+ and N_A^- ; these will be connected to the plates by geometrical consideration,
- transport (free) charges ρ ; these will be connected to the plates by ancestry consideration, i.e. from where the particles are coming;
- the surface charges at the interfaces between the contacts and the system, σ_1 and σ_2 ; these will be connected to the plate to which the contact belongs.

So that, in our formalism we allow for net charges everywhere outside the contacts ('system charges' in Fig. 2.8, $z_1 \leq z \leq z_2$). Inside the contacts there are net charges in the surface region ('interface charges' in Fig. 2.8, $-d \leq z \leq z_1$ and $z_2 \leq z \leq d$). In the bulk of the contacts, for $|z| > d$, there is no net charge and the effective potential

is flat. In the scattering region defined by $-d \leq z \leq d$ we distinguish between free charges that can be exchanged with the bulk of the contacts and bound charges.

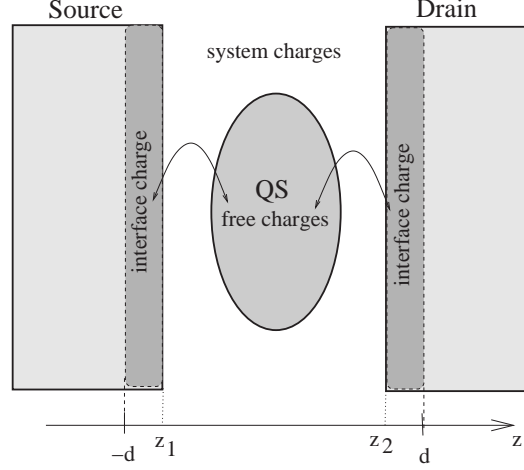


Figure 2.8: General structure of the considered systems.

At the definition of the "plate" charges we want to keep the classical meaning of the capacitance: at a variation of the potential difference between the plates, the variation of the charges on the plates have to be equal and of opposite sign.

2.6.2 Plate charges Σ_1 and Σ_2

We use the Gauss law for calculating the sheet charges at the interfaces between the system and the contacts (see Fig. 2.9) and obtain

$$\sigma_1 = \frac{\epsilon_0 \epsilon_r}{e} \left(\frac{\partial V_c}{\partial z} \right)_{z=-d+\delta}, \quad \sigma_2 = -\frac{\epsilon_0 \epsilon_r}{e} \left(\frac{\partial V_c}{\partial z} \right)_{z=d-\delta} \quad (2.138)$$

where σ_1 is placed at $z = -d$ and σ_2 at $z = d$ and $\delta \rightarrow 0$. We have used that outside the interval $[-d, d]$, the potential is constant according to the local charge neutrality. The Gauss box is chosen so that $\delta \rightarrow 0$. Inside the scattering system the Coulomb potential is given by Eq. (2.99). For the chosen configuration, $l_1 = -d$ and $l_2 = d$, the term $(1/2)(l_2 + l_1)/(l_2 - l_1)(z + z')$, which takes into account the asymmetry in the boundary position, will be zero. The boundary values V_1 and V_2 , which depend on the external applied bias V_{SD} , will be calculated from the boundary conditions for the total potential energy $V(z)$:

$$V(z = -d) = V_L \quad (2.139)$$

$$V(z = d) = V_R \quad (2.140)$$

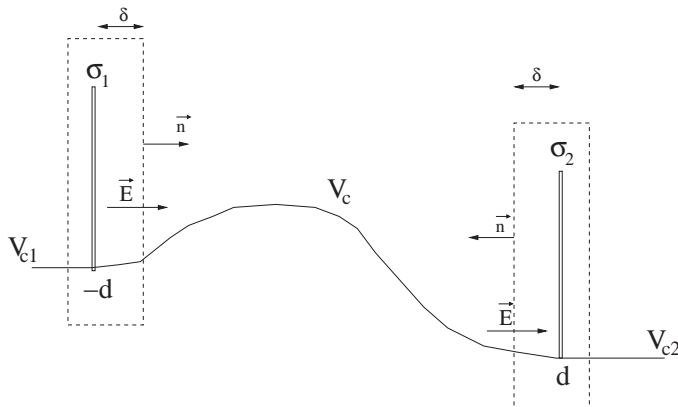


Figure 2.9: The electrostatic potential and the use of Gauss law for calculating the sheet charges at the interfaces between the system and the contacts.

so that $V_L - V_R = eV_{sd}$, where V_{sd} is the total bias which drops in the active region considered in our problem, and it can differ from V_{SD} by a constant, as it will be presented in the particular analyzed cases. So that the Coulomb potential energy felt by one electron in the field of all others

$$V_c(z) = \frac{e}{\epsilon_0 \epsilon_r} \int_{-d}^d \left(\frac{1}{2} |z - z'| + \frac{1}{2d} z \cdot z' - \frac{d}{2} \right) q(z') dz' + V_1 + (V_2 - V_1) \frac{z + d}{2d}, \quad \text{for } -d \leq z \leq d \quad (2.141)$$

where $q(z) = e [N_D^+(z) - N_A^-(z) - \rho(z)]$. The derivative of the electrostatic potential V_c is well defined at the points $\pm d$. One can see this, if the modulus function is expressed in terms of step functions $|z - z'| = (z - z')\Theta(z - z') + (z' - z)\Theta(z' - z)$. Inserting the expression (2.141) of the Coulomb potential in Eqs. (2.138) we obtain

$$\sigma_1 = -\frac{1}{2}Q + \Pi - \frac{\epsilon_0 \epsilon_r}{e} \frac{V_2 - V_1}{2d} \quad (2.142)$$

$$\sigma_2 = -\frac{1}{2}Q - \Pi + \frac{\epsilon_0 \epsilon_r}{e} \frac{V_2 - V_1}{2d} \quad (2.143)$$

with the notations

$$Q = \int_{-d}^d q(z) dz, \quad (2.144)$$

$$\Pi = \frac{1}{2d} \int_{-d}^d z q(z) dz. \quad (2.145)$$

One can immediately observe that $\sigma_1 + \sigma_2 = -Q$.

We can construct now the charges on the plates:

- on the left plate

$$\Sigma_1 = \sigma_1 + \sigma_1^{free} + \sigma_1^{bound}, \quad (2.146)$$

- on the right plate

$$\Sigma_2 = \sigma_2 + \sigma_2^{free} + \sigma_2^{bound}, \quad (2.147)$$

where

$$\sigma_1^{bound} = e \int_{-d}^0 (N_D^+(z) - N_A^-(z)) dz \quad (2.148)$$

$$\sigma_1^{free} = -e \int_{-d}^d \rho_1(z) dz \quad (2.149)$$

$$\sigma_2^{bound} = e \int_0^d (N_D^+(z) - N_A^-(z)) dz \quad (2.150)$$

$$\sigma_2^{free} = -e \int_{-d}^d \rho_2(z) dz \quad (2.151)$$

with $\rho_1(z)$ and $\rho_2(z)$ the charge density produced by the electrons incident from the left and right contact, respectively (see Eq. (2.88)):

$$\rho_1(z) = 2 \frac{L_z}{(2\pi)^2} \int_0^{k_F} dk_z \frac{(k_F^2 - k_z^2)}{2} |\psi^L(k_z, z)|^2 \quad (2.152)$$

$$\rho_2(z) = 2 \frac{L_z}{(2\pi)^2} \int_0^{k_F} dk_z \frac{(k_F^2 - k_z^2)}{2} |\psi^R(k_z, z)|^2 \quad (2.153)$$

With the above definitions, the neutrality condition

$$\Sigma_1 + \Sigma_2 = 0, \quad (2.154)$$

is implicitly fulfilled.

We can define now the capacitance per area:

$$C = \left| \frac{d\Sigma_1}{dV_{sd}} \right| = \left| \frac{d\Sigma_2}{dV_{sd}} \right| \quad (2.155)$$

and with the above expressions we have

$$\frac{d\Sigma_1}{dV_{sd}} = \frac{1}{2} \frac{d}{dV_{sd}} (\sigma_1^{free} - \sigma_2^{free}) + \frac{d}{dV_{sd}} \Pi - \frac{\epsilon_0 \epsilon_r}{e2d} \frac{d(V_2 - V_1)}{dV_{sd}} \quad (2.156)$$

$$\frac{d\Sigma_2}{dV_{sd}} = -\frac{1}{2} \frac{d}{dV_{sd}} (\sigma_1^{free} - \sigma_2^{free}) - \frac{d}{dV_{sd}} \Pi + \frac{\epsilon_0 \epsilon_r}{e2d} \frac{d(V_2 - V_1)}{dV_{sd}} \quad (2.157)$$

which shows that the variation of the Σ_1 and Σ_2 are equal and with opposite sign for the same variation of the applied bias. The capacitance per area describes the absolute value of the net charge coming into the system from either of the contacts L (left) or R (right) when the voltage is changed. The charge coming from the left

contact is stored in σ_1 and σ_1^{free} , while the charge coming from the right contact is stored in σ_2 and σ_2^{free} . In contrast to a plate capacitor the charges belonging to σ_1^{free} and σ_2^{free} have a spatial overlap. However both charge types are distinguishable in our model and there is no exchange between these charges.

Because the capacitance is the derivative of $\Sigma_{1/2}$ at the applied bias V_{sd} , and we consider that the bound charges $N_A^-(z)$ and $N_D^+(z)$ do not depend on the applied bias, then in the definitions of $\sigma_{1/2}^{bound}$, (2.148) and (2.150), it is not important how the bound charges are associated to the capacitor plates. The integral limits can be chosen arbitrarily, but should cover the whole system in order to obey the neutrality condition (2.154).

2.7 Characteristics of GaAs/Al_xGa_{1-x}As/GaAs structures

One of the most used material for the nanodevices is the ternary alloy system Al_xGa_{1-x}As, because GaAs and AlAs form a solid solution over the entire composition range ($0 \leq x \leq 1$) with very little variation (< 0.15 per cent) of the lattice constant. These facts mean that semiconductor multilayers of very high quality with different x values can be relative easy prepared. The most exploited aspect of the Al_xGa_{1-x}As alloys is their band structure. At $x = 0$ (i.e. GaAs) we have a direct-bandgap semiconductor with a room temperature bandgap of 1.42eV. At $x = 1$, AlAs is an indirect-gap semiconductor with the minimum energy separation at the X point. At somewhere about $x = 0.45$ there is a crossover from direct to indirect-gap structure [76] Chap.1.6. The transport properties of Al_xGa_{1-x}As near the indirect-direct crossover are not well known, but majority exploited heterostructure devices are using alloys with $x < 0.4$ to ensure a direct-bandgap semiconductor and to avoid a transition from Γ minimum to X minimum.

Guéret et al. in [77] have accounted for the band-edge effective mass in Al_xGa_{1-x}As dependence on the Al mole fraction x according to

$$m^* = 0.067(1 + 1.244x)m_0 \quad (2.158)$$

where the m_0 stands for the free-electron mass.

A recent detailed analysis of the material parameters for different alloys used in nanodevices is provided by Vurgaftman et al. [78].

Chapter 3

Capacitance of a field-induced 2DEG

We will consider in this chapter semiconductor devices composed of a small quantum structure as the active device region and two classical environments constituting the source- and the drain contact. The contacts are taken as free electron gases with infinite conductivity, whose concentrations define the chemical potentials in the contacts. The transport through the quantum structure is described in the Landauer-Büttiker formalism using electronic scattering wave functions which define the electron density in the quantum system. In our Hartree approximation these charges and the induced charges in the contacts are the sources of the self-consistent Coulomb field. As a particular quantum structure we study a GaAs heterostructure device consisting of a two-dimensional electron gas sandwiched between a gate contact and an AlGaAs blocking barrier [71]. We demonstrate the quantitative agreement of our theory with the experimental results.

3.1 The structure

As a particular quantum structure we study a special high-mobility AlGaAs/GaAs heterostructure device consisting of a two-dimensional electron gas sandwiched between a back contact and an AlGaAs blocking barrier [71], optimized for investigations of electron systems at low densities [73, 79]. This structure differs from the semiconductor devices used for magneto-capacitance spectroscopy through the second metallic electrode buried in the crystal below the 2DEG [80, 81]. The very good quality of the sample made possible to study the quantum effects.

The AlGaAs/GaAs single-heterojunction structure [71] represented in Fig. 3.1, consists of a sequence of layers grown on a GaAs substrate, given by, first, 20nm n -GaAs as a back contact, $n_{Si} = 4 \times 10^{18} \text{cm}^{-3}$ silicon doping, second, 100 nm intrinsic GaAs as a spacer, with $N_A = 10^{15} \text{cm}^{-3}$ residual (nonintentional) p-doping, third, a short period AlAs/GaAs superlattice: 7x9ML (monolayers) AlAs alternating 6x9ML GaAs with the total width of 32nm, as a blocking barrier, a thin 9nm GaAs cap

layer and finally a metallization as a top gate. These parameters of the sample (see Fig. 3.2) define the *nominal structure*.

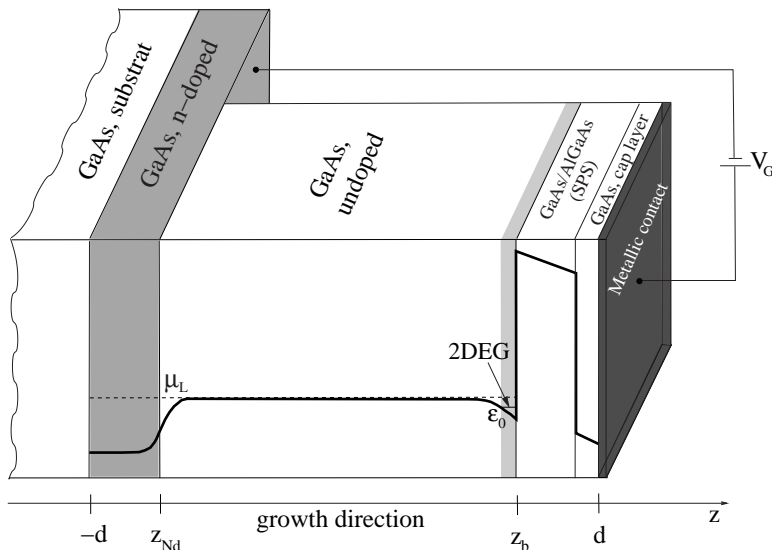


Figure 3.1: The AlGaAs/GaAs heterostructure device [71] and the schematic band diagram in growth direction.

Here the quantum system basically consists of a field induced two-dimensional electron gas (2DEG) formed at the interface between the GaAs spacer and the blocking barrier for gate voltages V_G above a certain threshold value. The 2DEG is separated from the back contact by a wide and shallow tunneling barrier.

The back contact plays the role of a source contact, while the top metallic gate plays the role of a drain contact. We choose the zero-reference of the potential energy in the system to be the conduction band minimum on the left, $E_{c,L} = 0$.

Conventionally the sign of the V_G bias applied between the top gate and the GaAs substrate is given by the polarity on the gate with respect to the GaAs substrate. Positive bias on the gate attracts electrons to the barrier surface. Making V_G negative with respect to the GaAs substrate repels electrons from the gate surface and attracts holes to the gate surface.

As well known, the scattering potential in the growth direction breaks the translational symmetry in this direction, so that the local charge neutrality is destroyed (but not the total charge neutrality) and the charge distribution has spatial variations. This process is intensified by the external electric field.

The region between $(-d, d)$ is fully quantum mechanically described. We treat the metallic gate and the back contact as ideal metals with infinite conductivity which ensures constant potential outside the scattering region $(-d, d)$ [94]. The electron motion can be described by the Schrödinger equation (2.2). Because of the

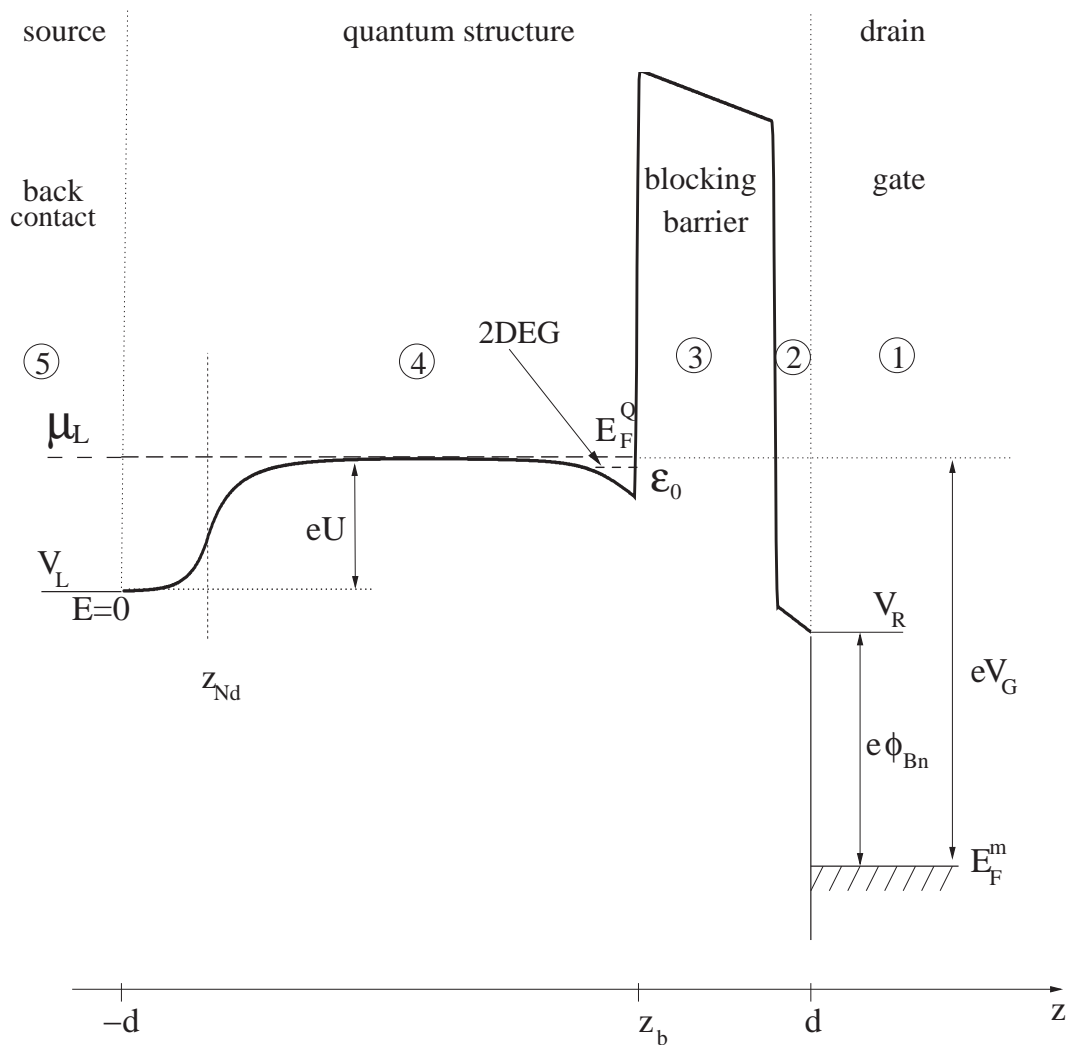


Figure 3.2: Schematic band diagram of the heterostructure device measured in Ref. [71]. The structure parameters are: 1.) Top gate metalization, 2.) 9 nm GaAs cap-layer, 3.) 7x9ML (monolayers) AlAs alternating 6x9ML GaAs (short period superlattice of width 32nm), 4.) 100 nm GaAs spacer, with $N_A = 10^{15} \text{cm}^{-3}$ residual p-doping, 5.) 20nm GaAs back contact with $N_D = 4 \times 10^{18} \text{cm}^{-3}$ silicon doping, 6.) 1 μm GaAs buffer, and 7.) GaAs substrate (semi-insulating). We take $\epsilon_r = 12.5$, $m^* = 0.0655m_0$. The 2DEG is formed at the interface between the GaAs spacer and the blocking barrier by applying a dc bias between the gate electrode and back contact. μ_L is the chemical potential in the back contact, E_F^Q is the Fermi level of the 2DEG. ϵ_0 is the quasi bound level formed in the quantum well in front of the blocking barrier. $e\phi_{Bn}$ represents the barrier height of (gate) metal-semiconductor contact.

translational invariance of our system in the lateral directions the structure allows for a separable potential,

$$V_{eff}(\mathbf{r}) = V_{\perp}(\mathbf{r}_{\perp}) + V(z) \quad (3.1)$$

where $V(z)$ represents the scattering potential in the growth direction and $V_{\perp}(\mathbf{r}_{\perp})$ is the potential in the plane parallel to the heterostructure interfaces, and perpendicular to the growth direction. We do not have supplementary gate induced constrictions, so that $V_{\perp}(\mathbf{r}_{\perp})$ is constant and can be taken as zero, $V_{\perp}(\mathbf{r}_{\perp}) = 0$. In turn, electrons are free in the parallel directions and can be described by plane waves. Within the standard envelope function approximation, the motion of the electrons in the growth direction is described by the 1D Schrödinger type equation (2.6).

The electronic charge is calculated quantum mechanically as in Sec. 2.2. The Coulomb potential is considered in the Hartree approximation, so that the 1D eigenvalue problem (2.6) becomes a nonlinear one, which is solved iteratively, self-consistently, as described in Sec. 2.4.

3.2 Flat band configuration

In order to calculate the self-consistent potential and charge distribution we want to obtain first the *flat band* configuration. There are more properties which define the flat band configuration: in a MOS (metal-oxide-semiconductor) system, the bands are flat throughout the semiconductor; the hole and electron densities are uniform throughout the semiconductor and have the same values at the surface as in the bulk of the semiconductor. If the bands are flat, this provides another condition, namely the derivative of the potential is zero. This condition will be used also in our model, so that the flat band configuration is achieved if

$$\left. \frac{dV(z)}{dz} \right|_{z_0} = 0, \quad (3.2)$$

where z_0 is chosen in our system as the middle of the blocking barrier. This condition will be automatically fulfilled if we consider an *auxiliary symmetrical structure* with similar parameters as the nominal structure: the same width and height of the blocking barrier, but two identical GaAs spacers on every side of the barrier with the same size as in the nominal structure, sandwiched by two identical n-GaAs layers with the same doping as in the nominal structure.

We take the effective mass of the electron in GaAs as the effective mass over the whole structure $m^* = 0.0655m_0$, and we consider ϵ_r , the relative permittivity, equal over all the structure and, equal with the value in GaAs, $\epsilon_r = 12.5$. The temperature is considered $T \cong 0\text{K}$.

The initial negative charge density ρ_0 is chosen as a linear profile on the order of λ_F around the interfaces between high doped region and undoped region, as it

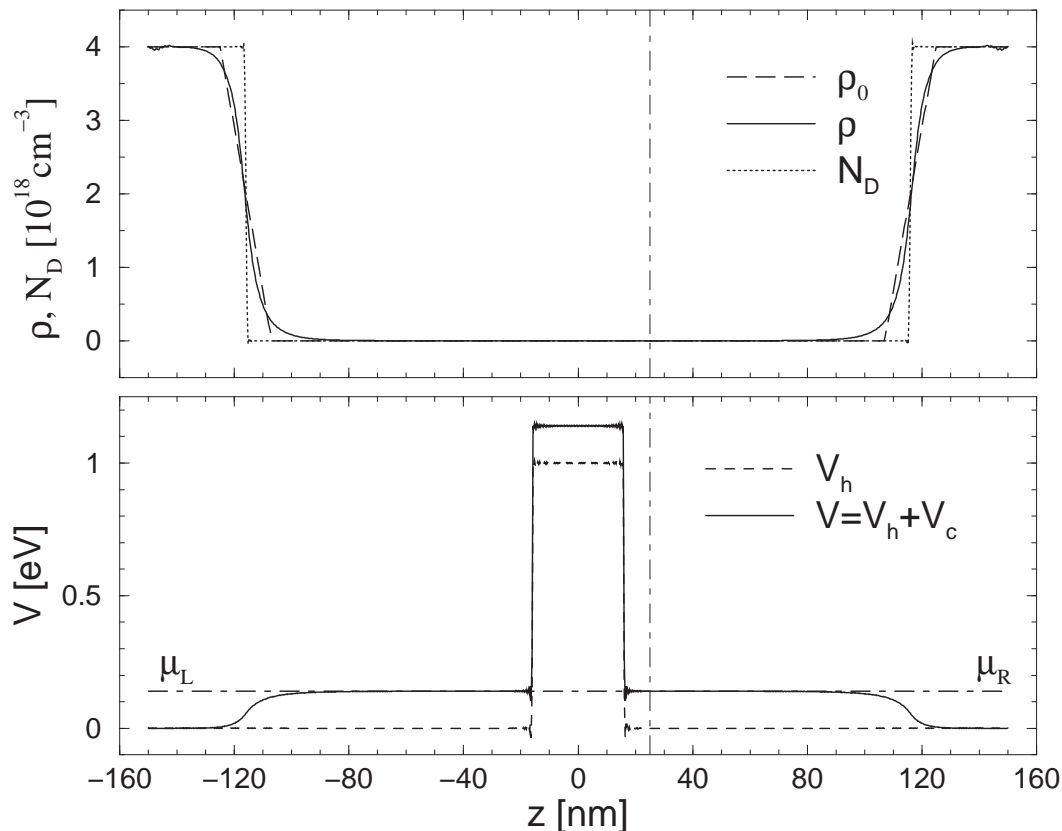


Figure 3.3: The self-consistent potential (lower part) and electronic density distribution (upper part) for the auxiliary symmetrical structure, which construction is based on the nominal structure (see text). The residual N_A doping is not taken into account.

was shown in Sec. 2.4. The self-consistent electronic density distribution does not depend on this initial guess and this was verified numerically, but a good guess shortens the convergence time.

We first present in Fig. 3.3 the results for the structure without considering the residual N_A doping of the GaAs layers. In the upper part are presented the initial electronic charge guess ρ_0 , the doping profile, N_D , $N_D = 4 \times 10^{18} \text{cm}^{-3}$ in the contact regions, and the self-consistent electronic density distribution ρ . The chemical potential is established by the contact doping using Sommerfeld model for free and independent electron gas [47], Chap.2, $E_F = \hbar^2(3\pi^2 N_D)^{2/3}/(2m^*)$. For the considered system $E_F = 0.1402831 \text{eV}$ and the Fermi wave length, $\lambda_F = 2\pi/k_F$, is $\lambda_F = 12.8 \text{nm}$.

In the lower part of Fig. 3.3 is presented the heterostructure potential V_h due to band off-sets and the self-consistent potential energy (solid line) $V = V_h + V_c$, where

V_c denotes the Coulomb potential. The chemical potentials, μ_L and μ_R , in the left and right reservoirs, respectively are equal because the structure is symmetric.

As one can see, the self-consistent potential raises on the undoped region with a quantity, denoted eU (see Fig. 3.2), and remains practically constant over the undoped semiconductor regions. This quantity, similarly to a p-n junction, can be called *built in* potential, and is determined mainly because the doping concentration changes abruptly at z_{Nd} in GaAs semiconductor layer. This quantity will not be modified by the applied bias. There are some differences between eU and the built-in potential in a p-n junction: the dependence of eU on other factors, like doping of the n- and p-regions, length of n- and p-regions, will be analyzed.

To obtain the nominal structure, we cut the symmetrical structure (the self-consistent potential V and electronic distribution ρ) at the coordinate $z = -136\text{nm}$ (120 nm in front of the blocking barrier) and at $z = 25\text{nm}$ (vertical dot-dashed line; 9 nm behind the blocking barrier) and this will constitute the starting point for the self-consistent calculations of the nominal structure. We have to work with

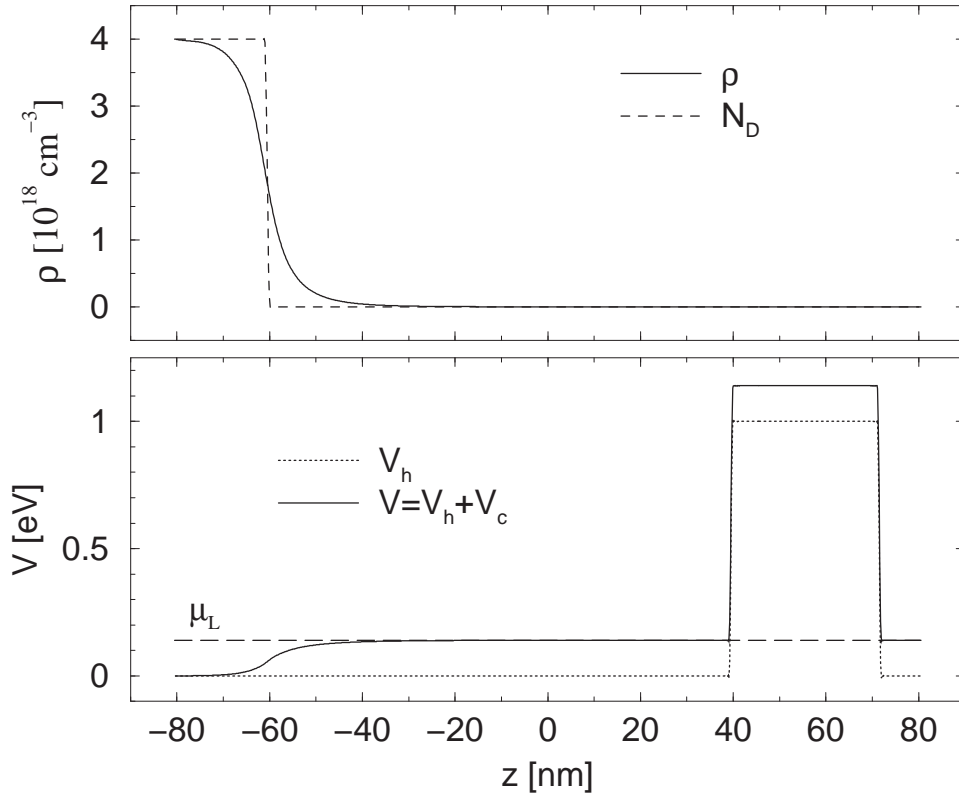


Figure 3.4: The self-consistent electronic density distribution (upper part) and potential V_{flat} (lower part) for the nominal structure, at the flat band bias V_G^f . The residual N_A doping is neglected,

a symmetrical interval in z , so our structure is between $[-80.5, 80.5]$ nm, because the total length of the active region is 161nm (20 nm high doped GaAs region, 100 nm spacer, 32 nm barrier, 9 nm cap layer). Now we can give also a quantitative evaluation of the built-in potential, namely the difference between potential values at the boundaries after the cutting process:

$$eU = V_{flat}(d) - V_{flat}(-d). \quad (3.3)$$

In our calculations, $eU = 0.13993$ eV. In the self-consistent calculations for the nominal structure (i.e. after cutting of the auxiliary structure) the value eU is kept fixed, this is the reason why a in Eq. (3.3) there is a 'flat' index. We also consider that there are no incident waves from the right side (see Fig. 3.2). This is based on the particular configuration of the analyzed structure: We can neglect the contribution of the right-incident scattering states because the occupied states in the gate contact lie about one electron volt below the conduction band edge in the back contact, due to the large barrier height of (gate) metal-semiconductor contact. [71]

The self-consistent potential and electronic density distribution for flat band configuration are presented in Fig. 3.4. One can read now the constant potential values outside the scattering region: i.e. $V_L = V_{flat}(-d)$ and $V_R = V_{flat}(d)$.

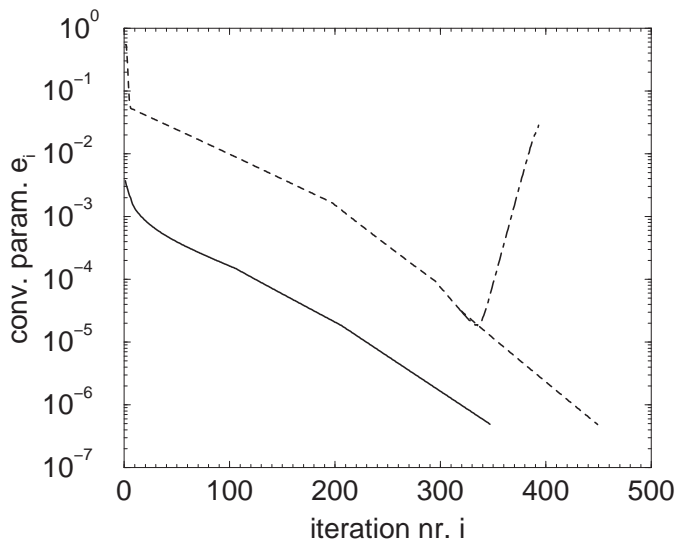


Figure 3.5: The convergence parameter during the iterations in the self-consistent calculations for auxiliary (dashed line) and nominal structure (solid line). With dot-dashed line is represented an evolution for out of convergence.

In Fig. 3.5 we plot the convergence parameter Eq. (2.112) during the iterations for the auxiliary symmetrical structure and for the nominal structure. This parameter gives information about the evolution of the self-consistent calculations.

The convergence limit is set to $\epsilon = 5 \cdot 10^{-7}$. Because the starting point for the nominal structure calculations is part of the self-consistent results for the symmetrical structure, the convergence is achieved faster. The evolution of the convergence parameter depends on the mixing factor f (see Eq. (2.111)). For the auxiliary symmetrical structure, we considered $f=0.015$ for the first 200 iterations, $f=0.025$ for the next 100 iterations, and we tried to accelerate the convergence process after the 300-th iteration by increasing f at $f=0.04$. But the calculations ran out of convergence, which is shown by the dot-dashed line in Fig. 3.5. So, we turned back at the iteration 330, and we set $f=0.03$ until convergence was achieved. The changes in f factor determine slope changes in the plot of convergence parameter. At the beginning of the self-consistent procedure, the evolution of the convergence parameter is abrupt (especially for the auxiliary symmetrical structure) because of the chosen start point.

For the nominal structure, f factor was $f=0.01$ for the first 10 iterations, $f=0.015$ for the next 100 iterations, increases after that at $f=0.02$ for the next 100 iterations and for the last iterations $f=0.025$.

The flat band structure is obtained for an external applied bias between the back contact and the top metallic gate (see Fig. 3.2),

$$eV_G^f = e\phi_1 = e\phi_{Bn} + (\mu_L - eU), \quad (3.4)$$

and will be taken as reference point for our numerical calculations. $e\phi_{Bn}$ denotes the barrier height of (gate) metal-semiconductor contact.

3.2.1 N_A doping effect

We can now make a discussion about the effect of the residual, unwanted, acceptor doping N_A in the GaAs layer. We consider the following doping profiles

$$\begin{cases} N_D - N_A = 4 \times 10^{18} \text{cm}^{-3} & \text{in contacts} \\ N_A - N_D = 10^{15} \text{cm}^{-3} & \text{in "undoped" regions} \end{cases} \quad (3.5)$$

which are introduced in the Poisson equation (2.90) and the effect on the potential and electronic density distribution for the auxiliary symmetrical structure is presented in Fig. 3.6.

One can see from Fig. 3.6 that the N_A doping rises the potential, so that around the blocking barrier $V > \mu_L$, and in turn the electronic charge distribution decreases drastically around the blocking barrier. The total negative charge density distribution $\rho + N_A^-$ is practically constant and equal with the acceptor doping in the middle of the structure. The built-in potential is changed with respect to the previous calculations, and has the value $eU = 0.14335\text{eV}$. This value is kept constant, as the difference between V_L and V_R , $eU = V_R - V_L$, during the self-consistent calculations for the nominal structure.

The self-consistent potential and electronic density distribution for the nominal structure, considering the residual N_A doping are presented in Fig. 3.7(a) and 3.7(b).

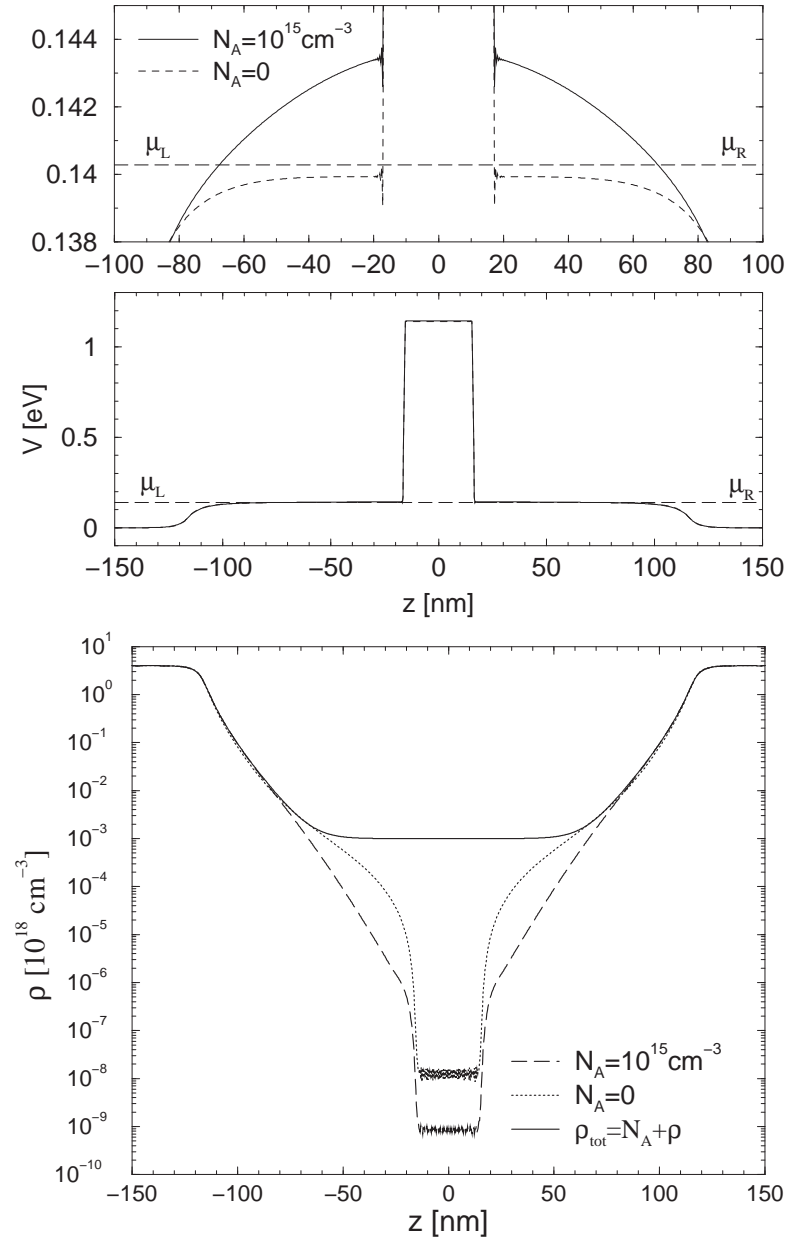
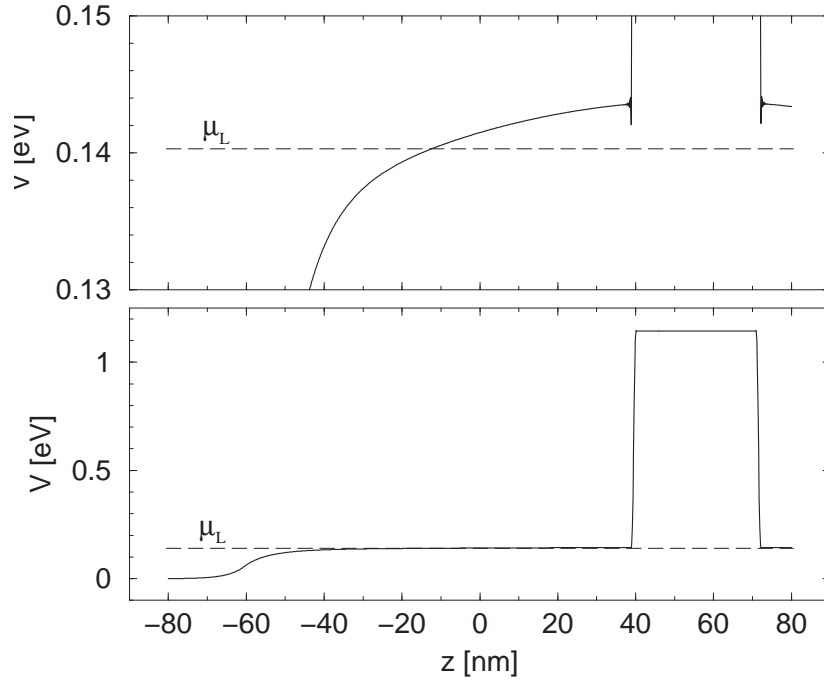
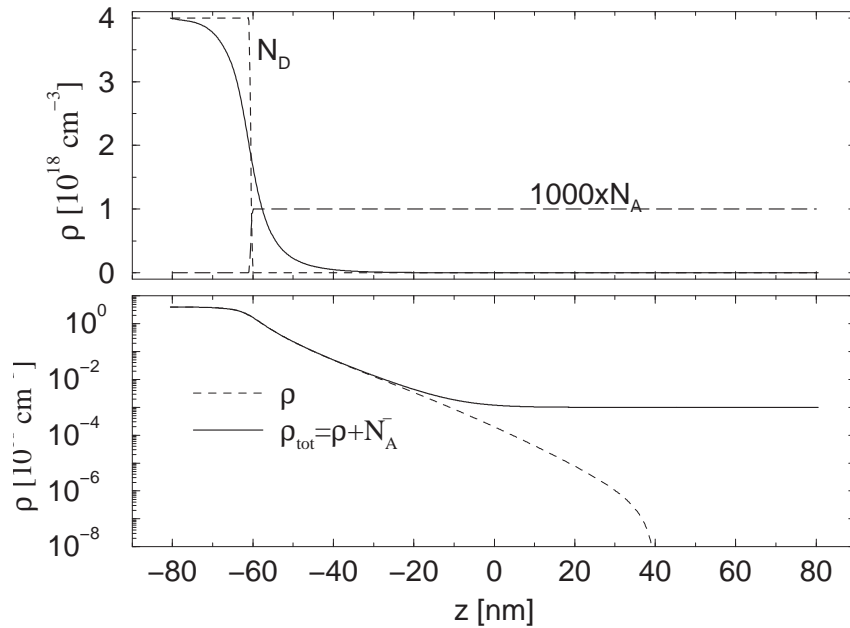


Figure 3.6: The effect of the acceptor doping N_A on the self-consistent potential and electronic density distribution for the auxiliary symmetrical structure. Middle part: the self-consistent potential with a detail (upper part) around the chemical potential and the blocking barrier. Lower part: the self-consistent electronic density distribution ρ for taking (dashed line) and without taking (dotted line) in account the N_A doping. With solid line is presented the total negative charge density distribution $\rho_{tot} = N_A + \rho$.



(a) Self-consistent potential. Upper part: detail around the chemical potential μ_L .



(b) Self-consistent electronic density distribution. Upper part: linear scale, lower part: logarithmic scale.

Figure 3.7: Self-consistent results for the nominal structure with acceptor doping N_A , at flat band bias V_G^f .

3.3 Applied bias

In this section we characterize the quasi-bound states which appear at positive applied bias, and which are directly related to the field induced two dimensional electron gas (2DEG).

We can see from Fig. 3.8 that the flat band structure is obtained for an applied positive bias V_G^f where $eV_G^f = e\phi_1 = e\phi_{Bn} + (\mu_L - eU)$. The flat band configuration and the corresponding applied bias will be taken as reference point for our numerical calculations.

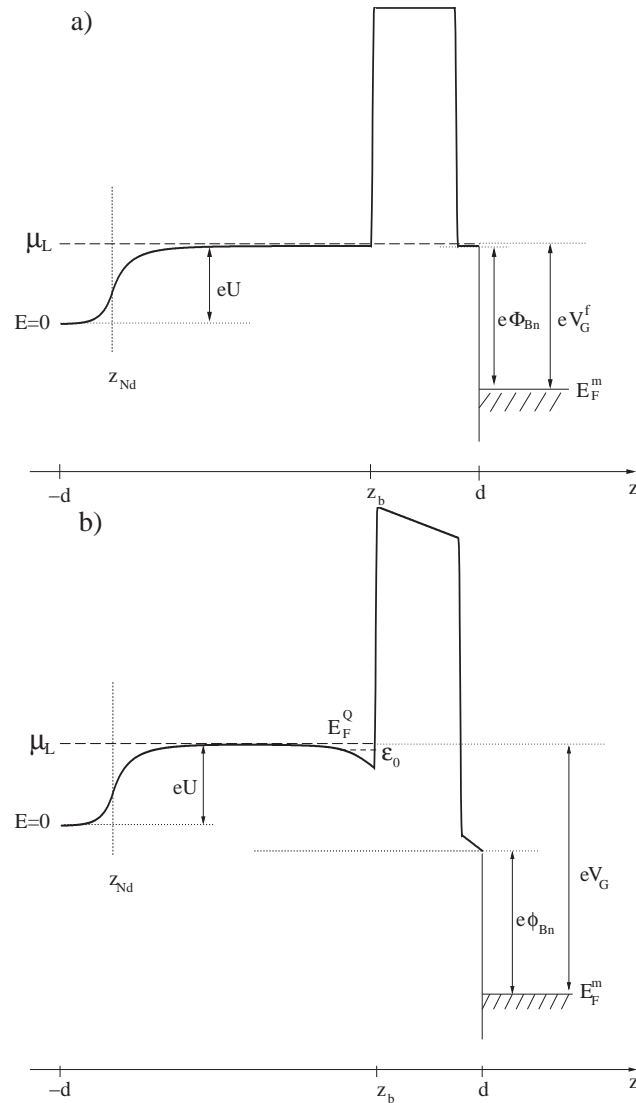


Figure 3.8: The band diagram scheme for the whole structure: a) for the applied bias V_G^f at which the flat band configuration is obtained and b) for $V_G > V_G^f$.

If we increase the forward bias V_G then we can write

$$eV_G = e\phi_1 + eV_g \quad (3.6)$$

and the quantity V_g will represent further the "applied" bias on the active structure between $[-d, d]$.

In Fig. 3.9 it is shown that the quantity eV_g is exactly the modification of the potential energy at the boundary point $z = d$ from the flat band configuration to the applied bias configuration:

$$eV_g = V_{flat}(d) - V(d), \quad (3.7)$$

where $V_{flat}(z)$ is the potential in the flat band configuration and $V(z)$ is the potential for the structure under the bias V_g .

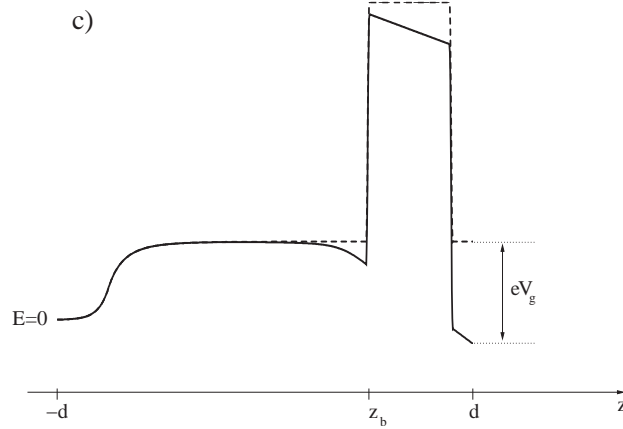


Figure 3.9: The band diagram scheme in the scattering region, for flat band configuration (dashed line) and for an applied bias (continuous line), which shows that eV_g is the difference between the potential values at the right boundary point $z = d$.

3.3.1 Wigner Eisenbud functions

In this section we analyze the effect of the external electrical field on the closed counter part of our scattering problem, i.e. the effect on the Wigner-Eisenbud functions. The self-consistent calculations are performed as in Sec. 2.4. The number of zeros for the Wigner Eisenbud functions, their order, do not change in the self-consistent procedure. But their form, i.e. the position of their maxima and minima, changes during iterations, because it is directly related to the form of potential, calculated iteratively. A typical configuration of the Wigner Eisenbud functions at the end of the self-consistent procedure is presented in Fig. 3.10 a)

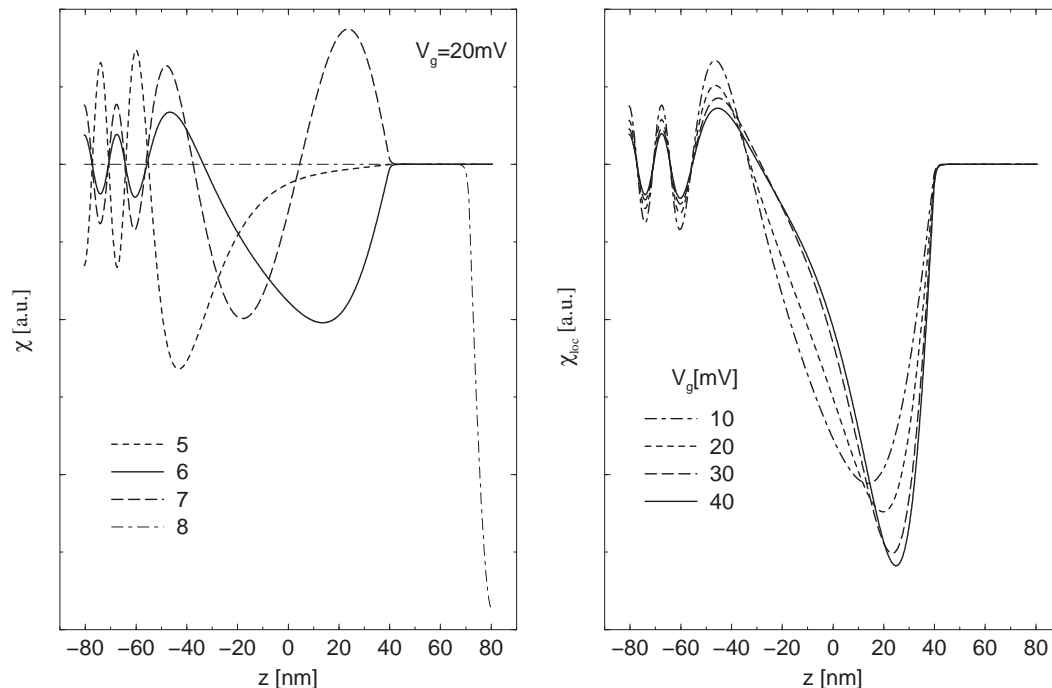


Figure 3.10: Left: The Wigner Eisenbud functions around the localized one for applied bias $V_g = 20$ mV. Right: the localized Wigner Eisenbud function for different applied biases.

Because the Wigner-Eisenbud problem is a closed one, one can discuss about a localized Wigner Eisenbud function, which in our case is the 6th one in the left part of Fig. 3.10. In the right part of Fig. 3.10 we can observe how its localization character changes with increasing applied bias: the maximum of the function increases while the width of the function and the coupling with the external region decrease.

The energy corresponding to the localized Wigner-Eisenbud function, can be taken as a first approximation for the energy of the quasi-bound state which appears by increasing the applied bias. This approach is reasonable for small V_g biases, but for bigger ones one needs a more accurate method to find the energy and the width of the quasi-bound state (see Sec. 3.6.1).

3.3.2 Wave functions and quasi bound states

As one can see from Fig. 3.7(a), our potential energy configuration is so that $V_L < V_R$, which means that the Schrödinger equation (2.6) has a continuous non-degenerate eigenvalue spectrum between V_L and V_R , and also for this energy interval can appear quasi-localized states. They are not localized states, because the energies $\epsilon > V_R$ correspond to the classically allowed spectrum so that we call them

quasi-bound states. Their energies generally manifest as maxima in the tunneling spectrum. Because of the blocking barrier between the back contact and the top metallic gate, the tunneling probability is practically zero, so we should find another quantity on whose structure the presence of the quasi-bound states can be identified. Such a quantity is the probability distribution density $P_\epsilon(z) = |\psi^L(\epsilon, z)|^2$, to find an electron in the state $\psi^L(\epsilon, z)$ in a volume element at the given z -coordinate as is also suggested recently by Magnus [82].

We plotted in the left part of Fig. 3.11 $P_\epsilon(z)$ at a fixed point $z_p \leq z_b = 39.5\text{nm}$ for an interval of energies around the energy of the localized Wigner Eisenbud function. The function $P_\epsilon(z_p)$ has a peak with the maximum at ϵ_0 . We can define an interval centered on ϵ_0 , where the peak extends, and all scattering states with energy in this interval are referred to as quasi-bound states. This interval becomes smaller and smaller by increasing the gate voltage V_g and the integration over this interval for calculating the contribution to charge density Eq. (2.88) should be done finer. Finding correctly this interval is essential for an accurate determination of the accumulated charges in the quantum well. If this quantity is over- or under-evaluated then the self-consistent procedure does not work properly.

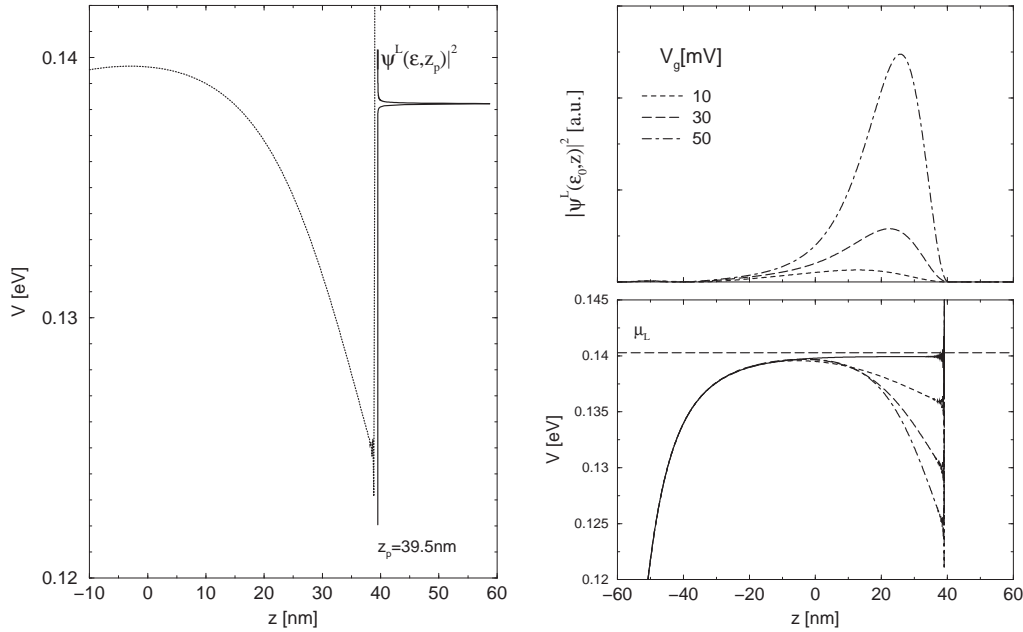


Figure 3.11: Left: The wave function $|\psi^L(\epsilon, z_p)|^2$ at a fixed point z_p , for an interval of energies around the energy of the localized Wigner Eisenbud function. With dotted line is plotted the potential of the quantum well in front of the blocking barrier, for $V_g = 0.06V$. Right: The localized wave function $|\psi^L(\epsilon_0, z_p)|^2$ (upper part) and the corresponding self-consistent potential (lower part) for $V_g = 10, 30, 50\text{mV}$.

The absolute value of the wave function for the energy ϵ_0 is plotted in Fig. 3.12. This wave function does not tend to zero at the left edge of the scattering region. Its oscillations for $z \sim -d$ shows that the associated state is not totally decoupled from the left reservoir and consequently not bound. But it is usual to call it quasi-bound state because the probability distribution density $P_\epsilon(z)$ has a very sharp maximum for this energy as it is shown in the left part of Fig. 3.11 for the fixed point $z = z_p$. In the same time, this wave function has zero values on the right edge of the scattering region, which shows explicitly that it is totally decoupled from the right reservoir (i.e. metallic gate).

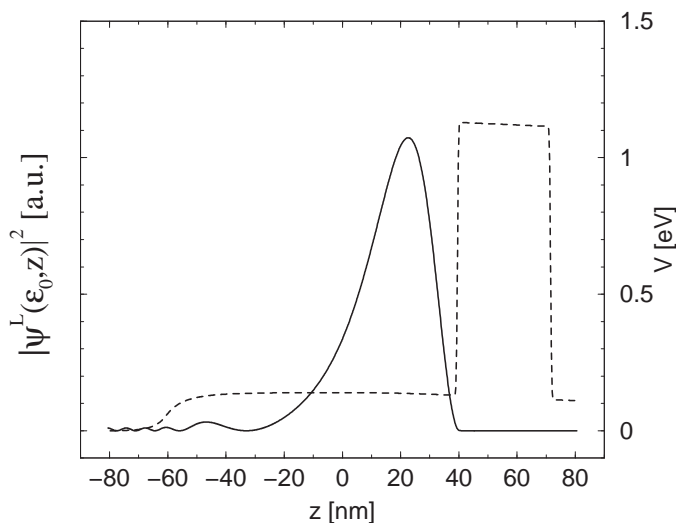


Figure 3.12: The wave function of the quasi-bound state (solid line) and the self-consistent potential (dotted line) for $V_g = 0.03V$. The energy and the width of the quasi-bound state are $\epsilon_0 = 0.139137\text{eV}$ and $\Gamma = 0.105 \times 10^{-3}\text{eV}$, respectively.

The self-consistent potential and electronic density distribution for some applied biases are presented in Fig. 3.13 a). These figures shows that the two distributions do not practically change in the back contact region, around $z_{Nd} = -60.5\text{nm}$. We present in Fig. 3.13 b) the potential and the charge density only for the accumulation layer. Increasing the applied bias, the band bending at the interface between the GaAs spacer and the blocking barrier increases, forming a quantum well which can support quasi bound states. The system is open for electron exchange with the back contact and these states are populated leading to charge accumulation at the interface between the spacer GaAs layer and the blocking barrier. With applied bias increases also the accumulated charge in the quantum well, Fig. 3.13 b), upper part.

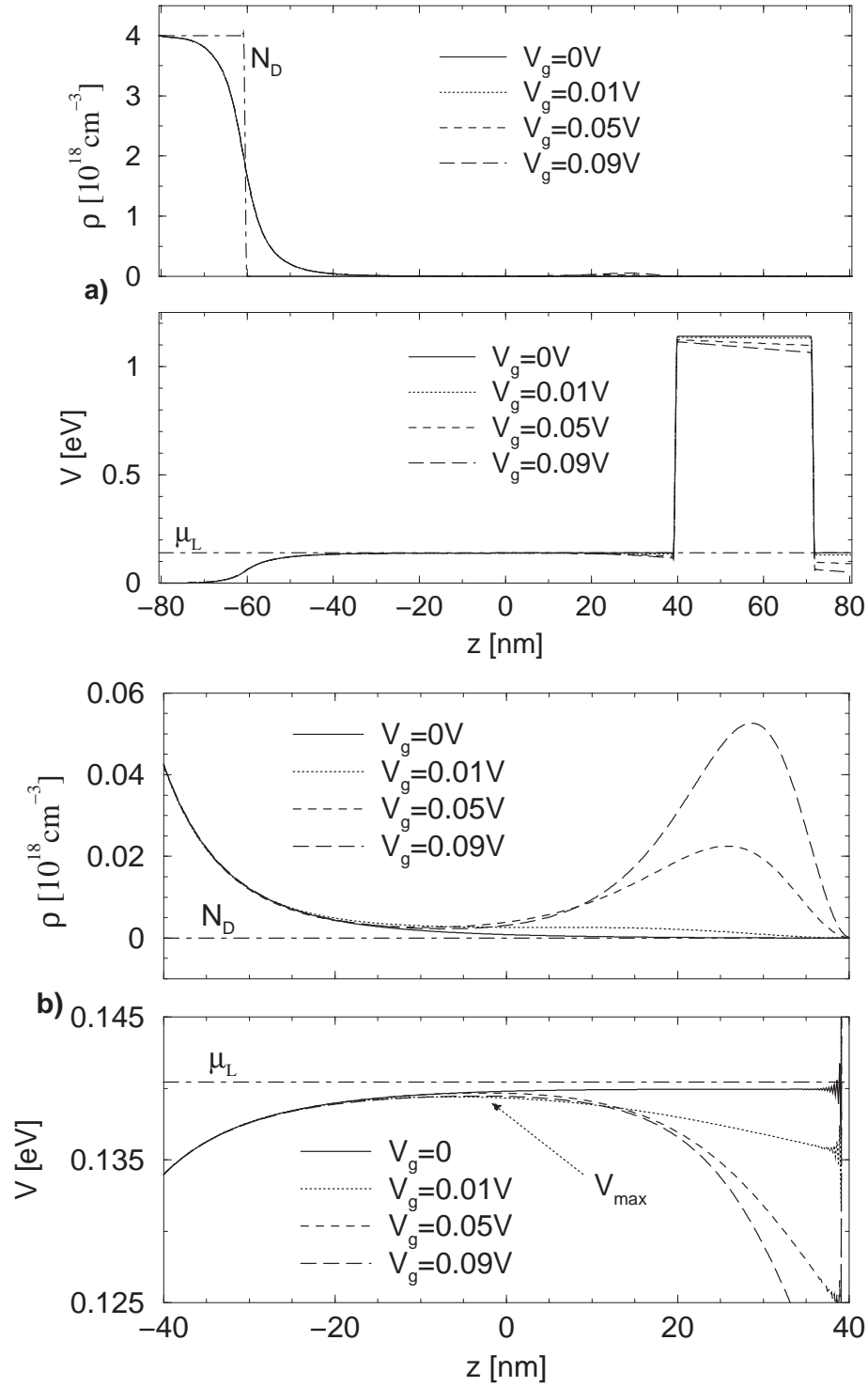


Figure 3.13: a) The self-consistent potential (lower part) and electronic density distribution (upper part) for the nominal structure at biases $V_g = 0, 10, 50, 90 \text{ mV}$. b) Electronic density distribution (upper part) and potential (lower part) in detail for the accumulation layer.

3.4 Comparison to the MOS

If we compare our structure with the MOS (metal-oxide-semiconductor) structure, which was very intensively studied in the Si-SiO₂ systems [53], we can observe some useful similarities but also some differences.

In Fig. 3.14 we sketch the band diagrams for both structures: the MOS structure (in the upper part) and the GaAs/Al_xGa_{1-x}As heterostructure (in the lower part).

A typical MOS structure with n-type inversion region consists of a p-type semiconductor (e.g. silicon), an oxide barrier and metal contact [50]. For the semiconductor region the bulk equations (for charge density, energy levels, ...) are valid and we can call this "bulk region". The chemical potential is equal everywhere in the semiconductor. The band-bending approximation is valid. This means that the density of states in the conduction and valence bands is not changed by an electric field. In the band-bending approximation the effect of an electric field is only to shift all the energy levels in the conduction and valence bands by a constant amount determined by the potential at every given point in the semiconductor. The inversion layer appears at the gate voltage for that the intrinsic Fermi level bends down to the chemical potential. The active region consists of the depletion region, of micrometers order, and inversion region, of nanometer order. For high applied voltages and high electron concentration in the inversion layer the surface quantization appears, the band-bending approximation is not anymore valid (the density of states is changed by the electric field) and the quantum mechanical calculations are necessary [53].

The present structure consists of i.) a heavily doped region of GaAs, for which the bulk model is taken valid, and the chemical potential is already in the conduction band, ii.) continued with intrinsic region of the same material GaAs, iii.) a blocking barrier and iv.) metallic gate. The field induced 2DEG, which constitutes the active region, appears at the interface between the GaAs spacer and the blocking barrier for an applied bias for which the conduction band bends under chemical potential. The active region is of nanometer order and the 2DEG can be in contact with n-doped region. The barrier, consisting of different layers of GaAs and Al_xGa_{1-x}As may be penetrable which is a major difference to the classical MOS structures, although there exist also leakage current for thin oxide barriers. In the present modeling we do not consider penetrable barriers, so there is no current flow.

Another difference between these two structures is that the distance between the active region and the "bulk region" in MOS structure is fixed through the depletion length, while for the present structure can be engineered in the growing process. Thus, the free electrons in the active region are for MOS structure far away from the free carriers in the p-type silicon, while for the present structure the electrons in the active region can be in contact with the free electrons in the n heavily doped GaAs region. While for the classical MOS structure, for low gate voltages a drift diffusion model can be applied, for the present structure purely quantum mechanically calculations for any applied bias should be performed to find the free

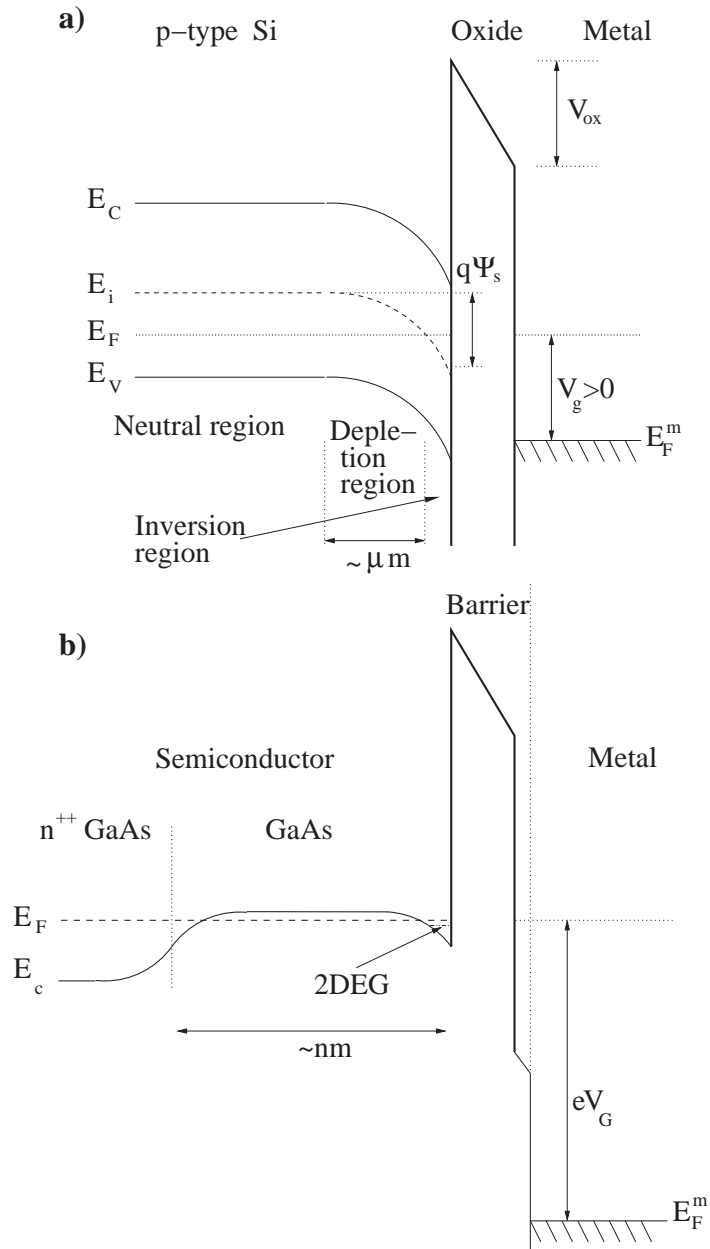


Figure 3.14: Comparison with MOS structure. a) Energy diagram of the MOS system for p-type silicon in depletion-inversion. b) Conduction band diagram for the analyzed GaAs/Al_xGa_{1-x}As heterostructure, which yields a field induced 2DEG.

carriers concentration.

Both structures can be analyzed within capacitance spectroscopy. For both structures one plate of the capacitor is the metallic gate and the second plate is the "bulk material": semi-infinite p-Si or n-doped GaAs (back gate), respectively. When the field induced inversion layer or 2DEG, respectively, appears then it plays the role of the second plate.

3.5 Capacitance

By modulating V_G with a small ac voltage, the ac current through the sample can be measured. The real part of the current depends on the tunnel resistance while the imaginary component is determined by the capacitance of the structure. The experimental data [71] were obtained by studying the imaginary component of the ac current through the sample as a function of the gate voltage (C-V curve), at low frequency $\approx 100\text{Hz}$ and temperatures $\approx 25\text{mK}$. The amplitude of the ac voltage does not exceed 1mV and corresponds to the linear regime. The gate surface is $S = 20 \times 40\mu\text{m}^2$.

As we emphasized in Sec. 3.2 the particular configuration of the analyzed structure (Fig. 3.2) does not allow incident electrons from the right contact (top metallic gate). That means that only the scattering states incident from the left (back) contact have a contribution to the electronic density distribution. According to Eqs. (2.152) and (2.153), $\rho(z) = \rho_1(z)$ and $\rho_2(z) = 0$.

Following the capacitance model presented in detail in Sec. 2.6, we identify the free charges in the system with

$$\sigma_1^{free} = -e \int_{-d}^d \rho(z) dz, \quad (3.8)$$

$$\sigma_2^{free} = 0, \quad (3.9)$$

and the bound charges with

$$\sigma_1^{bound} = e \int_{-d}^d (N_D(z) - N_A(z)) dz, \quad (3.10)$$

$$\sigma_2^{bound} = 0. \quad (3.11)$$

We consider all impurities completely ionized, $N_A^-(z) = N_A(z)$ and $N_D^+(z) = N_D(z)$.

In contrast to Eqs. (2.148) and (2.150), for our structure which does not allow incident states from the right it is more convenient to associate all fixed charges with σ_1^{bound} . As was pointed out in Sec. 2.6 these charges do not vary with the applied bias and consequently have no contribution to the capacitance.

According to the definitions (2.146) and (2.147) we can now express the charges corresponding to the plates of the capacitor:

$$\Sigma_1 = \sigma_1 + Q, \quad \Sigma_2 = \sigma_2, \quad (3.12)$$

where the sheet charges at the interfaces between the quantum system and the contacts, σ_1 and σ_2 , respectively, are given by Eqs. (2.142) and (2.143) and Q is the total electrical charge inside the quantum system, (2.144). We have the general form (2.154) of the neutrality condition which becomes

$$\sigma_1 + Q = -\sigma_2 \quad (3.13)$$

in our particular case. The differential capacitance per area is

$$C = \left| \frac{d\Sigma_1}{dV_g} \right| = \left| \frac{d\Sigma_2}{dV_g} \right|. \quad (3.14)$$

Note that V_{sd} which appears in Sec. 2.6 means for our structure V_g . The capacitance given by Eq. (3.14) is presented in Fig. 3.15, together with the quantities $\Sigma_{1/2}$, $\sigma_{1/2}$ and $\sigma_1^{free} + \sigma_1^{bound}$. σ_1 is constant because the self-consistent potential in the contact region, $-d < z < z_{Nd}$, does not practically change with applied bias.

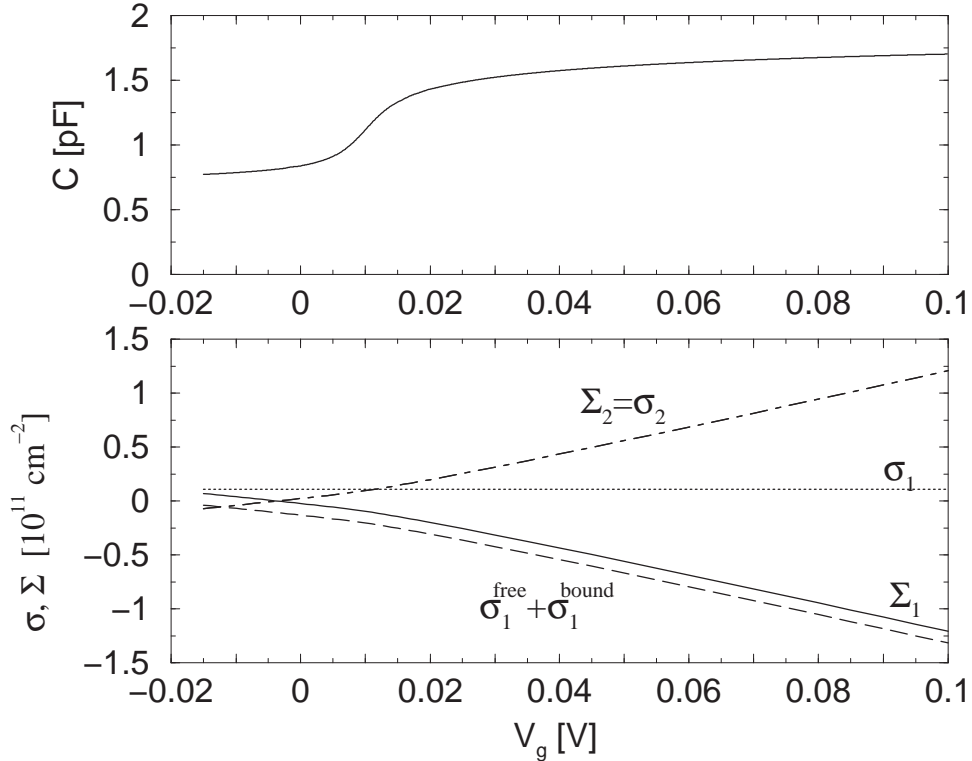


Figure 3.15: Lower part: The areal charge densities defined in our capacitance model, $\Sigma_{1/2}$, $\sigma_{1/2}$ and $\sigma_1^{free} + \sigma_1^{bound}$. Upper part: The capacitance given by Eq. (3.14), multiplied with the surface S . The residual N_A doping is taken into account.

In Fig. 3.16 we present for comparison the experimental data and the capacitance calculated in our model. Qualitatively, the C-V-traces take the form of a broadened

step located between a low-voltage, $V < V_-$, and a high-voltage, $V > V_+$, plateau. Both plateaus have a weak positive slope. We define the center of the step through the condition $d^2C/dV_g^2 = 0$ and V_- and V_+ correspond to the gate voltages where $|dC/dV_g|$ takes half of its maximum value. Because the work function of the metal contact is not precisely known we shift the theoretical voltage scale V_g with respect to the experimental one V_G , so that the centers of the steps coincide. The applied bias for the flat band configuration, which determine the shift between V_G and V_g (Eq. (3.6)) is $\Phi_1 = 0.701V$ when the N_A doping is taken into account, and $\Phi_1 = 0.71V$ when $N_A = 0$ (see Fig. 3.2). One can see in Fig. 3.16 that considering the residual N_A doping, the numerical C-V curve closes with the experimental one.

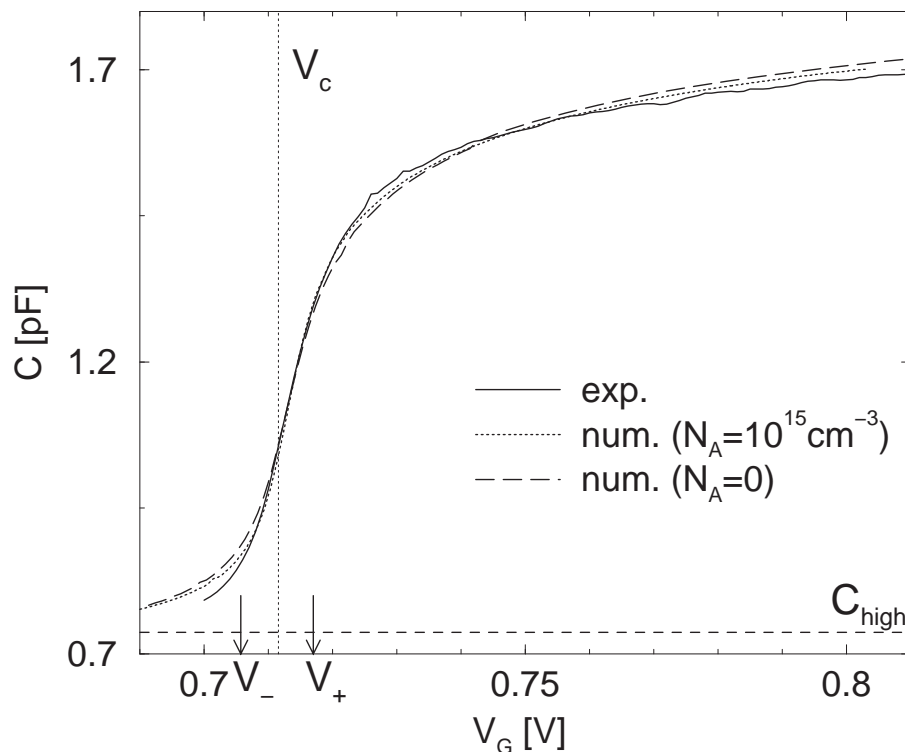


Figure 3.16: The experimental data and the calculated values for the capacitance of the nominal structure. C_{high} is the high frequencies capacitance limit.

We can estimate the limit values of the capacitance using the classical formula

$$C = \frac{\epsilon_0 \epsilon_r \cdot S}{l}, \quad (3.15)$$

where S is the area of the plates, l the distance between the plates and ϵ_r the relative permittivity of the material between the plates, Fig. 3.17. For our system, $\epsilon_r = 12.5$ and $S = 800\mu\text{m}^2$.

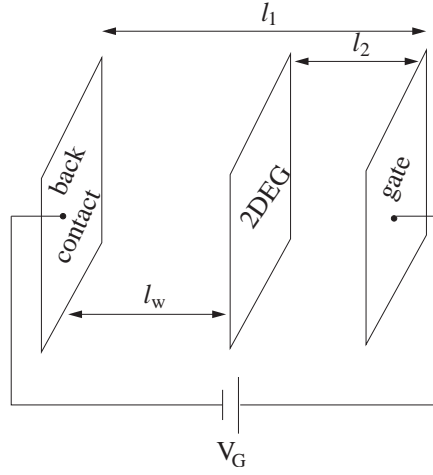


Figure 3.17: The geometrical scheme for the limit values of the capacitance.

At high frequencies the charge is not accumulating at the interface between the GaAs spacer and the blocking barrier and the capacitance will be determined regarding the two contacts as the capacitor plates. The distance between the plates can be taken from the geometrical considerations as $l_1 = d - z_{Nd} = 141\text{nm}$, which gives

$$C_{inf} = 0.628 \text{ pF}.$$

But, the free charges (electrons) from the back contact enter the system, so that a better evaluation of the distance between plates is given by the experimental value [71], $l_1 = l_g = 120\text{nm}$, which leads to

$$C_{high} = 0.7375 \text{ pF}.$$

In the opposite limit, for low frequencies, the two dimensional electron gas (2DEG) is formed in front of the blocking barrier and plays the role of the left plate of the capacitor. Also in this case, the right plate is the metal gate, so that the distance between the plates can be considered $l_2 = d - z_b = 41\text{nm}$ which gives

$$C_{sup} = 2.16 \text{ pF}.$$

But the 2DEG is not a δ -charge distribution located at $z = z_b$, as would be considered within a classical image of the spatial location of the charges in front of the blocking barrier. So, we should consider the spatial spreading of the 2DEG and should take the distance between the plates as the experimental value $l_2 = l_g - l_w = 50\text{nm}$. In this case

$$C = 1.77 \text{ pF},$$

which is in good agreement with the value of the high voltage capacitance plateau.

In Fig. 3.16 we indicate by a horizontal line the capacitance limit value C_{high} which is approached in the small voltage regime. For these voltages there are net charges only in the source contact region of the scattering area ($-d \leq z \leq z_{Nd}$) and these charges are only weakly dependent on the applied bias.

In Fig. 3.18 we plot the numerical values of the capacitance for different structures at which the distance between the blocking barrier and the doped region, $s = z_b - z_{Nd}$, was modified from 100nm as for the nominal structure to 80nm and 70nm. One can immediately observe, that the value of the low-voltage plateau increases, because the distances between the plates in the C_{high} limit decreases. At $s = 70$ nm the high voltage plateau value is evidently smaller as in other cases. We think that there is a superposition between the Thomas-Fermi screening length in the back contact and the penetration length of the wave function of the 2DEG into the shallow barrier which separates the 2DEG from the back contact. This needs to be verified in future experiments.

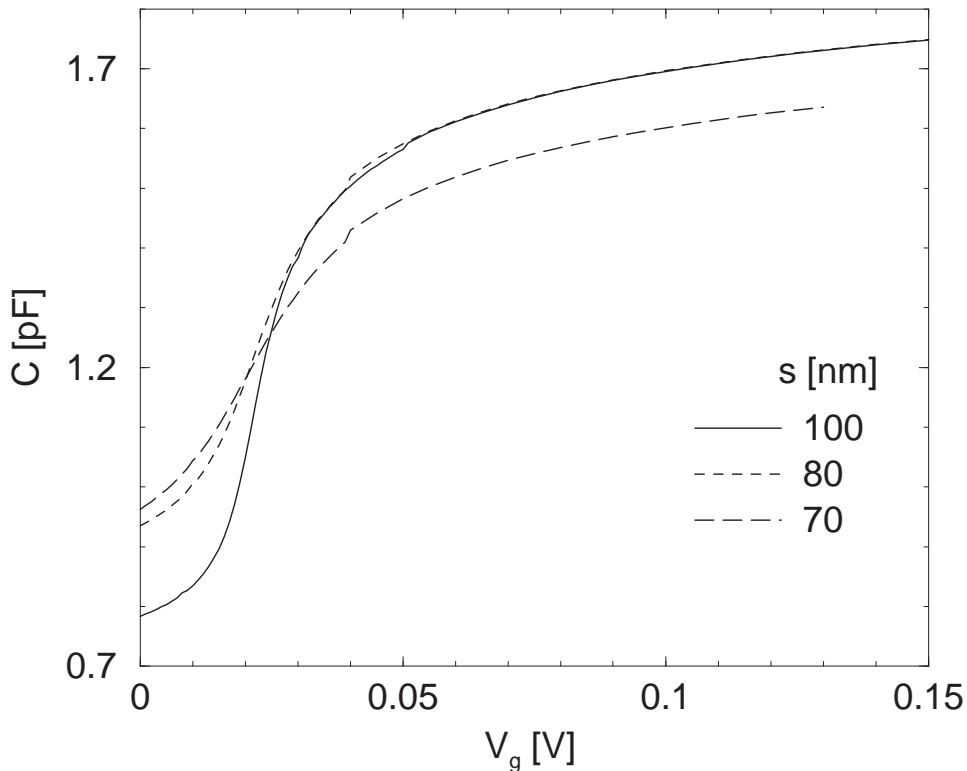


Figure 3.18: The numerical capacitance values (without considering the N_A doping) for different distances s between the blocking barrier and the doped region, $s = z_b - z_{Nd}$.

3.5.1 Impenetrable barrier

Our analyzed structure contains a blocking barrier (see Fig. 3.2) which was considered of 1eV height and it is practically an impenetrable barrier. The self-consistent calculations for the electronic density distribution, Figs. 3.7(b) and 3.13 b), show that the penetration of the electrons in the blocking barrier is practically negligible. In this case one can calculate the capacitance with Gauss' law as it is done by Schmarek [79]:

$$\frac{C}{S} = \epsilon_0 \epsilon_r \frac{\partial}{\partial V_g} \left(\oint_{\Gamma} \nabla V(z) \cdot \mathbf{n} ds \right), \quad (3.16)$$

where the surface Γ encloses the free charge of the 2DEG and has the boundaries inside the blocking barrier and inside the back contact (see Fig. 3.19); \mathbf{n} is the external normal at this surface.

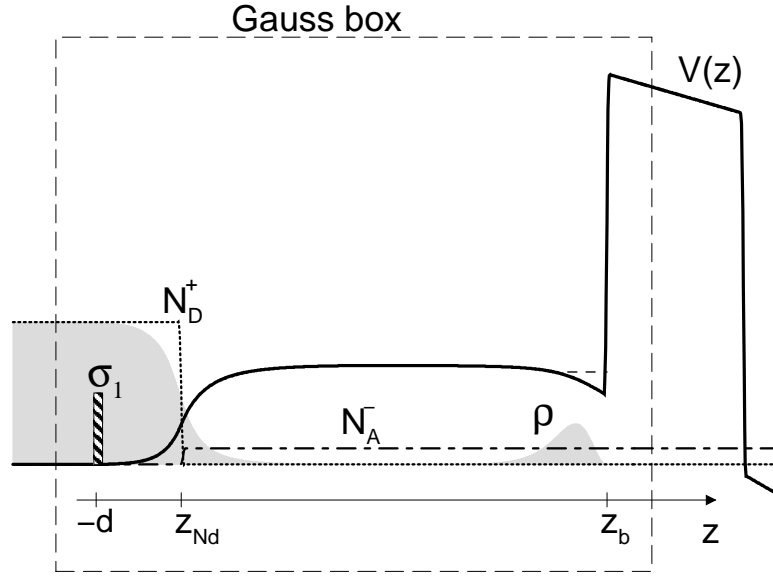


Figure 3.19: The Gauss box which includes the free and bound charges and extends over the back contact and into the blocking barrier. The potential is plotted with solid line, the ionized donors distribution N_D^+ with dashed line and the ionized acceptors distribution N_A^- with dot-dashed line. The gray area corresponds to the the electronic charge density ρ and the dashed area represents the δ sheet charge, σ_1 , at $z = -d$.

The Gauss' law gives

$$\int_{\mathcal{V}} \text{div} \mathbf{E} d^3r = \oint_{\Gamma} \mathbf{E} \cdot \mathbf{n} ds, \quad (3.17)$$

where \mathcal{V} is the volume enclosed by the surface Γ . Because the potential varies only in the growth direction z , the electric field \mathbf{E} has only the z -component different

from zero. In the back contact ($z < -d$) the potential is constant ($V(z) = V_L$) so that the electric field is zero. The right side of the Gauss box is taken exactly at the beginning of the blocking barrier and the electric field here is

$$E_z(z_b) = \frac{1}{e} \left. \frac{dV(z)}{dz} \right|_{z=z_b}, \quad (3.18)$$

so that

$$\oint_{\Gamma} \mathbf{E} \cdot d\mathbf{s} = S \frac{1}{e} \left. \frac{dV(z)}{dz} \right|_{z=z_b}. \quad (3.19)$$

From the Maxwell equation we have

$$\text{div} \mathbf{E} = \frac{e}{\epsilon_0 \epsilon_r} [N_D^+(z) - N_A^-(z) - \rho(z)] \quad (3.20)$$

and performing the integral over the volume \mathcal{V} in Eq. (3.17), one obtains the total charge inside the Gauss box

$$\begin{aligned} SQ_{in} &= \int_{\mathcal{V}} \text{div} \mathbf{E} d^3r = S \int_{-d-\eta}^{z_b} dz (\sigma_1 \delta(z+d) - N_A^-(z) + N_D^+(z) - \rho(z)) \\ &= S(\sigma_1 + \sigma_1^{bound} + \sigma_1^{free}), \end{aligned} \quad (3.21)$$

where $\eta > 0$. This charge represents in fact the charge on one plate of the capacitor, Σ_1 (Eq. (2.146)), and its variation with applied bias gives the capacitance

$$C = S \frac{dQ_{in}}{dV_g}. \quad (3.22)$$

This expression is equivalent with the definition (3.14).

So, we have demonstrated that for a system which contains an impenetrable barrier the charge on a plate of the capacitor is straightforwardly obtained with the Gauss law knowing the potential slope in front of the impenetrable barrier. The capacitance is given as usual by the variation of the plate charge with respect to the applied bias. We would like to emphasize, that this method is not anymore helpful for a penetrable barrier, because the Gauss law takes into account the spatial distribution of the charges but not their ancestry (i.e. from which reservoir they are coming)!

3.6 Intermediate resonance

In this section we will analyze the critical voltage regime, i.e. the step in the C-V curve between the low- and high- voltage plateaus, Fig. 3.20 and we will show that it can be described by a single resonance which we call intermediate resonance. We emphasize the excellent quantitative agreement between theory and experiment. From Fig. 3.20 it can be seen that the step in the C-V characteristic is located in

a regime of gate voltages where the maximum V_{\max} of the potential barrier which separates the back contact from the potential pocket at the interface between the GaAs spacer and the blocking barrier (see Fig. 3.13) is below the chemical potential, μ_L . Consequently there is an open channel of classically allowed motion, $V_{\max} < \epsilon < \mu_L$. This finding resulted in a number of calculations with varying distance of the back gate to the barrier and varying background doping concentration in the GaAs-spacer layer.

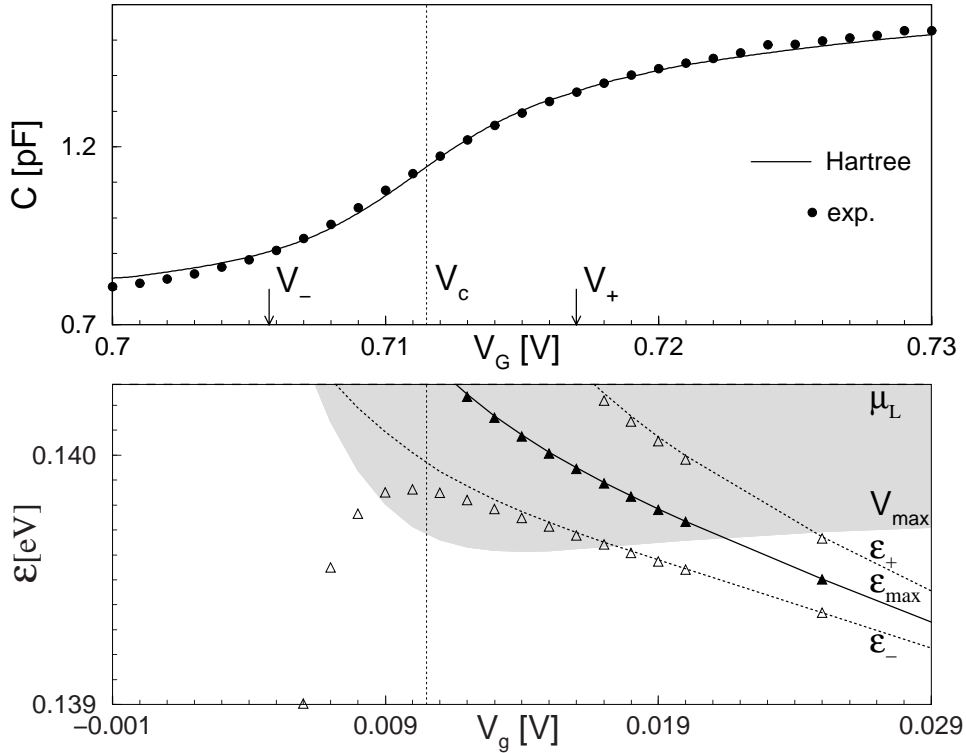


Figure 3.20: Upper part: The C-V curve, experimental data [71] (filled circles) and theory (solid line) in the step region. Lower part: As the result of the complete numerical calculation the resonance energy ϵ_{\max} (solid line), and the energies ϵ_{\pm} at which the absolute value of the wave function takes half the maximum value at constant $z = z_{\max}$ (dotted lines). The corresponding values ϵ_{\max}^F (filled triangle) and ϵ_{\pm}^F (triangle) in the Fano approximation. Shaded area: energies with $V_{\max} < \epsilon < \mu_L$.

To analyze the physical process that underlies the step in the C-V curve we plot in Fig. 3.21 the energy- and space-dependence of the probability distribution density, $P_{\epsilon}(z) = |\psi^L(\epsilon, z)|^2$, to find an electron in the state $\psi^L(\epsilon, z)$ in a volume element at the given z -coordinate. We would like to point out that the analyzed system has zero transmission because of the blocking barrier, therefore the appropriate quantity to study is the probability distribution density.

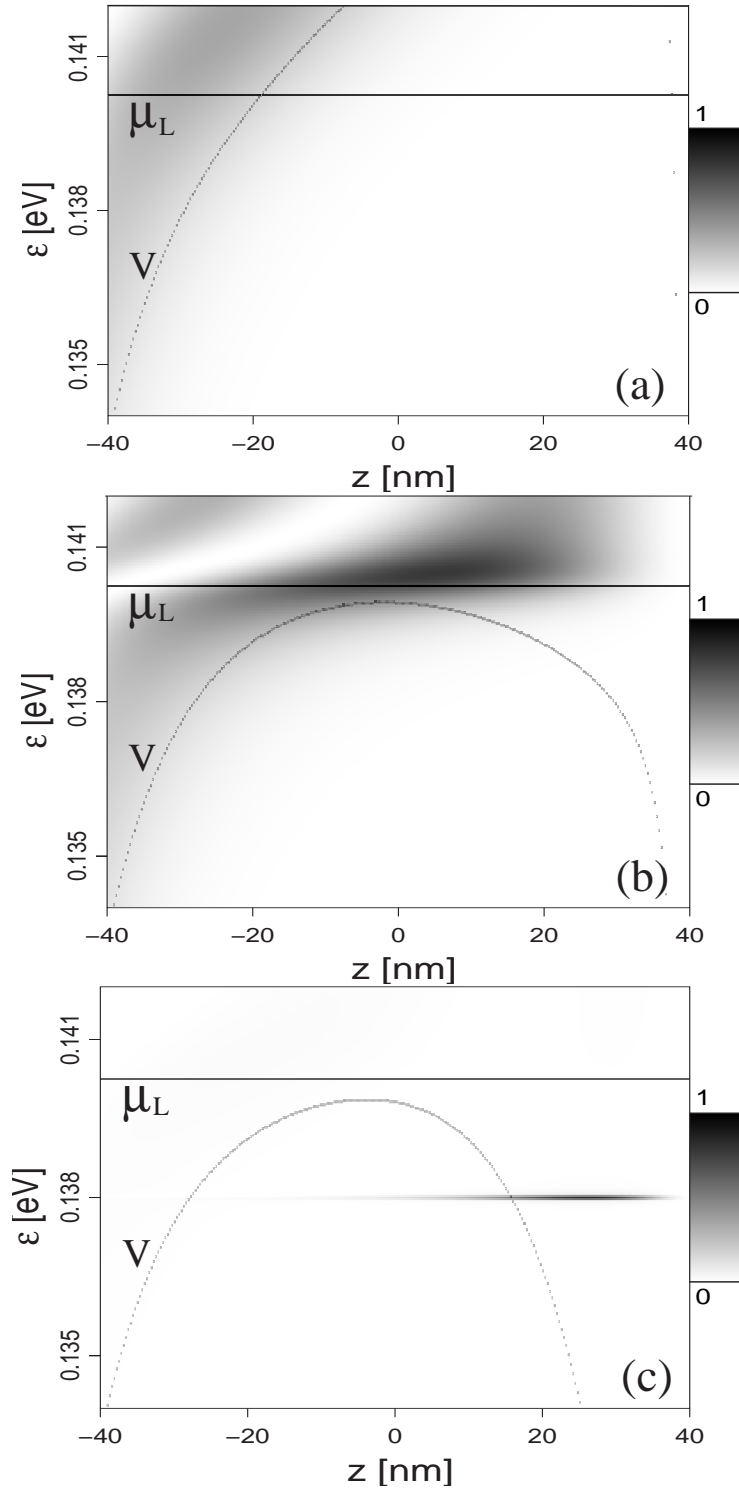


Figure 3.21: The energy- and space-dependence of the electron probability distribution density $P_\epsilon(z)/P_{\max}$ for three values of applied bias: a.) $V_g = -0.005V$, b.) $V_g = 0.01V$, and c.) $V_g = 0.06V$. $P_{\max} = P_{\epsilon_{\max}}(z_{\max})$ is the maximum value of $P_\epsilon(z)$ in the considered energy and space domain, and depends on V_g . We can not keep the same units for all three plots because the total charge in the system varies with V_g .

In the low-voltage plateau, Fig. 3.21(a), the wave functions are confined in the back contact (apart from an exponential decay outside). There is no particular energy structure of the scattering functions. In contrast, in the center of the step, around V_c , Fig. 3.21(b), there is a pronounced maximum of P at $\epsilon = \epsilon_{\max}$ and $z = z_{\max}$ which defines the *intermediate resonance* (IR). The resonance energy lies in the classically allowed range and the intermediate resonance thus has a Fabry-Perot character. The spatial center of the intermediate resonance, z_{\max} , is close to the place of maximum potential, V_{\max} , i. e. the intermediate resonance is located in space between the back contact and the potential pocket in which the isolated 2DEG is formed at higher voltages. Finally, in the high-voltage-plateau, Fig. 3.21(c), the resonance corresponds to a quasi-bound state (QBS). Because of the weak penetration of the wave functions into the back contact the life time of this resonance becomes large and its width narrows considerably. Furthermore, z_{\max} is located in the middle of the potential pocket of the 2DEG.

In the lower part of Fig. 3.20 we show ϵ_{\max} and the energies ϵ_{\pm} at which the probability distribution takes half its maximum value, $P_{\epsilon_{\max}}(z_{\max})$, at constant $z = z_{\max}$ (see Fig. 3.21). It is seen that the center of the step in the C-V trace nearly coincides with the gate voltage at which $\epsilon_{\max} = \mu_L$. Furthermore, the voltage V_- occurs roughly at $\epsilon_- = \mu_L$ and the onset of the high-voltage plateau V_+ can be associated with $\epsilon_+ = \mu_L$. This confirms the view that the capacitance step for an open system is dominated by the IR: At no coupling to the contacts (i.e. a closed quantum system) one would expect a jump in the capacitance which occurs if the chemical potential in the back contact reaches a new energy level of the quantum system (QS). Instead, one sees in the open system a gradual increase of the capacitance in the voltage regime between V_- and V_+ whose width is determined to a great extent by the energetic width of the IR.

3.6.1 Analytical calculations: Fano resonances

To demonstrate further that the step in the C-V-characteristic and the subsequent high-voltage plateau are dominated by a single resonance which changes its character from an intermediate resonance to a quasi-bound state, we apply the resonance theory developed by E.R. Racec and U.Wulf in Ref. [46].

The main idea is to connect directly the probability distribution density $P_{\epsilon}(z)$ to the current scattering matrix, whose poles in the complex energy plane are associated to resonances. Using the expressions (2.79) and (2.80) of the scattering wave functions inside the scattering region, $z \in (-d, d)$, we can write for every energy $\epsilon > \max(V_L, V_R)$,

$$\begin{pmatrix} \Psi^L(\epsilon, z) \\ \Psi^R(\epsilon, z) \end{pmatrix} = \frac{1}{\sqrt{L_z}} \begin{pmatrix} \Psi_S^L(\epsilon, -d) & \Psi_S^L(\epsilon, d) \\ \Psi_S^R(\epsilon, -d) & \Psi_S^R(\epsilon, d) \end{pmatrix} \begin{pmatrix} R(\epsilon; z, -d) \\ R(\epsilon; z, d) \end{pmatrix} \quad (3.23)$$

As follows from Eqs. (2.72)-(2.76)

$$\hat{\Psi}_S = \frac{i}{m^*} \hat{K} (\hat{S} - 1) \hat{\Psi}^{in}, \quad (3.24)$$

where \hat{S} is the scattering matrix given by Eq. (2.43) and \hat{K} is the wave vector matrix (2.72);

$$\hat{\Psi}_L^{in} = \begin{pmatrix} \theta(\epsilon - V_L) \\ 0 \end{pmatrix} \quad (3.25)$$

for the scattering state associated with the electron incident from the left contact and

$$\hat{\Psi}_R^{in} = \begin{pmatrix} 0 \\ \theta(\epsilon - V_R) \end{pmatrix} \quad (3.26)$$

for electrons incident from the right contact. Now we can write,

$$\begin{pmatrix} \Psi_S^L(\epsilon, -d) & \Psi_S^L(\epsilon, d) \\ \Psi_S^R(\epsilon, -d) & \Psi_S^R(\epsilon, d) \end{pmatrix} = \frac{i}{m^*} \hat{\Theta}(\epsilon) [\hat{S}^t(\epsilon) - 1] \hat{K}(\epsilon), \quad (3.27)$$

where

$$\hat{\Theta}(\epsilon) = \begin{pmatrix} \theta(\epsilon - V_L) & 0 \\ 0 & \theta(\epsilon - V_R) \end{pmatrix}, \quad (3.28)$$

and \hat{S}^t is the transpose of the scattering matrix. With the definition of the current transmission matrix [93, 46],

$$\hat{\tilde{S}} = \hat{K}^{1/2} \hat{S} \hat{K}^{-1/2}, \quad (3.29)$$

the expression (3.23) of the scattering wave functions becomes

$$\begin{pmatrix} \Psi^L(\epsilon, z) \\ \Psi^R(\epsilon, z) \end{pmatrix} = \frac{i}{m^* \sqrt{L_z}} \hat{K}^{1/2}(\epsilon) (\hat{\tilde{S}}(\epsilon) - 1) \hat{K}^{1/2}(\epsilon) \begin{pmatrix} R(\epsilon; z, -d) \\ R(\epsilon; z, d) \end{pmatrix}. \quad (3.30)$$

Using the relation (2.78) between the R- and S-matrix which can be written into the equivalent form

$$\hat{\tilde{S}} = 1 - 2 [1 + i\hat{\Omega}]^{-1}, \quad (3.31)$$

where

$$\hat{\Omega} = \hat{K}^{1/2} \hat{R} \hat{K}^{1/2} = \sum_{n=1}^{\infty} \frac{\hat{\omega}_n}{\epsilon - \epsilon_n}, \quad (3.32)$$

with

$$\hat{\omega}_n = \hat{K}^{1/2} \begin{pmatrix} \chi_n(-d)\chi_n(-d) & \chi_n(-d)\chi_n(d) \\ \chi_n(d)\chi_n(-d) & \chi_n(d)\chi_n(d) \end{pmatrix} \hat{K}^{1/2} \quad (3.33)$$

as if follows from the definition (2.65) of the R matrix.

Inserting (3.31) in (3.30) one obtains

$$\begin{pmatrix} \Psi^L(\epsilon, z) \\ \Psi^R(\epsilon, z) \end{pmatrix} = -\frac{2i}{m^*\sqrt{L_z}} \hat{\Theta}(\epsilon) \hat{K}^{1/2}(\epsilon) [1 + i\hat{\Omega}(\epsilon)]^{-1} \hat{K}^{1/2}(\epsilon) \begin{pmatrix} R(\epsilon; z, -d) \\ R(\epsilon; z, d) \end{pmatrix}. \quad (3.34)$$

From here it is obvious that the scattering wave functions have the *same* poles in the complex energy plane as the scattering matrix (see Eq. (3.31)) given by the zeros of $\det[1 + i\hat{\Omega}]$ and these poles are independent on the space coordinate z .

Based on the method described in Ref. [46] we perform an exact reformulation of Eq. (3.35) in a vicinity of every Wigner Eisenbud energy ϵ_λ

$$\begin{pmatrix} \Psi^L(\epsilon, z) \\ \Psi^R(\epsilon, z) \end{pmatrix} = \frac{1}{\epsilon - \epsilon_\lambda - \bar{\mathcal{E}}_\lambda(\epsilon)} \begin{pmatrix} Z_\lambda^L(\epsilon, z) \\ Z_\lambda^R(\epsilon, z) \end{pmatrix}, \quad (3.35)$$

where

$$\bar{\mathcal{E}}_\lambda(\epsilon) = -i\text{Tr}[\hat{\omega}_\lambda(\mathbf{1} + i\hat{\Omega}_\lambda)^{-1}], \quad (3.36)$$

with regular matrix $\hat{\Omega}_\lambda = \hat{\Omega} - \hat{\omega}_\lambda/(\epsilon - \epsilon_\lambda)$. The z dependent part of the scattering wave functions is given by

$$\begin{pmatrix} Z_\lambda^L(\epsilon, z) \\ Z_\lambda^R(\epsilon, z) \end{pmatrix} = -\frac{2i\Theta(\epsilon)}{m^*\sqrt{L_z}} \hat{K}^{1/2}(\epsilon) \frac{[\mathbf{1} + i\hat{\Omega}^-(\epsilon)](\epsilon - \epsilon_\lambda)}{\det[\mathbf{1} + i\hat{\Omega}_\lambda(\epsilon)]} \hat{K}^{1/2}(\epsilon) \begin{pmatrix} R(\epsilon; -d, z) \\ R(\epsilon; d, z) \end{pmatrix}, \quad (3.37)$$

with $\hat{\Omega}^-(\epsilon) = \hat{\Omega}^{-1}(\epsilon) \det \hat{\Omega}(\epsilon)$.

The representation (3.35) of the scattering wave functions has the advantage that it directly yields the equation

$$\bar{\epsilon}_{0\lambda} - \epsilon_\lambda - \bar{\mathcal{E}}_\lambda(\bar{\epsilon}_{0\lambda}) = 0 \quad (3.38)$$

to determine the positions $\bar{\epsilon}_{0\lambda}$ of the poles in the complex energy plane. From general theory [83] it follows that the *resonance* λ corresponds to the pole $\bar{\epsilon}_{0\lambda}$. The upper part of Fig. 3.22 shows the imaginary part of the poles closest to the real axis in dependence on the gate voltage. It is clearly seen that at the end of the low-voltage plateau a single pole becomes separated from all other resonances. For simplicity we denote it with $\lambda = 0$ and the associated complex energy with $\bar{\epsilon}_{00} = \epsilon_0 - i\Gamma/2$. For gate voltages larger than V_c this pole corresponds to a narrow resonance so that in its vicinity the functions $Z_\lambda^L(\epsilon, z)$ and $\bar{\mathcal{E}}_\lambda(\epsilon)$ can be linearized and one obtains for the wave function ψ^L at a fixed z a *Fano distribution*

$$\psi^L(\epsilon, z) \simeq i\psi^L(\epsilon_0, z) \frac{\frac{1}{q^L(z)}e + 1}{e + i}, \quad (3.39)$$

with a z dependent complex asymmetry parameter

$$\frac{1}{q^L(z)} = \frac{\Gamma/2}{Z_\lambda^L(\epsilon_0, z)} \left. \frac{d}{d\epsilon} Z_\lambda^L(\epsilon, z) \right|_{\epsilon=\epsilon_0}, \quad (3.40)$$

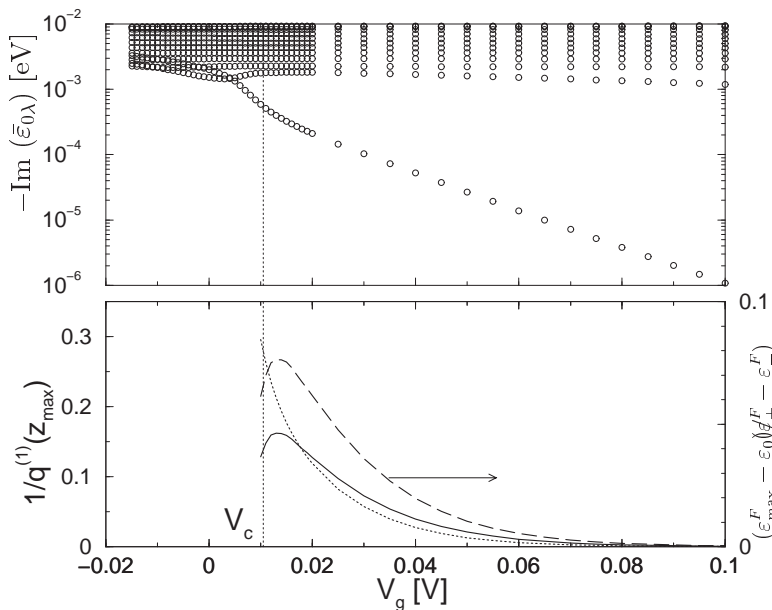


Figure 3.22: Upper part: The imaginary part of $\bar{\epsilon}_{0\lambda}$ (see text) vs. gate voltage V_g . Lower part: Real part (solid line) and imaginary part (dotted line) of the complex asymmetry parameter $1/q^L(z_{\max})$ and the deviation of the maximum of the Fano distribution from the pole energy (dashed line) at gate voltages for which the Fano approximation of the wave function is valid. V_c is marked by the vertical dotted line.

where $e = 2(\epsilon - \epsilon_0)/\Gamma$. From here the probability distribution density is obtained as an asymmetric Fano profile at every z coordinate

$$P_\epsilon(z) = P_{\epsilon_0}(z) \frac{\left| \frac{1}{q^L(z)} e + 1 \right|^2}{e^2 + 1}. \quad (3.41)$$

We plot in the lower part of Fig. 3.20 the energy ϵ_{\max}^F of the maximum of $P_\epsilon(z_{\max})$ calculated in the linearized theory Eq. (3.41). Furthermore, we include the energies ϵ_\pm^F at which the absolute value of the Fano function takes half its maximum value at constant $z = z_{\max}$. For voltages larger than V_c there is an excellent agreement between ϵ_{\max}^F and ϵ_\pm^F and their counterparts ϵ_{\max} , ϵ_\pm resulting from the complete numerical calculation. In the lower part of Fig. 3.22 we plot the real and the imaginary part of $1/q^L$ at $z = z_{\max}$. For gate voltages in the step region both quantities are large and cause a distinct separation of ϵ_0 (real part of the pole) and ϵ_{\max}^F . This is the domain of the intermediate resonance (IR) which is characterized by an asymmetric profile of $P_\epsilon(z_{\max})$. With increasing voltage IR transforms into a quasi bound

state; the asymmetry decreases to become negligible in the high-voltage plateau and Eq. (3.41) provides a Breit-Wigner distribution with the symmetry center given by ϵ_0 . Since Γ decreases rapidly with increasing voltage the Breit-Wigner distribution turns into a δ -function expected for an isolated 2DEG.

3.7 Models for high voltages: quasi bound states

In this section we will analyze the high-voltage plateau in the C-V curve, Fig. 3.20, and we will show that it is dominated by the quasi-bound state which yields the 2DEG.

As was shown in Sec. 3.2 conventionally $V_g = 0$ corresponds to the flat band configuration of the structure for which there are no electrons accumulated at the interface between the spacer layer and the blocking barrier. The electrons are confined in the region close to the back contact. The electronic density distribution $\rho(z; V_g = 0)$ is well described by the Thomas-Fermi approximation [84], sometimes also called semi-classical approximation [48],

$$\rho(z; V_g = 0) = \rho_{TF}(z; V_g = 0) = \int \frac{d^3k}{4\pi^3} \frac{1}{\exp \left[\left(\frac{\hbar^2 k^2}{2m^*} - (\mu_L - eV_{flat}(z)) \right) / k_B T \right] + 1}. \quad (3.42)$$

We can see from Fig. 3.23 that for the flat band configuration the above formula provides a very good approximation for the quantum mechanical calculations Eq. (2.88). The temperature was considered $T=4K$, and the numerical integration in (3.42) was performed between $\epsilon \in (0, 2\mu_L)$. Increasing V_g a potential quantum well is formed inside the spacer layer at the interface with the blocking barrier (Fig. 3.11 right, lower part) and new allowed states for electrons appear. These states are populated with electrons coming from the back contact. The scattering system is open and allows for the variation of the electron number inside the system. In other words increasing V_g increases also the charge in the accumulation layer without modifying the charge distribution in the back contact. The high charge density in the region close to the back contact screens out the external electric field so that the potential and, consequently, the electronic density distribution remains practically unchanged in this region,

$$\rho(z; V_g) \approx \rho(z; V_g = 0), \quad \text{for } z < z_m, \quad (3.43)$$

where z_m denotes the separation point between the domains where different approximations are valid:

- for $z < z_m$ the Thomas Fermi approximation is valid;
- for $z > z_m$ the 2DEG contribution becomes essential and changes with the gate bias.

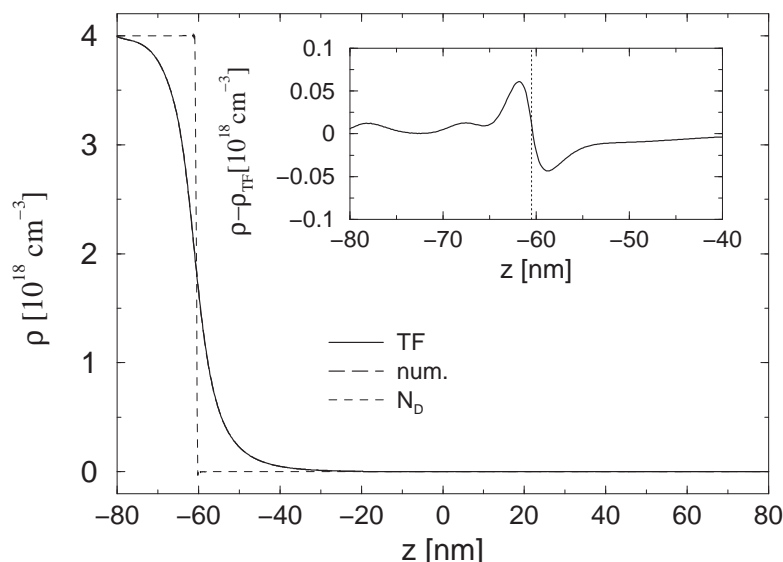


Figure 3.23: The electron distribution density given by Eq. (2.88) (dashed line) and in Thomas Fermi approximation (solid line) Eq. (3.42) for the self-consistent flat band potential. The temperature was considered $T=4\text{K}$. In inset is presented the difference between both distributions in the region close to the back contact.

The difference between the electronic density distribution for an applied bias and for flat band configuration gives the charge accumulated in front of the blocking barrier, regarded as the charge of 2DEG,

$$e\rho_q(z; V_g) = e(\rho(z; V_g) - \rho(z; V_g = 0)). \quad (3.44)$$

For gate biases in the high voltage plateau, $V_g > V_+$, the self consistent electronic density distribution $\rho(z)$ has a minimum, which we can take as a good approximation for z_m . Furthermore, the whole electron density distribution can be written as

$$\rho(z; V_g) = \rho_{TF}(z; V_g = 0) + \rho_q(z; V_g). \quad (3.45)$$

3.7.1 Charge distribution

As we have stated at the end of Sec. 3.6.1, for high gate biases, the 2DEG becomes quasi isolated and we can use the Fang-Howard test wave functions [51] for describing the electronic density distribution associated to it:

$$\rho_{FH}(z, N_s, b) = N_s \frac{b^3}{2} (z - z_b)^2 e^{-b(z_b - z)}, \quad (3.46)$$

which depends on two parameters N_s and b . There are two possible procedures to determine these parameters. First, we can ask that the maximum of modeled

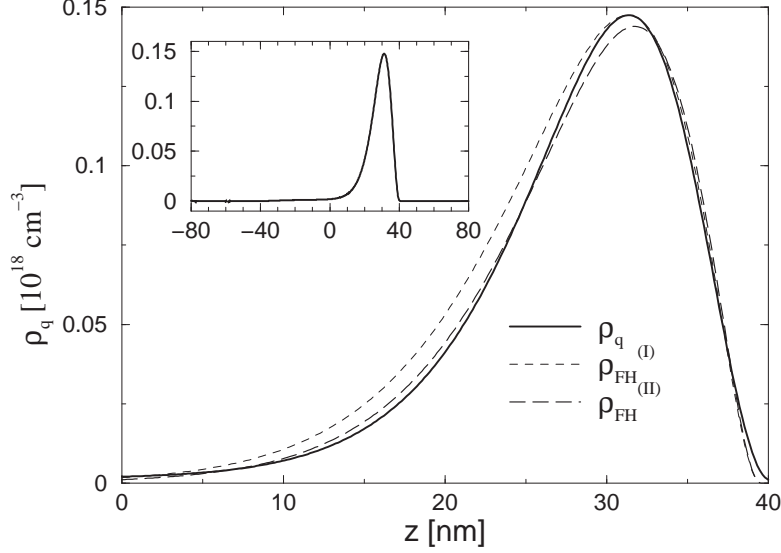


Figure 3.24: The electronic density distribution ρ_q (Eq. 3.44) $V_g = 0.185\text{V}$ and ρ_{FH} (Eq. 3.46) with the parameters N_s and b determined within the two presented methods, in the accumulation region and for the whole scattering region in inset.

electronic density distribution coincide with the maximum of the quantum charge (3.44), $\rho_{q,\text{max}}$, located at z_0 . A distribution of the form (3.46) has the maximum at $z_b - z_0 = 2/b$, so from the previous condition we can find

$$b = 2/(z_b - z_0). \quad (3.47)$$

From the maximum value, we obtain

$$N_s = \frac{2}{b^3} \rho_{q,\text{max}}(z_0) \frac{\exp(b(z_b - z_0))}{(z_0 - z_b)^2}. \quad (3.48)$$

The electronic density distribution ρ_{FH} with the parameters (3.47) and (3.48) is represented in Fig. 3.24 as $\rho_{FH}^{(I)}$. We see that these parameters produce an over-estimation of the electronic density distribution ρ_q . It is necessary to find a better method to evaluate these parameters. We construct a function

$$S(N_s, b) = \frac{1}{N} \sum_{i=1}^N [\rho_{FH}(z_i, N_s, b) - \rho_q(z_i)]^2, \quad z_m < z_i < z_b \quad (3.49)$$

where N is the number of grids for the z coordinate, and find the parameters N_s and b for which this function has a minimum. From a practical point of view, the parameters given by the first procedure can be used to start the second one. The electronic density distribution ρ_{FH} with N_s and b determined in this way is

represented as $\rho_{FH}^{(II)}$ in Fig. 3.24. We can see that the second procedure yields a better approximation for the area under the curve which expresses, in fact, the total amount of charges, N_s . So, N_s and b will be considered further as determined from the second method: minimum of the function $S(N_s, b)$ and their variation with the applied bias is presented in Fig. 3.25. We analyze comparatively N_s and the total number of electrons in the accumulation layer,

$$N_{s,num} = \int_{-d}^d \rho_q(z) dz. \quad (3.50)$$

For $V_g > V_+$, there are no significant differences between the two quantities and we can conclude that the Fang-Howard test describes well the charges accumulated in front of the blocking barrier. As expected, for small biases ($V_g < 0.01V$) the model does not work anymore.

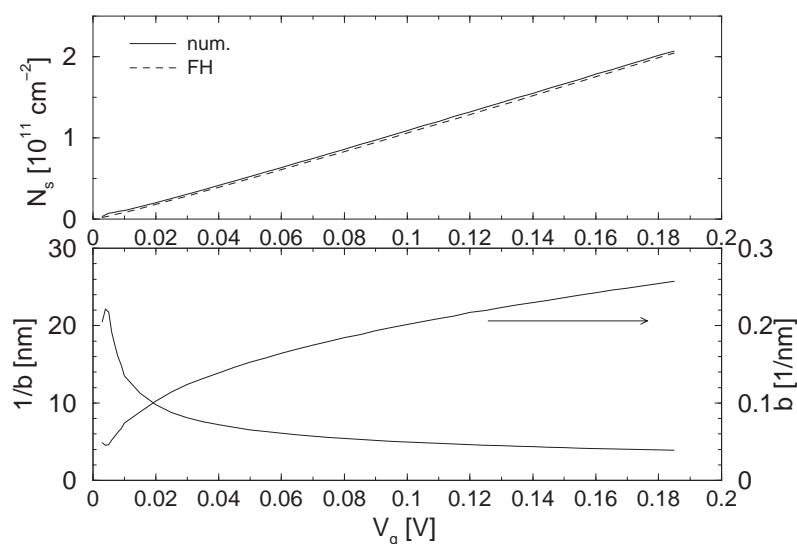


Figure 3.25: Upper part: N_s values obtained by numerical integration of $\rho_q(z)$ (solid line) and by fitting $\rho_q(z)$ with a Fang-Howard test function. Lower part: The model parameter b and $1/b$ for Fang Howard test wave functions.

The linear variation of N_s with applied bias, which is known for the strongly inverted or accumulated space-charge layers [53] p.619, shows that a plane capacitor is formed between the top gate and the 2DEG. Further, the capacitance for high voltages can be expressed as variation of the N_s parameter to the applied bias

$$C = eS \frac{dN_s}{dV_g}, \quad (3.51)$$

which is represented in Fig. 3.26.

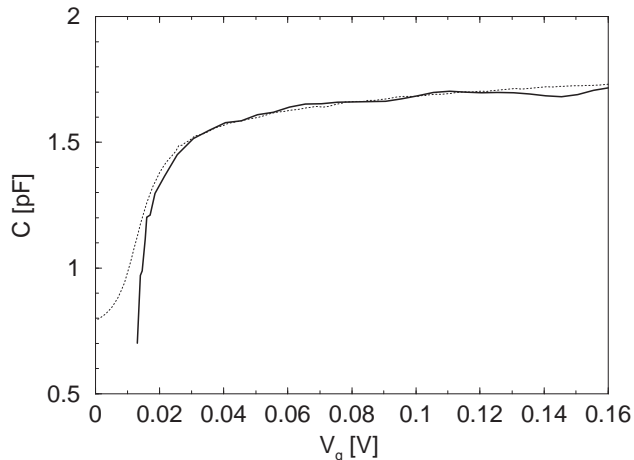


Figure 3.26: Capacitance vs. gate bias: experimental data (dotted line) and calculated values in Fang-Howard model, Eq. (3.51), (solid line).

3.7.2 The potential energy

We can model also the potential energy using the same idea: the difference between the potential energy for an applied bias V_g and for bias zero, should be due to the quantum charges in the 2DEG

$$V_q(z; V_g) = V(z; V_g) - V(z; V_g = 0). \quad (3.52)$$

This is represented in Fig. 3.27.

We can see that for $z > z_b$ the potential energy difference is a linear function on z as in the case of a plane capacitor with the plates at z_b and d :

$$V_S(z > z_b) = -eV_g + e \frac{N_s}{\epsilon_0 \epsilon_r} (d - z). \quad (3.53)$$

For only one occupied band in the 2DEG the potential energy for $z < z_b$ can be written as in Ref. [53], p. 463,

$$V_S(z < z_b) = \frac{e^2}{\epsilon_0 \epsilon_r} N_s (z_b - z) + \frac{e^2}{\epsilon_0 \epsilon_r} \int_z^{z_b} dz' (z - z') \rho_q(z'). \quad (3.54)$$

In Fig. 3.28 we represent for $-d < z < z_b$ the potential energy modeled through the Eq. (3.54) with $\rho_q(z)$ and $\rho_{FH}(z)$. The electronic density distribution $\rho_q(z)$, calculated numerically, provides a very good approximation for the potential bending for $z < z_b$, but the slope around $-d$ is not zero, as for $V_q(z)$, because of the differences in the boundary conditions. The formula (3.54) consider an infinite semiconductor layer in front of an infinitely high barrier (as in Si/SiO₂ system), while our potential

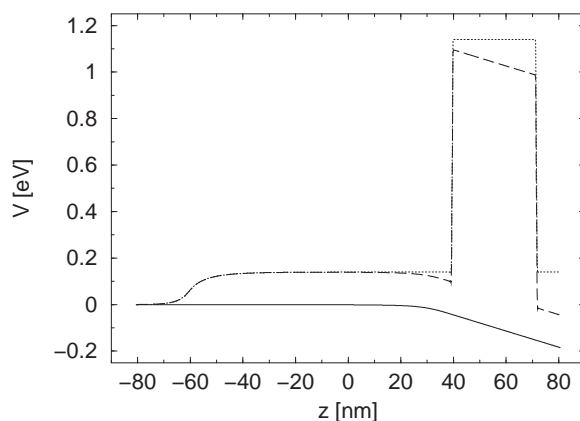


Figure 3.27: The potential energy for flat band configuration (dotted line), for $V_g = 0.185V$ (dashed line) and the difference between them, $V_q(z)$, (solid line).

Eq. (2.99) is for a finite system with a constant potential outside the scattering region (i.e. $V(z < -d) = V_L$). The potential (3.54) calculated with $\rho_{FH}(z)$ does not describe very well the bending for z close to z_b because $\rho_{FH}(z)$ provides only a global description of the charges on 2DEG.

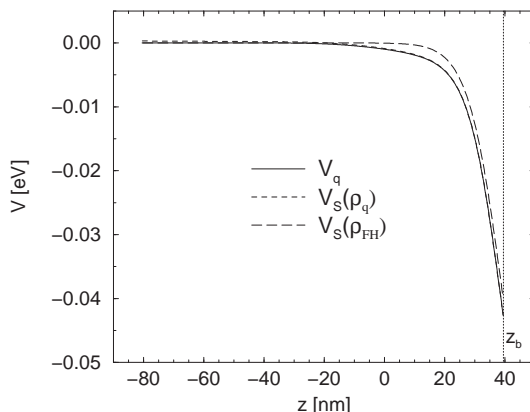


Figure 3.28: Models for the potential energy V_q at $V_g = 0.185V$. Left part: V_s , Eq. (3.54), with ρ_q and ρ_{FH} ; Right and upper part V_s for $z \in [-d, x_b]$ and V_2 for $z \in [z_b, d]$ with ρ_q ; Right and lower part: the difference to V_q .

The detailed distribution of the charges in 2DEG is not exactly described by Fang-Howard test wave functions. The slope for z close to $-d$ is better described because the Fang-Howard test functions consider all the charges in the scattering region as 2DEG, (i.e. does not consider the interfaces charges σ_1). In Fig. 3.29

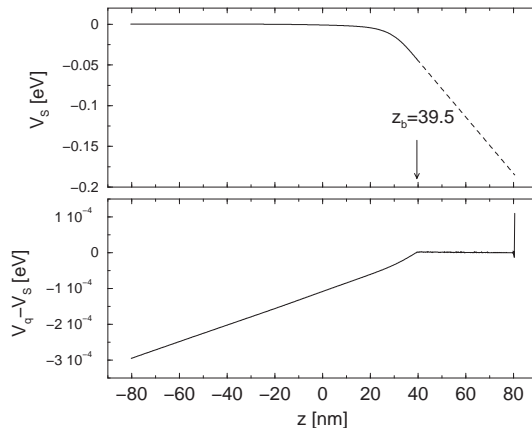


Figure 3.29: Models for the potential energy V_q at $V_g = 0.185\text{V}$ knowing ρ_q . Upper part: V_s , Eq. (3.54), for $z \in [-d, x_b]$ and V_S , Eq. 3.53, for $z \in [z_b, d]$ Lower part: the difference to V_q .

we present the differences between the modeled potential and the self-consistent potential. We can conclude that knowing the potential distribution inside the 2DEG, the potential can be calculated with a good approximation through the formulae (3.54) and (3.53).

3.8 Exchange correlations effects

In this section we would like to go beyond the Hartree approximation and to treat another aspect of many-body nature of our problem, namely the exchange-correlations effects. We will use the same approximation as in Ref. [79], where the exchange and correlations effects are calculated in the local density approximation (LDA). This approximation is part of the density-functional theory, and it is an alternative way to study the exchange-correlations effects on the semiconductor band structure. Hohenberg, Kohn, and Sham [85] have shown that the density distribution of an interacting electron gas under an external field can be obtained by an one-particle Schrödinger-type equation containing an exchange correlation potential V_{xc} in addition to the usual Hartree and external potentials. So, Schrödinger equation for our problem (z is the direction of transport) has the form

$$\left[-\frac{\hbar^2}{2m^*} \frac{d^2}{dz^2} + V_h(z) + V_c(z) + V_{xc}(z) \right] \psi_n^{L/R}(z) = \epsilon_n \Psi_n^{L/R}(z), \quad (3.55)$$

where $V_h(z)$ is the potential coming from heterostructure band-offsets, $V_c(z)$ is the Coulomb potential. $V_c(z)$ solves, like in the Hartree approximation, the Poisson

equation for the total charge in the system

$$\frac{d^2}{dz^2}V_c(z) = -\frac{e}{\epsilon_0\epsilon_r}[N_D^+(z) - N_A^-(z) + \rho(z)]. \quad (3.56)$$

The exchange-correlation potential is given by [79]

$$V_{xc}(z) = -\frac{1.22}{r_s(z)}Ry^* \left[1 + 3.68 \cdot 10^{-2}r_s(z) \ln \left(1 + \frac{21}{r_s(z)} \right) \right], \quad (3.57)$$

with the dimensionless quantity

$$r_s(z) = \left[\frac{4}{3}\pi a^*{}^3 \rho(z) \right]^{-1/3}. \quad (3.58)$$

given only by the mobile electronic charge $\rho(z)$. r_s supplies the local character of the model. The mobile electron charge $-e\rho(z)$ is calculated from the electronic wave functions provided by Schrödinger equation (3.55) using Eq. (2.88). For GaAs, we have the effective Bohr radius $a^* \approx 10$ nm and Rydberg constant $Ry^* \approx 5.6$ meV [79]. Though application of the local density scheme should be restricted to situations with a slowly varying density, it is well known that the method works surprisingly well even for systems beyond this limit [79].

Including the exchange-correlations effects, the self-consistent scheme, Fig. 3.30, changes a little: one has also to calculate from the charge distribution the exchange correlation potential (3.57) which is added to the Coulomb potential to give the scattering potential $V(z)$ which enters the Schrödinger equation. We would like to note that we do not use different mixture coefficients f for the exchange and Coulomb potential; the mixture is done globally and a good guess for the initial potential (or charge) will help a lot for a rapid convergence.

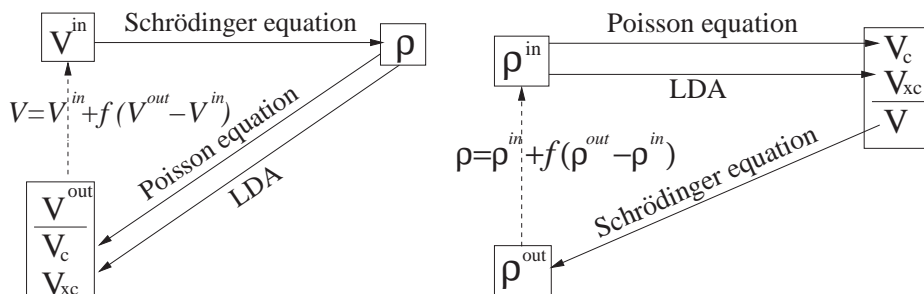


Figure 3.30: The self-consistent iteration scheme considering besides the Hartree approximation also the exchange correlations effects in LDA approximation. Left part: starting with a potential guess; Right part: starting with a charge distribution guess.

Boundary conditions

We have to establish the boundary conditions for the Poisson equation. They have to be connected with the boundary conditions for the total potential, which are written as (see Eq. (3.7))

$$V(-d) = 0 \quad V_{flat}(d) - V(d) = eV_g. \quad (3.59)$$

We have

$$\begin{aligned} V(-d) - V(d) &= V_h(-d) - V_h(d) + V_c(-d) - V_c(d) + V_{xc}(-d) - V_{xc}(d) \\ &= -V_{flat}(d) + eV_g, \end{aligned} \quad (3.60)$$

so that we can obtain the boundary conditions for the Coulomb potential (i.e. V_1 and V_2 in Eq. (2.99))

$$V_1 = V_c(-d) = 0, \quad (3.61)$$

$$V_2 = V_c(-d) - V_c(d) = -V_{flat}(d) + eV_g - \Delta_h - \Delta_{xc}, \quad (3.62)$$

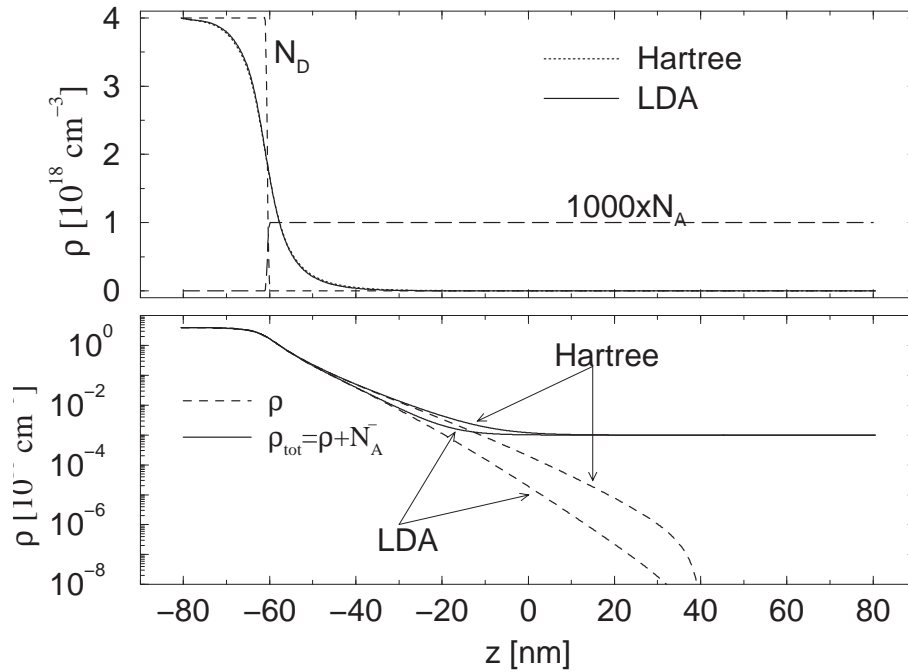
where $\Delta_h = V_h(-d) - V_h(d)$ is zero for our structure and $\Delta_{xc} = V_{xc}(-d) - V_{xc}(d)$ can be calculated having the electron charge distribution.

We present in Fig. 3.31(a) for the flat band configuration the self-consistent potential and electronic density distribution in LDA approximation, in comparison with the Hartree approximation. There are no significant differences between both approximations in the region close to the back contact, $z < -40\text{nm}$. We want to point out that for LDA calculations the built-in potential, Eq. (3.3), has the value $eU = 0.14676\text{eV}$.

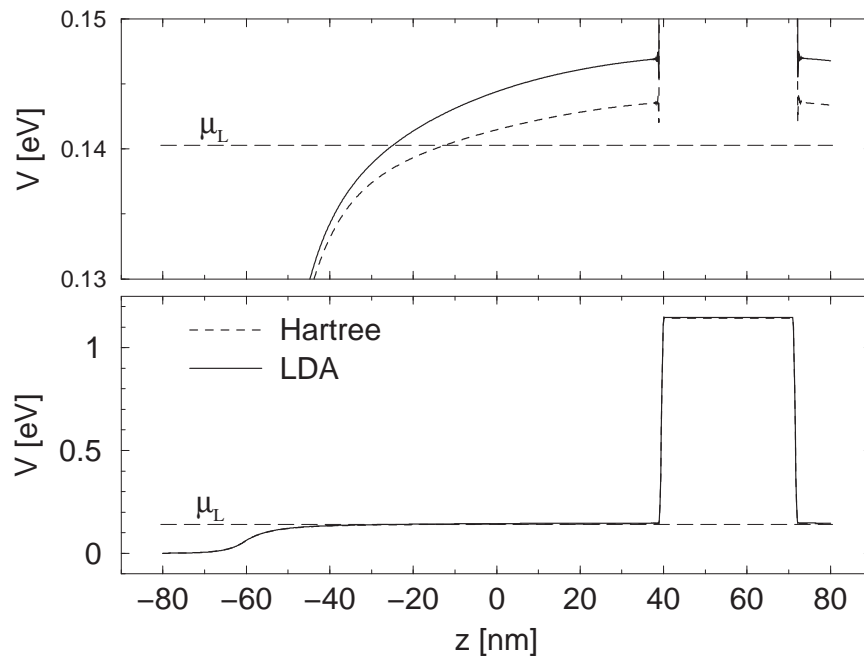
In Fig. 3.32 we present the self-consistent potential and electronic density distribution in Hartree and LDA approximation for two applied bias configurations: $V_g = 0.015\text{V}$ which corresponds to the step in the capacitance and $V_g = 0.09\text{V}$, corresponding to high voltage plateau. We restrict to the region of the accumulation layer because only there the differences between both approximations are significant. For the same applied bias, the exchange correlations effects allow for accumulations of more electrons at the interface between blocking barrier and GaAs spacer.

The capacitance of the system is calculated using the Gauss law as described in Sec. 3.5.1. The modeled C-V curve is presented in Fig. 3.33 upper part, together with the experimental data. We want to point out that the shift between V_G and V_g (Eq. (3.6)), $\Phi_1 = 0.693\text{V}$, is different from the value provided by Hartree approximation.

Qualitatively, Fig. 3.33 is similar with Fig. 3.20: for small applied voltages, there exist also in LDA approximation a classically allowed channel for the electron motion (shaded area), but the channel is open in a much smaller bias interval then in Hartree approximation. Consequently, a much steeply step in the capacitance occurs. However, the step in the capacitance keeps his meaning: it happens on the region of the biases for which the coupling to the contacts is strong and the



(a) Self-consistent electronic density distribution. Upper part: linear scale; Lower part: logarithmic scale.



(b) Self-consistent potential (lower part) with a detail around the chemical potential μ_L (upper part).

Figure 3.31: Self-consistent results for the nominal structure at flat band configuration: comparison between Hartree and LDA approximation.

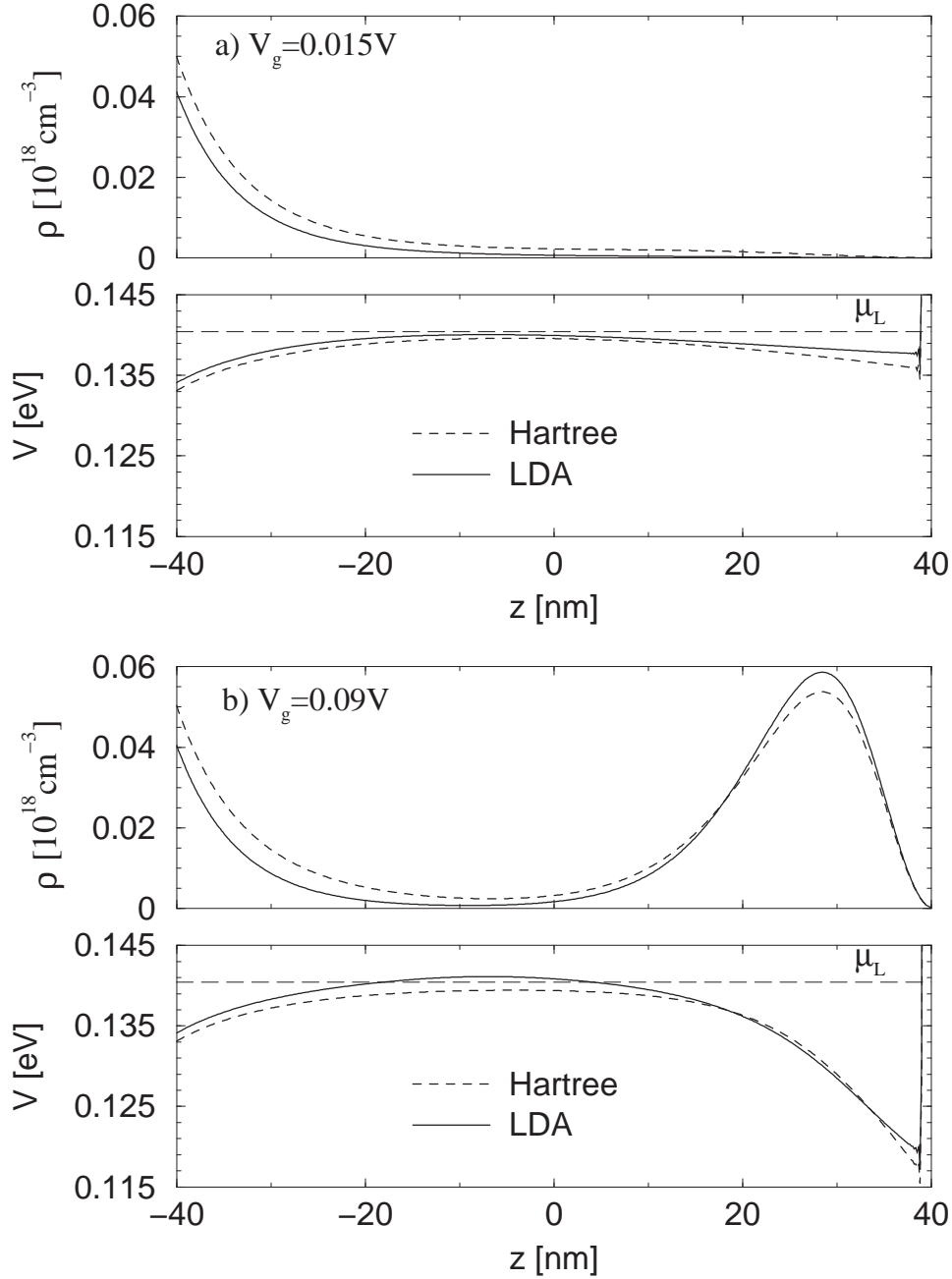


Figure 3.32: Self-consistent potential (lower part) and electronic density distribution (upper part) at the interface between blocking barrier and GaAs spacer layer for a) $V_g = 0.015 \text{ V}$ and b) $V_g = 0.09 \text{ V}$. Solid and dashed lines correspond to LDA and Hartree approximation, respectively.

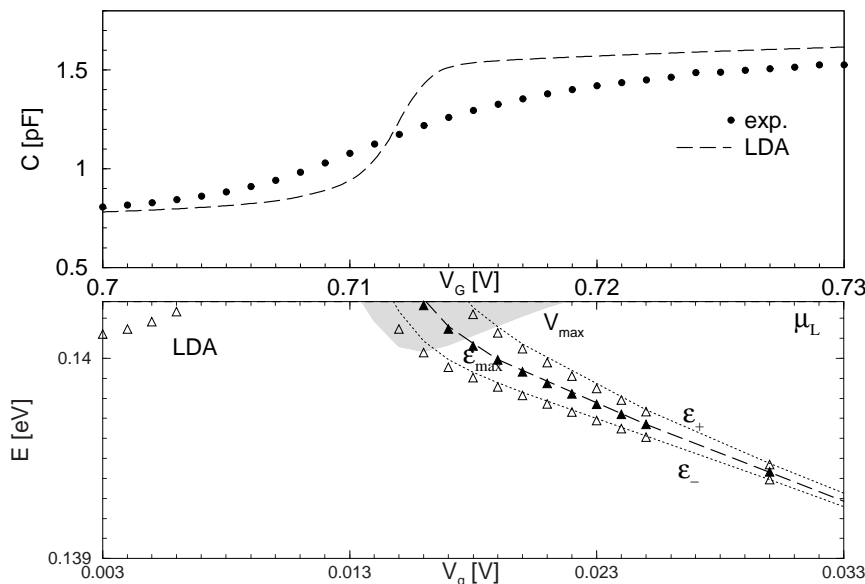


Figure 3.33: Upper part: C-V curve in the step region, experimental data [71] (filled circles) and numerical calculations in LDA approximation. Lower part: as result of the complete numerical calculation the resonance energy ϵ_{\max} (dashed line), and the energies ϵ_{\pm} at which the absolute value of the wave function takes half the maximum value at constant $z = z_{\max}$ (dotted lines). The corresponding values ϵ_{\max}^F (filled triangle) and ϵ_{\pm}^F (triangle) in the Fano approximation. Shaded area: energies with $V_{\max} < \epsilon < \mu_L$.

intermediate resonance (IR) exists in the classically allowed motion channel. Also in this case Fano approximation (see Sec. 3.6.1) provides a very good description of the relevant resonance for the capacitance, which evolves with applied bias from an intermediate resonance to a quasi bound state and after that to a δ function specific to a closed 2DEG.

3.9 Summary

Here we perform a microscopic study of the interaction of a quantum system, in our case a field-induced two dimensional electron gas (2DEG), with the contacts through particle exchange and identify the signature of the electron-electron interaction in the capacitance variation with applied bias. The electronic states and the associated charge distribution in the system are investigated in detail, in the cases of the Coulomb interaction taken in Hartree- and LDA approximation. These states depend critically on the strength of the coupling between quantum system and contacts; we consider here a structure in which the entire transition from weak

to strong coupling can be examined experimentally and theoretically. This transition is dominated by a single relevant resonance which changes its character from a quasi bound state (QBS) for an almost-closed system to an intermediate resonance (IR) for an open one. As expected, in the weak coupling regime the bound state of the quantum system turns into a narrow quasi bound state with nearly identical location in space. We find that with increasing coupling the quasi bound state turns into an intermediate resonance. In contrast to the quasi bound state the intermediate resonance has the following properties: First, it is located in the space between the probes and the isolated quantum system. Second, it is coupled to the probes via particles exchange through a classically allowed channel (see shaded area in the lower part of Figs. 3.20 and 3.33). Third, since the decay of the intermediate resonance into the probe is classically allowed it has the character of a Fabry-Perot resonance. Fourth, the intermediate resonance is strongly asymmetric and can well be described by a Fano distribution with a complex asymmetry parameter. Finally, if the coupling becomes too strong a resonant state cannot exist any more.

Because of the excellent quantitative agreement with our theory we can demonstrate that the transition between quasi bound state and intermediate resonance is directly seen in capacitance experiments by Dolgoplov et al. [71]: The step in C-V-characteristic associated with formation of the two dimensional electron gas (see upper part of Fig. 3.20) is broadened because of energetic overlapping of the channel of allowed classical motion and the intermediate resonance. In our calculations the classically allowed channel in which the IR exists results only when the Coulomb interaction between the electrons is taken into account. As long as the system is open, the Hartree approximation provides a very good mean-field description of the electron-electron interaction.

Chapter 4

Capacitance of a single-tunneling barrier

In Chap. 3 we have analyzed a system for which the blocking barrier was supposed to suppress charge transfer from one contact to another. In this chapter we will analyze several single-barrier structures with different barrier heights to allow for different degrees of charge transfer between contacts. Decreasing the height of the barrier, the Fabry-Perot resonances will be encountered in the capacitance oscillations [94].

We choose for the beginning the same parameters as in Ref. [48], for which the $I - V$ characteristic has been examined experimentally and theoretically. In that paper two different theories were employed, one with a semiclassical model and the other with a quantum model to calculate the electronic density distribution. Both were found to agree well with the experiments within 10% uncertainty of the fitting parameters: width and height of the barrier, donors concentration in the contacts, and the aluminum content in the $\text{Al}_x\text{Ga}_{1-x}\text{As}$ barrier layer.

In the first part of this chapter we show that a certain type of small shoulders in the $I - V$ characteristic resulting from the existence of quasi-bound states in the barrier should distinguish qualitatively the cases of coherent- or incoherent transport. To bypass the problem that various models can give a good fitting to the $I - V$ curve, we propose in the second part of the chapter the measurement of the $C - V$ characteristic as a powerful independent test. Here the quasi-bound states in the barrier should result in oscillations in the differential capacitance that have a well defined relation to the shoulders in the $I - V$ curve.

4.1 The structure

The analyzed single-barrier structure consists of a sequence of layers of n -doped GaAs - $\text{Al}_x\text{Ga}_{1-x}\text{As}$ - n -doped GaAs, as depicted in Fig. 4.1b). The $\text{Al}_x\text{Ga}_{1-x}\text{As}$ bilayer will constitute the barrier potential because its band gap is larger than for GaAs. We point out that there is no spacer (undoped layer) between the n -doped GaAs layers and the $\text{Al}_x\text{Ga}_{1-x}\text{As}$ tunneling barrier. The parameters used for model-

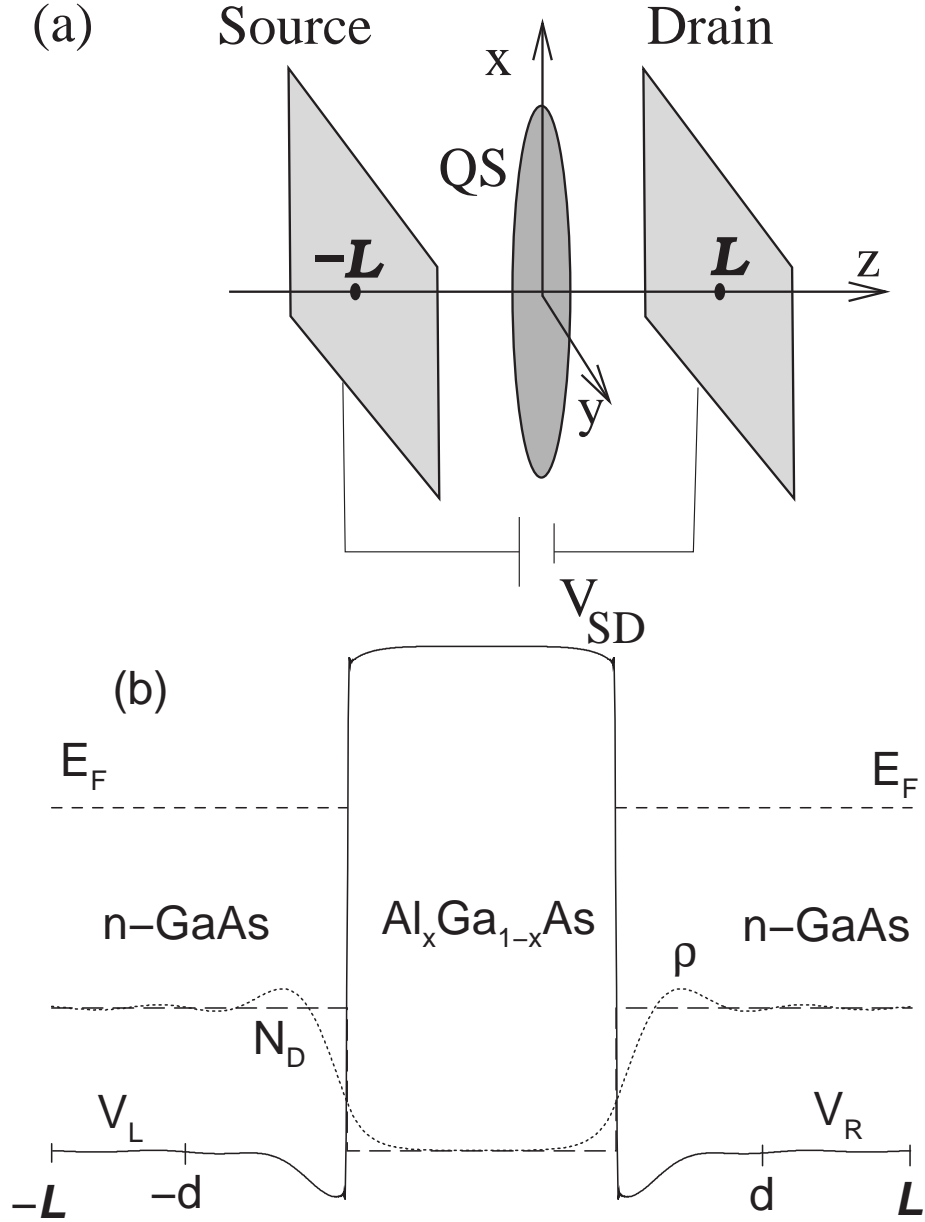


Figure 4.1: (a) General geometry of the considered systems (QS=quantum system) for capacitance spectroscopy. (b) Specific example for a quantum system: Tunneling barrier as described in Ref. [48]. The self consistent scattering potential $V(z)$ (continuous line) is localized in the interval $[-d,d]$ so that $V(z < -d) = V_L$ and $V(z > d) = V_R$, N_D (long dashed line) is the donors doping profile and ρ (dotted line) is the electronic density distribution.

ing are [48]: relative permittivity $\epsilon_r = 10.9$, donor doping concentration in the contacts $N_D = 10^{17} \text{cm}^{-3}$, Fermi level $E_F = 12 \text{meV}$ and effective mass $m^* = 0.0655m_0$. The height of the tunneling barrier, fixed by the Al content, will be specified for each structure. If the donor concentration is greater than $5 \cdot 10^{16} \text{cm}^{-3}$, an impurity band forms within the conduction band such that even at low temperatures all donors are ionized. This was suggested by Zimmermann [48] based on the fact that resistivity of an n-doped GaAs probe ($N_D \geq 5 \cdot 10^{16} \text{cm}^{-3}$) exhibits very little temperature dependence. Because we analyze structures with n-doped injection layers where the current is carried mainly by electrons, we can neglect the hole transport.

4.2 Potential and electronic density distributions

For the systems for which the highly doped regions extends until the barrier, there is not a clear delimitation between the quantum system, for which the quantum mechanical calculations will be applied, and the contact regions, considered as ideal metal-like contacts. While the heterostructure potential is set up by the growth parameters, we have to find a good choice for d so that the Coulomb interaction does not modify considerably the heterostructure potential outside the interval $[-d, d]$. The total scattering potential should be localized in the region $[-d, d]$ in order to apply our R-matrix formalism. This means that the delimiting point d is a free parameter, and we shall analyze its influence on the calculated data. The regions $z < -d$ and $z > d$ are the emitter- and the collector electrode, respectively. In these regions the phase coherence of the scattering functions, which determine the transport through scattering region $-d \leq z \leq d$, is lost [22]. In consequence, there is a local charge balance in the electrodes and the total potential is constant.

As we have specified in Sec. 2.1 we solve the scattering problem associated with the potential given in Fig. 4.1 using the R-matrix formalism. The boundary points for the Wigner-Eisenbud problem (2.47) are chosen very close to d , namely $\mathcal{L} - d = 1 \times 10^{-5} \text{nm}$. In the region $[-d, d]$, the scattering functions are given by Eqs. (2.79) and (2.80) and we can obtain the electronic density distribution $\rho(z)$ as described in Sec. 2.2.

To account for the effects of the (accumulated) charges in the system on the transport properties, we perform self-consistent calculations (see Sec. 2.4). We use a simplified form for the charge distribution which enters the Poisson equation (2.90)

$$q(z) = e[N_D^+(z) - \rho(z)], \quad (4.1)$$

where we neglect the hole density and consider no acceptors in the system. For simplicity, we assume a constant value for the relative permittivity ϵ_r in the whole structure. To ensure charge neutrality of the entire system we allow for contact charges, distributed as sheet charges at the interfaces $z = \pm \mathcal{L}$ between the active region and the contacts. Our self-consistent calculations show that, in fact, the total scattering potential is independent of the location of the sheet charge and the

absolute value of the sheet charges $\sigma_{1/2}$ is small in comparison with other charges in the system (see Fig. 4.12).

First, we analyze one of the structures presented by Zimmermann [48], with the height of the barrier $V_{b,0} = 33.4\text{meV}$ for Al content $x = 0.04$. $V_{b,0}$ is the height of the barrier obtained from the conduction band-offsets between GaAs and $\text{Al}_x\text{Ga}_{1-x}\text{As}$.

4.2.1 Without applied bias

We have started the self-consistent calculations with a linear electronic density distribution around the abrupt variations of the doping profile at the edge of the barrier (see Sec. 2.4) and we take $\lambda_F = 10\text{nm}$ and $\alpha = 0$, because we neglect the residual N_A doping inside de barrier. We computed the electronic density and potential distribution for different d values between 50nm and 80nm and present here only the results for $d = 50, 60, 66$ and 75nm.

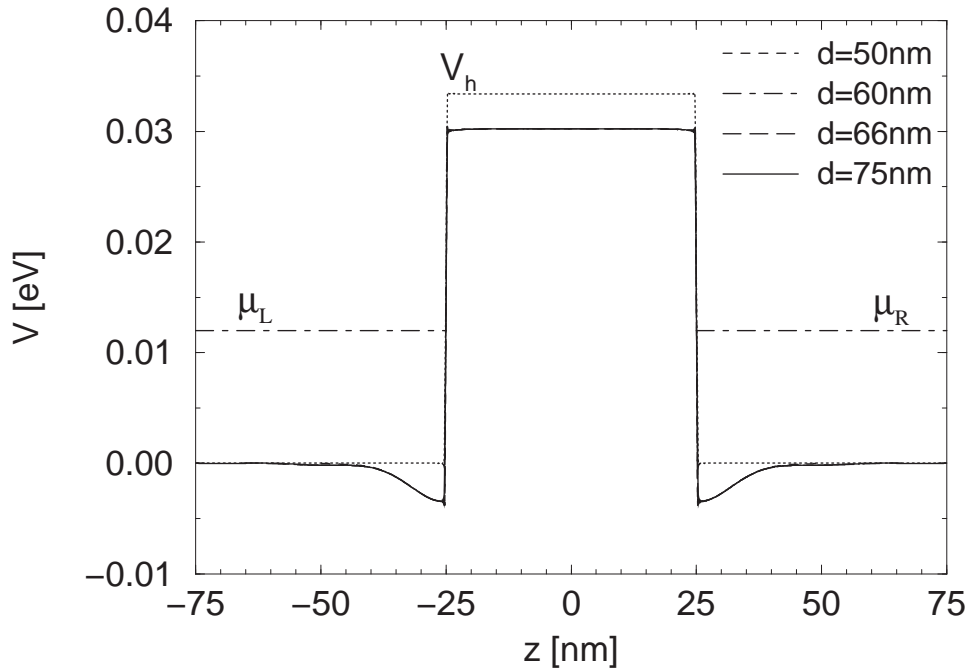


Figure 4.2: The self-consistent potential profile for a single-barrier structure, with $V_{b,0} = 33.4\text{meV}$ for $d = 50, 60, 66$ and 75nm. With dashed line is shown the heterostructure band-offsets V_h .

To verify the self-consistent procedure, which is applied here for an *open system*, both convergence schemes (see Fig. 2.4) were used for comparison. For the self-consistent charge approximation scheme we started either from a linear distribution of electronic density distribution around the abrupt variations of the doping or from

the self consistent charge distribution from a previous d value. In addition we also varied the mix parameter f . The typical values for f are $1 \div 5$ %. All these attempts provided for each structure the same convergent point, in the limits of the imposed accuracy for the self-consistent procedure (i.e. the upper limit imposed for the convergence parameter e_i , Eq. (2.112)). This shows that the numerical method is consistent.

In Fig. 4.2 we present the self-consistent potential for different d values and no applied bias ($V_{SD} = 0V$). We choose the minimum of the conduction band on the left side, far from the barrier, as energy reference, $E_{cL} = 0$. The downward shift of the barrier due to the self-consistent calculations is 3.20meV ($\approx 10\% V_{b,0}$), so that the effective height of the barrier becomes $V_b = 30.2\text{meV}$. The notch which forms on each side of the barrier proves to be too shallow and narrow to sustain bound states.

In Fig. 4.3 we present the self-consistent electronic density distribution for different d values and for $V_{SD} = 0V$. These profiles present Friedel-type oscillations due to the constant phase difference between the incident and the reflected waves on the barrier [86].

As shown in Figs. 4.2 and 4.3 the plots for different d values are practically indistinguishable. Therefore, the choice of d value is unimportant, as long as it is far enough from the barrier to allow for the first period of the Friedel oscillations of $\rho(z)$. The Friedel oscillations yield non negligible deviations from the local electrical neutrality, so that a significant spatial variation of the potential occurs in the region where they extend and we have to include this domain in the scattering region ($z \in [-d, d]$).

4.2.2 With applied bias

Further we analyze the effects of the external applied bias. Fig. 4.4 shows the self-consistent potential and charge-distribution for a single-barrier structure with $V_{b,0} = 33.4\text{meV}$ and for $d = 75\text{nm}$ for different applied biases $V_{SD} = 4, 8$ and 12 mV.

Fig.4.5 shows the self-consistent potential and the electronic density distribution for the same single barrier tunneling structure under the applied bias $V_{SD} = 16\text{mV}$ but for different d values. As one can see, the plots in Fig. 4.5 are practically indistinguishable which proves the consistency of the numerical method.

From the plot for the electronic density distribution, Figs. 4.4a) and 4.5, one can observe that in front of the barrier appears an accumulation region, i.e. the charge density is bigger than for the case without applied bias, and in the same time behind the barrier appears a depletion region, i.e. the charge density is smaller than for $V_{SD} = 0$. Thus, a dipole moment appears parallel to the external electric field.

We did not obtain the bound states in the notch formed in the accumulation layer which are reported by Zimmerman *et al.* for $V_{SD} = 16\text{mV}$, but these states are anyway neglected by them.

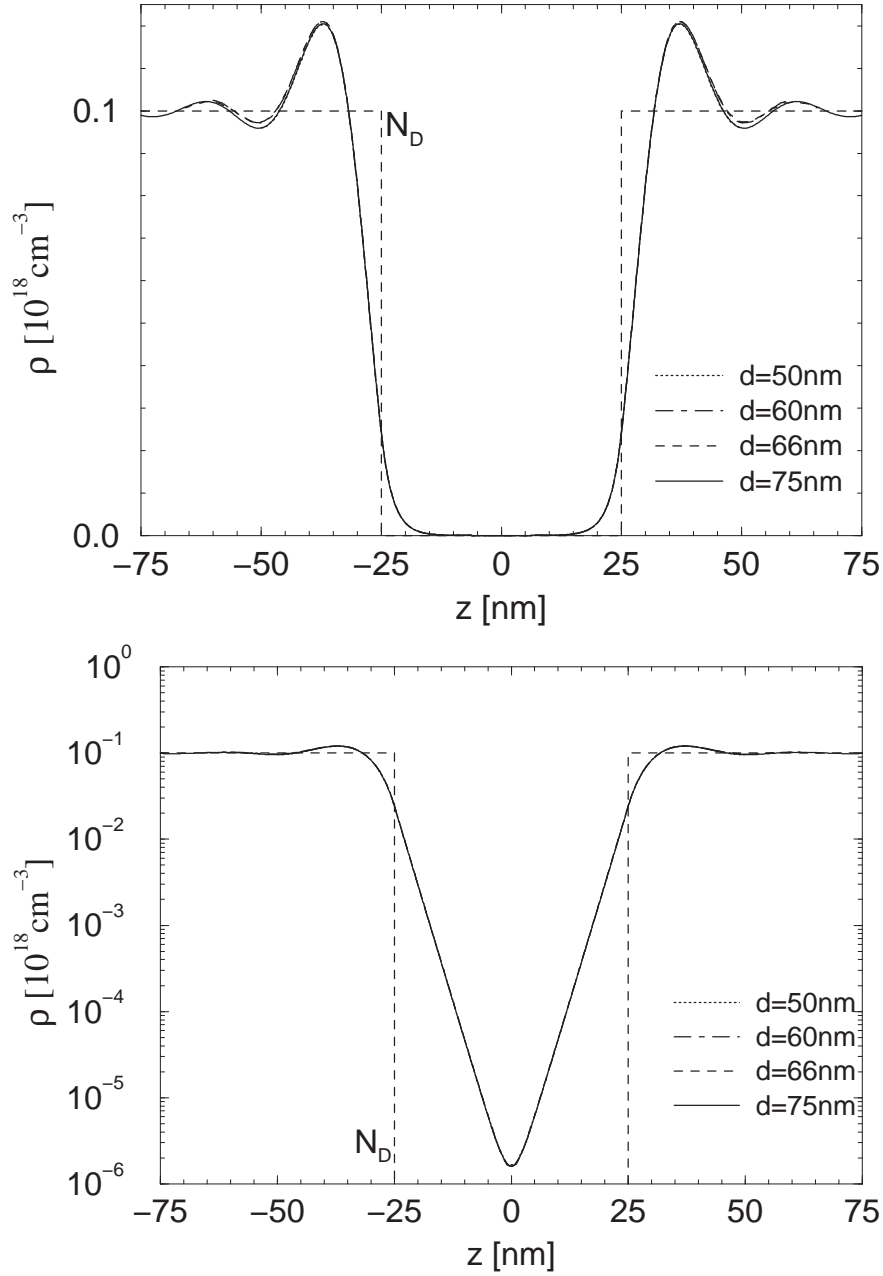


Figure 4.3: The self-consistent electronic density distribution (linear and logarithmic scale) for a single-barrier structure with $V_{b,0} = 33.4 \text{ meV}$ for $d = 50, 60, 66$ and 75 nm . With dashed line is shown the donors doping profile N_D .

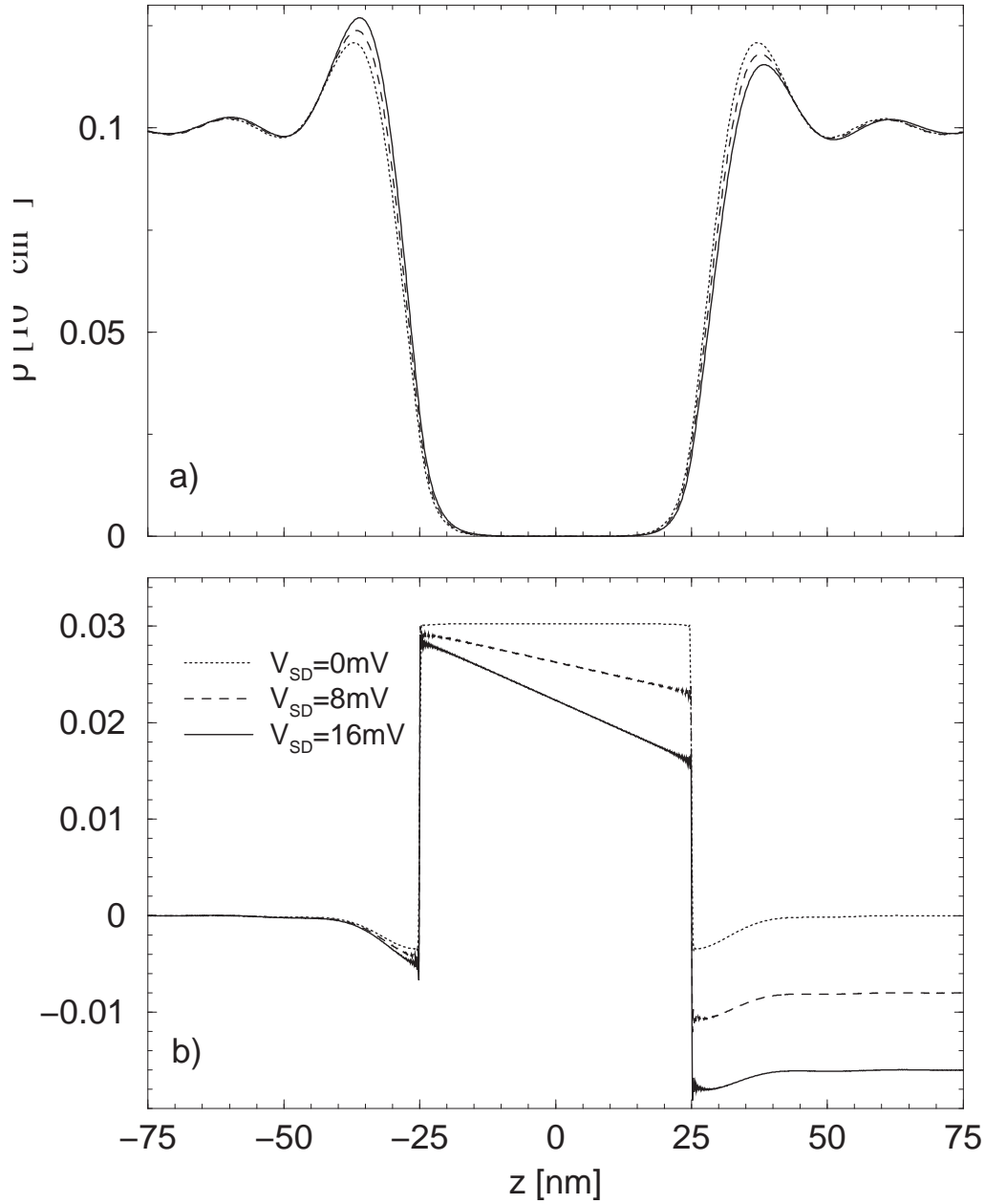


Figure 4.4: a) Self-consistent electronic density distribution and b) self-consistent potential for the single-barrier structure with $V_{b,0} = 33,4$ meV and $d = 75$ nm under biases $V_{SD} = 0, 8$ and 16 mV.

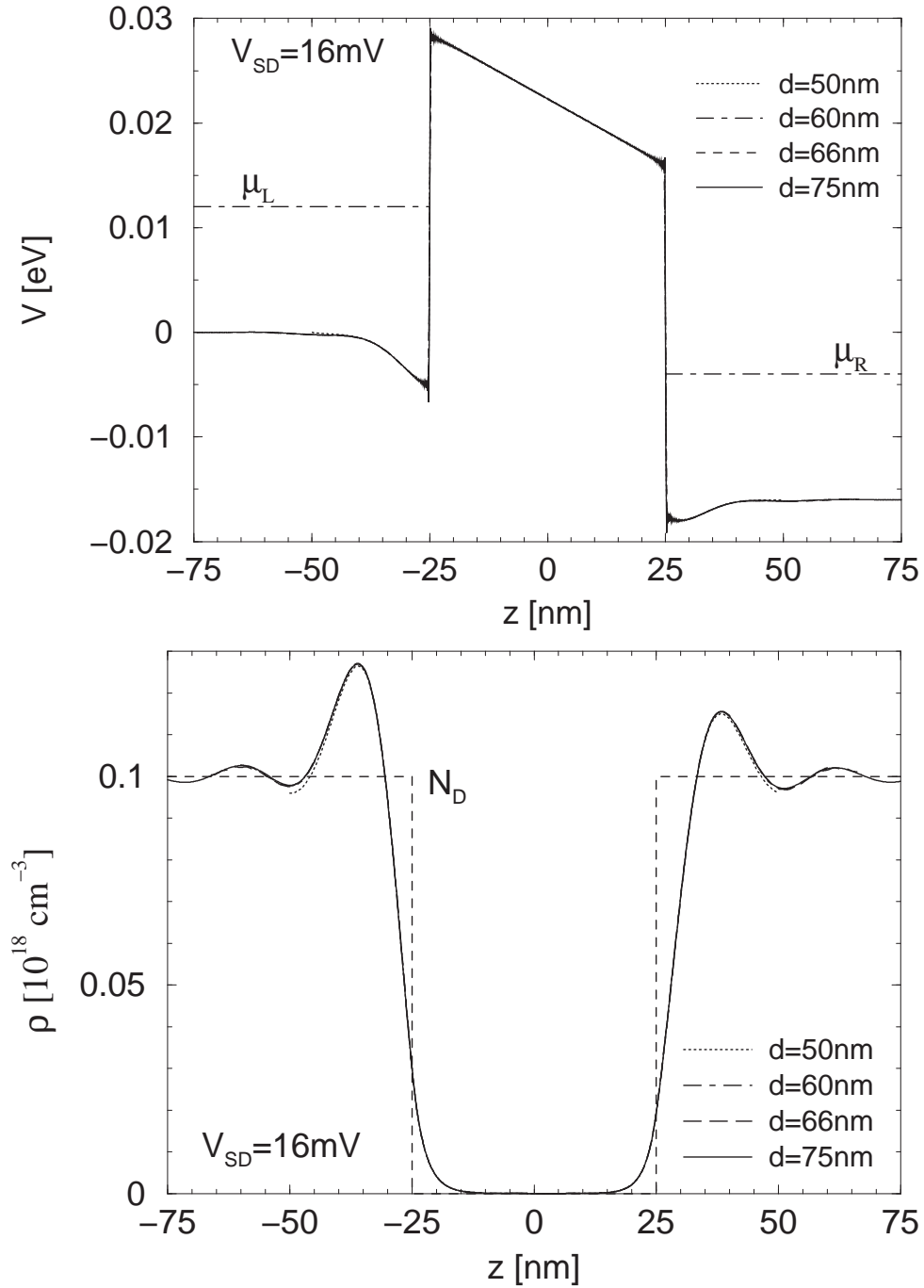


Figure 4.5: The self-consistent potential (upper part) and electronic density distribution (lower part) for the single-barrier structure with $V_{b,0} = 33,4$ meV under bias $V_{SD} = 16$ mV. With dashed line is the donors doping profile.

4.3 Tunneling current

Using the self-consistent results for the charge distribution and the potential shape for different applied biases, we can calculate further the tunneling current and the conductance of the single tunneling barrier system. The tunneling current is given by the Tsu-Esaki formula (2.129) in terms of the tunneling probability for every incident electron energy, $T(\epsilon)$. Because the shape of the potential experienced by the electrons is changing with applied bias, the tunneling probability is also function of the applied bias V_{SD} . We present in Fig. 4.6 the tunneling probability dependence

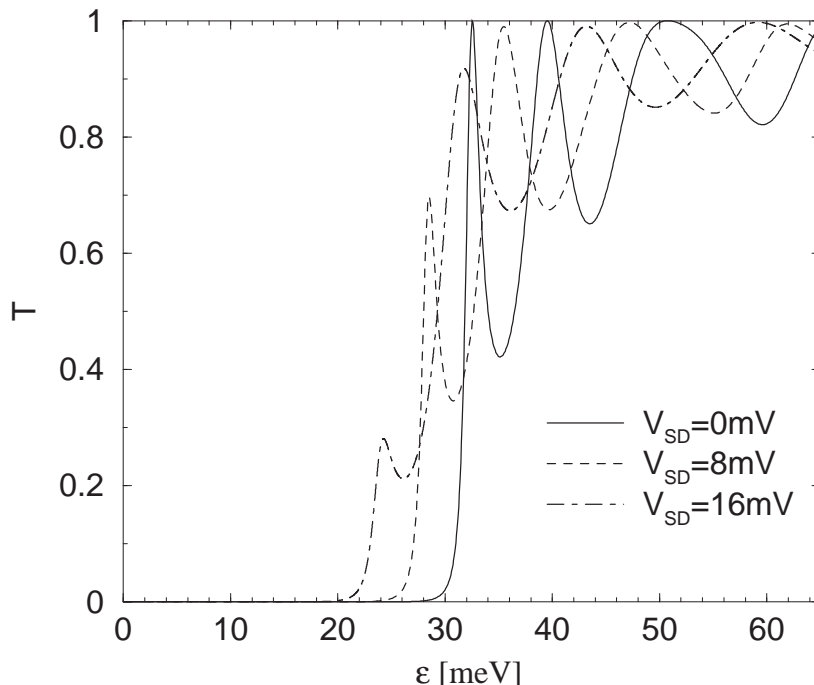


Figure 4.6: Tunneling probability dependence on the incident energy ϵ for a single-barrier structure under applied biases $V_{SD} = 0, 8, 16\text{mV}$. The potential barrier is presented in Fig. 4.4b).

on the incident energy ϵ for a single-barrier structure under applied biases $V_{SD} = 0, 8, 16\text{mV}$. The potential shapes of the barrier under these biases are presented in Fig. 4.4. The tunneling probability exhibits maxima for energies larger than the height of the barrier, energies which corresponds to Fabry-Perot resonances. They are also called quasi-bound states, because the corresponding wave functions present pronounced maxima in the barrier region. One can see that with applied bias the resonance energies are shifted, approximately with $eV_{SD}/2$ and also the tunneling peak value decreases. The tunneling probability is determined only by the scattering potential, and therefore does not depend on d . Further, in the next calculations we

consider $d = 50\text{nm}$. In consequence, the tunneling current does not depend on the positions of the delimiter point d . It was also verified that the tunneling current does not depend on the boundary points for the Wigner Eisenbud problem $\pm\mathcal{L}$.

We plot below the experimental data of a single barrier structure presented in Ref. [48], Figs. 8 and 9, together with the calculated current, varying the parameters of the structure within 10%. There are three sets of parameters: two of them inspired by the modeling parameters used in the above cited reference i) the width of the barrier $b = 52.6\text{nm}$, and the effective height of the barrier $V_b = 31.6\text{meV}$, ii) $b = 51.9\text{nm}$ and $V_b = 31.6\text{meV}$. The height of the barrier, before the self-consistent calculations, was chosen in the above cases $V_{b,0} = 35.02\text{meV}$. As it can be seen in Fig. 4.7 the calculated $I(V_{SD})$ characteristics do not provide a very good fitting of the measured data. We choose the third set of parameters, where we modify the width of the barrier at $b = 55\text{nm}$, and the height is kept the same $V_{b,0} = 35,02\text{meV}$. The effective height of the barrier becomes $V_b = 31.63\text{meV}$. For all calculated data, the temperature is taken $T = 4.2\text{K}$ and the area of the sample is $125 \times 125\mu\text{m}^2$. The conclusion is that, the tunneling current stays within 10%-inaccuracy between experimental and modeled results due to the same uncertainty of the parameters defining the structure [48].

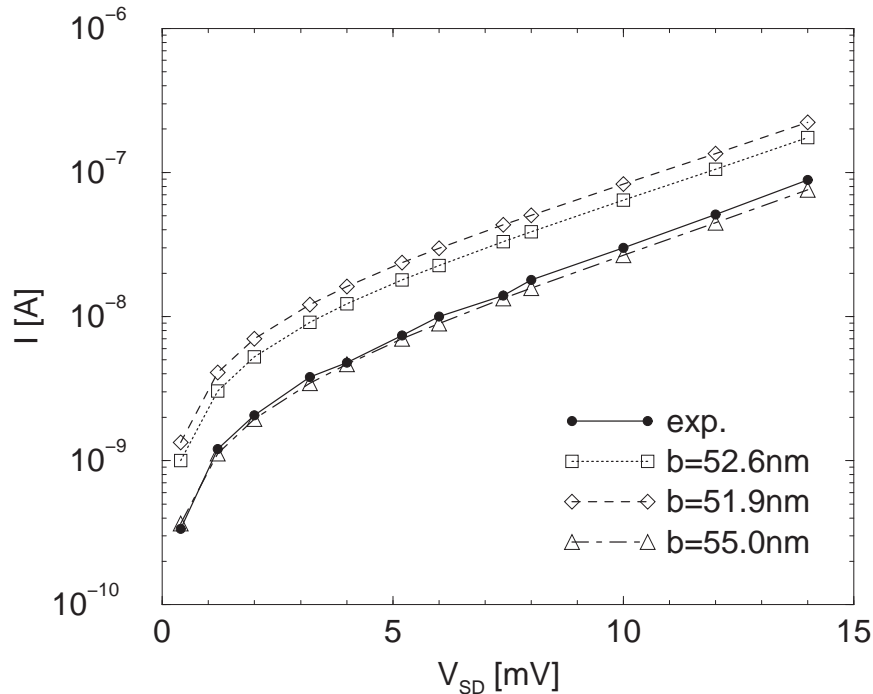


Figure 4.7: Calculated and measured [48] $I(V_{SD})$. The calculations have been performed keeping the height of the barrier constant $V_{b,0} = 35,02\text{meV}$, and changing the width of the barrier within 10% $b = 51.9, 52,6$ and 55nm .

4.3.1 Connection between current and quasi-bound states

In the dependence of the current on the bias, even for one barrier, one can observe "oscillations", i.e. maxima and minima. This variations are connected to the positions of the resonances above the barrier. To access these resonances, one needs to have a small barrier, so that the resonances come under E_F and contribute to the current. For this we analyze further a smaller barrier than that used until now, namely $V_{b,0} = 18.4\text{meV}$ and all other parameters remain the same. The effective height of the barrier after the self-consistent calculations becomes $V_b = 17.6\text{meV}$. We have also performed non self-consistent calculations, which means that we impose on the heterostructure potential V_h , coming from the band-offsets, a potential which is flat in the doped layers and varies linearly by the applied bias in the barrier region. We present in Fig. 4.8 the current dependence on the applied bias V_{SD} , for the cases of self-consistent and non self consistent calculations, together with the conductance dependence

$$G(V_{SD}) = dI(V_{SD})/dV_{SD}. \quad (4.2)$$

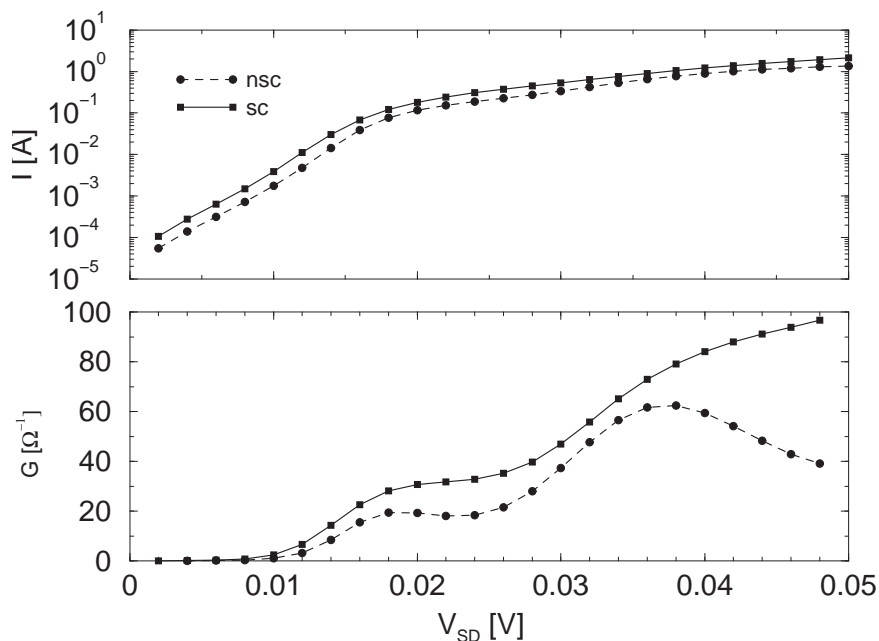


Figure 4.8: Calculated $I(V_{SD})$ (upper part) and $G(V_{SD})$ (lower part) within self-consistent (sc) and non self-consistent (nsc) models for a single barrier structure with $V_{b,0} = 18.4\text{meV}$.

We can see from Fig. 4.8 upper part that the current curves are practically parallel, which means that even for self-consistent calculations the major drop of the potential occurs in the barrier region. The Coulomb interaction decreases the

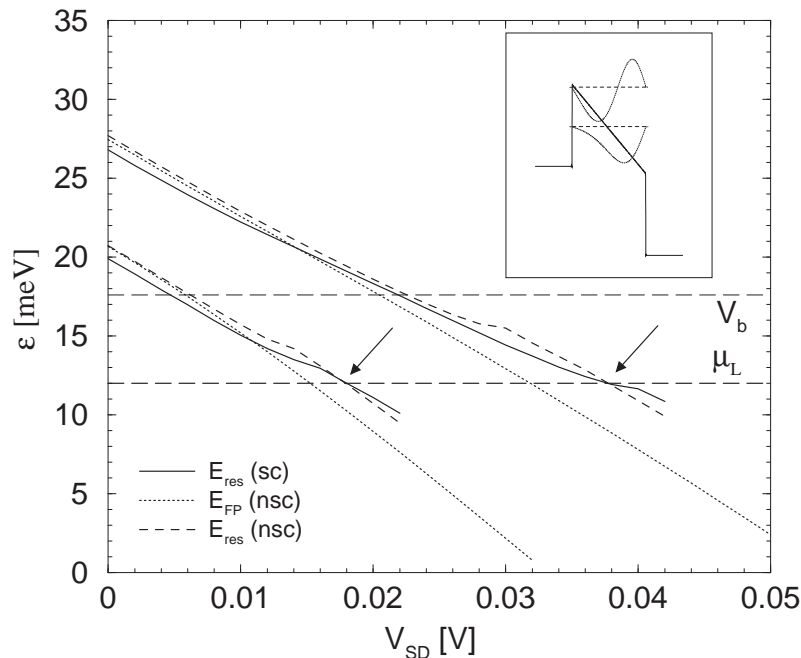


Figure 4.9: Resonance energies as a function of applied bias, for self-consistent (solid line) and non self-consistent (dashed lines) calculations. With dashed lines are represented the chemical potential in the left reservoir μ_L and the effective height of the barrier V_b . With dotted lines are represented the Fabry-Perot energies for non self-consistent calculations (see text). In the inset the first two Fabry-Perot wave functions are shown schematically with their eigenenergies.

effective height of the barrier, yielding a bigger current flow. But the shape of the barriers top are not really parallel for all biases. If this would be the case, then the biases where the oscillations occur will differ from one curve to another, but they are in reality practically the same. From Fig. 4.8 lower part one can observe that the Coulomb interaction between electrons smoothes the oscillations in the current (the first derivative is smoother than in the case of non self-consistent calculations).

There are more biases which play an important role in the current curve:

- the bias for which chemical potential on the right side, μ_R , moves under zero energy level; at this point the total current flow is given by the current which flows from left to to right, $j = j_L$ and $j_R = 0$.
- each bias at which one (quasi) resonant level moves under μ_L ; at this bias the current will increase because the transmission coefficient has a maximum for incident electrons.
- each bias at which one resonance energy moves under $\epsilon = 0$ level; at this bias

the current drops because the transmission coefficient maximum is no more available for the incident carriers.

We present in Fig. 4.9 the dependence of the quasibound states on the applied bias, for self-consistent and non self-consistent calculations of the scattering potential. The first quasi resonant level is between μ_L and $\epsilon = 0$ for $V_{SD} \in [18, 32]$ mV. G has a minimum (in turn the current has a shoulder) at $V_{SD} = 24$ mV, when the resonance is entirely in $[0, \mu_L]$ energy interval. The current increases with the applied bias because the "off-resonance" transmission coefficients increase, while the effective tunneling barrier decreases. In Fig. 4.9 the position of the Fabry-Perot resonances is plotted for the non self-consistent case (the bias drops completely over the barrier). They are determined through the condition of vanishing wave functions outside the barrier. The positions of the maxima of the tunneling coefficient in the self-consistent (sc) and in the non self-consistent (nsc) calculation are practically identical with the energies of the Fabry-Perot resonances revealing the physical origin of the transmission resonances.

4.3.2 Conductance

Though the differential conductance G is, as expected, a monotonously increasing function of V_{SD} , it develops two shoulders at $V_{SD} = 18$ mV and $V_{SD} = 38$ mV (see Fig. 4.8). In the following we want to demonstrate that these shoulders arise when the energy of the (Fabry-Perot-type) quasi-bound states in the barrier coincides with the chemical potential in the source contact (see the arrows in Fig. 4.9). As shown in Fig. 4.10, the quasi-bound states lead to maxima in $T(E)$ below the height of the tunneling barrier which move to lower energies with increasing V_{SD} . Differentiating Eq. (2.129) with respect to V_{SD} one obtains:

$$\frac{dJ_T}{dV_{SD}} \propto \int_0^\infty d\epsilon \frac{dT(\epsilon; V_{SD})}{dV_{SD}} \xi(\epsilon; V_{SD}) + \int_0^\infty T(\epsilon; V_{SD}) \frac{d\xi(\epsilon; V_{SD})}{dV_{SD}}. \quad (4.3)$$

Since $\frac{d\xi(\epsilon; V_{SD})}{dV_{SD}} = \frac{e}{k_B T} f_{FD}(\epsilon - (\mu_L - eV_{SD}))$ is zero for $eV_{SD} > \mu_L$, i. e. in the region of interest in Fig. 4.8, then only the term with the derivative of the tunneling coefficient in Eq. 4.3. gives the variation of the current. When the energy of a resonance approaches from above the Fermi level dT/dV_{SD} is positive for every energy in $[0, \mu_L]$ (see Fig.4.10(a).). When the resonance falls below the Fermi energy a region around the Fermi energy appears for which dT/dV_{SD} is negative (Fig.4.10(b).) and dJ_T/dV_{SD} increases more slowly (see Fig.4.8). For further increased values of V_{SD} the resonance vanishes (Fig.4.10(c).). After that, the second quasi-resonance comes closer to μ_L (Fig.4.10(d).).

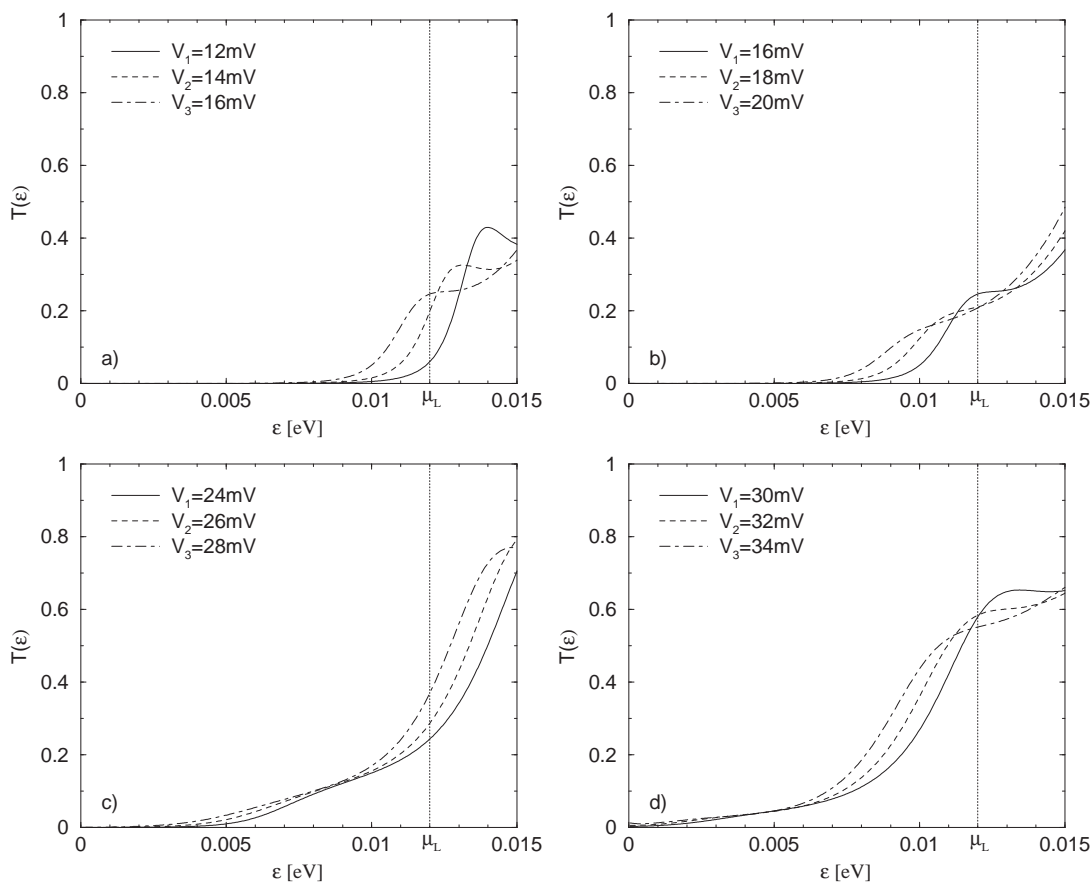


Figure 4.10: The tunneling coefficient $T = \frac{k^R}{k^L} |t^L|^2$ versus energy for different applied biases $V_3 > V_2 > V_1$ and self consistent calculations. With vertical dotted line is marked the chemical potential in the left reservoir μ_L .

4.4 Capacitance

In this section we analyze the capacitance (see Sec. 2.6) for a single-barrier structure with the height of the barrier $V_{b,0} = 18.4 meV$. For the considered system, the barrier allows for a significant tunneling current, so that our capacitance model which takes into account the openness of the system is suitable. For this system, the Gauss law can not provide the correct amount of charges on the plates of the capacitor, because the charge variation on the plates with the applied bias is not equal and of opposite sign. As it will be shown (Fig. 4.11 left part) at a variation of the applied bias, the quantity of charges which enter the system from the source differs from the quantity of charges which go towards the drain. This is a characteristic of open systems.

To ensure that the potential outside the interval $[-\mathcal{L}, \mathcal{L}]$ is constant (which is

equivalent to ensure the charge neutrality in $[-\mathcal{L}, \mathcal{L}]$ we place two sheets of charges σ_1 and σ_2 at the boundaries $\pm\mathcal{L}$. Their sheet densities are given by Eq. (2.138), and using Eq. (2.141) for the potential we obtain the expressions (2.142) and (2.143) with the notations (2.144) and (2.145) for the total areal charge (Q) and the dipole moment (Π). We present in Fig. 4.11 the variation of Q and Π with applied bias V_{SD} for the analyzed single-barrier structure. It follows that $\sigma_1 + \sigma_2 = -Q$.

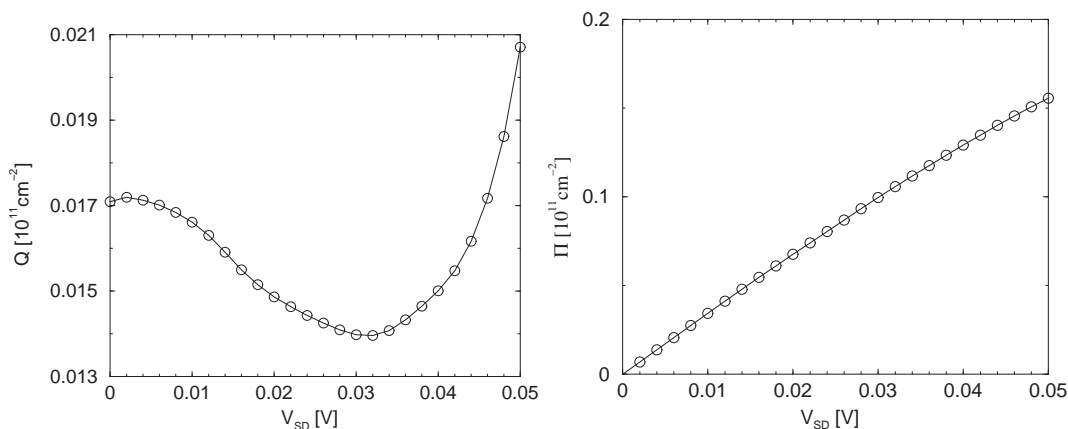


Figure 4.11: Dependence of the total areal charge Q , and total dipole moment Π on the applied bias V_{SD} for a single barrier structure with $V_{b,0} = 18.4 \text{ meV}$.

We present in Fig. 4.12 the variation of σ_1^{free} , σ_2^{free} and the sheet charges σ_1 and σ_2 with applied bias V_{SD} for the analyzed single-barrier structure.

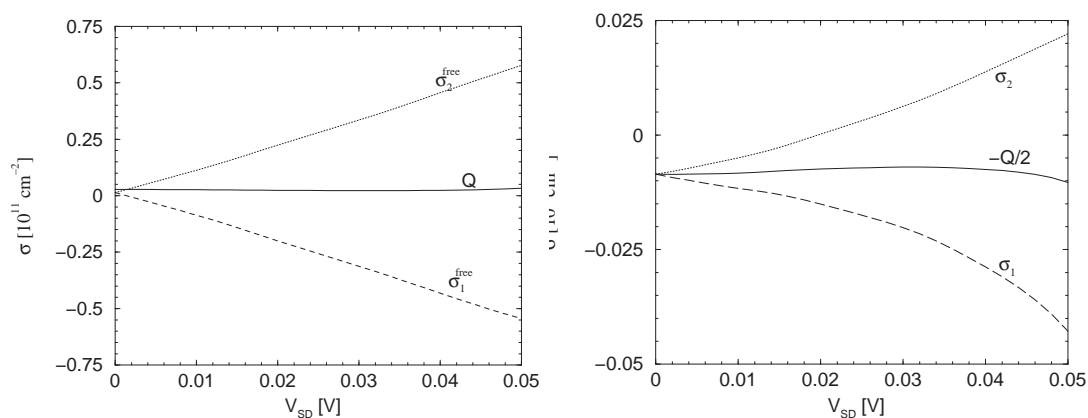


Figure 4.12: As function on applied bias V_{SD} σ_1^{free} , σ_2^{free} (Left part) and σ_1 and σ_2 (Right part) which are symmetric with respect to $-Q/2$.

The charges on the plates Σ_1 and Σ_2 are given by the Eqs. (2.146) and (2.147). Because σ_1 (σ_2) is located directly at the left (right) contact and is separated from the right (left) contact by the barrier it is natural to assume that σ_1 (σ_2) comes entirely from the left (right) contact so that Σ_1 (Σ_2) is the total charge coming from the left (right) contact. We thus define the differential capacitance per area

$$C = \left| \frac{d\Sigma_1}{dV_{SD}} \right| = \left| \frac{d\sigma_2}{dV_{SD}} \right|. \quad (4.4)$$

Since $\sigma_1^{free} + \sigma_2^{free} = Q$, this definition satisfies the classical concept of the capacitance, that the variation of Σ_1 and Σ_2 are equal and with opposite sign. We have $\sigma_1^{free} + \sigma_2^{free} = Q$ and $\sigma_1 + \sigma_2 = -Q$.

We can write C as

$$C = C_q + C_0 - C_{\Pi}, \quad (4.5)$$

where

$$C_q(V_{SD}) = -\frac{1}{2} \frac{d}{dV_{SD}} (\sigma_1^{free} - \sigma_2^{free}), \quad C_{\Pi}(V_{SD}) = \frac{d}{dV_{SD}} \Pi, \quad C_0 = \frac{\epsilon_0 \epsilon_r}{2\mathcal{L}}. \quad (4.6)$$

C_0 corresponds to the capacitance of a plane capacitor formed by the source- and drain contact in the absence of charges between $[-\mathcal{L}, \mathcal{L}]$. The differential capacitance per area depends only on σ_1^{free} , σ_2^{free} , and Π entering as independent quantities which reflect the quantum behavior of the electrons in this system.

We represent in Fig. 4.13 the differential capacitance per area for a single barrier structure with the height of the barrier $V_{b,0} = 18.4\text{meV}$. There are also represented the contributions C_0 , C_q and C_{Π} to the capacitance. To put in evidence the oscillations in the capacitance, we subtract the value at bias zero, $C(V_{SD}) - C(V_{SD} = 0)$, and represent this on the right side of Fig. 4.13.

One can see from Fig.4.14 that there are oscillations in the differential capacitance where the positions of the maxima are identical with the positions of the shoulders in the differential conductance, which further are given by the crossing points between the resonant energies and chemical potential on the left reservoir. These oscillations are largely due to the function $\sigma_1^{free} - \sigma_2^{free}$: When the energy of the Fabry-Perot state hits the chemical potential on the left side, more electrons enter the barrier region from the left reservoir. The monotonous increase of C underlying the oscillations is mostly caused by Π . We attribute this to the enhanced electric field in the barrier which leads to a super proportional increase of Π .

4.5 Summary

We have analyzed a single-barrier tunneling structure in a noninteracting particle approximation. We provided a quantum mechanical model predicting the charge distribution in the scattering region and the tunneling currents between source and

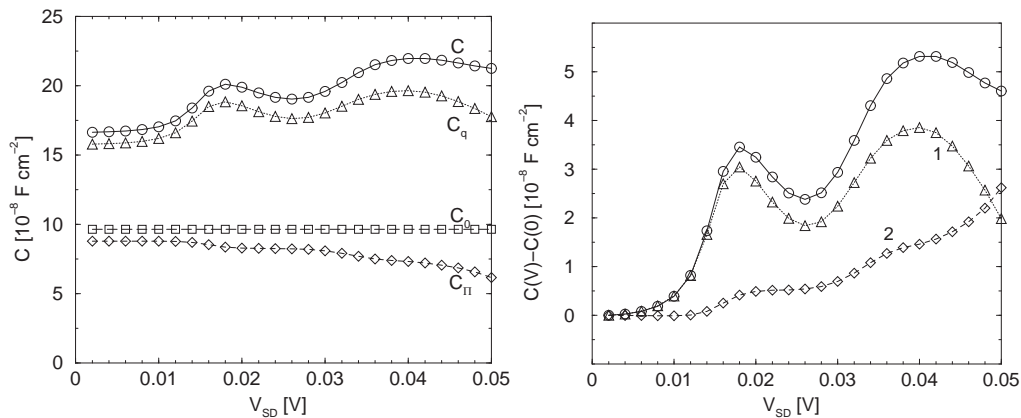


Figure 4.13: As function of applied bias V_{SD} , capacitance per area (left part) and the differences to the capacitance for bias zero (right part). 1 represents $C_q(V_{SD}) - C_q(V_{SD} = 0)$ and 2 represents $C_{II}(V_{SD} = 0) - C_{II}(V_{SD})$, where C_q and C_{II} are defined by Eq. (4.6).

drain contacts. We performed fully self-consistent calculations (we did not use a parametrized expression for the electrostatic potential) for an open system in contact with two reservoirs. We used a new capacitance model for the open systems which accounts for the openness of the system and the influence of contact embedding the system. The capacitance exhibits oscillations with maxima every time a (Fabry-Perot like) resonance crosses the chemical potential in the source reservoir. At the same biases, the conductance presents shoulders.

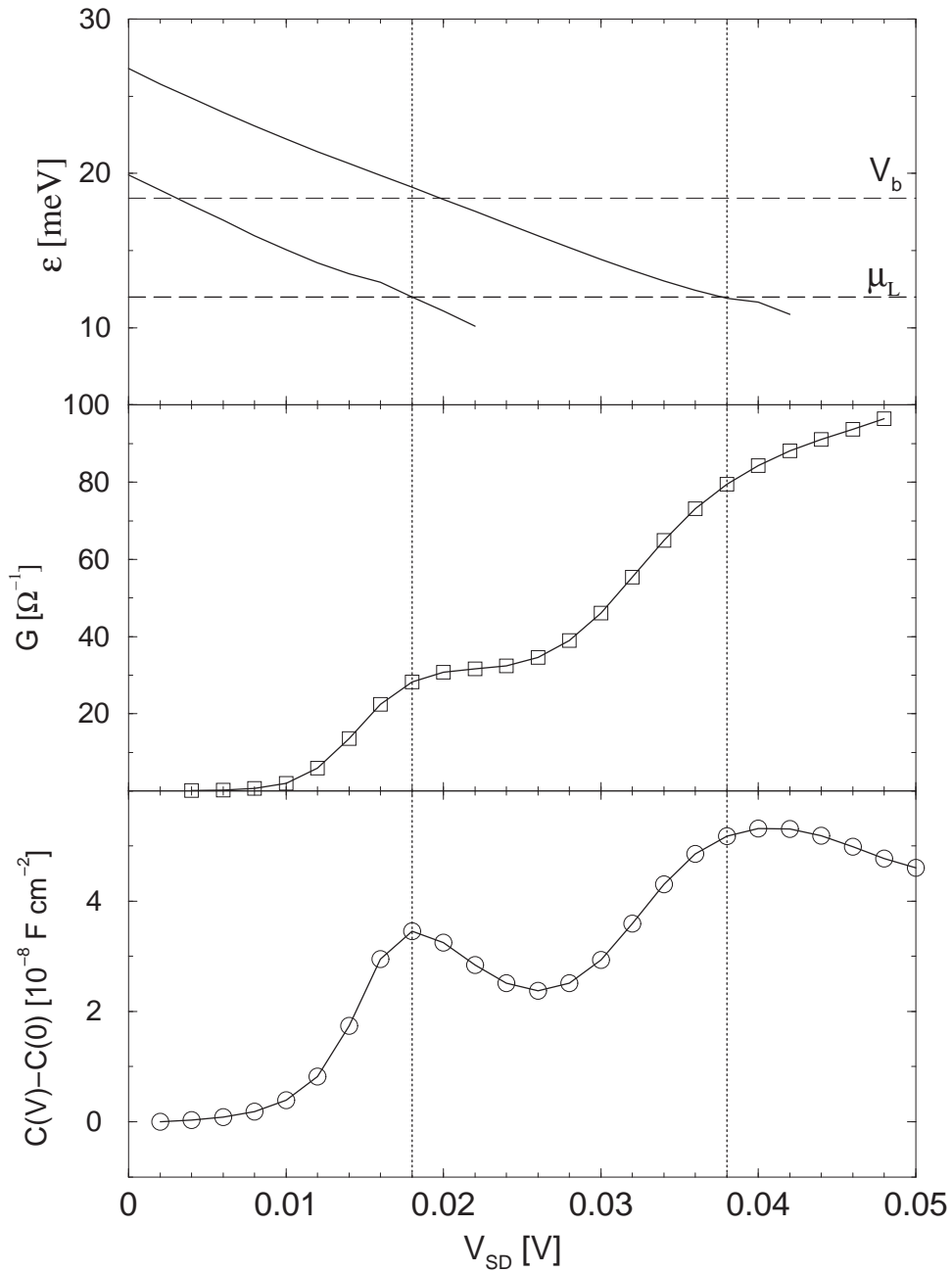


Figure 4.14: As a function of V_{SD} the resonance energies (upper part), the differential conductance G (middle part), and the differential capacitance per area $C(V_{SD}) - C(V_{SD} = 0)$ (lower part).

Chapter 5

Laterally modulated tunneling barrier

In this chapter we extend further the R-matrix formalism to general multidimensional mesoscopic structures, including non resonant transport and transport in the classically allowed regime [93]. In our case we use semi-infinite homogeneous electron gases as contacts, which allow us to treat single mesoscopic structures as well as periodic systems.

After developing the formalism for two-dimensional geometry in Sec. 5.1 we revisit the resonant tunneling problem of isolated levels in Sec. 5.3. In addition to Refs. [18, 34] we show that there is a shift between the resonant energies and the Wigner-Eisenbud energies resulting from components of the Wigner-Eisenbud functions that are bound to the barrier.

Exploring the regime of classically allowed transport, we apply our results to a tunneling barrier with a lateral periodic modulation shown in Fig. 5.1. A similar system was created recently to study, in the ac-transport regime, the wave-mixing properties of a sequence of quantum point contacts [87]. Here we consider the dc conductivity in various limits: For strong modulation (large V_m) we find a transition from the known quantized conductivity in e^2/h of a single point contact for small average barrier height (small V_0) to a series of resonant peaks of height e^2/h for high barriers. Similar peaks which result from the mismatch of wave function inside and outside the scattering region were studied recently in quantum dots in Ref. [88]. For our system we show that in the classically allowed regime ($V_0 < E < V_0 + 2V_m$), these resonant peaks only approximately exhibit the usual algebraic Breit-Wigner distribution. Instead they follow a distribution described by a transcendental tangent function. At weak modulation we demonstrate that the miniband structure of the lateral dispersion can be resolved in dc transport in the forward direction in the limit of large average barrier height (see Fig. 5.1).

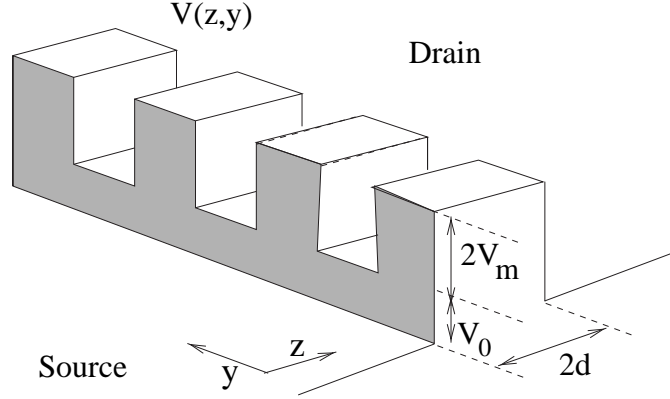


Figure 5.1: Laterally modulated tunneling barrier.

5.1 Formalism for two-dimensional systems

5.1.1 Transmission probabilities with the R -matrix

We describe coherent transport in a system with a two-dimensional Hamiltonian

$$\left[-\frac{\hbar^2}{2m^*} \left(\frac{\partial^2}{\partial z^2} + \frac{\partial^2}{\partial y^2} \right) + V(z, y) - E \right] \Psi(z, y) = 0. \quad (5.1)$$

Extension to three dimensions is trivial. In Eq. (5.1), V is the barrier potential that vanishes outside the scattering region, $V(z, y) = 0$ for $|z| \geq d$. For example our formalism is directly suitable for tunneling processes of the two-dimensional electron gas \leftrightarrow quantum systems (e.g., quantum dots or array of quantum dots) \leftrightarrow two-dimensional electron gas structure. These systems are often created in GaAs heterostructure using a top gate. For our theory to be applicable, we assume that the coherence length is larger than the size of the quantum system. Perpendicular to the tunneling direction the system is periodic in the y -coordinate, $V(z, y + a) = V(z, y)$. Introducing a Bloch vector k_y in the first Brillouin zone $[-\pi/a, \pi/a]$ for the scattering states (see Sect. 5.1.2) we can write

$$\Psi = \Psi^{L/R; k_y, n}(z, y) = e^{ik_y y} \sum_m w_m^{L/R; k_y, n}(z) e^{i(2\pi/a)my}. \quad (5.2)$$

Here $\Psi^{L/R; k_y, n}$ is the scattering state that derives from an incoming plane wave from the left/right reservoir with the momentum in the y direction of $k_{y;n} = k_y + n2\pi/a$, and in the z direction of

$$k_{z;n} = \sqrt{\frac{2m^*}{\hbar^2} \left(E - \frac{\hbar^2}{2m^*} k_{y;n}^2 \right)}, \quad (5.3)$$

where we have to take the first branch of the square root function. The functions $w_m(z)$ obey the scattering boundary conditions

$$w_m^{L;k_y,n}(z) = \begin{cases} \exp[ik_{z;n}z]\delta_{m,n} + r_m^{L;n} \exp[-ik_{z;m}z], & \text{for } z \leq -d \\ t_m^{L;n} \exp[ik_{z;m}z], & \text{for } z \geq d \end{cases} \quad (5.4)$$

and

$$w_m^{R;k_y,n}(z) = \begin{cases} t_m^{R;n} \exp[-ik_{z;m}z], & \text{for } z \leq -d \\ \exp(-ik_{z;n}z)\delta_{m,n} + r_m^{R;n} \exp[ik_{z;m}z], & \text{for } z \geq d \end{cases} \quad (5.5)$$

Through Eq. (5.3) an interval $[m_{min}, m_{max}]$ is defined with m values for which $k_{z;m}$ is real. The corresponding components of the wave function are free waves. If $k_{z;m}$ is complex the corresponding component is bound to the barrier. The functions $w_m(z)$ can be formally constructed solving a Lippmann-Schwinger equation with V as the potential perturbation (see Sect. 5.1.2). However, this approach would, in practical calculations, require for each energy the solution of an integral matrix equation. To avoid this problem we follow the scheme described in Ref. [33] for the application of the R -matrix formalism to one-dimensional transport problems in semiconductor systems. In the first step we introduce the S -matrix that is defined as usual through the relation between ingoing and outgoing parts of the wave function (see Sect. 2.1.2)

$$\begin{bmatrix} \mathbf{w}^{out}(-\mathcal{L}) \\ \mathbf{w}^{out}(+\mathcal{L}) \end{bmatrix} = \begin{bmatrix} \mathbf{S}(-\mathcal{L}, -\mathcal{L}) & \mathbf{S}(-\mathcal{L}, +\mathcal{L}) \\ \mathbf{S}(+\mathcal{L}, -\mathcal{L}) & \mathbf{S}(+\mathcal{L}, +\mathcal{L}) \end{bmatrix} \begin{bmatrix} \mathbf{w}^{in}(-\mathcal{L}) \\ \mathbf{w}^{in}(+\mathcal{L}) \end{bmatrix}, \quad (5.6)$$

or

$$w_{m,s}^{out} = \sum_{m',s'} S_{m,s;m',s'} w_{m's'}^{in}. \quad (5.7)$$

Equation (5.6) is a matrix equation for each k_y where $\mathbf{w}(\pm\mathcal{L}) = \mathbf{w}^{out}(\pm\mathcal{L}) + \mathbf{w}^{in}(\pm\mathcal{L})$ is a vector containing the components $w_m(z) = w_m^{out}(z) + w_m^{in}(z)$ at $z = \pm\mathcal{L}$. $w_m(z)$ results from a decomposition as in Eq. (5.2), of a general scattering state for given k_y and E (i.e., a superposition of states $\Psi^{L/R;k_y,n}$ with different n and different index L/R). For $z \leq -d$, w_m^{out} is the part of $w_m(z)$ containing the factor $\exp[-ik_{z;m}z]$ and w^{in} is the part containing $\exp[+ik_{z;m}z]$. For $z \geq d$, w_m^{out} is the part of $w_m(z)$ containing the factor $\exp[ik_{z;m}z]$ and w^{in} the part containing $\exp[-ik_{z;m}z]$. $\mathcal{L} \geq d$ defines an arbitrarily chosen "surface" of the scattering area. In Eq. (5.7) the index $s = 0$ and 1 denotes the argument $z = (-1)^s \mathcal{L}$. The derivation of Eq. (5.6) and the formal definition of the decomposition $w_m = w_m^{out} + w_m^{in}$ are given in Sect. 5.1.3. Also in Sect. 5.1.3 we derive the following relations between the S -matrix and the reflection and transmission coefficients

$$\begin{aligned} S_{mn}(-\mathcal{L}, -\mathcal{L}) &= \exp[i(k_{z;m} + k_{z;n})\mathcal{L}] r_m^{L;n}, \\ S_{mn}(-\mathcal{L}, \mathcal{L}) &= \exp[i(k_{z;m} + k_{z;n})\mathcal{L}] t_m^{R;n}, \\ S_{mn}(\mathcal{L}, -\mathcal{L}) &= \exp[i(k_{z;m} + k_{z;n})\mathcal{L}] t_m^{L;n}, \\ S_{mn}(\mathcal{L}, \mathcal{L}) &= \exp[i(k_{z;m} + k_{z;n})\mathcal{L}] r_m^{R;n}. \end{aligned} \quad (5.8)$$

The R -matrix is introduced as

$$w_{m,s} = \sum_{m',s'} R_{m,s;m',s'} w_{m',s'}^S. \quad (5.9)$$

As usual the R -matrix relates the value of the wave function to its normal derivatives $w_{m,s}^S = (-1^{s+1}/m^*) \nabla_z w_{m,s}$ at the surface $z = \pm \mathcal{L}$ of the scattering area. In order to construct the R -matrix we start from the Wigner-Eisenbud functions

$$\chi_l(z, y) = e^{ik_y y} \sum_{m=-\infty}^{+\infty} e^{i\frac{2\pi}{a} m y} v_m^l(z), \quad (5.10)$$

which are the solutions of the Schrödinger equation (5.1) with the boundary condition

$$\frac{\partial}{\partial z} \chi_l(z = -\mathcal{L}, y) = \frac{\partial}{\partial z} \chi_l(z = +\mathcal{L}, y) = 0. \quad (5.11)$$

The normalization is chosen so that $2\mathcal{L} \delta_{l,l'} = \sum_m \int_{-\mathcal{L}}^{-\mathcal{L}} dz v_m^l(z) v_m^{l'}(z)$. The corresponding Wigner-Eisenbud eigenenergies are E_l . Using standard techniques it can be shown (see Sect. 5.1.4) that

$$R_{m,s;m',s'} = -\frac{\hbar^2}{4\mathcal{L}} \sum_l \frac{v_m^l(-1^s \mathcal{L}) v_{m'}^{l'}(-1^{s'} \mathcal{L})}{E - E_l}. \quad (5.12)$$

with real functions v_m^l . Eq. (5.12) shows that R-matrix has the form of a Green's function. However, the boundary conditions (5.11) have to be contrasted with "scattering boundary conditions" (evanescent plane waves outside the scattering area) for the Green's functions. In the latter case the transmission coefficients, and therefore the S -matrix, follow directly from the Green's function [25]. Making use of $w_m^S = (w_m^{in})^S + (w_m^{out})^S = ik_{z,m}/m^* (w_m^{out} - w_m^{in})$ in Eq. (5.9) we obtain

$$\mathbf{S} = -\left(1 - \frac{i}{m^*} \mathbf{Rk}\right)^{-1} \left(1 + \frac{i}{m^*} \mathbf{Rk}\right) \quad (5.13)$$

which is the desired formula to express the S -matrix in terms of the R -matrix. Here $(\mathbf{R})_{m,s;m',s'} = R_{m,s;m',s'}$, $(\mathbf{S})_{m,s;m',s'} = S_{m,s;m',s'}$, $(1)_{m,s;m',s'} = \delta_{m,m'} \delta_{s,s'}$ and $\mathbf{k}_{m,s;m',s'} = \delta_{s,s'} \delta_{m,m'} k_{z,m}$. In addition to the corresponding result Eq. (2.78) which is in the space of 2×2 matrices, but has the same form as Eq. (5.13) here the index m is included which describes the lateral modulation.

5.1.2 Scattering states as Bloch functions

In this section we show that the scattering states are Bloch functions as given by Eq. (5.2), with the boundary conditions of Eqs. (5.4) and (5.5). We obtain a set of coupled integral equations to determine the Fourier components $w_m^{L/R;k_y,n}(z)$.

We start by recasting the Schrödinger equation [Eq. (5.1)] in the form of a Lippmann-Schwinger integral equation [89]

$$\Psi^{L/R;\lambda}(z, y) = \Phi^{L/R;\lambda}(z, y) + \int_{-d}^d dz' \int dy' \mathcal{G}_0(z - z', y - y') V(z', y') \Psi^{L/R;\lambda}(z', y'). \quad (5.14)$$

Here $\Psi^{L/R;\lambda}$ are the scattering states, and

$$\Phi^{L/R;\lambda}(z, y) = \exp \left[i \left(k_y + \frac{2\pi}{a} n \right) y + (-1)^u i k z \right] \quad (5.15)$$

are plane waves which are the solutions of the unperturbed problem ($V = 0$). We have $u = 0$ for Φ^L and $u = 1$ for Φ^R , and $E = \hbar^2/2m^*([k_y + (2\pi/a)n]^2 + k^2)$. The unperturbed waves define the channels $\lambda = (k_y, n)$, and k is determined by the energy E . As usual $\mathcal{G}_0(z - z', y - y')$ is the Green's function of the unperturbed problem,

$$\delta(z - z')\delta(y - y') = \left[E + \frac{\hbar^2}{2m^*} \left(\frac{d^2}{dz^2} + \frac{d^2}{dy^2} \right) \right] \mathcal{G}_0(z - z', y - y'). \quad (5.16)$$

In our case \mathcal{G}_0 obeys radiation boundary conditions in the z direction [see Eq. (5.21)] and periodic boundary conditions in the y direction. In Eq. (5.14) we insert the barrier potential as

$$V(z, y) = \sum_m V_m^{bar}(z) \exp \left(i \frac{2\pi}{a} m y \right), \quad (5.17)$$

and obtain

$$\begin{aligned} e^{-ik_y y} \Psi^{L/R;k_y,n}(z, y) &= \exp \left(i \frac{2\pi}{a} n y + (-1)^u i k z \right) \\ &+ \int_{-d}^d dz' \sum_m V_m^{bar}(z') \int dy' e^{-ik_y(y-y')} \mathcal{G}_0(z - z', y - y') \\ &\times \exp \left(i \frac{2\pi}{a} m y' \right) e^{-ik_y y'} \Psi^{L/R;k_y,n}(z', y'), \end{aligned} \quad (5.18)$$

where we have multiplied both sides with a factor $e^{-ik_y y}$. After the transformation $y \rightarrow y + a$ the same equation follows for $\exp[-ik_y(y + a)]\Psi_n(z, y + a)$. Therefore, we can write

$$\exp(-ik_y y) \Psi^{L/R;k_y,n}(z, y) = \sum_m w_m^{L/R;k_y,n}(z) \exp \left(i \frac{2\pi}{a} m y \right), \quad (5.19)$$

which is the desired Bloch-type representation of the scattering states. Inserting this representation into Eq. (5.18), we find

$$\begin{aligned} w_m^{L/R;k_y,n}(z) &= \delta_{m,n} \exp [(-1)^u i k z] \\ &+ \int_{-d}^d dz' \mathcal{G}_0(z - z', k_y + \frac{2\pi}{a} m) \sum_{m'} V_{m'}^{bar}(z') w_{m-m'}^{L/R;k_y,n}(z'), \end{aligned} \quad (5.20)$$

with $\mathcal{G}_0(z - z', q_y) = \int dy \exp(-iq_y y) \mathcal{G}_0(z - z', y - y')$. To obtain the S -matrix this set of coupled integral equations may be solved directly and represents thus the generic alternative to the R -matrix formalism. For each energy E a separate set of equations must be solved. The advantage of the R -matrix formalism is that one has to solve an equivalent problem only once to obtain the Wigner-Eisenbud functions and energies. From these the R -matrix can be calculated *for all energies* by a simple summation. The S -matrix can then be found using Eq. (5.13) by an inversion of a matrix in the Fourier space of the components m which does not contain z as a degree of freedom, and thus has a dimension smaller by 1 than the problem in Eq. (5.20). Using standard methods, with $k_z = \sqrt{2m^*E/\hbar^2 - q_y^2}$ we find

$$\mathcal{G}_0(z - z', q_y) = -i \frac{m^*}{\hbar^2} \frac{1}{k_z} \exp(+ik_z|z - z'|). \quad (5.21)$$

This expression can be inserted into Eq. (5.20), and we obtain immediately the lower line in Eq. (5.4) with

$$r_m^{L;n} = -i \frac{m^*}{\hbar^2 k_{z;m}} \sum_{m'} \int_{-d}^d dz' V_{m'}^{bar}(z') \exp(ik_{z;m}z') w_{m-m'}^{L;k_y,n}(z'), \quad (5.22)$$

where $k_{z;m}$ is defined in Eq. (5.3). Analogous expressions can be found for $t_m^{L;n}$, $r_m^{R;n}$, and $t_m^{R;n}$.

5.1.3 S -matrix theory

Any scattering wave is composed of incoming and outgoing (scattered) parts:

$$\Psi = \Psi^{in} + \Psi^{out}. \quad (5.23)$$

The S -matrix elements are defined as coefficients between the outgoing and incoming parts of the scattering waves. Obviously, they can be expressed in terms of the coefficients $t_m^{L;n}$, $t_m^{R;n}$, $r_m^{L;n}$, and $r_m^{R;n}$.

In general, an incoming wave can be expressed as linear combination of incident plane waves:

$$\Psi^{in}(z, y) = \sum_n a_n \Phi_{in}^{L;k_y,n}(z, y) \quad (5.24)$$

$$= \sum_n a_n \exp(ik_{z;n}z) \exp \left[i \left(k_y + \frac{2\pi}{a} n \right) y \right] \quad (5.25)$$

for $z \leq -d$ and

$$\Psi^{in}(z, y) = \sum_n b_n \Phi_{in}^{R;k_y,n}(z, y) \quad (5.26)$$

$$= \sum_n b_n \exp(-ik_{z;n}z) \exp \left[i \left(k_y + \frac{2\pi}{a} n \right) y \right] \quad (5.27)$$

for $z \geq +d$. The corresponding outgoing wave is then:

$$\begin{aligned}
\Psi^{out}(z, y) &= \sum_n a_n [\Psi^{L;k_y,n}(z, y) - \Phi_{in}^{L;k_y,n}(z, y)] + \sum_n b_n \Psi^{R;k_y,n}(z, y) \\
&= \sum_n a_n \sum_m r_m^{L;n} \exp \left[-ik_{z;m}z + i \left(k_y + \frac{2\pi}{a}m \right) y \right] \\
&\quad + \sum_n b_n \sum_m t_m^{R;n} \exp \left[-ik_{z;m}z + i \left(k_y + \frac{2\pi}{a}m \right) y \right] \tag{5.28}
\end{aligned}$$

for $z \leq -d$, and

$$\begin{aligned}
\Psi^{out}(z, y) &= \sum_n a_n \Psi^{L;k_y,n}(z, y) + \sum_n b_n [\Psi^{R;k_y,n}(z, y) - \Phi_{in}^{R;k_y,n}(z, y)] \\
&= \sum_n a_n \sum_m t_m^{L;n} \exp \left[ik_{z;m}z + i \left(k_y + \frac{2\pi}{a}m \right) y \right] \\
&\quad + \sum_n b_n \sum_m r_m^{R;n} \exp \left[ik_{z;m}z + i \left(k_y + \frac{2\pi}{a}m \right) y \right] \tag{5.29}
\end{aligned}$$

for $z \geq d$. We now eliminate the coefficients a_n and b_n :

$$\begin{aligned}
a_n &= e^{ik_{z;n}\mathcal{L}} \frac{1}{a} \int_0^a dy' e^{-i(k_y + 2\pi/an)y'} \Psi^{in}(-\mathcal{L}, y'), \\
b_n &= e^{ik_{z;n}\mathcal{L}} \frac{1}{a} \int_0^a dy' e^{-i(k_y + \frac{2\pi}{a}n)y'} \Psi^{in}(+\mathcal{L}, y'),
\end{aligned}$$

and find a general expression of Ψ^{out} in terms of $\Psi^{in}(\pm\mathcal{L}, y)$:

$$\begin{aligned}
\Psi^{out}(z, y) &= \sum_m \exp \left[-ik_{z;m}z + i \left(k_y + \frac{2\pi}{a}m \right) y \right] \tag{5.30} \\
&\quad \times \left[\sum_n r_m^{L;n} \exp(ik_{z;n}\mathcal{L}) \frac{1}{a} \int_0^a dy' e^{-i[k_y + (2\pi/a)n]y'} \Psi^{in}(-\mathcal{L}, y') \right. \\
&\quad \left. + \sum_n t_m^{R;n} \exp(ik_{z;n}\mathcal{L}) \frac{1}{a} \int_0^a dy' e^{-i[k_y + (2\pi/a)n]y'} \Psi^{in}(+\mathcal{L}, y') \right]
\end{aligned}$$

for $z \leq -d$, and

$$\begin{aligned}
\Psi^{out}(z, y) &= \sum_m \exp \left[ik_{z;m}z + i \left(k_y + \frac{2\pi}{a}m \right) y \right] \tag{5.31} \\
&\quad \times \left[\sum_n t_m^{L;n} \exp(ik_{z;n}\mathcal{L}) \frac{1}{a} \int_0^a dy' e^{-i[k_y + (2\pi/a)n]y'} \Psi^{in}(-\mathcal{L}, y') \right. \\
&\quad \left. + \sum_n r_m^{R;n} \exp(ik_{z;n}\mathcal{L}) \frac{1}{a} \int_0^a dy' e^{-i[k_y + (2\pi/a)n]y'} \Psi^{in}(+\mathcal{L}, y') \right]
\end{aligned}$$

for $z \geq d$. When we further introduce the components

$$\Psi^{in}(z, y) = \sum_{m=n_{min}}^{n_{max}} e^{i[k_y + (2\pi/a)m]y} w_m^{in}(z) \tag{5.32}$$

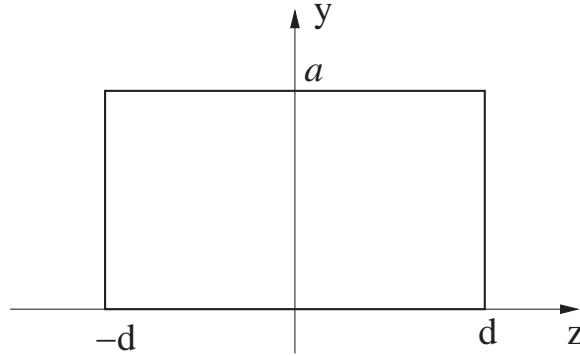


Figure 5.2: Domain of integration.

and

$$\Psi^{out}(z, y) = \sum_{m=-\infty}^{+\infty} e^{i[k_y + (2\pi/a)m]y} w_m^{out}(z) \quad (5.33)$$

we obtain the desired formal expression of Eq. (5.6), where the S -matrix is related to the transmission and reflection coefficients through Eq. (5.8).

Remark The incoming wave has only a finite number of components, whereas the outgoing wave may contain an infinite number of terms, of which, however, only a finite number are not damped and may thus carry current.

5.1.4 Construction of the R -matrix

In this section we want to derive Eq. (5.12). We begin with the Schrödinger equations

$$\left[-\frac{\hbar^2}{2m^*} \left(\frac{\partial^2}{\partial z^2} + \frac{\partial^2}{\partial y^2} \right) + V(z, y) - \epsilon \right] \Psi(z, y) = 0 \quad (5.34)$$

and

$$\left[-\frac{\hbar^2}{2m^*} \left(\frac{\partial^2}{\partial z^2} + \frac{\partial^2}{\partial y^2} \right) + V(z, y) - \epsilon_l \right] \chi_l(z, y) = 0. \quad (5.35)$$

Here Ψ is a scattering function and χ_l is a Wigner-Eisenbud function with given k_y . Multiplying Eq. (5.35) by χ_l^* , and integrating the result over the rectangle depicted in Fig. 5.2 we find that ϵ_l are real.

Multiplying Eq. (5.34) by χ_l^* , and the complex conjugate of Eq. (5.35) by Ψ , subtracting both equations, and integrating the result over the same rectangle, we obtain

$$-\frac{\hbar^2}{2m^*} \int dz dy [\Psi \nabla^2 \chi_l^* - \chi_l^* \nabla^2 \Psi] = (\epsilon - \epsilon_l) \int dz dy \Psi \chi_l^*. \quad (5.36)$$

Using Green's second theorem we can express the area integral on the left-hand side of the above equation as a contour integral

$$\begin{aligned}
& -\frac{\hbar^2}{2m^*} \int_0^a dy [(\Psi \nabla_z \chi_l^* - \chi_l^* \nabla_z \Psi)|_{z=\mathcal{L}} - (\Psi \nabla_z \chi_l^* - \chi_l^* \nabla_z \Psi)|_{z=-\mathcal{L}}] \\
& + \frac{\hbar^2}{2m^*} \int_{-\mathcal{L}}^{+\mathcal{L}} dz [(\Psi \nabla_y \chi_l^* - \chi_l^* \nabla_y \Psi)|_{y=a} - \Psi \nabla_y \chi_l^* - \chi_l^* \nabla_y \Psi|_{y=0}] \\
& = (\epsilon_l - \epsilon) \int dz dy \Psi \chi_l^* .
\end{aligned} \tag{5.37}$$

Due to the periodicity in the y direction, the second integral on the left-hand side of Eq. (5.37) vanishes. Because of the boundary condition (5.11) for the Wigner Eisenbud functions we can drop terms with $\nabla_z \chi_l^*$ in the first integral and we can write

$$\begin{aligned}
& -\frac{\hbar^2}{2} \int_0^a dy \left[\chi_l(\mathcal{L}, y)^* \frac{1}{m^*} \nabla_z \Psi(\mathcal{L}, y) - \chi_l(-\mathcal{L}, y)^* \frac{1}{m^*} \nabla_z \Psi(-\mathcal{L}, y) \right] \\
& = (\epsilon - \epsilon_l) \int dz dy \Psi \chi_l^* .
\end{aligned} \tag{5.38}$$

If we replace Ψ in Eq. (5.34) with $\chi_{l'}$, and ϵ with $\epsilon_{l'}$, and repeat the procedure in this case we obtain that the right-hand side of Eq. (5.38) vanishes. This proves directly the orthogonality of the χ_l . Because of the structural similarity of Eqs. (5.35) and (5.11) to a Sturm-Liouville problem here we simply assume completeness,

$$\Psi(z, y) = \sum_l a_l \chi_l(z, y), \tag{5.39}$$

with

$$a_l = \frac{1}{2\mathcal{L}a} \int_{-\mathcal{L}}^{\mathcal{L}} dz' \int_0^a dy' \chi_l^*(z', y') \Psi(z', y'). \tag{5.40}$$

Inserting Eq. (5.39) into Eq. (5.38) leads to the following expression for Ψ

$$\Psi(z, y) = \int_0^a dy' [R(z, y; -\mathcal{L}, y') \Psi^S(-\mathcal{L}, y') + R(z, y; +\mathcal{L}, y') \Psi^S(+\mathcal{L}, y')], \tag{5.41}$$

with the R -matrix

$$R(z, y, ; (-1)^{s'} \mathcal{L}, y') = -\frac{\hbar^2}{4\mathcal{L}a} \sum_l \frac{\chi_l(z, y) \chi_l^*(-1^{s'} \mathcal{L}, y')}{\epsilon - \epsilon_l}. \tag{5.42}$$

Writing Eq. (5.42) for the argument $z = (-1)^s \mathcal{L}$ and inserting expansions (5.2) for the scattering states and Eq. (5.10) for the Wigner-Eisenbud functions, we immediately obtain Eqs. (5.9) and (5.12).

5.2 Conductance

We define the current density averaged over one period in the y direction, $\bar{j}_z = \int_0^a dy j_z(y, z_0)/a$, z_0 fixed, and write $\bar{j}_z = \bar{j}_z^L - \bar{j}_z^R$ where $\bar{j}_z^{L/R}$ is the z component of the density of the current coming from the L/R reservoir with

$$\bar{j}_z^{L/R} = 2 \sum_{k_y \in \text{1.B.Z.}} \sum_{n=m_{\min}}^{m_{\max}} \sum_k f_{FD}(E - \mu_{L/R}) \frac{1}{a} \int_0^a dy \langle \Psi^{L/R; k_y, n} | \hat{j}_z | \Psi^{L/R; k_y, n} \rangle, \quad (5.43)$$

and $E = \hbar^2(k^2 + k_{y;n}^2)/(2m^*)$. Inserting Eqs. (5.2), (5.4), and (5.5) one finds ($z_0 \geq d$ for \bar{j}_z^L and $z_0 \leq -d$ for \bar{j}_z^R)

$$\begin{aligned} \frac{1}{a} \int_0^a dy \langle \Psi^{L/R; k_y, n} | \hat{j}_z | \Psi^{L/R; k_y, n} \rangle &= \frac{1}{a} \frac{e\hbar}{2m^*i} \int_0^a \left[(\Psi^{L/R; k_y, n})^* \frac{\partial}{\partial z} \Psi^{L/R; k_y, n} \right. \\ &\quad \left. - \Psi^{L/R; k_y, n} \frac{\partial}{\partial z} (\Psi^{L/R; k_y, n})^* \right] \\ &= \frac{\hbar e}{m^*} \sum_{m=m_{\min}}^{m_{\max}} |t_m^{L/R; n}|^2 k_m, \end{aligned} \quad (5.44)$$

with $e = -|e|$. Since we used as incident waves unnormalized plane waves [see Eq. (5.15)] which corresponds to $L_z = L_y = 1$ we set $\sum_{k_y} \rightarrow L_y/(2\pi) \int dk_y \rightarrow 1/(2\pi) \int dk_y$ and $\sum_k \rightarrow 1/(2\pi) \int dk$ to obtain

$$\bar{j}_z^{L/R} = \frac{2e\hbar}{(2\pi)^2 m^*} \int_{-\pi/a}^{\pi/a} dk_y \sum_{m, n=m_{\min}}^{m_{\max}} \int_0^\infty dk f_{FD}(E - \mu_{L/R}) k_m |t_m^{L/R; n}(E)|^2. \quad (5.45)$$

We now for fixed n substitute $E = \hbar^2(k^2 + k_{y;n}^2)/(2m^*)$ and $dk/dE = m^*/k_{z;n}(E)\hbar^2$ [see Eq. (5.3)] to find

$$\begin{aligned} \bar{j}_z^{L/R} &= \frac{2e}{\hbar(2\pi)^2} \int_{-\pi/a}^{\pi/a} dk_y \sum_{m, n=m_{\min}}^{m_{\max}} \int_{E_0}^\infty dE f_{FD}(E - \mu_{L/R}) k_{z;m}(E) |t_m^{L/R; n}(E)|^2 k_{z;n}^{-1}(E) \\ &= \frac{e}{\hbar(2\pi)^2} \int_{-\pi/a}^{\pi/a} dk_y \sum_{m, n=m_{\min}}^{m_{\max}} \int_{E_0}^\infty dE f_{FD}(E - \mu_{L/R}) |\tilde{S}_{m, 0/1; n, 1/0}|^2. \end{aligned} \quad (5.46)$$

Here

$$\tilde{S}_{m, s; m', s'} = k_{z;m}^{1/2} S_{m, s; m', s'} k_{z;m'}^{-1/2} \quad (5.47)$$

is the current transmission matrix, and $E_0 = \hbar^2 k_{y;n}^2/(2m^*)$. From Eq. (5.13) we obtain

$$\tilde{S} = -\frac{1 - i\Omega}{1 + i\Omega} = 1 - \frac{2}{1 + i\Omega}, \quad (5.48)$$

with

$$\Omega_{m,s;m',s'} = -\frac{\hbar^2 k_{z;m}^{1/2} k_{z;m'}^{1/2}}{4\mathcal{L}m^*} \sum_l \frac{v_l^m(-1^s \mathcal{L}) v_l^{m'}(-1^{s'} \mathcal{L})}{E - E_l}. \quad (5.49)$$

The current transmission matrix is symmetric: $\tilde{S}_{m,s;m',s'} = \tilde{S}_{m',s';m,s}$. Going back to Eq. (5.46) we thus obtain

$$\bar{j}_z = \frac{2e}{\hbar(2\pi)^2} \int_{-\pi/a}^{\pi/a} dk_y \sum_{m,n=m_{\min}}^{m_{\max}} \int_{E_0}^{\infty} dE [f_{FD}(E - \mu_L) - f_{FD}(E - \mu_R)] |\tilde{S}_{m,0;n,1}|^2. \quad (5.50)$$

In this paper we are interested in the limit of small applied potentials ΔV_{sd} and zero temperature, e.g., $\mu_L \equiv E_F = \mu_R + e\Delta V_{sd}$. We use $f_{FD}(E - E_F) - f_{FD}(E - E_F + e\Delta V_{sd}) \xrightarrow{T \rightarrow 0} e\Delta V_{sd} \delta(E - E_F)$ and find

$$G \equiv \frac{I_a}{\Delta V_{sd}} = \frac{\bar{j}_z a}{\Delta V_{sd}} = \frac{e^2}{h\pi} \int_{-\pi}^{\pi} d\tilde{k}_y \sum_{m,n=m_{\min}}^{m_{\max}} |\tilde{S}_{m,0;n,1}(E_F)|^2, \quad (5.51)$$

where G is the conductance, I_a is the current through one period, and $\tilde{k}_y = k_y a$.

5.3 Single-level approximation

In this section our general formalism is specialized to the case of resonant tunneling through a single isolated level. We assume the validity of a single-level approximation for the R -matrix with the resonant level λ :

$$\Omega = \sum_l \frac{\vec{\alpha}^l \otimes \vec{\alpha}^l}{E - E_l} \approx \frac{\vec{\alpha}^\lambda \otimes \vec{\alpha}^\lambda}{E - E_\lambda}, \quad (5.52)$$

where the vectors $\vec{\alpha}^l$ are given by

$$(\vec{\alpha}^l)_{m,s} = \frac{i\hbar}{2\sqrt{m^* \mathcal{L}}} k_{z;m}^{1/2} v_l^m(-1^s \mathcal{L}), \quad (5.53)$$

and \otimes denotes the dyadic product. The approximation Eq. (5.52) holds when the separation of the Wigner-Eisenbud energies is much larger than the width of the resonant level, so that we can neglect the influence of the nonresonant levels. With standard procedures described in the first of Ref. [31] [see also Eq. (5.69)] we then find

$$\frac{1}{1 + i\Omega} = 1 - i \frac{\vec{\alpha}^\lambda \otimes \vec{\alpha}^\lambda}{E - E_\lambda - \Delta + i\frac{\Gamma}{2}}, \quad (5.54)$$

with

$$\frac{\Gamma}{2} + i\Delta = \frac{-\hbar^2}{4m^* \mathcal{L}} \sum_m k_{z;m} \left[v_\lambda^m(-\mathcal{L})^2 + v_\lambda^m(\mathcal{L})^2 \right]. \quad (5.55)$$

The relevant current transmission coefficients are thus

$$|\tilde{S}_{m,0;m',1}|^2 = \frac{\Gamma_{m,\lambda}^0 \Gamma_{m',\lambda}^1}{(E - E_\lambda - \Delta)^2 + \Gamma^2/4}, \quad (5.56)$$

with

$$\Gamma_{m,\lambda}^s = \frac{\hbar^2}{2m^* \mathcal{L}} k_{z;m} v_\lambda^m (-1^s \mathcal{L})^2. \quad (5.57)$$

Here m and m' are restricted to modes that propagate in the z direction. The denominator in Eq. (5.56) corresponds to a Breit-Wigner distribution with a width given by Γ . Such a distribution follows from the general R -matrix theory [31] and can also be derived in other approaches [90]. In our specialization of the R -matrix theory to laterally modulated tunneling barriers the intensity of the Bragg reflections is described by the enumerator and can be determined from the Wigner-Eisenbud functions. In addition to Ref. [34] there is a shift Δ between the position of the resonances and the Wigner-Eisenbud energy E_λ in the single-level approximation. As Eq. (5.55) shows, this shift arises from the components of the Wigner-Eisenbud functions with complex $k_{z;m}$ which are bound to the barrier region. If we neglect those components we can directly compare our results with Eq. (5) of Refs. [34]. First, we identify the lead index i with our s and the channel index c with m . In agreement with Ref. [34] it results that $|\Gamma| = \sum_m (\Gamma_{m,\lambda}^0 + \Gamma_{m,\lambda}^1)$. Second, we identify $y_{c\lambda}^i \rightarrow \sqrt{\hbar^2/(4m^* \mathcal{L})} v_m(-1^s \mathcal{L})$ and compare Eq. (5.57) with Eq. (6) from Ref. [34]. It directly follows that the penetration factor P_c^i defined in the latter equation is exactly equal to 1 for the considered type of systems. In Ref. [34] the penetration factor has been estimated to be smaller than or equal to 1. In Sec. 5.4.1 it is shown that our formalism directly applies to single tunneling structures which are the subject of Ref. [34].

5.4 Laterally modulated barrier

To explore the features of our R -matrix formalism we consider transport through a barrier with a periodic lateral structure. It will be shown that this system has interesting resonant and nonresonant features in the classically allowed regime. As a specific example we choose a rectangular barrier in the z direction of height V_0 and width $2d$ with a superimposed Kronig-Penney-type potential in the y direction with a modulation strength V_m (see Fig. 5.1)

$$V(z, y) = [\Theta(z + d) - \Theta(z - d)] [V_0 + 2V_m \Theta(|y| - s)], \quad (5.58)$$

for $-a/2 < y \leq a/2$ and $V(z, y + a) = V(z, y)$ and $s < a/2$ (see Fig. 5.1). We work with the boundary condition of vanishing derivative of the Wigner-Eisenbud functions at $\mathcal{L} = d$. The potential is then separable in the interval $[-\mathcal{L}, \mathcal{L}]$, and the

Wigner-Eisenbud functions take the product form

$$\chi_l(z, y) = \chi_{k_y, \nu, n_z}(z, y) = \sqrt{\frac{2}{(1 + \delta_{n_z, 0})}} \cos \left[(z + d) \frac{n_z \pi}{2d} \right] g_{k_y, \nu}(y), \quad (5.59)$$

where n_z is the number of nodes in the z direction. $g_{k_y, \nu}$ are the eigenfunctions of the Kronig-Penney Hamiltonian

$$\left[-\frac{\hbar^2}{2m^*} \frac{\partial^2}{\partial y^2} + 2V_m \Theta(|y| - s) - E_{k_y, \nu}^{k.p.} \right] g_{k_y, \nu}(y) = 0. \quad (5.60)$$

The Wigner-Eisenbud eigenenergies are

$$E_{k_y, \nu, n_z} = E_{k_y, \nu}^{k.p.} + \frac{\hbar^2}{2m^*} \left(\frac{n_z \pi}{2d} \right)^2 + V_0 = \left[\epsilon_{k_y, \nu}^{k.p.} + \frac{n_z^2}{4} + \bar{V}_0 \right] E_n, \quad (5.61)$$

where $\epsilon^{k.p.}$ and \bar{V}_0 are normalized to the energy $E_n = \hbar^2/(2m^*)(\pi/d)^2$. Note, that the Wigner-Eisenbud functions are independent of V_0 which enters the R -matrix only through a shift of the Wigner-Eisenbud energies as described in Eq. (5.61).

We first consider the situation of strong modulation that we define through the absence of a markable k_y dispersion of the $\epsilon^{k.p.}$ (see the inset in Fig. 5.3). In this limit of vanishing overlap of the wave functions in the y direction we can write

$$g_{k_y, \nu}(y) \approx g_{n_y}(y) = \frac{1}{\sqrt{s}} \sin \left[\frac{(n_y + 1)\pi}{2s} (y + s) \right], \quad (5.62)$$

in the potential well ($|y| < s$) and $g_{k_y, \nu}(a > |y| > s) = 0$. Here $n_y \geq 0$ is the number of nodes in the y -direction. For the Wigner-Eisenbud energies we obtain

$$\epsilon_{k_y, \nu, n_z} \approx \epsilon_{n_y, n_z} = \frac{1}{4} \left(\frac{d^2}{s^2} (n_y + 1)^2 + n_z^2 \right) + \bar{V}_0, \quad (5.63)$$

which agree with the positions of the energy bands in the inset of Fig. 5.3, and with the Wigner-Eisenbud energies plotted with symbols in this figure. For $V_0 = 0$ a sequence of point contacts in the y direction with a width of $2s$ and a lateral distance of a results. For $V_0 \gg V_m$ one obtains a laterally modulated tunneling barrier. The change of the transport properties in the transition between these extremes is demonstrated in Fig. 5.3. For $V_0 = 0$ we find a quantized conductance in units of e^2/h , which is the signature of a single point contact [16]. As expected, when the Fermi energy reaches one energy out of the series of Wigner-Eisenbud energies with $n_z = 0$, the plateau is changed. With increasing V_0 the plateaus of the conductance decrease and single conductance peaks develop. Note that in Fig. 5.3 on the x-axis we plot the energy $E_F - V_0$ which is the part of the kinetic energy of the incident electrons that exceeds the potential minimum of the barrier. On this energy scale the position of the peaks is independent of V_0 . The open symbols in

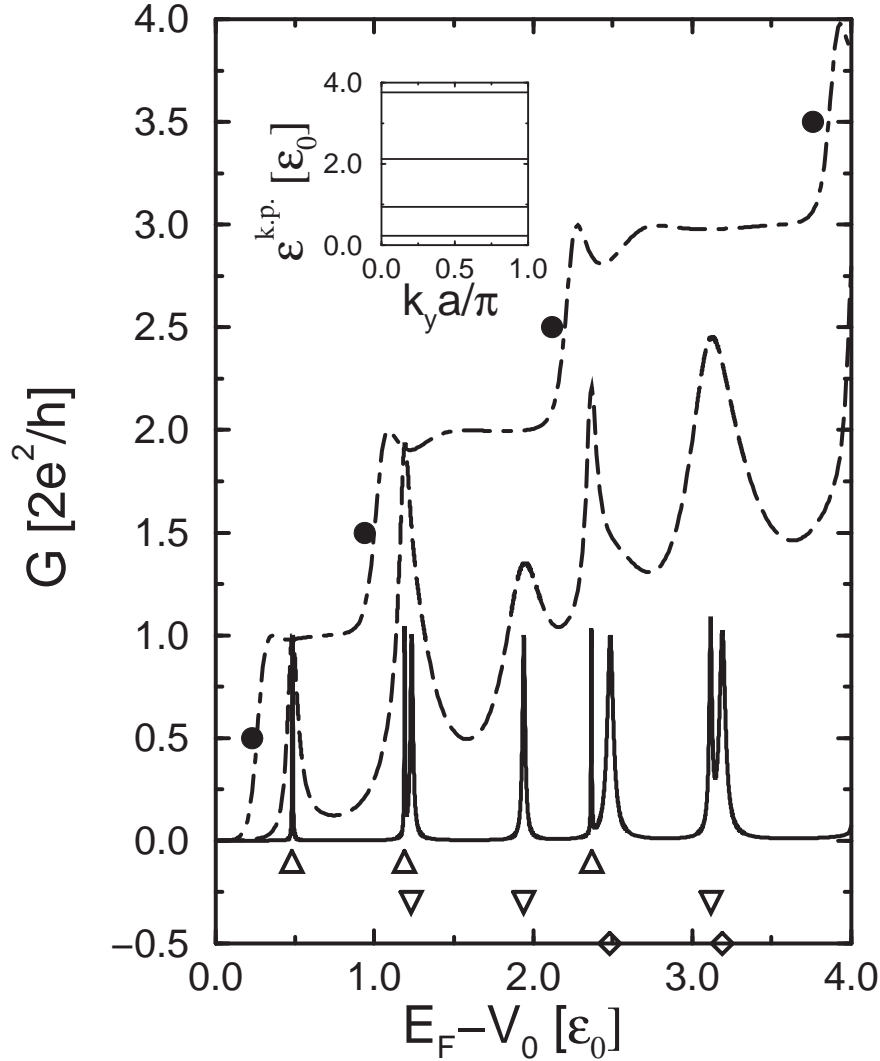


Figure 5.3: Conductance vs chemical potential for a structure with $a = 4d$ and $s = a/4$. The potential modulation is $\bar{V}_m = 50$, and \bar{V}_0 varies between 0 (dot-dashed line), 2 (dashed line), and 16384 (solid line). Inset: $\epsilon_{k_y, \nu}^{k.p.}$ for the first four degenerate Bloch bands ($\nu = 1, 2, 3, \text{ and } 4$) in the first Brillouin zone. The position of the Wigner-Eisenbud energies for $n_z = 0$ (full circles), $n_z = 1$ (triangles up), $n_z = 2$ (triangles down), and $n_z = 3$ (diamonds).

Fig. 5.3 mark the positions of the Wigner-Eisenbud energies for $n_z \neq 0$ which are found to be identical with the energies of the conductance peaks. Further increasing V_0 , only the conductance peaks remain, and their peak value goes to $2e^2/h$.

The mismatch of the wave functions inside and outside the barrier can provide an intuitive explanation for the conductance peaks at large V_0 . Outside the barrier the kinetic energy of the electrons is drastically enhanced by V_0 . This generally means a small lateral momentum inside the barrier and a large lateral momentum outside the barrier. As consequence, the overlap of the wave function in the y direction at the interfaces ($z = \pm d$) becomes small and the electron wave is reflected. Neglecting again the overlap of the wave functions in the y direction we describe the resonant states as standing waves in the interval $-d \leq z \leq d$,

$$\Psi_{res} \approx \frac{1}{\sqrt{sd}} \sin \left[\frac{(n_y + 1)\pi}{2s}(y + s) \right] \sin \left[\frac{(n_z + 1)\pi}{2d}(z + d) \right], \quad (5.64)$$

within the potential well ($|y| < s$). The energies of these states are

$$\epsilon_{res} = \frac{1}{4} \left(\frac{d^2}{s^2} (n_y + 1)^2 + (n_z + 1)^2 \right) + \bar{V}_0. \quad (5.65)$$

The resonance energies ϵ_{res} describe well the position of the resonances in Fig. 5.3 and correspond to the Wigner-Eisenbud energies given in Eq. (5.63) for $n_z \neq 0$.

An analytical description of the considered conductance peaks in the classically allowed transport regime will demonstrate that there are qualitative differences to the resonant tunneling peaks described in Sec. 5.3: We start by writing Ω as

$$\begin{aligned} \Omega_{m,s;m',s'} &\approx \frac{k_{z;m}^{1/2} v_{N_y}^m k_{z;m'}^{1/2} v_{N_y}^{m'}}{m^*} \rho_{s;s'}(E - E_{N_y}) \\ &= A_0 \vec{\alpha}_0 \otimes \vec{\alpha}_0 + A_1 \vec{\alpha}_1 \otimes \vec{\alpha}_1, \end{aligned} \quad (5.66)$$

with

$$\rho_{s;s'}(E - E_{N_y}) = -\frac{\hbar^2}{4\mathcal{L}} \sum_{n_z} \frac{\phi_{n_z}(-1^s \mathcal{L}) \phi_{n_z}(-1^{s'} \mathcal{L})}{(E - E_{N_y}) - E_{n_z}}, \quad (5.67)$$

$$(\vec{\alpha}_i)_{m,s} = -1^{is} k_{z;m}^{1/2} v_{N_y}^m / (m^*)^{1/2}, \quad (5.68)$$

and $2A_i = \rho_{0;0} + (-1)^i \rho_{0;1}$, $i = 0$ and 1 . In the first step of Eq. (5.66) we write the Wigner-Eisenbud functions [see Eq. (5.10)] as a product $v_m^l(z) = v_{n_y}^m \phi_{n_z}(z)$ with the eigenenergies $E_l = E_{n_y} + E_{n_z}$. We thus assume a general separable potential $V(z, y) = V(z, y + a)$ with vanishing overlap in the y -direction and wave functions characterized by the number of nodes n_y in the y direction and n_z in the z direction. We further assume a strong quantization in the y direction, so that we can expect, for an energy range $E \approx E_{N_y} + V_0$, that only Wigner-Eisenbud levels with $n_y = N_y$ contribute. The second step of Eq. (5.66) is correct for a barrier that is symmetric

with respect to the plane $z = 0$, so that $\rho_{0;0} = \rho_{1;1}$. With the scalar product $(\vec{\alpha}_0, \vec{\alpha}_1) = 0$ it is easy to show that

$$\frac{1}{1 + i\Omega} = 1 - \frac{iA_0\vec{\alpha}_0 \otimes \vec{\alpha}_0}{1 + i(\vec{\alpha}_0\vec{\alpha}_0)A_0} - \frac{iA_1\vec{\alpha}_1 \otimes \vec{\alpha}_1}{1 + i(\vec{\alpha}_1\vec{\alpha}_1)A_1}. \quad (5.69)$$

The square of the current transmission matrix can therefore be expressed as a product

$$|\tilde{S}_{m,0;m',1}|^2 = \mathcal{F}(m, m'; N_y)\mathcal{G}(E; N_y). \quad (5.70)$$

Here

$$\mathcal{F}(m, m'; N_y) = 4k_{z;m}(v_{N_y}^m)^2 k_{z;m'}(v_{N_y}^{m'})^2 / u^2 \quad (5.71)$$

is a normalized function [$\sum_{m,m'} \mathcal{F}(m, m'; N_y) = 1$] with u given by the scalar product

$$(\vec{\alpha}_0, \vec{\alpha}_0) = \sum_{m,s} (\vec{\alpha}_0)_{m,s}^2 = u + iv = (\vec{\alpha}_1, \vec{\alpha}_1). \quad (5.72)$$

The function \mathcal{F} involves only modes with real $k_{z;m'}$ and describes the intensity of the Bragg reflexes in dependence of their order. Further,

$$\mathcal{G}(E; N_y) = \left| \frac{A_0 u}{1 - A_0 v + iA_0 u} - \frac{A_1 u}{1 - A_1 v + iA_1 u} \right|^2 \quad (5.73)$$

yields the energy distribution. In Eq. (5.73) resonant transport can occur if either the first factor with A_0 or the second factor with A_1 shows resonant behavior.

The case of the single-level approximation can be recovered assuming that only one relevant Wigner-Eisenbud level $\lambda = (N_z, N_y)$ contributes, and

$$\rho_{s;s'}(E - E_\lambda) \approx -\frac{\hbar^2}{4\mathcal{L}} \frac{\phi_{N_z}(-1^s \mathcal{L})\phi_{N_z}(-1^{s'} \mathcal{L})}{E - E_\lambda}, \quad (5.74)$$

with $E_\lambda = E_{N_y} + E_{N_z}$. Depending on the parity of the state ϕ_{N_z} either A_0 or A_1 vanishes. We obtain the Breit-Wigner distribution given in Eqs. (5.56) and (5.57).

However, the conductance peaks of Fig. 5.3 in the classically allowed transport regime show qualitative differences from the resonant tunneling resonances with a Breit-Wigner distribution. To demonstrate this point we evaluate the sum over n_z in Eq. (5.67), which can be done analytically in our simple system using the z -dependent factor of the Wigner-Eisenbud functions in Eq. (5.59). We find

$$\Omega_0 = A_0 u = -\frac{\sum_m k_{z;m}(v_{N_y}^m)^2}{k_b} \cot(k_b d) \quad (5.75)$$

and

$$\Omega_1 = A_1 u = \frac{\sum_m k_{z;m}(v_{N_y}^m)^2}{k_b} \tan(k_b d), \quad (5.76)$$

where

$$k_b d = \pi \sqrt{\epsilon - \epsilon_{N_y} - \bar{V}_0}. \quad (5.77)$$

[Note the normalization of Eq. (5.61), $E_{N_y} = \epsilon_{N_y} E_n$). For large V_0 we can write $(k_{z;m}d/\pi)^2 \approx \hat{V}_0$, and since $k_{z;m}$ is real it follows that v is equal to zero and therefore vanishes in Eqs. (5.72) and (5.73). In the limit $\hat{V}_0 \rightarrow \infty$ the factor in front of the cotangent (tangent) diverges in Eq. (5.75) [Eq. (5.76)]. Therefore, outside a small interval around the zeros of either tangent or cotangent $\mathcal{G}(E, N_y)$ vanishes in accord with Eq. (5.73). Only close to the zeros of $\tan(k_b d)$ can the function Ω_1 become small and $\mathcal{G}(E, N_y)$ approach unity. (As will be shown later, for the zeros with $N_z = 0$ the function Ω_1 does not become small.) An analogous finding results in the zeros of $\cot(k_b d)$. The zeros of \tan and \cot are found at $2k_b d = N_z \pi$, $N_z = 0, 1, 2, \dots$, which, according to Eq. (5.77), corresponds to energies

$$\epsilon_0 = \epsilon_{N_y} + \frac{N_z^2}{4} + \bar{V}_0. \quad (5.78)$$

Again assuming a y dependence of the Wigner-Eisenbud functions as in Eq. (5.62), it follows that $\epsilon_{N_y} = (d^2/s^2)(N_y + 1)^2/4$. Equation (5.78) then represents the same condition as Eq. (5.63) which does not describe the conductance peaks correctly. To show that our analytical approach nevertheless reproduces the correct condition of Eq. (5.65), and to calculate the shape of the conductance peaks, we write $\epsilon = \delta\epsilon + \epsilon_0$, and for small $\delta\epsilon$ and $N_z \neq 0$ obtain the expression

$$\Omega_{0/1} = \frac{2\sqrt{V_0}}{N_z} \tan(\pi \delta\epsilon/N_z) \quad (5.79)$$

for Ω_0 and Ω_1 , which goes to zero for $\delta\epsilon \rightarrow 0$. Therefore, conductance peaks can be expected around these ϵ_0 . However, for $N_z = 0$ one obtains $\Omega_{0/1} = \pi V_0$, which diverges uniformly around ϵ_0 . This means that $\mathcal{G}(E, N_y)$ and the conductance vanish around the ϵ_0 with $N_z = 0$ in Eq. (5.78). We thus obtain Eq. (5.65) as a condition for the resonant tunneling peaks. From Eq. (5.79) it follows directly that

$$\mathcal{G}(\delta\epsilon, N_y, N_z \neq 0) = \left[1 + \frac{4V_0}{N_z^2} \tan^2(\pi \delta\epsilon/N_z) \right]^{-1}. \quad (5.80)$$

In contrast to the Breit-Wigner distribution in resonant tunneling, for the resonances in the classically allowed region we obtain a transcendental distribution.

The conductance follows from Eq. (5.51). Since there is no overlap of the wave functions in the y direction, the integral $\int_{-\pi}^{\pi} d\tilde{k}_y$ reduces to 2π , and it is found that

$$G = \frac{2e^2}{h} \mathcal{G}(\delta\epsilon, N_y, N_z) \quad (5.81)$$

in the vicinity of $\epsilon = \epsilon_{N_y} + \epsilon_{N_z}$. This formula reproduces the numerical results to a great precision (deviations are not visible in the graphical resolution of Fig. 5.3). The maximum of the conductance peaks of $2e^2/h$ results from the fact that the maximal value of $\mathcal{G}(\delta\epsilon, N_y, N_z)$ is 1. The peaks shown in Fig. 5.3 are very narrow, so that

$\epsilon \ll 1$, and in $\tan^2(\alpha \delta \epsilon) \approx (\alpha \delta \epsilon)^2 [1 + (2/3)(\alpha \delta \epsilon)^2 + \dots]$, we can neglect $\alpha = \pi/N_z$, the fourth order term in e . This leads back to a Breit-Wigner distribution like Eq. (5.56) with $\Delta = 0$ and $\Gamma/\epsilon_0 = N_z^2/(\pi\sqrt{V_0})$. Using Eq. (5.57) we find, in the single-level approximation of Sec. 5.3, $\Gamma/\epsilon_0 = \sqrt{V_0}/\pi$. This expression predicts that the linewidth grows with V_0 , that it is independent of N_z , and also includes a conductance peak at $N_z = 0$. These predictions are in clear contradiction to the numerical results, and show the failure of the single-level approximation. We thus state that in contrast to the tunneling regime isolated resonances in the classically allowed regime generally cannot be described in a single-level approximation. Though resonances might have a shape similar to a Breit-Wigner distribution in general, their shape deviates, and the width calculated in the single level approximation is wrong.

The energy dependence of the conductance at weak lateral modulation is shown in Fig. 5.4 with $\bar{V}_m = 0.2$. The small modulation strength is defined through the band structure $\epsilon_{k_y, \nu}^{k.p.}$, which is depicted in Fig. 5.5: A nearly free-electron dispersion with energy gaps at the edge and in the center of the first Brillouin zone results for $\nu \geq 2$. The lowest subband $\nu = 1$ is flat. For vanishing V_0 only the lowest plateau in the conductance with $G = 2e^2/h$ is developed. Higher plateaus are very strongly washed out. As expected, the change in the plateaus coincides with the position of the Wigner-Eisenbud bands for $n_z = 0$. Broader energy bands lead to softer transitions between the less-developed plateaus. With increasing V_0 the plateaus vanish and broad maxima develop, first at Wigner-Eisenbud energy bands with $\nu = 1$. For very large V_0 the conductance maxima develop a fine structure that directly reflects the density of all Wigner-Eisenbud states with $n_z \neq 0$: The conductance vanishes in the band gaps of the Wigner-Eisenbud spectrum, and develops van Hove singularities at the band edges.

5.4.1 Transport through a single structure

In this section we want to generalize our formalism to systems consisting of a single lateral structure. The situation is illustrated in Fig. 5.6. In Fig. 5.6(b) a single basis structure of length $L_y = a$ is depicted. In the center of the basis there is a quantum system QS which is restricted to the range $-s/2 \leq y \leq s/2$. Outside this interval there is a barrier which is homogeneous in the y direction. In Fig. 5.6(a) a system with $N = 3$ repetitions of the basis and length $L_y = Na$ is shown. In both cases we require periodic boundary conditions at $y = \pm L_y/2$ so that the allowed wave vectors are $k_y^n = n2\pi/L_y$ with $n = 0, \pm 1, \pm 2, \dots$. By definition the primitive lattice vector of the periodic system is given by $k_0 = 2\pi/a = N\pi/L_y$. The first Brillouin zone defined by $-k_0/2 < k_y \leq k_0/2$ thus contains N elements k_y^i $-N/2 < i \leq N/2$. The ideal periodic structure is obtained in the limit $L_y \rightarrow \infty$ with $N = L_y/a \rightarrow \infty$, where a is constant. The single structure results in the limit $L_y \rightarrow \infty$ and $N = 1$. The length $L_y = a$ is increased by keeping a QS which is between $-s/2 < y < s/2$ constant, and extending the unstructured barrier for $L_y/2 \geq |y| \geq s/2$. For $N = 1$ we only have one element in the first Brillouin zone with $i = 0$ and thus $k_y = 0$.

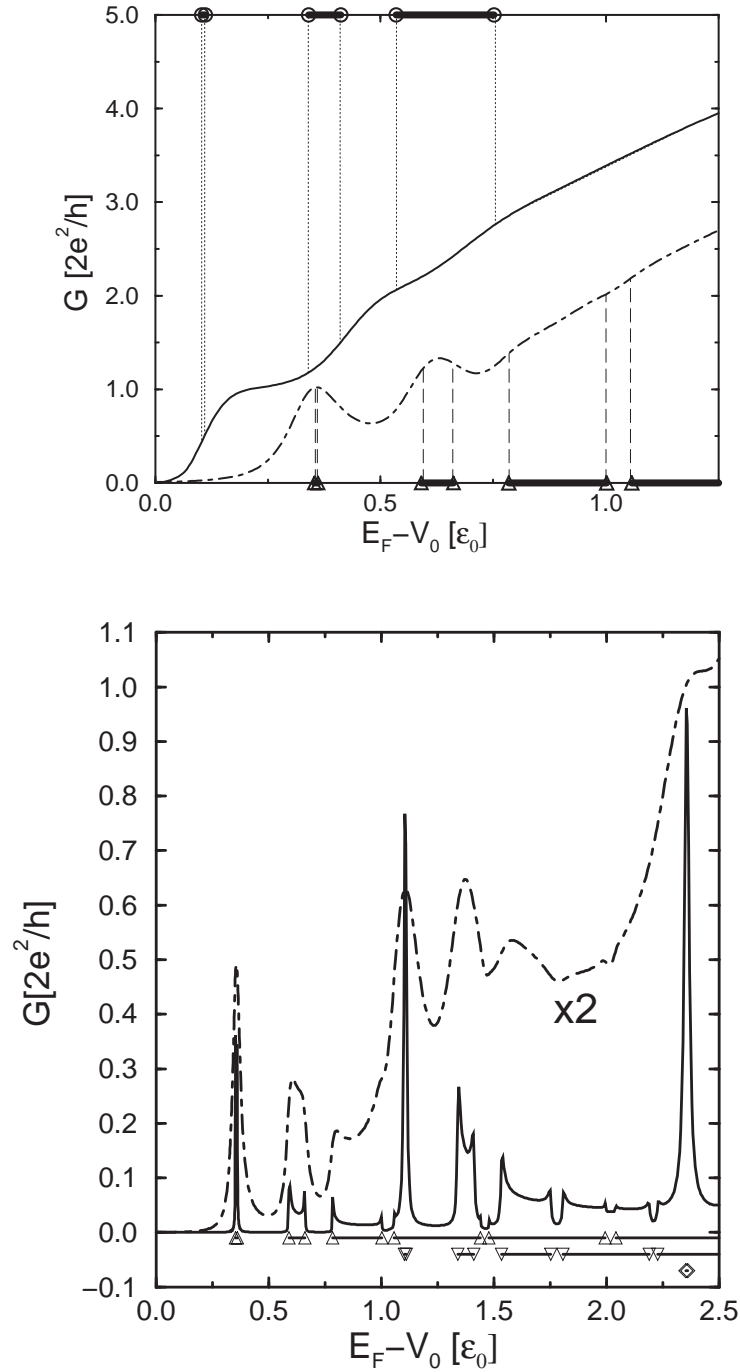


Figure 5.4: Conductance vs the chemical potential at $T = 0$ for a structure with $a = 4d$ and $s = a/4$ with $\bar{V}_m = 0.2$. In the upper part, $\bar{V}_0 = 0$ (solid line) and 4 (dash-dotted line). In the lower part $\bar{V}_0 = 64$ (dash-dotted line, values must be multiplied by 2) and 16384 (solid line). The extent of the energy bands $\epsilon_{k_y, \nu}^{k.p.} + n_z^2/4$ is plotted for $n_z = 0$ (circles, upper part for $\nu = 1, 2, \text{ and } 3$), $n_z = 1$ (triangles up, upper and lower parts) $n_z = 2$ (triangles down, lower part), and $n_z = 3$ (diamonds, lower part).

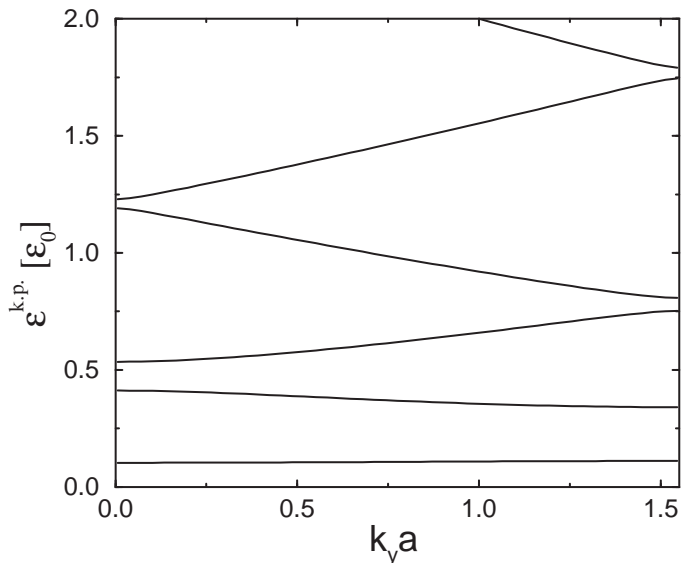


Figure 5.5: The lowest-energy bands $\epsilon_{k_y, \nu}^{k.p.}$ in the first Brillouin zone for the structure in Fig. 5.4.

The expansion of the scattering states given in Eq. (5.2) then is

$$\Psi(z, y) = \Psi^{L/R;n}(z, y) = \sum_m w_m^{L/R;n}(z) e^{i(2\pi/L)my} . \quad (5.82)$$

$\Psi^{L/R;n}(z, y)$ derives from an incoming plane wave from the left-/right reservoir with the momentum in the y direction of $k_y^n = k_{y;n} = n2\pi/L_y$. We can adopt all results for $k_y = 0$ in Sec. 5.1. In Sec. 5.2 we have to perform the replacement $\int d\tilde{k}_y \rightarrow 2\pi \sum_{\tilde{k}_y} \delta_{\tilde{k}_y, 0}$ in Eq. (5.51) to obtain

$$G = \frac{I}{V_{sd}} = \frac{2e^2}{h} \sum_{m,n=m_{min}}^{m_{max}} |\tilde{S}_{m,0;n,1}|^2 . \quad (5.83)$$

5.5 Summary

We derived a theory in the R -matrix formalism that is applicable to multidimensional mesoscopic semiconductor nanostructures, including nonresonant transport and transport in the classically allowed regime. As an example, coherent transport through a tunneling barrier with a lateral periodic modulation was discussed. For high barriers, resonances result at strong lateral modulation in the classical transport regime that show qualitative differences from resonant tunneling peaks. At weak lateral modulation the mini-band structure of the lateral dispersion can be resolved in the dc transport and van Hove singularities occur.

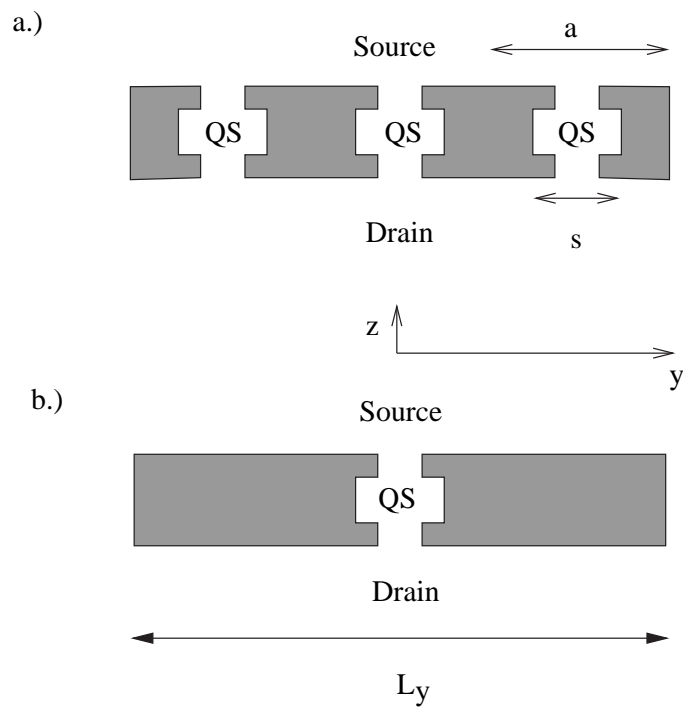


Figure 5.6: Scattering potentials.

Chapter 6

Conclusions

We have analyzed open quantum semiconductor nanostructures in non-interacting particle approximation at very low temperatures. We have provided a quantum mechanical model predicting the charge distribution in the scattering region and the capacitance of this region as well as the tunneling currents between source and drain contacts.

The scattering wave functions are calculated in the R-matrix formalism. To consider the effect of the charge accumulation in the quantum system, we have performed fully self-consistent calculations in the mean-field approximation taking properly into account the open nature of the system. Exploiting the analytical properties of the scattering matrix we find its resonant poles and we count exactly the contribution of the quasi-bound states to the charge density.

For characterizing the transport in the mesoscopic structures we have calculated the tunneling current and the capacitance of the quantum system. The tunneling current is evaluated using the Landauer-Büttiker formalism. For the capacitance, we proposed a new model which takes into account the openness of the system and the presence of the contacts embedding the system. Based on our self-consistent calculations, we are able to perform a detailed analysis of the interaction between the quantum system and the contact reservoir. The capacitance model has been applied to describe two types of quantum heterostructures.

First we analyze an electron system coupled only with a probe (contact) and separated from another one by a blocking barrier. Decreasing this coupling by increasing applied bias a broadened step in the C-V characteristic is obtained. We find that the quasi-bound state that exists in the nearly closed system develops at the transition to the open system into a separate type of resonance with distinct characteristics: in contrast to the quasi-bound state i) it is localized in the space between the probe and the isolated quantum system, ii) its energy lies in the classically allowed regime, and iii) its line shape is strongly asymmetric. Excellent quantitative agreement shows that this transition is seen in capacitance experiments on a MIS-type semiconductor heterostructure: the measured step in the C-V-characteristic associated with the formation of a field induced two dimensional electron gas is due

to the formation of this asymmetric resonance.

For an open quantum system in contact with two reservoirs our model can also describe the capacitance when a current flows through the structure. The capacitance presents oscillations with maxima every time a (Fabry-Perot like) resonance crosses the chemical potential in the source reservoir. At the same biases the conductance presents shoulders.

We have extended the R-matrix formalism to general multidimensional mesoscopic structures, including non resonant transport and transport in the classically allowed regime. We have analyzed a tunneling barrier with a lateral periodic modulation. For strong modulation we find a transition from the known quantized conductivity in e^2/h of a single point contact for small average barrier height, to a series of resonant peaks of height e^2/h for high barriers. We have shown that in the classically allowed regime, the resonant peaks only approximately exhibit the usual algebraic Breit-Wigner distribution. Instead they follow a distribution described by a transcendental tangent function. At weak modulation we have demonstrated that the miniband structure of the lateral dispersion can be resolved in dc transport in the forward direction in the limit of large average barrier height.

Appendix A

Hartree-Fock equations

The *Hartree-Fock approximation* [91] consists in the assumption of the many-particle wave function as Slater determinant

$$\Psi(\mathbf{r}_1, \mathbf{r}_2, \dots, \mathbf{r}_N) = \frac{1}{\sqrt{N!}} \sum_{P \in S_N} (-1)^{\chi_P} \Phi_{P(1)}(\mathbf{r}_1) \Phi_{P(2)}(\mathbf{r}_2) \dots \Phi_{P(N)}(\mathbf{r}_N), \quad (\text{A.1})$$

where P is a permutation of N numbers, from the total possible permutations S_N , χ_P is the parity of the permutation P and $\Phi_\alpha(\mathbf{r})$ is the one-particle wave function, which will be determined through variational calculations. The form (A.1) has the correct symmetry: the wave function changes sign, when the position of two particle is interchanged,

$$\Psi(\dots, \mathbf{r}_k, \dots, \mathbf{r}_j, \dots) = -\Psi(\dots, \mathbf{r}_j, \dots, \mathbf{r}_k, \dots), \quad (\text{A.2})$$

which is a general statement of the Pauli exclusion principle for fermions. An important special case is that the wave function vanishes if the two coordinates are equally. We will use further the "bra-ket" notations:

$$\langle \mathbf{r} | \alpha \rangle = \Phi_\alpha(\mathbf{r}) \quad (\text{A.3})$$

so that we can write

$$|\Psi\rangle = \frac{1}{\sqrt{N!}} \sum_{P \in S_N} (-1)^{\chi_P} |\alpha_{P(1)}\rangle^{(1)} |\alpha_{P(2)}\rangle^{(2)} \dots |\alpha_{P(N)}\rangle^{(N)}, \quad (\text{A.4})$$

where $|\alpha_{P(i)}\rangle^{(i)}$ represents the one-particle state of the electron i . α is a general notation for the quantum numbers set which characterizes the one-particle state.

From the quantum mechanics it is known that for a given Hamiltonian H the energy functional

$$E = \frac{\langle \Psi | H | \Psi \rangle}{\langle \Psi | \Psi \rangle} \quad (\text{A.5})$$

has an absolute minimum for the ground state $|\Psi_0\rangle$. If one does not know the groundstate, then we choose a family of kets that depends on a certain number of

parameters $\alpha_1, \dots, \alpha_N$. We calculate the mean value of the Hamiltonian H and we minimize it with respect to the parameters α_i . This is the *variational method*.

If we want to count only the interaction between pair of electrons, the Hamiltonian H has two components $H = H_0 + H_1$. H_0 is the Hamiltonian of the non-interacting particles,

$$H_0 = \sum_{j=1}^N h(\mathbf{r}_j) = \sum_{j=1}^N \left[-\frac{\hbar^2}{2m^*} \Delta_j + V_{ext}(\mathbf{r}_j) \right], \quad (\text{A.6})$$

with $V_{ext}(\mathbf{r}_j)$ the potential produced by external sources (i. e. heterostructure interfaces, impurities, etc.) which acts on the position \mathbf{r}_j and does not depend on the number of electrons in the system. H_1 counts for the pair interactions and it is written for the Coulomb interaction as

$$H_1 = \frac{1}{2} \sum_{\substack{i,j=1 \\ j \neq i}}^N u(\mathbf{r}_i, \mathbf{r}_j) = \frac{1}{2} \sum_{\substack{i,j=1 \\ j \neq i}}^N \frac{e^2}{4\pi\epsilon_0\epsilon_r |\mathbf{r}_j - \mathbf{r}_i|}, \quad (\text{A.7})$$

where $1/2$ prevents double counting of the pair interactions.

We are looking for orthonormalized one-particle wave functions,

$$\langle \alpha_i | \alpha_j \rangle = \delta_{ij}, \quad (\text{A.8})$$

so that the many-particle wave function is also normalized $\langle \Psi | \Psi \rangle = 1$. The functional energy becomes then $E = \langle \Psi | H | \Psi \rangle$.

Let's calculate $\langle \Psi | H_0 | \Psi \rangle$:

$$\begin{aligned} \langle \Psi | H_0 | \Psi \rangle &= \sum_{i=1}^N \langle \Psi | h(\mathbf{r}_i) | \Psi \rangle \\ &= \sum_{i=1}^N \frac{1}{N!} \sum_{P, P' \in S_N} (-1)^{X_P} (-1)^{X_{P'}} \langle \alpha_{P'(N)} | \dots \langle \alpha_{P'(1)} | h(\mathbf{r}_i) | \alpha_{P(1)} \rangle \dots | \alpha_{P(N)} \rangle \\ &= \sum_{i=1}^N \frac{1}{N!} \sum_{P, P' \in S_N} (-1)^{X_P + X_{P'}} \langle \alpha_{P'(N)} | \alpha_{P(N)} \rangle \dots \langle \alpha_{P'(i)} | h(\mathbf{r}_i) | \alpha_{P(i)} \rangle \\ &\quad \dots \langle \alpha_{P'(1)} | \alpha_{P(1)} \rangle \\ &= \sum_{i=1}^N \frac{1}{N!} \sum_{P, P' \in S_N} (-1)^{X_P + X_{P'}} \prod_{j \neq i} \delta_{P'(j)P(j)} \langle \alpha_{P'(i)} | h(\mathbf{r}_i) | \alpha_{P(i)} \rangle, \end{aligned} \quad (\text{A.9})$$

where we have denoted explicitly by (i) as superscript the single particle Hilbert space associated to the particle i . The δ 's which appear in the last relation are a consequence of the orthogonality of the one-particle wave functions and establish that the permutation P' and P have to coincide for every $j \neq i$. In turn they have to coincide also for the last position, i.e. $P'(i) = P(i)$, so that $P = P'$ and

$$\langle \Psi | H_0 | \Psi \rangle = \sum_{i=1}^N \frac{1}{N!} \sum_{P \in S_N} \langle \alpha_{P(i)} | h(\mathbf{r}_i) | \alpha_{P(i)} \rangle. \quad (\text{A.10})$$

When P runs through all $N!$ possible permutations, then $P(i)$ takes all the values from 1 to N , and for every fixed value i all other positions are free to permute $(N-1)!$ times. So we have

$$\langle \Psi | H_0 | \Psi \rangle = \sum_{i=1}^N \frac{(N-1)!}{N!} \sum_{\tau=1}^N \langle \alpha_\tau | h(\mathbf{r}_i) | \alpha_\tau \rangle^{(i)} = \sum_{\tau=1}^N \langle \alpha_\tau | h(\mathbf{r}) | \alpha_\tau \rangle. \quad (\text{A.11})$$

where we have used the property that the matrix element

$$\langle \alpha_\tau | h(\mathbf{r}_i) | \alpha_\tau \rangle^{(i)} = \int d^3 r_i \Phi_{\alpha_\tau}^*(\mathbf{r}_i) h(\mathbf{r}_i) \Phi_{\alpha_\tau}(\mathbf{r}_i) = \int d^3 r_i \Phi_{\alpha_\tau}(\mathbf{r}_i) h(\mathbf{r}_i) \Phi_{\alpha_\tau}^*(\mathbf{r}_i) \quad (\text{A.12})$$

does not depend on the particle index i (it is defined as an integral over the space variable \mathbf{r}_i). In consequence, the total energy corresponding to the Hamiltonian H_0 is a simple sum of the one-particle state energies.

We can rewrite Eq. (A.11) as

$$\langle \Psi | H_0 | \Psi \rangle = \sum_{\tau=1}^N \int d^3 r \Phi_{\alpha_\tau}^*(\mathbf{r}) h(\mathbf{r}) \Phi_{\alpha_\tau}(\mathbf{r}) = \sum_{\tau=1}^N \int d^3 r \Phi_{\alpha_\tau}(\mathbf{r}) h(\mathbf{r}) \Phi_{\alpha_\tau}^*(\mathbf{r}) \quad (\text{A.13})$$

where we have used that one-particle Hamiltonian h is Hermitian.

We will proceed analogously for $\langle \Psi | H_1 | \Psi \rangle$:

$$\begin{aligned} \langle \Psi | H_1 | \Psi \rangle &= \sum_{\substack{i,j=1 \\ j \neq i}}^N \langle \Psi | u(\mathbf{r}_i, \mathbf{r}_j) | \Psi \rangle \\ &= \frac{1}{2} \sum_{\substack{i,j=1 \\ j \neq i}}^N \frac{1}{N!} \sum_{P, P' \in S_N} (-1)^{\chi_P} (-1)^{\chi_{P'}} \langle \alpha_{P'(N)} | \dots \langle \alpha_{P'(1)} | u(\mathbf{r}_i, \mathbf{r}_j) | \alpha_{P(1)} \rangle \dots | \alpha_{P(N)} \rangle \\ &= \frac{1}{2} \sum_{i=1}^N \frac{1}{N!} \sum_{P, P' \in S_N} (-1)^{\chi_P + \chi_{P'}} \prod_{k \neq j, i} \delta_{P'(k)P(k)} \langle \alpha_{P'(j)} | \langle \alpha_{P'(i)} | u(\mathbf{r}_i, \mathbf{r}_j) | \alpha_{P(i)} \rangle | \alpha_{P(j)} \rangle. \end{aligned} \quad (\text{A.14})$$

In this case the permutations P and P' have to coincide for $N-2$ elements, so that we have two possibilities a) $P'(i) = P(i)$ and $P'(j) = P(j)$ or b) $P'(i) = P(j)$ and $P'(j) = P(i)$. In the case a) the permutations P and P' are the same, while in the case b) they differ exactly by an interchange of two positions, so that $(-1)^{\chi_P} (-1)^{\chi_{P'}} = -1$. We obtain further

$$\begin{aligned} \langle \Psi | H_1 | \Psi \rangle &= \frac{1}{2} \sum_{\substack{i,j=1 \\ j \neq i}}^N \frac{1}{N!} \sum_{P \in S_N} \left[\langle \alpha_{P(j)} | \langle \alpha_{P(i)} | u(\mathbf{r}_i, \mathbf{r}_j) | \alpha_{P(i)} \rangle | \alpha_{P(j)} \rangle \right. \\ &\quad \left. - \langle \alpha_{P(i)} | \langle \alpha_{P(j)} | u(\mathbf{r}_i, \mathbf{r}_j) | \alpha_{P(i)} \rangle | \alpha_{P(j)} \rangle \right]. \end{aligned} \quad (\text{A.15})$$

When P runs through all the permutations, $P(i)$ takes all the values from 1 to N and $P(j)$ takes all other $(N-1)$ values; all other values for $P(k)$, with $k \neq i, j$ can be permuted in $(N-2)!$ combinations, so that

$$\begin{aligned} \langle \Psi | H_1 | \Psi \rangle &= \frac{1}{2} \sum_{\substack{i,j=1 \\ j \neq i}}^N \frac{(N-2)!}{N!} \sum_{\tau \neq \tau'} \left[\langle \alpha_\tau | \langle \alpha_{\tau'} | u(\mathbf{r}_i, \mathbf{r}_j) | \alpha_{\tau'} \rangle | \alpha_\tau \rangle \right. \\ &\quad \left. - \langle \alpha_{\tau'} | \langle \alpha_\tau | u(\mathbf{r}_i, \mathbf{r}_j) | \alpha_\tau \rangle | \alpha_{\tau'} \rangle \right] \end{aligned} \quad (\text{A.16})$$

The matrix elements are independent on i and j

$$\begin{aligned} \langle \alpha_{\tau'} | \langle \alpha_\tau | u(\mathbf{r}_i, \mathbf{r}_j) | \alpha_\tau \rangle | \alpha_{\tau'} \rangle &= \int d^3 r_j \int d^3 r_i \Phi_{\alpha_{\tau'}}^*(\mathbf{r}_j) \Phi_{\alpha_\tau}^*(\mathbf{r}_i) \frac{e^2}{4\pi\epsilon_0\epsilon_r |\mathbf{r}_i - \mathbf{r}_j|} \\ &\quad \cdot \Phi_{\alpha_\tau}(\mathbf{r}_i) \Phi_{\alpha_{\tau'}}(\mathbf{r}_j) \end{aligned} \quad (\text{A.17})$$

$$\begin{aligned} \langle \alpha_\tau | \langle \alpha_{\tau'} | u(\mathbf{r}_i, \mathbf{r}_j) | \alpha_{\tau'} \rangle | \alpha_\tau \rangle &= \int d^3 r_j \int d^3 r_i \Phi_{\alpha_\tau}^*(\mathbf{r}_j) \Phi_{\alpha_{\tau'}}^*(\mathbf{r}_i) \frac{e^2}{4\pi\epsilon_0\epsilon_r |\mathbf{r}_i - \mathbf{r}_j|} \\ &\quad \cdot \Phi_{\alpha_\tau}(\mathbf{r}_i) \Phi_{\alpha_{\tau'}}(\mathbf{r}_j) \end{aligned} \quad (\text{A.18})$$

so that the sum over $j \neq i$ gives the factor $N(N-1)$ and it results

$$\begin{aligned} \langle \Psi | H_1 | \Psi \rangle &= \frac{1}{2} \sum_{\substack{\tau, \tau'=1 \\ \tau \neq \tau'}}^N \left[\langle \alpha_\tau | \langle \alpha_{\tau'} | u(\mathbf{r}_i, \mathbf{r}_j) | \alpha_{\tau'} \rangle | \alpha_\tau \rangle \right. \\ &\quad \left. - \langle \alpha_{\tau'} | \langle \alpha_\tau | u(\mathbf{r}_i, \mathbf{r}_j) | \alpha_\tau \rangle | \alpha_{\tau'} \rangle \right] \end{aligned} \quad (\text{A.19})$$

which can be written

$$\begin{aligned} \langle \Psi | H_1 | \Psi \rangle &= \frac{1}{2} \sum_{\tau, \tau'=1}^N \int d^3 r \int d^3 r' \left[\Phi_{\alpha_\tau}^*(\mathbf{r}) \Phi_{\alpha_{\tau'}}^*(\mathbf{r}') \frac{e^2}{4\pi\epsilon_0\epsilon_r |\mathbf{r} - \mathbf{r}'|} \Phi_{\alpha_{\tau'}}(\mathbf{r}') \Phi_{\alpha_\tau}(\mathbf{r}) \right. \\ &\quad \left. - \Phi_{\alpha_{\tau'}}^*(\mathbf{r}) \Phi_{\alpha_\tau}^*(\mathbf{r}') \frac{e^2}{4\pi\epsilon_0\epsilon_r |\mathbf{r} - \mathbf{r}'|} \Phi_{\alpha_{\tau'}}(\mathbf{r}') \Phi_{\alpha_\tau}(\mathbf{r}) \right]. \end{aligned} \quad (\text{A.20})$$

The restriction $\tau \neq \tau'$ can be lifted-off because for $\tau = \tau'$ the contribution is zero.

We can construct now the energy functional as sum of the contributions given by (A.13) and (A.20). The problem is: we have to find a set of functions $\{\Phi_{\alpha_\tau}\}$, with $\tau = 1, \dots, N$, so that the total energy is minimum. The answer is provided by the variational calculations: we vary the test functions $\{\Phi_\alpha\}$ which depend on the parameter α . Because these wave functions have to be normalized, then we have the supplementary conditions

$$\langle \alpha_\beta | \alpha_\beta \rangle = 1, \quad \beta = 1, \dots, N \quad (\text{A.21})$$

which will be considered by using the Lagrange multipliers ϵ_β . The new functional to be minimized is

$$\mathcal{F} = \langle \Psi_{\alpha_1, \dots, \alpha_N} | H_0 + H_1 | \Psi_{\alpha_1, \dots, \alpha_N} \rangle - \sum_{\beta=1}^N \epsilon_\beta (\langle \alpha_\beta | \alpha_\beta \rangle - 1) = \mathcal{F}(\alpha_1, \dots, \alpha_N) \quad (\text{A.22})$$

The wave function Φ_α is a complex quantity, so that either its real and imaginary parts or Φ and its complex conjugate Φ^* can be considered as independent variables.

The variation of the functional \mathcal{F} is

$$\delta\mathcal{F} = \sum_{i=1}^N \sum_{j=1}^N \left[\frac{\delta\mathcal{F}}{\delta\Phi_{\alpha_j}} \frac{\delta\Phi_{\alpha_j}}{\delta\alpha_i} \delta\alpha_i + \frac{\delta\mathcal{F}}{\delta\Phi_{\alpha_j}^*} \frac{\delta\Phi_{\alpha_j}^*}{\delta\alpha_i} \delta\alpha_i \right] \quad (\text{A.23})$$

Because the one-particle wave function depends only on one parameter,

$$\frac{\delta\Phi_{\alpha_j}}{\delta\alpha_i} = \frac{\delta\Phi_{\alpha_i}}{\delta\alpha_i} \delta_{ij}, \quad \frac{\delta\Phi_{\alpha_j}^*}{\delta\alpha_i} = \frac{\delta\Phi_{\alpha_i}^*}{\delta\alpha_i} \delta_{ij} \quad (\text{A.24})$$

and

$$\delta\mathcal{F} = \sum_{i=1}^N \left[\frac{\delta\mathcal{F}}{\delta\Phi_{\alpha_i}} \frac{\delta\Phi_{\alpha_i}}{\delta\alpha_i} \delta\alpha_i + \frac{\delta\mathcal{F}}{\delta\Phi_{\alpha_i}^*} \frac{\delta\Phi_{\alpha_i}^*}{\delta\alpha_i} \delta\alpha_i \right]. \quad (\text{A.25})$$

The functional \mathcal{F} is minimal if and only if

$$\frac{\delta\mathcal{F}}{\delta\Phi_{\alpha_i}} = 0, \quad \frac{\delta\mathcal{F}}{\delta\Phi_{\alpha_i}^*} = 0. \quad (\text{A.26})$$

We want to remind the definition of the functional derivation

$$\frac{\delta G[\varphi_i(x')]}{\delta\varphi_j(x)} = \lim_{\epsilon \rightarrow 0} \frac{G[\varphi_i(x') + \epsilon\delta_{ij}\delta(x-x')] - G[\varphi_i(x')]}{\epsilon}, \quad (\text{A.27})$$

with the special case

$$\frac{\delta\varphi_i(x')}{\delta\varphi_j(x)} = \delta_{ij}\delta(x-x'). \quad (\text{A.28})$$

Inserting (A.13) and (A.20) in (A.22) and using the above definition we obtain

$$\begin{aligned} \frac{\delta\mathcal{F}}{\delta\Phi_{\alpha_i}(\mathbf{r}'')} &= \sum_{\tau=1}^N \int d^3r \delta_{i\tau} \delta(\mathbf{r} - \mathbf{r}'') h(\mathbf{r}) \Phi_{\alpha_\tau}^*(\mathbf{r}) \\ &+ \frac{1}{2} \sum_{\tau, \tau'=1}^N \int d^3r \int d^3r' \left[\Phi_{\alpha_\tau}^*(\mathbf{r}) \Phi_{\alpha_{\tau'}}^*(\mathbf{r}') - \Phi_{\alpha_{\tau'}}^*(\mathbf{r}) \Phi_{\alpha_\tau}^*(\mathbf{r}') \right] \frac{e^2}{4\pi\epsilon_0\epsilon_r |\mathbf{r} - \mathbf{r}'|} \\ &\quad \left[\delta_{i\tau'} \delta(\mathbf{r}' - \mathbf{r}'') \Phi_{\alpha_\tau}(\mathbf{r}) + \Phi_{\alpha_{\tau'}}(\mathbf{r}') \delta_{i\tau} \delta(\mathbf{r} - \mathbf{r}'') \right] \\ &- \sum_{\beta=1}^N \epsilon_\beta \int d^3r \Phi_{\alpha_\beta}^*(\mathbf{r}) \delta_{i\beta} \delta(\mathbf{r} - \mathbf{r}'') \end{aligned}$$

$$\begin{aligned}
&= h(\mathbf{r}'')\Phi_{\alpha_i}^*(\mathbf{r}'') \\
&+ \frac{1}{2} \sum_{\tau=1}^N \int d^3r \frac{e^2}{4\pi\epsilon_0\epsilon_r|\mathbf{r}-\mathbf{r}''|} \Phi_{\alpha_\tau}^*(\mathbf{r})\Phi_{\alpha_i}^*(\mathbf{r}'')\Phi_{\alpha_\tau}(\mathbf{r}) \\
&+ \frac{1}{2} \sum_{\tau'=1}^N \int d^3r' \frac{e^2}{4\pi\epsilon_0\epsilon_r|\mathbf{r}'-\mathbf{r}''|} \Phi_{\alpha_i}^*(\mathbf{r}'')\Phi_{\alpha_{\tau'}}^*(\mathbf{r}')\Phi_{\alpha_{\tau'}}(\mathbf{r}') \\
&- \frac{1}{2} \sum_{\tau=1}^N \int d^3r \frac{e^2}{4\pi\epsilon_0\epsilon_r|\mathbf{r}-\mathbf{r}''|} \Phi_{\alpha_i}^*(\mathbf{r})\Phi_{\alpha_\tau}^*(\mathbf{r}'')\Phi_{\alpha_\tau}(\mathbf{r}) \\
&- \frac{1}{2} \sum_{\tau'=1}^N \int d^3r' \frac{e^2}{4\pi\epsilon_0\epsilon_r|\mathbf{r}'-\mathbf{r}''|} \Phi_{\alpha_{\tau'}}^*(\mathbf{r}'')\Phi_{\alpha_i}^*(\mathbf{r}')\Phi_{\alpha_{\tau'}}(\mathbf{r}') \\
&- \epsilon_i\Phi_{\alpha_i}^*(\mathbf{r}'')
\end{aligned} \tag{A.29}$$

which using Eq.(A.26) and interchanging $\mathbf{r} \leftrightarrow \mathbf{r}''$ provides the *Hartree-Fock equations*:

$$\begin{aligned}
h(\mathbf{r})\Phi_{\alpha_i}^*(\mathbf{r}) &+ \sum_{\tau=1}^N \int d^3r'' \frac{e^2|\Phi_{\alpha_\tau}(\mathbf{r}'')|^2}{4\pi\epsilon_0\epsilon_r|\mathbf{r}-\mathbf{r}''|} \Phi_{\alpha_i}^*(\mathbf{r}) - \sum_{\tau=1}^N \int d^3r'' \frac{e^2\Phi_{\alpha_i}^*(\mathbf{r}'')\Phi_{\alpha_\tau}(\mathbf{r}'')}{4\pi\epsilon_0\epsilon_r|\mathbf{r}-\mathbf{r}''|} \Phi_{\alpha_\tau}^*(\mathbf{r}) \\
&= \epsilon_i\Phi_{\alpha_i}^*(\mathbf{r}), \quad i = 1, \dots, N.
\end{aligned} \tag{A.30}$$

Analogously we can obtain the equations for $\Phi_{\alpha_i}(\mathbf{r})$:

$$\begin{aligned}
h(\mathbf{r})\Phi_{\alpha_i}(\mathbf{r}) &+ \sum_{\tau=1}^N \int d^3r'' \frac{e^2|\Phi_{\alpha_\tau}(\mathbf{r}'')|^2}{4\pi\epsilon_0\epsilon_r|\mathbf{r}-\mathbf{r}''|} \Phi_{\alpha_i}(\mathbf{r}) - \sum_{\tau=1}^N \int d^3r'' \frac{e^2\Phi_{\alpha_i}(\mathbf{r}'')\Phi_{\alpha_\tau}^*(\mathbf{r}'')}{4\pi\epsilon_0\epsilon_r|\mathbf{r}-\mathbf{r}''|} \Phi_{\alpha_\tau}(\mathbf{r}) \\
&= \epsilon_i\Phi_{\alpha_i}(\mathbf{r}), \quad i = 1, \dots, N.
\end{aligned} \tag{A.31}$$

The Eq.(A.30) is the complex conjugate of the Eq. (A.31). If we would let the restriction $\tau \neq \tau'$ in the Eq. (A.20), then we had obtained $\tau \neq i$ in both sums. The first term and the second term represent the kinetic energy and the potential energy of the i -th electron. The $\tau = i$ contribution is very small considering that the total number of electrons in discussed system is about 10^{23} . The third term is the *exchange* term, which is a 'non-local' potential, that cannot be written as a simple function that multiplies the wave function $\Phi_{\alpha_i}(\mathbf{r})$. This term is also called *Fock* term and makes the Hartree-Fock equations a nonlinear integro-differential equation. It is a direct consequence of the antisymmetrization of the many-particle wave functions Ψ .

Here we should note that α represents in fact a set of quantum numbers that characterizes an one-particle state. In the second term appears \sum_{α} which means also sum over spin. The exchange term has no such a sum, so it causes repulsion between electrons of the same spin, which is hardly surprising as this is the new feature that we have built into the many-particle wave function (A.1) by forcing it to obey the Pauli principle.

The energies ϵ_{β} were introduced as Lagrange multiplier. If one interprets the Hartree-Fock equations as one-particle Schrödinger equation for one electron in an

effective potential, then they receive the meaning of the eigenenergies. It is a well known feature of the self-consistent mean-field theory that the total energy is not equal to the sum of occupied single-particle energies ϵ_i [91]. The total energy is $E_{HF} = \langle \Psi | H_0 + H_1 | \Psi \rangle$ and if one multiplies the Eq. (A.31) by $\Phi_{\alpha_i}^*(\mathbf{r})$ and integrates over d^3r and sums over i then obtains on the right side $\sum \epsilon_i$. On the left side, in comparison with the total energy, appears the Hartree and Fock contributions two times bigger. This happened because we counted also the interaction of the electron i with itself, so that

$$\sum_i \epsilon_i = E\{|\Psi\rangle\} + E_{SE} = E\{|\Psi\rangle\} + \langle \Psi | H_1 | \Psi \rangle = \langle \Psi | H_0 | \Psi \rangle + 2\langle \Psi | H_1 | \Psi \rangle \quad (\text{A.32})$$

If one neglects the exchange term in Eq. (A.31), then what remain are the *Hartree* equations which have a direct physical meaning as it is discussed in the Sec. 2.4.

Appendix B

List of symbols

Symbol	Meaning
e	elementary charge ($e=1.60218 \times 10^{-19}$ C)
ρ	electronic density distribution ($1/\text{cm}^3$)
n	quantum number for the quantization on the transport direction
m_0	free-electron mass (Kg)
k_F	Fermi wave vector ($1/\text{m}$)
ϕ_{n,k_x,k_y}	total wave function
$\psi_n(z)$	wave function in growth direction z
$\psi_n^L(z)$	wave function coming from left reservoir
$\psi_n^R(z)$	wave function coming from right reservoir
\mathbf{k}_t	transverse components of the wavevector relative to the barrier ($1/\text{m}$)
k_z	perpendicular component of the wavevector relative to the barrier ($1/\text{m}$)
μ_L	chemical potential in left reservoir (eV)
μ_R	chemical potential in right reservoir (eV)
V_L	constant potential in left reservoir (eV)
V_R	constant potential in right reservoir (eV)
V_1	left boundary value for Poisson equation (eV)
V_2	right boundary value for Poisson equation (eV)
$e\Phi_{Bn}$	the barrier height at metal-semiconductor contact
j, J	current density (A/cm^2)
σ_1, σ_2	concentration of δ sheet charge distributions ($1/\text{m}^2$)
G	conductance
σ	conductivity
L_ϕ	dephasing length (nm)
z	growth direction (perpendicular to the interfaces of the sample)
x, y	directions perpendicular to the growth direction (parallel with the interfaces)
E	total energy of an electron (eV)

ϵ	energy on transport direction, perpendicular to interfaces (eV)
E_t	energy on transverse directions, parallel with interfaces (eV)
μ_0	permeability in vacuum
ϵ_0	permittivity in vacuum
V_{SD}	applied bias between source and drain (V)
V_{sd}	effective drop bias on active region (V)
V_G	applied bias between substrate and gate (V)
V_g	applied bias between substrate and gate, with respect to flat band configuration (V)
V_c	electronic potential energy due to the Coulomb interaction (eV)
φ	electrostatic potential (V)

Bibliography

- [1] S.M. Sze *Physics of semiconductor devices* 2nd edition, John-Wiley & Sons, Inc. New York 1981.
- [2] David K. Ferry, Stephen M. Goodnick *Transport in Nanostructures*, Cambridge University Press, 1997.
- [3] H. Fukuyama and T. Ando (Eds.), *Transport Phenomena in Mesoscopic Systems* Springer-Verlag, Berlin, 1992.
- [4] L. L. Chang and K. Ploog (Eds.), *Molecular Beam Epitaxy and Heterostructures*, M. Nijhof, Dordrecht, The Netherlands 1985.
- [5] R. Dingle, H.L. Störmer, A.C. Gossard, and W. Wiegmann, *Electron mobilities in modulation-doped semiconductor heterojunction superlattices*, Appl. Phys. Lett. **33**, 665, (1978). H.L. Störmer, R. Dingle, A.C. Gossard, W. Wiegmann and M.D. Sturge *2-dimensional electron-gas at a semiconductor-semiconductor interface* Solid State Comm. **29**, 705, (1979).
- [6] Y. Hirayama, K. Muraki and T. Saku, *Two-dimensional electron gas formed in a back-gated undoped heterostructure*, Appl. Phys. Lett. **72**, 1745, (1998); J. Herfort and Y. Hirayama, *Transport in gated undoped GaAs/Al_xGa_{1-x}As heterostructures in the high density and high mobility range*, Appl. Phys. Lett. **69**, 3360, (1996)
- [7] H. Mizuta and T. Tanoue, *The Physics and Applications of Resonant Tunneling Diodes*, Edited by H. Ahmed, M. Pepper, A. Broers Cambridge University Press 1995.
- [8] E.R. Brown, T.C.L.G. Sollner, C.D. Parker, W.D. Goodhue, and L.C. Chen, *Oscillations up to 420 GHz in GaAs/AlAs resonant tunneling diodes*, Appl. Phys. Lett. **55**, 1777 (1989).
- [9] M.A. Reed, W.R. Frensley, R.J. Matyi, J.R. Randal, and A.C. Seabaugh, *Realization of a three-terminal resonant tunneling device: The bipolar quantum resonant tunneling transistor* Appl. Phys. Lett. **54**, 1034 (1989).

- [10] S. Datta, *Electronic Transport in Mesoscopic Systems* Cambridge University Press, UK, 1995.
- [11] For review articles see, for example T. Dittrich et al., *Quantum Transport and Dissipation* Wiley-VCH, Weinheim, 1998; H. Haug and A.-P. Jauho, *Quantum Kinetics in Transport and Optics of Semiconductors* Springer, Berlin, 1996.
- [12] A. B. Fowler, A. Hartstein, and R. A. Webb, *Conductance in restricted-dimensionality accumulation layers*, Phys. Rev. Lett. **48**, 196 (1982); P. A. Lee, A. D. Stone, and H. Fukuyama, *Universal conductance fluctuations in metals - effects of finite temperature, interactions, and magnetic-field*, Phys. Rev. B **35**, 1039 (1987).
- [13] D. Yu. Sharvin and Yu. v. Sharvin, *Magnetic-flux quantization in a cylindrical film of a normal metal*, Pis'ma Zh.Eksp.Teor.Fiz. **34**, 285 (1981) [JETP Lett **34**, 272 (1981)]; M. Büttiker, Y. Imry, R. Landauer, and S. Pinhas, *Generalized many-channel conductance formula with application to small rings*, Phys. Rev. B **31**, 6207 (1985).
- [14] P. Středa, J. Kučera, and A. H. MacDonald, *Edge states, transmission matrices, and the Hall resistance*, Phys. Rev. Lett. **59**, 1973 (1987); M. Büttiker, *Absence of backscattering in the quantum Hall-effect in multiprobe conductors*, Phys. Rev. B **38**, 9375 (1988).
- [15] M. L. Roukes et al., *Quenching of the Hall-effect in a one-dimensional wire*, Phys. Rev. Lett. **59**, 3011 (1987); H. U. Baranger and A. D. Stone, *Quenching of the Hall resistance in ballistic microstructures - a collimation effect* *ibid.* **63**, 414 (1989).
- [16] B. J. van Wees et al., *Quantized conductance of point contacts in a two-dimensional electron gas*, Phys. Rev. Lett. **60**, 848 (1988); L. I. Glazman, G. B. Lesovick, D. E. Kmel'nitskii, and R. I. Shekhter, *Reflectionless quantum transport and fundamental ballistic-resistance steps in microscopic constrictions*, Pis'ma Zh.Eksp.Teor.Fiz. **48**, 218 (1988) [JETP Lett. **48**, 238 (1988)]; A. Szafer and A.D. Stone, *Theory of Quantum Conduction through a Constriction*, Phys. Rev. Lett. **62**, 300 (1989).
- [17] U. Meirav, M. A. Kastner, and S. J. Wind, *Single-electron charging and periodic conductance resonances in GaAs nanostructures* Phys. Rev. Lett. **65**, 771 (1990); Y. Meir, N. S. Wingreen, and P. A. Lee, *Transport through a strongly interacting electron system: Theory of periodic conductance oscillations* *ibid.* **66**, 3048 (1991); Y. Meir and N. S. Wingreen, *Landauer formula for the current through an interacting electron region*, *ibid.* **68**, 2512 (1992).
- [18] R. A. Jalabert, A. D. Stone, and Y. Alhassid, *Statistical theory of Coulomb blockade oscillations: Quantum chaos in quantum dots* Phys. Rev. Lett. **68**,

- 3468 (1992); Y. Alhassid and C. H. Lewenkopf, *Signatures of chaos in the statistical distribution of conductance peaks in quantum dots*, Phys. Rev. **B 55**, 7749 (1997). A. D. Stone, R. A. Jalabert, and Y. Alhassid, in *Transport Phenomena in Mesoscopic Systems* (Ref. [11]);
- [19] R. Landauer, *Spatial variation of currents and fields due to localized scatterers in metallic conduction*, IBM J. Res. Develop. **1**, 223, (1957)
- [20] R. Landauer, *Electrical transport in open and closed systems*, Z. Phys. **B 68**, 217, (1987).
- [21] M. Büttiker, *Four terminal phase-coherent conductance*, Phys. Rev. Lett. **57**, 1761 (1986); M. Büttiker, *Symmetry of electrical conduction*, IBM J. Res. Develop. **32**, 317 (1988).
- [22] M. Büttiker, *Scattering theory of current and intensity noise correlations in conductors and wave guides* Phys. Rev. B **46**, 12485, (1992).
- [23] A. D. Stone and A. Szafer, *What is measured when you measure a resistance - the Landauer formula revisited*, IBM J. Res. Develop. **32**, 384 (1988).
- [24] R. Tsu and L. Esaki, *Tunneling in a finite superlattice* Appl. Phys. Lett. **22**, 562 (1973)
- [25] D. S. Fisher and P. A. Lee, *Relation between conductivity and transmission matrix*, Phys. Rev. B **23**, 6851 (1981);
- [26] A. MacKinnon, *The calculation of transport-properties and density of states of disordered solids*, Z. Phys. B **59**, 385 (1985); T. Ando, *Quantum point contacts in magnetic fields*, Phys. Rev. B **44**, 8017 (1991).
- [27] T. Usuki, M. Saito, M. Takatsu, R. A. Kiehl, and N. Yokoyama, *Numerical analysis of ballistic-electron transport in magnetic fields by using a quantum point contact and a quantum wire*, Phys. Rev. B **52**, 8244 (1995); J. P. Bird, R. Akis, D. K. Ferry, D. Vasileska, J. Cooper, Y. Aoyagi, and T. Sugano, *Lead-orientation-dependent wave function scarring in open quantum dots*, Phys. Rev. Lett. **82**, 4691 (1999).
- [28] For a comprehensive review of the S-matrix theory see for example M. L. Goldberger and K. Watson, *Collision Theory*, John Wiley and sons, New York, 1964; A. Bohm, *Quantum Mechanics*, Springer, New York, 1994; A. Galindo, P. Pascual, *Quantum Mechanics*, Springer, Berlin, 1990.
- [29] Neumaier A, V. A. Mandelshtam, *Pseudotime Schrodinger equation with absorbing potential for quantum scattering calculations*, Phys. Rev. Lett. **86**, 5031, (2001).

- [30] E. Persson, I. Rotter, H. J. Stöckmann, and M. Barth, *Observation of Resonance Trapping in an Open Microwave Cavity*, Phys. Rev. Lett. **85**, 2478 (2000); P. Seba, I. Rotter, M. Mller, E. Persson, K. Pichugin, *Open microwave cavities*, Physica E **9**, 484 (2001).
- [31] For reviews of the method see, for example, A. M. Lane, and R. G. Thomas, *R-Matrix Theory of Nuclear Reactions*, Rev. Mod. Phys. **30**, 257 (1958); J. M. Blatt and V. Weisskopf, *Theoretische Kernphysik*, (Teubner 1959); *Atomic and Molecular Processes: an R -Matrix Approach* edited by P. G. Burke and K. A. Berrington, Institute of Physics Publishing, Bristol, 1993.
- [32] J. Stein, H.-J. Stöckmann, and U. Stoffregen, Phys. Rev. Lett. **75**, 53 (1995); for a review see H.-J. Stöckmann, *Quantum Chaos*, Cambridge University Press, Cambridge 1999
- [33] L. Smrčka, *R-matrix and the coherent transport in mesoscopic systems*, Superlattices and Microstructures, **8**, 221 (1990).
- [34] Y. Alhassid and H. Attias, *Universal correlations of Coulomb-blockade conductance peaks and the rotation scaling in quantum dots* Phys. Rev. B **54**, 2696 (1996); Y. Alhassid and H. Attias, *Universal Parametric Correlations of Conductance Peaks in Quantum Dots* Phys. Rev. Lett. **76**, 1711 (1996).
- [35] Y. Alhassid, *The statistical theory of quantum dots*, Rev. Mod. Phys. **72**, 895 (2000).
- [36] G. Bastard, *Superlattice band structure in the envelope-function approximation* Phys. Rev. B **24**, 5693, (1981); G. Bastard, *Theoretical investigations of superlattice band structure in the envelope-function approximation* Phys. Rev. B **25**, 7584, (1982).
- [37] M.G. Burt *The justification for applying the effective-mass approximation to microstructures*, J. Phys.: Condens. Matter **4**, 6651, (1992).
- [38] J. Kučera, U. Wulf and P.N. Racec, *Seminar notes*, BTU Cottbus, 1996.
- [39] R. Shankar, *Principles of Quantum Mechanics*, 2nd ed. Plenum Press New York, 1994.
- [40] Claude Weisbuch and Birge Vinter, *Quantum semiconductor structures - fundamentals and applications*, Academic Press Inc. 1991.
- [41] E.P.Wigner, L.Eisenbud, *Higher angular momenta and long range interaction in resonance reactions* Phys. Rev. **72**, 29, (1947).

- [42] Yan V. Fyodorov and Hans-Jürgen Sommers *Statistical of resonance poles, phase shifts and time delays in quatum chaotic scattering: Random matrix approach for systems with broken time-reversal invariance*, J.Math.Phys. **38**, 1918, (1997).
- [43] E.E. Mendez *Physics of resonant tunneling in semiconductors*, Proceedings of "NATO Advanced" Study Institute, Ed. E.E. Mendez and K. von Klitzing, NATO ASI Series Series, Series B, Physics **170**, 159, (1987).
- [44] B. Ricco and M.Ya Azbel, *Physics of resonant tunneling. The one-dimensional double-barrier case*, Phys. Rev. B **29**, 1970, (1984)
- [45] S.S. Allen and S.L. Richardson, *Theoretical investigations of resonant tunneling in asymmetric multibarrier semiconductor heterostructures in an applied constant electric field*, Phys. Rev. B **50**, 11693, (1994).
- [46] E.R. Racec and U. Wulf, *Resonant quantum transport in semiconductor nanostructures*, Phys. Rev. B **64**, 115318, (2001).
- [47] Neil W. Ashcroft and N. David Mermin, *Solid state physics*, W.B. Saunders Company 1976.
- [48] B. Zimmermann, E. Marclay, and M. Ilegems *Self-consistent calculations of tunneling currents in n-GaAs/i-Al_xGa_{1-x}As/n-GaAs structures and comparison with measurements* J. Appl. Phys. **64**, 3581, (1988).
- [49] William H.Press (Ed.), et al *Numerical Recipies in FORTRAN The Art of Scientific Computing*, Chapt. 4, Cambridge University Press, 1992.
- [50] E.H. Nicollian and J.R. Brews, *MOS (Metal Oxide Semiconductor) Physics and Technology*, Wiley, New York, 1982.
- [51] F.F. Fang and W.E. Howard *Negative field-effect mobility on (100) Si surface* Phys. Rev. Lett. **16**, 797, (1966).
- [52] H. Stumpf, W. Schuler *Elektrodynamik*, Vieweg & Sohn, Braunschweig/Wiesbaden, 1973.
- [53] T. Ando, A.B. Fowler, F. Stern *Electronic properties of two-dimensional systems*, Reviews of Modern Physics **54**, 437 (1982).
- [54] F. Stern and S. Das Sarma, *Electron energy levels in GaAs-Ga_{1-x}Al_xAs heterojunctions* Phys. Rev. B **30**, 840, (1984).
- [55] T. Jungwirth and L. Smrčka, *Self - consistent electron subbands of GaAs/AlGaAs heterostructures in magnetic fields parallel to the interface* J. Phys.: Condens. Matter **5** L217, (1993).

- [56] W. Xu, *Self-consistent subband structure of modulation-doped $Al_xGa_{1-x}As$ - $GaAs$ - $Al_xGa_{1-x}As$ double quantum wells* International Journal of Modern Physics B, **10**, 1293, (1996).
- [57] Chihiro Hamaguchi, Kazuo Miyatsuji and Hiroki Hihara *A proposal of single quantum well transistor (SQWT) -Self-consistent calculations of 2D Electrons in a quantum well with external voltage*, Jpn. J. Appl. Phys. **23**, L132, (1984)
- [58] Yukihiro Tanaka and Hiroshi Akera, *Self-Consistent Calculation of the Charging Energy in a Quantum Dot Coupled to Leads*, J. Phys. Soc. Jpn. **66**, 15, (1997).
- [59] Supriyo Datta *Exclusion principle and the Landauer-Büttiker formalism*, Phys. Rev. B **45**, 1347, (1992).
- [60] J. J. Liou, Phys. Stat. Sol. (a) **112**, 651, (1989).
- [61] Y. Hu and S. Stapleton, *Quantum capacitance of resonant tunneling diodes* Appl. Phys. Lett. **58**, 167, (1991).
- [62] J. P. Sun, R. K. Mains, W. L. Chen, J. R. East, and G. I. Haddad, *C-V and I-V characteristics of quantum well varactors* J. Appl. Phys. **72**, 2340, (1992).
- [63] T. Wei and S. Stapleton, *Effect of spacer layers on capacitance of resonant tunneling diodes* J. Appl. Phys. **76**, 1287, (1994).
- [64] C. R. Moon, B. Choe, D. W. Kwon, and H. Lim, *Electron distribution and capacitance-voltage profiles of multiple quantum well structure from self-consistent simulations* Appl. Phys. Lett. **70**, 2987, (1997).
- [65] Y. Zhang, Y. Li, D. Jiang, X. Xiaoping, and P. Zhang, *Giant capacitance oscillations related to the quantum capacitance in $GaAs/AlAs$ superlattices*, Appl. Phys. Lett. **64**, 3416, (1994).
- [66] W. Hansen, A. Schmeller, H. Drexler, J. P. Kotthaus, M. Holland, G. Tränkle, G. Bohm, and G. Weimann, *Semiconductor Science and Technology* **9**, 1946, (1994).
- [67] S. Luryi, *Quantum capacitance devices*, Appl. Phys. Lett. **52**, 501, (1988).
- [68] J. Jo, E. A. Garcia, K. M. Abkemeier, M. Santos, and M. Shayegan, *Probing the subband structure of a wide electron system in a parabolic quantum well via capacitance-voltage measurements*, Phys. Rev. B **47**, 4056, (1993).
- [69] T. Jungwirth and L. Smrčka, *Capacitance of gated $GaAs/Al_xGa_{1-x}As$ heterostructures subject to in plane magnetic fields*, Phys. Rev. B **51**, 10181, (1995).

- [70] J. Hampton, J. P. Eisenstein, L. N. Pfeiffer, K. W. West, *Capacitance of two-dimensional electron systems subject to an in-plane magnetic field*, Solid State Commun. **94**, 559, (1995).
- [71] V.T. Dolgoplov, A.A. Shashkin, A.V. Aristov, D. Schmerek, H. Drexler, W. Hansen, J.P. Kotthaus, and M. Holland, *Nonlinear Screening in two-dimensional electrons systems*, Phys.Low-Dim. Struct. **6**, 1, (1996).
- [72] S. Kundu, D. Biwas, and R. Datta, *Anomalous capacitance-voltage profiles in quantum wells explained by a quantum mechanical model*, J. Appl. Phys. **81**, 2030, (1997).
- [73] H. Drexler, W. Hansen, S. Manus, J. P. Kotthaus, M. Holland, and S. P. Beaumont, *One-dimensional electron channels in the quantum limit*, Phys. Rev. B **49**, 14074, (1994). *idem*. *Quantum wires with a widely tunable confining potential*, Physica Scripta **55**, 65 (1994); *idem*, *Transport studies and infrared-spectroscopy on ALAs/GaAs MIS heterojunctions without dopants in the barrier*, Semicond. Sci. Technol. **7**, 10098, (1992)
- [74] W. Hansen, T. P. Smith III, K. Y. Lee, J. A. Brum, C. M. Knoedler, J. M. Hong, and D. P. Kern, *Zeeman bifurcation of quantum-dot spectra*, Phys. Rev. Lett. **62**, 2168, (1989).
- [75] R. C. Ashoori, H. L. Stormer, J. S. Weiner, L. N. Pfeiffer, S. J. Pearton, K. W. Baldwin, and K. W. West, *Single-electron capacitance spectroscopy of discrete quantum levels*, Phys. Rev. Lett. **68**, 3088, (1992) D. Berman, N. B. Zhitenev, R. C. Ashoori, and M. Shayegan, *Observation of Quantum Fluctuations of Charge on a Quantum Dot*, Phys. Rev. Lett. **82**, 161, (1999).
- [76] M.J. Kelly *Low-dimensional semiconductors: materials, physics, technology, devices* Oxford Science Publications Clarendon Press Oxford, 1995.
- [77] P. Guéret, C. Rossel, E. Marclay, and H. Meier, *Investigations on resonant tunneling in III-V heterostructures*, J. Appl. Phys. **66**, 278, (1989).
- [78] I. Vurgaftman, J.R. Meyer and L.R. Ram-Mohan, *Band parameters for III-V compound semiconductors and their alloys*, J. Appl. Phys. **89**, 5815, (2001).
- [79] D. Schmerek and W. Hansen, *Exchange and correlation effects on the ground states of quantum wires*, Phys. Rev. B **60**, 4485, (1999).
- [80] T.P. Smith III, W.I. Wang, and P.J. Stiles, *Two-dimensional density of states in the extreme quantum limit*, Phys. Rev. B **34**, 2995, (1986).
- [81] J. P. Eisenstein, L. N. Pfeiffer, and K. W. West *Negative compressibility of interacting two-dimensional electron and quasiparticle gases* Phys. Rev. Lett. **68**, 674, (1992); *idem*. *Compressibility of the two-dimensional electron gas:*

- Measurements of the zero-field exchange energy and fractional quantum Hall gap* Phys. Rev. B **50**, 1760, (1994).
- [82] W. Magnus and W. Schoenmaker, *Full quantum mechanical model for the charge distribution and the leakage currents in the ultrathin metal-insulator-semiconductor capacitors*, J. Appl. Phys. **88**, 5833 (2000).
- [83] I. Kukulín, M. Krasnopolsky, and J. Horacek, *Theory of Resonances: Principles and Applications* Kluwer, Dordrecht, 1989.
- [84] J.C.Inkson, *Many-body theory of solids*, Plenum Press, New York and London, 1984.
- [85] P. Hohenberg and W. Kohn, *Inhomogeneous Electron Gas*, Phys. Rev. **v136**, B864, (1964); W. Kohn and L.J. Sham, *Self-consistent equations including exchange and correlations effects* Phys. Rev **140**, A1133 (1965).
- [86] G.A. Baraff and J.A. Appelbaum, *Effect of electric and magnetic fields on the self-consistent potential at the surface of a degenerate semiconductor* Phys. Rev. B **5**, 475 (1972).
- [87] A. G. C. Haubrich, D. A. Wharam, H. Kriegelstein, S. Manus, A. Lorke, J. P. Kotthaus, and A. C. Gossard, *Parallel quantum-point-contacts as high-frequency-mixers*, Appl. Phys. Lett. **70**, 3251 (1997).
- [88] R. Buczko and F. Bassani, *Bound and resonant electron states in quantum dots: The optical spectrum*, Phys. Rev. B **54**, 2667 (1996).
- [89] See for example R. H. Landau, *Quantum Mechanics II* (John Wiley & Sons, New York, 1996, Chap. 5.
- [90] M.Y.Azbel and D.P.DiVicenzo, *Finite-temperature conductance in one dimension*, Phys. Rev. B **30**, 6877, (1984); J.L.D'Amato and H.M.Pastawski, *Conductance of a disordered linear chain including inelastic scattering events*, *ibid.* **41** 7411 (1990).
- [91] Gerd Czycholl *Theoretische Festkörperphysik*, Chap. 5.3. Vieweg Verlag, Braunschweig/Wiesbaden, 2000.
- [92] P.N. Racec, T. Stoica, C. Popescu, M. Lepsa and Th.G.van de Roer *Physics of optimal resonant tunneling*, Phys. Rev. B **56**, 3595, (1997).
- [93] U. Wulf, J. Kučera, P.N. Racec, and E. Sigmund, *Transport through semiconductor quantum systems in the R-matrix formalism*, Phys. Rev. B **58** 16209,(1998).
- [94] P.N. Racec, U. Wulf, and J. Kučera, *Integration of quantum transport models in classical device simulators*, Solid-State Electronics **44**, 881, (2000).

- [95] P.N. Racec, E.R.Racec, and U. Wulf, *Capacitance theory of open quantum systems with classical contacts*, Computational Materials Science **21**, 475, (2001)
- [96] P.N. Racec, E.R.Racec, and U. Wulf, *Capacitance in open quantum structures*, Phys. Rev. B **65**, 193314, (2002)

Danksagung

Ich möchte die Gelegenheit nutzen, um allen, die mir auf dem Weg zu dieser Arbeit geholfen haben, Dank auszusprechen.

Herrn Prof. Dr. Ernst Sigmund danke ich für seine großzügige Unterstützung und für die Aufnahme an seinem Lehrstuhl.

Mein ganz herzlicher Dank gilt Herrn Dr. Ulrich Wulf. Zahlreiche fruchtbare Diskussionen haben dieser Arbeit stets einen Impuls gegeben. Er hat mich ermutigt, viel auszuprobieren und immer selbständige Wege zu gehen. Nicht zu vergessen ist seine Hilfsbereitschaft in allen Problemen, die eine Promotion im Ausland mit sich bringt. Herrn Dr. Jan Kučera danke ich für die vielen Gespräche und wertvollen Hinweise betreffs des R-matrix Formalismus und der mit Transportphänomenen verbundenen Fragen, von welchen ich vor allem im fünften Kapitel dieser Arbeit profitieren konnte. Bei Herrn Prof. Dr. Wolfgang Hansen möchte ich mich für die hilfreichen Diskussionen über die Kapazitätsspektroskopie und für die Bereitstellung experimenteller Messdaten bedanken.

Ich möchte mich bei Herrn Prof. Dr. Andreas Wieck für die Einladung nach Bochum bedanken. Während meines Aufenthaltes an der Ruhr-Universität bin ich an seinem Lehrstuhl mit experimentellen Verfahren und den damit verbundenen Fragen näher gekommen.

I would like to express my gratitude to Dr. Corneliu Popescu and Dr. Toma Stoica from National Institute for Research and Development Materials Physics, Bucharest Romania. They offered me the opportunity to start the research in this very interesting field of physics and their valuable discussions opened me the view into the important questions of quantum semiconductor phenomena. They constituted for me the permanent connection with the research interest in my country. I am also very grateful their research group for helping in the administrative problems connected with my absence during my PhD study in Germany. I would like to thank Dr. Andrei Manolescu who recommended me for this PhD position at BTU Cottbus.

Ein Teil dieser Arbeit wurde von der Deutschen Forschungsgemeinschaft (DFG) im Rahmen des Projektes "Theoretische Untersuchung von Transport in Halbleiternanostrukturen unter Verwendung von kohärenten Streuzustände" (SI 304/5) finanziert.

Bei Herrn Prof. Dr. Michael Bestehorn bedanke ich mich für die finanzielle Unterstützung im letzten Jahr, die den Abschluss meiner Promotion erleichtert hat.

Meinen Kollegen an den Lehrstühlen der Theoretischen Physik der BTU Cottbus gilt mein Dank für die fröhliche Umgebung, in der es sich gut arbeiten ließ.

Für das Verstehen, Lesen und Schreiben der deutschen Sprache, möchte ich mich bei Frau Dr. Renate Kranzusch und Herrn Dr. Jochen Schöttner ganz herzlich bedanken. In ihrem Sprachkurs lernten sie uns die Schönheit der deutschen Sprache in voller Pracht kennen.

Mein ganz persönlicher Dank gilt meiner geliebten Frau Roxana und meinen Eltern, die mir durch ihre ständige Unterstützung diese Arbeit erst ermöglicht haben.

Lebenslauf

Persönliche Daten

Name Paul Nicolae Racec
Adresse Str. Delinesti nr. 2
Bl. A5, Sc. B, Ap. 23
77494 Bucuresti, sect.6
Rumänien
geboren am 15. April 1972 in Campulung Moldovenesc, Rumänien
Familienstand verheiratet

Schulausbildung

1978-1982 Grundschule in Moldovita, Rumänien
1982-1986 Gymnasium in Moldovita, Rumänien
1986 -1990 Gymnasium "Stefan cel Mare" in Suceava, Rumänien
6.1990 Abitur

Studium

10.1990-6.1995 Fakultät für Physik, Fach Festkörper Physik
Universität Bukarest, Rumänien
6.1995 Diplom Physiker
10.1995-6.1996 Vertiefende Studium, Fach Halbleiter Physik
Universität Bukarest, Rumänien
6.1996 Master's Degree

Berufliche Tätigkeiten

seit 10.1995 Wissenschaftlicher Mitarbeiter am National Institut für
Materialienwissenschaften Bukarest, Rumänien
seit 11.1996 Wissenschaftlicher Mitarbeiter und Doktorand
BTU Cottbus, Lehrstuhl für Theoretische Physik
06.-07. 2000 Gast Wissenschaftler, Ruhr-Universität Bochum,
Lehrstuhl für Angewandte Festkörperphysik